MICROSTRUCTURAL DESIGN OF TOUGH CERAMICS FOR CONTACT DAMAGE RESISTANCE

HELEN M. CHAN and BRIAN R. LAWN

Department of Materials Science and Engineering
Lehigh University
Bethlehem, PA 18015

FINAL REPORT

AFOSR Contract No. F49620-95-1-0187
Amendment P00001

for

Air Force Office of Scientific Research
801 N. Randolph St.
Arlington VA 22203

DISTRIBUTION STATEMENT A
Approved for Public Release
Distribution Unlimited

19990629 060

DTIC QUALITY INSPECTED 4

REPORT DOCUMENTATION PAGE

AFRL-SR-BL-TR-99-

0160

JUN 1999

Public reporting burden for the collection of information is estimated to average 1 hour per response, including the time for reviewing instructions, searching existing data sources, gathering and maintaining the data needed, and collecting and reviewing the collection of information. Send comments regarding this burden estimate or any other aspect of this collection of information, including suggestions for reducing this burden, to Washington Headquarters Services, Directorate for Information Operations and Reports, 1215 Jefferson Davis Highway, Suite 1204, Arlington, VA 22202-4302, and to the Office of Management and Budget, Paperwork Reduction Project (0704-0183), Washington, D.C. 20503.

1. AGENCY USE ONLY (*Leave blank*)	2. REPORT DATE	3. REPORT TYPE AND DATES COVERED
	May 1999	FINAL REPORT (2/95--8/98)

4. TITLE AND SUBTITLE

Microstructural Design of Tough Ceramics for Contact Damage Resistance

5. FUNDING NUMBERS

AFOSR# F49620-95-1-0187 Amendment P00001

6. AUTHOR(S)

Helen M. Chan and Brian R. Lawn

7. PERFORMING ORGANIZATION NAME(S) AND ADDRESS(ES)

Department of Materials Science and Engineering
Lehigh University
Bethlehem, PA 18015-3195

8. PERFORMING ORGANIZATION REPORT NUMBER

9. SPONSORING/MONITORING AGENCY NAME(S) AND ADDRESS(ES)

Air Force Office of Scientific Research
801 North Randolph Street
Arlington, VA 22203

10. SPONSORING/MONITORING AGENCY REPORT NUMBER

11. SUPPLEMENTARY NOTES

12a. DISTRIBUTION/AVAILABILITY STATEMENT

Unlimited

12b. DISTRIBUTION CODE

13. ABSTRACT (*Maximum 200 words*)

The results of research investigating contact damage and fatigue of ceramics is described, with particular attention to microstructural design. The aims were as follows: (i) To develop experimental testing methodologies, using Hertzian contacts, for studying the fundamental short-crack damage properties of tough ceramics, notably in silicon carbide and silicon nitride; (ii) To examine the role of critical microstructural variables (grain size and shape, grain boundary phase, interface energy, internal stress) on the nature of the ensuing contact damage; (iii) To investigate the effect of the damage on associated mechanical properties, e.g. strength degradation, fatigue resistance, wear resistance; (iv) To process and modify ceramic materials in order to improve the above properties; (v) To develop theoretical models of the damage micromechanics; (vi) To establish design engineering criteria for materials selection and optimization. The proposed program has led to new insights into the role of micromechanical phenomena in mechanical behavior of tough ceramics, insights that will ultimately bear on practical areas such as bearing mechanics, cyclic fatigue, ceramic design, and coating-substrate technology.

14. SUBJECT TERMS

15. NUMBER OF PAGES

20

16. Price code

17. SECURITY CLASSIFICATION OF REPORT	18. SECURITY CLASSIFICATION OF THIS PAGE	19. SECURITY CLASSIFICATION OF ABSTRACT	20. LIMITATION OF ABSTRACT
Unclassified	Unclassified	Unclassified	

MICROSTRUCTURAL DESIGN FOR TOUGH CERAMICS

		Page
1.	COVER SHEET	1
2.	OBJECTIVES	2
3.	STATUS	3
4.	ACCOMPLISHMENTS	4
5.	PERSONNEL SUPPORTED	6
6.	PUBLICATIONS	7
7.	INTERACTIONS/TRANSITIONS	11
8.	NEW DISCOVERIES, INVENTIONS, PATENTS	17
9.	HONORS/AWARDS	18
10.	SELECTED REPRINTS	20

2. OBJECTIVES

This program has been directed generally toward basic research into the role of microstructure in the damage resistance of tough monophase, multiphase, and layered ceramics, particularly in high-stress contact configurations. A specific goal was to provide basic materials design data for AFOSR sponsored programs in *bearing technology* and *coatings*. The toughest ceramics are those with a crack resistance that is not single-valued but rather an increasing function of crack size (*R*-curve), with strongly enhanced values in the "long-crack" region (i.e. long relative to the scale of the microstructure). The *R*-curve is most pronounced in those ceramics with large grains, weak interfaces, and high internal stresses. Accordingly, to gain long-crack toughness in ceramics one builds in *microstructural heterogeneity*. A primary feature of the *R*-curve is that it leads to a marked insensitivity of the strength to initial crack size, i.e. "flaw tolerance". This has a strong appeal to the structural engineer, because components may be designed to a specific stress without undue concern for variable flaw distributions, either pre-existing or service-induced. On the other hand, microstructural heterogeneity tends to enhance fracture in the "short-crack" region, leading to a degradation of wear resistance and surface integrity from microfracture at the grain level. Designing with ceramics is essentially an exercise in compromise, tailoring microstructures for specific applications.

Nowhere is the microstructural interaction between materials variables and fracture properties more important than in contact fields, where ceramic surfaces may be subjected to intense local stress concentrations over long periods of time or over many hundreds of thousands of loading cycles. Such concentrated stresses occur most notably in bearing applications, and in spurious local impacts at exposed surfaces. Ceramic engine components are highly susceptible to this kind of damage. Studies in our laboratories using the Hertzian contact test have provided new insights into the micromechanics of this kind of damage, especially in cyclic fatigue loading. Most importantly, these studies reveal that the entire nature of the damage can change with modifications to the material microstructure, from a classical single cone fracture in fine-grain homogeneous ceramics to multiple subsurface microfracture in coarse-grain heterogeneous ceramics [B.R. Lawn, N.P. Padture, H. Cai and F. Guiberteau, "Making Ceramics 'Ductile'," *Science* **263** 1114-16 (1994)]. Associated with this change in damage response is an increasing nonlinearity in the indentation stress-strain response, a "brittle-ductile" transition. The brittle and ductile responses have radically different influences on strength loss and material removal properties of the material. Implications concerning microstructural design for optimal mechanical properties, particularly in the crucial short-crack region, are profound.

Accordingly, the principal *objectives* of this program have been: (i) To develop experimental contact testing methodologies for studying the fundamental short-crack damage properties of tough ceramics, especially silicon nitride; (ii) To examine systematically the role of critical microstructural variables (grain size and shape, grain and glassy phases, interface energies, and internal stresses) on the nature of the ensuing contact damage in tough ceramics; (iii) To investigate the effect of the damage on associated mechanical properties, e.g. strength degradation, fatigue resistance, wear resistance; (iv) To design and process ceramic materials in order to improve the above properties; (v) To develop theoretical models of the damage micromechanics, and thereby establish design engineering criteria for materials selection and optimization. Another principal aim was to extend the study to layer structures, e.g. thermal barrier coatings.

(3) STATUS

Progress has been accomplished in all of the goals listed in the previous section. In particular:

(i) Contact testing methodologies for identifying and quantifying contact damage modes in several tough ceramics, and in ceramic layer structures, have been established. These test protocols represent a simple but powerful approach to damage characterization in tough ceramics.

(ii) New modes of indentation fracture and plasticity have been discovered and documented in monolithic ceramics, notably in silicon nitrides. The competition between these modes determines the service lifetime of bearing structures.

(iii) A new philosophy for the design of ceramic laminate structures has been proposed. Critical silicon nitride layered structures have been developed at NIST, and alumina layered structures at Lehigh.

(iv) An extensive study has been completed on thermal barrier coatings, in collaboration with Dr. C.C. Berndt at the Department of Materials Science and Engineering, State University of New York at Stony Brook.

(v) A finite element code for computing contact stress fields in monolithic and layer structures has been developed at NIST, and is now being routinely used to evaluate damage patterns in silicon nitride and other materials.

(vi) New micromechanical models for describing the contact damage in heterogeneous ceramic microstructures have been developed (in collaboration with D.B. Marshall, Rockwell International).

(vii) New silicon nitride microstructures have been designed, fabricated and tested at NIST. The contact responses are found to be highly sensitive to the microstructures.

(viii) Fatigue studies on the silicon nitride materials are being continued. Again, the fatigue responses are critically dependent on the microstructures. This element of the program is being coordinated with external bearing programs (notably via Michael Hilton at Aerospace Corporation).

The results of this work have been published in internationally recognized journals (or are in press), see section 6. Several others have been presented at conferences (see section 7).

(4) ACCOMPLISHMENTS

(i) Design of Tough Ceramics.

Silicon nitride ceramics for fatigue-resistant bearing applications, fabricated in-house as well as provided by external companies (Norton/TRW, Allied Signal), have been evaluated for mechanical and thermal properties. Grain size and shape and intergrain boundary phases are proving to be critical components of fatigue resistance, pointing the way to future improvements in processing and performance. The tests on the NIST materials show how the mode of contact damage changes dramatically, from essentially brittle to essentially plastic, as the grain heterogeneity is increased. Several papers on this aspect of the work have been published.

Processing variables, such as starting powder (particle size, Si_3N_4 phase), heat treatment time and temperature, are being systematically investigated. These variables all have a dramatic influence on ultimate mechanical properties, especially contact damage.

Tests in repeat contact loading (contact fatigue) are now being carried out on these materials. These tests are conducted in air and water environments. We are finding that the tougher (heterogeneous) ceramics suffer more from fatigue than their less tough (homogeneous) counterparts.

(ii) Design of Innovative Ceramic Multilayers.

We have pioneered a new philosophy for designing ceramic laminate structures, based on interleaving fine-grain *homogeneous* outer layers (for strength and wear resistance) with inner coarse-grain *heterogeneous* layers (for toughness and flaw tolerance). Uniquely, the interlayer interfaces are strongly bonded, so that penetrating cracks approach the sublayer and arrest, instead of the usual deflection along a weak interface. The principal model system studied has been silicon nitride, with elastic and plastic mismatch between adjoining layers. Laminates of alumina with calcium hexaluminate additives have also been studied. Extensive contact testing has been carried out on laminate structures. Several papers in this area have been published.

(iii) Thermal Barrier Coatings.

Extensive work has been carried out on the mechanical characterization of thermal barrier coatings, using our Hertzian test procedure. Under a spherical indenter contact, damage is produced in the brittle coating (distributed microcracking) and ductile substrate (plastic flow). Characterization of these damage modes is crucial to a basic understanding of failure modes of TBCs. The roles of elastic-plastic mismatch in the coating, bond coat and substrate have been critically examined. In cases of weak coating/substrate bonding, delamination occurs. Criteria for designing layer structures for maximum resistance to service damage are being constructed. Several papers in this area have been published.

(iv) **Contact Damage Modelling**. Work has continued on the development of analytical modelling procedures for describing damage modes in tough ceramics, including layered structures. Initial studies revealed an entirely new form of damage accumulation in heterogeneous ceramics. Finite element codes have been developed to be quantify this damage by elastic-plastic stress analysis. Such analyses enable determination of quasi-plastic yield zones and fracture paths.

Micromechanical models are being developed to relate the controlling material parameters, e.g. yield stress, fracture toughness, to the underlying material microstructures, and thus to provide a route to microstructural design of ceramics. A paper on this topic with D.B. Marshall is in press. The same kind of micromechanical modelling has been used to predict the strength properties of bearing materials after contact damage. A paper on this topic has been published.

A model for quantifying the stress-strain behavior of layer structures, with X-Z. Hu, has also been completed.

(5) PERSONNEL SUPPORTED

Dr. Helen M. Chan	(Principal Investigator)
Dr. Brian R. Lawn	(Principal Investigator, no cost to AFOSR)
Dr. Seung-Kun Lee	(Postdoctoral Fellow)
Mr. Hyoung-Chan Ha	(Graduate Student)
Mr. Sataporn Wuttiphan	(Graduate Student, no cost to AFOSR)
Dr. Herzl Chai	(NIST Guest Scientist)
Dr. Antonia Pajares	(NIST Guest Scientist, no cost to AFOSR)

(6) PUBLICATIONS

1. "Cyclic Fatigue of a Mica-Containing Glass-Ceramic at Hertzian Contacts"
H. Cai, M.A. Stevens Kalceff, B.M. Hooks, B.R. Lawn and K. Chyung
J. Mater. Res. **9** 2654 (1994).

2. "Toughness Properties of a Silicon Carbide With an In-Situ-Induced Heterogeneous Grain Structure," N.P. Padture and B.R. Lawn, J. Am. Ceram. Soc. **77** 2518 (1994).

3. "Enhanced Machinability of Silicon Carbide via Microstructural Design"
N.P. Padture, C.J. Evans, H.H.K. Xu and B.R. Lawn
J. Am. Ceram. Soc. **78** 215 (1995).

4. "Contact Fatigue of a Silicon Carbide With a Heterogeneous Grain Structure"
N.P. Padture and B.R. Lawn
J. Am. Ceram. Soc. **78** 1431 (1995).

5. "Effect of Microstructural Coarsening on Hertzian Contact Damage in Silicon Nitride"
H.H.K. Xu, L. Wei, N.P. Padture, B.R. Lawn and R.L. Yeckley
J. Mater. Sci. **30** 869 (1995).

6. "Fatigue in Ceramics with Interconnecting Weak Interfaces: A Study Using Cyclic Hertzian Contacts"
N.P. Padture and B.R. Lawn
Acta Metall. **43** 1609 (1995).

7. "Hertzian Contact Damage in Magnesia-Partially-Stabilized Zirconia"
A. Pajares, F. Guiberteau, B.R. Lawn and S. Lathabai
J. Am. Ceram. Soc. **78** 1083 (1995).

8. "Indentation Stress-Strain Curves for 'Quasi-Ductile' Ceramics"
A.C. Fischer-Cripps and B.R. Lawn
Acta Metall. **44** 519 (1996).

9. "Damage Accumulation and Cyclic Fatigue in Mg-PSZ at Hertzian Contacts"
A. Pajares, L. Wei, B.R. Lawn and D.B. Marshall
J. Mater. Res. **10** 2613 (1995).

10. "Contact Damage of Brittle Solids"
B.R. Lawn
Solid-Solid Interactions: Proceedings of the First Royal Society and Unilever Indo-UK Forum in Materials Science and Engineering, M.J. Adams, B.J. Briscoe and S.K. Biswas, eds., Royal Society of London, London, p.29, 1995.

11. "*In Situ* Processing of Silicon Carbide Layer Structures"
N.P. Padture, D.C. Pender, S. Wuttiphan and B.R. Lawn

J. Am. Ceram. Soc. **78** 3160 (1995).

12. "Damage-Resistant Alumina-Based Layer Composites"
L. An, H.M. Chan, N.P. Padture and B.R. Lawn
J. Mater. Res. **11** 204 (1996).

13. "Thermal Wave Analysis of Contact Damage in Ceramics: Case Study on Alumina"
L. Wei and B.R. Lawn
J. Mater. Res. **11** 939 (1996).

14. "Crack Suppression in Strongly-Bonded Homogeneous/Heterogeneous Laminates: A Study on Glass/Glass-Ceramic Bilayers"
S. Wuttiphan, B.R. Lawn and N.P. Padture
J. Am. Ceram. Soc. **79** 634 (1996).

15. "Hertzian Contact Response of Tailored Silicon Nitride Multilayers"
H. Liu, B.R. Lawn and S.M. Hsu
J. Am. Ceram. Soc. **79** 1009 (1996).

16. "Mechanical Characterization of Plasma Sprayed Ceramic Coatings on Metal Substrates by Contact Testing"
A. Pajares, L. Wei, B.R. Lawn, N.P. Padture and C.C. Berndt
Mater. Sci. and Eng. **A208** 158 (1996).

17. "Effect of Mechanical Damage on Thermal Conduction of Plasma Sprayed Coatings"
L. Wei, A. Pajares and B.R. Lawn
J. Mater. Res.**11** 1329 (1996).

18. "Contact Damage in Alumina-Based Plasma Sprayed Coatings"
A. Pajares, L. Wei, B.R. Lawn and C.C. Berndt
J. Am. Ceram. Soc. **79** 1907 (1996).

19. "Control of Calcium Hexaluminate Grain Morphology in In-Situ Toughened Ceramic Composites"
L. An and H.M. Chan and K.K. Soni
J. Mater. Sci. **31** 3223 (1996).

20. "R-Curve Behavior of In-Situ Toughened Al_2O_3:$CaAl_{12}O_{19}$ Ceramic Composites"
L. An, H.M. Chan
J. Amer. Ceram. Soc. **79** 3142 (1996)

21. "Stress Analysis of Contact Deformation in Quasi-Plastic Ceramics"
A.C. Fischer-Cripps and B.R. Lawn
J. Am. Ceram. Soc. **79** 2609 (1996).

22. "Stress Analysis of Elastic-Plastic Contact Damage in Ceramic Coatings on Metal

Substrates"
A.C. Fischer-Cripps, B.R. Lawn, A. Pajares and L. Wei
J. Am. Ceram. Soc. **79** 2619 (1996).

23. "Effect of Substrate and Bond Coat on Contact Damage in Zirconia-Based Plasma Coatings"
S. Wuttiphan, A. Pajares, B.R. Lawn and C.C. Berndt
Thin Solid Films **293** 251 (1997).

24. "Hertzian Contact Damage in Porous Alumina Ceramics"
B.A. Latella, B.H. O'Connor, N.P. Padture and B.R. Lawn
J. Am. Ceram. Soc. **80** 1027 (1997).

25. "Contact Damage in Alumina Reinforced with Silicon Carbide Platelets"
M. Belmonte, S.K. Lee
J. Mater. Sci. **16** 379 (1997).

26. "Role of Microstructure in Hertzian Contact Damage in Silicon Nitride: I. Mechanical Characterization"
S.K. Lee, S. Wuttiphan and B.R. Lawn
J. Am. Ceram. Soc. **80** 2367 (1997).

27. "Role of Microstructure in Hertzian Contact Damage in Silicon Nitride: II. Strength Degradation"
S.K. Lee and B.R. Lawn
J. Am. Ceram. Soc. **81** 997 (1998).

28. "Contact-Induced Transverse Fractures in Brittle Layers on Soft Substrates: A Study on Silicon Nitride Bilayers"
K.S. Lee, S. Wuttiphan, X.Z. Hu, S.K. Lee and B.R. Lawn
J. Am. Ceram. Soc. **81** 571 (1998).

29. "A Model of Strength Degradation From Hertzian Contact Damage in Tough Ceramics"
B.R. Lawn, K.S. Lee, I.M. Peterson and S. Wuttiphan
J. Am. Ceram. Soc. **81** 1509 (1998).

30. "Nonlinear Stress-Strain Curves for Solids Containing Closed Cracks With Friction"
B.R. Lawn and D.B. Marshall
J. Mech. Phys. Solids **46** 85 (1998).

31. "Indentation of Ceramics With Spheres: A Century After Hertz"
B.R. Lawn
J. Am. Ceram. Soc. **81** 1977 (1998).

32. "Effect of Starting Powder on Damage Resistance of Silicon Nitrides"
S.K. Lee, K.S. Lee, B.R. Lawn and D.K. Kim

J. Am. Ceram. Soc. **81** 2061 (1998).

33. "Contact Damage and Strength Degradation in Brittle/Quasi-Plastic Silicon Nitride Bilayers"
K.S. Lee, S.K. Lee, B.R. Lawn and D.K. Kim
J. Am. Ceram. Soc. **81** 2394 (1998).

34. "A Simple Indentation Stress-Strain Relation for Contacts with Spheres on Bilayer Structures"
X.Z. Hu and B.R. Lawn
Thin Solid Films **322** 225 (1998).

35. "Effect of Microstructure on Contact Damage and Strength Degradation in Micaceous Glass-Ceramics"
I.M. Peterson, S. Wuttiphan, A. Pajares and B.R. Lawn
Dental Materials **14** 80 (1998).

36. "Fracture and Deformation Damage Accumulation in Tough Ceramics"
B.R. Lawn, S.K. Lee and K.S. Lee
Proceedings of the Second International Symposium on the Science of Engineering Ceramics, EnCera 98, K. Niihara, T. Sekino, E. Yasuda, T. Sasa, ed., Ceramic Society of Japan, Tokyo, Japan, Vol. 2, p. 3, 1998.

(7) INTERACTIONS/TRANSITIONS

(a) Conferences, Meetings, Seminars

(* *Invited Paper)*

1995

* "In-Situ Toughened Silicon Carbide"
N.P. Padture and B.R. Lawn
Pacific Coast Regional Meeting of the American Ceramic Society, Los Angeles, CA, 1994.

* "Contact Damage and Fatigue of Tough Ceramics"
B.R. Lawn
Pacific Coast Regional Meeting of the American Ceramic Society, Los Angeles, CA, 1994.

* "Contact Damage in Mica-Containing Glass-Ceramics"
B.R. Lawn and A.C. Fischer-Cripps
National Meeting of the American Chemical Society, Los Angeles, CA, 1995.

* "Contact Damage in Tough Polycrystalline Ceramics"
B.R. Lawn
American Society of Mechanical Engineers Summer Meeting, Los Angeles, CA, 1995.

* "Microstructure, Toughness and Fatigue of Ceramics"
B.R. Lawn
International Symposium on Advanced Ceramics for Structural and Tribological Applications, Annual Conference of Metallurgists, Vancouver, Canada, 1995.

"Control of Contact Damage by Microstructural Design in Laminated Structures"
L. An, H.M. Chan, N.P. Padture and B.R. Lawn
Annual Meeting of the American Ceramic Society, Cincinnati, Ohio, 1995.

"Mechanical and Thermal Properties of Thermal Barrier Coatings in Cyclic Contact Degradation"
L. Wei, N.P. Padture and B.R. Lawn
Annual Meeting of the American Ceramic Society, Cincinnati, Ohio, 1995.

"Indentation Stress-Strain Curves and Evidence of 'Ductilitity' in Ceramics"
A.C. Fischer-Cripps and B.R. Lawn
Annual Meeting of the American Ceramic Society, Cincinnati, Ohio, 1995.

"Enhanced Machinability of Silicon Carbide via Microstructural Design"
N.P. Padture, C.J. Evans, H.H.K. Xu and B.R. Lawn

Annual Meeting of the American Ceramic Society, Cincinnati, Ohio, 1995.

"Damage and Fatigue in Mg-PSZ at Hertzian Contacts"
A. Pajares, L. Wei, F. Guiberteau and B.R. Lawn
Annual Meeting of the American Ceramic Society, Cincinnati, Ohio, 1995.

"Microstructure, Toughness and Fatigue of Ceramics"
* B.R. Lawn
International Symposium on Advanced Ceramics for Structural and Tribological Applications, Annual Conference of Metallurgists, Vancouver, Canada, 1995.

"Hertzian Indentation Behavior of Layered Composites of In-Situ Toughenened Al_2O_3:Ca $Al_{12}O_{19}$"
H.M. Chan, L. An, N.P. Padture and B.R. Lawn
Conference on Mechanics and Physics of Layered and Graded Materials, Davos, Switzerland, 1995.

"Contact Damage in In-situ Toughened Ceramics"
* B.R. Lawn
Fall Meeting of the Basic Science Division of the American Ceramic Society, New Orleans, Louisiana, 1995.

"Processing and Mechanical Behavior of Layered Composites of In-Situ Toughenened * Al_2O_3:Ca $Al_{12}O_{19}$"
H.M. Chan, L. An, N.P. Padture and B.R. Lawn
Fall Meeting of the Basic Science Division of the American Ceramic Society, New Orleans, Louisiana, 1995.

1996

"Contact Damage and Fatigue of Dental Ceramics"
* B.R. Lawn
74th Session of the International Association of Dental Research, San Francisco, California, 1996.

"Damage Accumulation Beneath Hertzian Contacts in Tough Ceramics"
* B.R. Lawn
Annual Meeting of the American Ceramic Society, Indianapolis, Indiana, 1996.

"Analysis of Contact Damage in YSZ Plasma Sprayed Coatings"
S. Wuttiphan, A. Pajares, B.R. Lawn and C.C. Berndt
Annual Meeting of the American Ceramic Society, Indianapolis, Indiana, 1996.

"Contact Damage and Contact Failure of Silicon Nitrides with Different Microstructures"
S-K. Lee, A.C. Fischer-Cripps and B.R. Lawn
Annual Meeting of the American Ceramic Society, Indianapolis, Indiana, 1996.

"Effect of Layer Thickness on the Hertzian Contact Response in Laminated Ceramics"
L. An, H.M. Chan, A.C. Fischer-Cripps and B.R. Lawn
Annual Meeting of the American Ceramic Society, Indianapolis, Indiana, 1996.

"Contact Damage Evolution in Designed Heterogeneous Microstructures"
* B.R. Lawn
Gordon Research Conference on Complex Ceramic Microstructures: Properties by Design, Meriden, NH, 1996.

"Mechanical Properties of Tough Ceramics: A Study Using Indentations"
* B.R. Lawn
Annual Meeting of the Korean Ceramic Society, Seoul, Korea, 1996.

1997

"Role of Microstructural Heterogeneity in Damage Accumulation in Bulk and Layered Ceramics"
* B.R. Lawn
Ninth International Conference on Fracture, Sydney, Australia, 1997.

"Damage Accumulation Beneath Hertzian Contacts in Ceramics"
* B.R. Lawn
International Workshop on Fracture and Inelasticity of Heterogeneous Materials, Perth, Australia, 1997.

"Cyclic Contact Fatigue of Silicon Nitrides with Controlled Microstructures"
S.K. Lee and B.R. Lawn
Annual Meeting of the American Ceramic Society, Cincinnati, OH, 1997.

"Effect of Coating Thickness and and Elastic/Plastic Mismatch on the Contact Fracture of Silicon Nitride Layer Structures"
S.K. Lee, K.S. Lee, X.-Z. Hu and B.R. Lawn
Annual Meeting of the American Ceramic Society, Cincinnati, OH, 1997.

"Analysis of Contact Damage in Silicon Nitride Layers"
S. Wuttiphan, S.K. Lee, K.S. Lee, and B.R. Lawn
Annual Meeting of the American Ceramic Society, Cincinnati, OH, 1997.

"Hertzian Contact Behavior of Alumina:CalciumHexaluminate (CA6)"
H.C. Ha, A. DiGiovanni, H.M. Chan and B.R. Lawn
Annual Meeting of the American Ceramic Society, Cincinnati, OH, 1997.

"Role of Microstructure in Contact Fracture and Deformation in Silicon Nitride"
* S.K. Lee, K.S. Lee and B.R. Lawn
Symposium on Material Microstructure, Heterogeneity, and Fracture, Joint

ASME/ASCE/SES Summer Meeting, Chicago, IL, 1997.

"Effect of Coating Thickness and Elastic-Plastic Mismatch on the Contact Fracture of Silicon Nitride Layer Structures"
B.R. Lawn, K.S. Lee and S.K. Lee
Conference on Composites: Design for Performance, Lake Louise, Canada, 1997.

"Contact Damage in Quasi-Brittle/Quasi-Plastic Silicon Nitride Bilayers"
S.K. Lee, K.S. Lee, X.-Z. Hu and B.R. Lawn
Fall Meeting of the American Ceramic Society, San Francisco, CA, 1997.

1998

"Microstructure, Strength and Fatigue of Tough Ceramics"
* B.R. Lawn
Annual Meeting of the American Ceramic Society, Cincinnati, OH, 1998.

"Indentation Mechanics: A Hundred Years Since Hertz"
* B.R. Lawn
Annual Meeting of the American Ceramic Society, Cincinnati, OH, 1998.

"Contact Damage in Brittle/Quasi-Plastic Silicon Nitride Bilayers"
S.K. Lee, K.S. Lee, D.K. Kim, B.R. Lawn
Annual Meeting of the American Ceramic Society, Cincinnati, OH, 1998.

"Effect of Starting Powder on Damage Resistance of Silicon Nitrides"
S.K. Lee, K.S. Lee, D.K. Kim, B.R. Lawn
Annual Meeting of the American Ceramic Society, Cincinnati, OH, 1998.

"Damage Accumulation Beneath Hertzian Contacts in Ceramics and Other Brittle Materials"
* B.R. Lawn
MesoMechanics 98: International Conference on Physical Mesomechanics and Computer-Aided Design of Advance Materials and Technologies, Tel Aviv, Israel, 1998.

"Indentation Mechanics: A Method for Evaluating Brittle Materials"
* B.R. Lawn
VIth National Meeting on Mechanical Properties of Solids, Badajoz, Spain, 1998.

"Contact Damage in Ceramics"
* B.R. Lawn
Gordon Research Conference on Frontiers of Tribology, Plymouth, NH, 1988.

"Fracture and Deformation Accumulation in Tough Ceramics"
* B.R. Lawn
ENCERA 98: Second International Symposium on the Science of Engineering Ceramics,

Osaka, Japan, 1998.

"Contact Damage and Fatigue of Silicon Nitride"
* B.R. Lawn and S.K. Lee
PacRim Meeting of the American Ceramic Society, Kyongju, Korea, 1998.

"Contact Damage of Silicon Nitrides with Controlled Microstructures"
* B.R. Lawn, S.K. Lee and K.S. Lee
The First China International Conference on High-Performance Ceramics, Beijing, China, 1998.

(b) **Transitions**

Our program has provided useful guidelines on microstructural design to other researchers working in related AFOSR bearing and coating programs:

(xi) The program has facilitated meaningful transfer of basic knowledge to the bearing industry. The Principal Investigators have established a cooperative arrangement with the Norton/TRW Ceramics Company, in which custom-made specimens of bearing quality silicon nitride have been provided by that company for experimental evaluation at Lehigh and NIST. Site visits and consultations with Norton have been made.

(ii) Collaborative work has been completed on layer and multilayer ceramic structures, specifically thermal barrier coatings, with Dr. C.C. Berndt at the Department of Materials Science and Engineering, State University of New York at Stony Brook. The goal of this aspect of the program was to develop simple procedures, using the Hertzian testing technology, for characterizing mechanical and thermal properties of TBCs, in order to provide material design guidelines.

(iii) Discussions have been held with Dr. Michael Hilton at Aerospace Corporation on a collaborative program to study the effects of microstructure on mechanical properties of silicon nitride bearings, as an adjunct to the AFOSR program.

8. NEW DISCOVERIES, INVENTIONS, PATENTS

1. Discovered and quantified new modes of indentation "plasticity" in Hertzian testing of ceramics, with direct relevance to microstructural damage in contact stress fields [B.R. Lawn, N.P. Padture, H. Cai and F. Guiberteau, "Making Ceramics 'Ductile'," *Science* **263** 1114-16 (1994)].

2. Proposed new philosophy of ceramic laminate structures, alternating layers with homogeneous microstructures (for strength and wear resistance) and heterogeneous microstructures (for toughness and energy absorption), with *strong* interlayer bonding to avoid delamination.

3. Developed simple but powerful new test procedure for mechanically characterizing brittle coatings (including TBCs) using Hertzian contact, and developed analytical routes to the design of these coatings for optimum resistance to service failure.

4. Developed new silicon nitride microstructures, using systematic array of starting powders and heat treatment times and temperatures. Demonstrated sensitivity of bearing properties to ensuing microstructures.

5. Extended contact testing to contact fatigue of silicon nitride materials. Demonstrated sensitivity of fatigue properties to microstructures.

9. **HONORS/AWARDS**

Helen M. Chan

Publications:	Author of over 100 scientific papers
Honors:	Alfred Noble Robinson Award ("Outstanding Performance and Unusual Promise of Professional Achievement") Lehigh University, 1990
	Outstanding Young Member Award Lehigh Valley Chapter of the American Society of Metals, 1990
	International Bradley Stoughton Award ("Outstanding Young Faculty in Materials Science and Engineering") American Society of Metals, 1990
	Class of 1961 Professorship ("Distinction in Teaching, Research and Service") Lehigh University, 1993
	New Jersey Zinc Professorship, 1999
Professional Societies:	Member of the American Ceramic Society Member of the American Society of Metals Associate Editor, Journal of the American Ceramic Society

Brian R. Lawn

Publications:	Author of over 200 scientific papers and a text book "Fracture of Brittle Solids" (two editions)
Honors:	Sosman Award ("Outstanding Contributions to Ceramic Science") American Ceramic Society, 1982
	Edward Uhler Condon Award ("Distinguished Achievement in Written Exposition") National Bureau of Standards, 1984
	Department of Commerce Silver Medal Award ("Meritorious Federal Service") National Bureau of Standards, 1986
	Hobart M. Kraner Award ("Distinguished Achievements and Outstanding Contributions to the Field of Ceramics, Especially Advancing the Field of Fracture Behavior of Brittle Solids") American Ceramic Society, 1991
	Ross Coffin Purdy Award for paper "Role of Microstructure in Hertzian Contact Damage in Silicon Nitride: I, Mechanical Characterization" American Ceramic Society, 1999
Professional Societies:	Fellow of the American Ceramic Society
Professional Activities:	Editor, Journal of American Ceramic Society, 1984-86
Citation Listing:	Listed in top 25 most cited materials scientists worldwide during the past five years (scientific survey in "Science Watch", Vol. 6, No. 9, 1995)

10. SELECTED REPRINTS

ELSEVIER

Thin Solid Films 322 (1998) 225–232

thin solid films

A simple indentation stress–strain relation for contacts with spheres on bilayer structures

Xiao Zhi Hu [a,*], Brian R. Lawn [b]

[a] *Department of Mechanical and Materials Engineering, University of Western Australia, Nedlands, WA 6907, Australia*
[b] *Materials Science and Engineering Laboratory National Institute of Standards and Technology, Gaithersburg, MD 20899, USA*

Received 14 August 1997; accepted 30 October 1997

Abstract

A simple formulation for the indentation stress–strain behavior of bilayers in contacts with hard spheres is proposed. The formulation is based on empirical power-law stress–strain relations for each of the individual constituent bulk materials, and thence for the bilayer coating/substrate composite. For the constituent materials, two regions of response are considered: at low loads, an elastic region, with linear stress–strain response (exponent = 1); at high loads, an elastic–plastic region, with nonlinear stress–strain response (exponent < 1). The material responses in each of these two regions are characterized by effective moduli. For the composite bilayer, the transition in load-bearing capacity from coating to substrate with increasing load is represented by a three-parameter Weibull asymptotic function of ratio contact radius to coating thickness. This function conveniently defines the geometrical aspects of the contact response separately from the material properties. The power-law formulation is tested, and the Weibull parameters calibrated, against FEM-generated and experimental indentation stress–strain data for selected coating/substrate systems with widely different interlayer elastic–plastic mismatch. The formulation allows a priori predictions of the composite bilayer indentation stress–strain curves from control data on the constituent materials. Conversely, measurements of indentation stress–strain responses on given bilayers may be used to evaluate otherwise undeterminable elastic–plastic properties of coatings on well-characterized substrates. © 1998 Elsevier Science S.A. All rights reserved.

Keywords: Stress–strain relation; Spheres; Bilayer structures

1. Introduction

The relationship between contact load (P) and characteristic contact radius (a) (or, alternatively, contact displacement (z)) represents an important material characteristic in indentations with spheres of given radius (r). Spherical indenters are widely studied experimentally, because of their relatively simple geometry; and theoretically, because of their facility to provide essential information on both elastic and plastic deformation properties of the test material [1]. By defining an indentation stress, $p_0 = P/\pi a^2$, and indentation strain, a/r, it is possible to generate an indentation function $p_0(a/r)$ which strikingly reflects the intrinsic stress–strain curve for any bulk material. Such functions have been routinely measured on homogeneous bulk materials, including ceramics [1–8].

The problem becomes considerably more complex in the indentation of bilayers, where the contact field can be strongly influenced by elastic–plastic mismatch between the 'coating' and 'substrate' materials. Recently, experimental measurements of indentation stress–strain curves using spherical indenters have been made on a wide variety of coating/substrate systems [9–16]. The complexities are especially severe when the mismatch in material response is large, especially in hard brittle (e.g., ceramic) coatings on soft plastic (e.g., metal, polymer) substrates (or vice versa). In such instances the stress–strain response undergoes a progressive transition, from coating-controlled at very low loads to substrate-controlled at very high loads. Detailed computations using finite element modelling (FEM) codes are able to account for such transitions [14,17]. However, the practical importance of bilayer systems makes it desirable to establish some means of representing the composite stress–strain relation in simple (if empirical) closed form, so that the prospective behavior of any given bilayer structure may be predicted from the properties of the two constituent materials without resort to lengthy numerical computation.

* Corresponding author.

0040-6090/98/$19.00 © 1998 Elsevier Science S.A. All rights reserved.
PII S0040-6090(97)00919-X

Accordingly, our objective is to formulate a simple $p_0(a/r)$ relation for bilayer composites so that the role of coating thickness and elastic–plastic mismatch as design parameters may be evaluated. We propose power-law relations for $p_0(a/r)$, starting with the separate bulk coating and substrate materials and leading to an analogous power-law expression for the composite bilayers. The relations for the individual materials are linked via an asymptotic function representing the transition in load-bearing capacity from coating to substrate, somewhat analogous to a functional methodology described by Gao et al. [18]. The bilayer relations are tested against FEM-generated and experimental indentation stress–strain data for selected bilayer systems with varying coating thicknesses and widely different interlayer elastic–plastic mismatch. Potential use of the formulation to deconvolute properties of otherwise uncharacterized coatings from indentation measurements on the composite bilayers is discussed.

2. Indentation stress–strain curves for bulk materials

The indentation stress–strain relation $p_0(a/r)$ for contacts with spheres is well defined by the classic Hertzian theory for ideally elastic, homogeneous bulk materials of Young's modulus E and Poisson's ratio ν [19,20]. The Hertzian solution for $p_0(a/r)$ has the linear form [2]

$$p_0 = (4E'/3\pi)(a/r) \tag{1}$$

where we define a modified Young's modulus for the indenter/specimen system,

$$E' = 1/\left[(1-\nu^2)/E + (1-\nu_I^2)/E_I\right] \tag{2}$$

with I referring to the indenter material. The indentation stress–strain curve in Eq. (1) reflects the elastic stress–strain response of the test material, and its uniqueness is unaffected by the size of the indenting sphere.

Experimental data on monolithic materials confirm that $p_0(a/r)$ is independent of sphere size even when plastic damage occurs below the contact ('geometrical similarity' [1]). To exploit the general usefulness of this result, Eq. (1) needs to be extended to cover nonlinearity. We propose the following simple modification:

$$p_0 = (4E^*/3\pi)(a/r)^n \tag{3}$$

with material parameters E^* a nonlinear modulus and n a strain-hardening parameter. Eq. (1) is recovered if $n = 1$ and $E^* = E'$. The parameters $n\ (\leq 1)$ and $E^*\ (\leq E')$ may be obtained by curve-fitting numerically (e.g., FEM) generated or direct experimental data on any given inelastic monolithic material.

Generally, it is necessary to assign different values of n and E^* in different regions of the stress–strain curve, to distinguish low-load elastic responses (Eq. (1)) from high-load plastic responses (Eq. (3)) in materials with distinctive elastic–plastic regions [21].

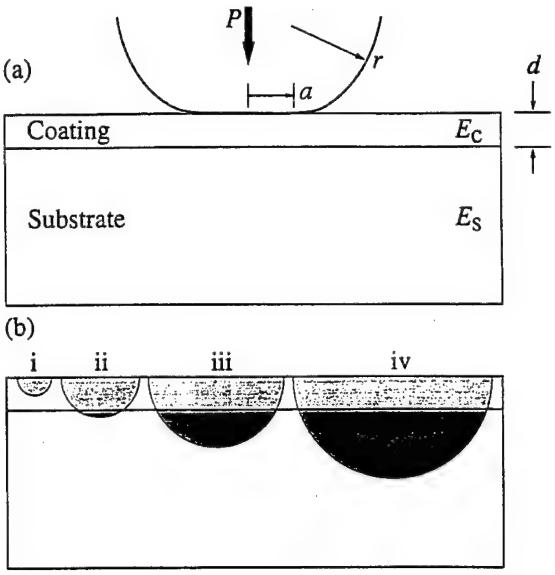

Fig. 1. Contact of a sphere on a coating/substrate bilayer system. (a) Showing key indentation variables. (b) Showing expansion of idealized deformation zone with increasing load. $i \rightarrow ii \rightarrow iii \rightarrow iv$. Load sequence represents transition from coating-controlled response in i to substrate-controlled response in iv. In real bilayers with large elastic–plastic mismatch the deformation zone may depart significantly from the hemispherical configuration depicted here.

3. Indentation stress–strain curves for composite bilayers

Consider the contact of a bilayer system with a sphere, as depicted in Fig. 1a. The volumes of influence of the deformation field are idealized by hemispherical zones about the contact center. Two factors distinguish the bilayer from the bulk structure: (i) a configurational factor d/r, representing the coating thickness d in relation to the sphere radius r; (ii) a material factor E_c/E_s (E'_c/E'_s or E_c^*/E_s^*) representing the coating/substrate elastic–plastic mismatch. It can be foreseen from the idealized deformation geometry in Fig. 1b that the substrate will have little influence on the $p_0(a/r)$ relation when the contacts are small, $a/d \ll 1$; conversely, the substrate will exert a strong, even dominant influence when the contacts are large, $a/d \gg 1$. The critical questions are: can we define a universal configurational function to describe the transition between these two limiting cases?—and how does the mismatch term E_c/E_s enter into this function? Of course, in real bilayers the deformation geometry may depart substantially from the idealized configuration shown in Fig. 1, with enhanced damage zone in either the coating or substrate depending on the mismatch, in which case the

universality of any derived configurational function is questionable. However, as we shall see, a reasonably well-defined function can be determined for a broad range of material bilayers.

As in the previous section, we begin by first considering elastic contacts (cf. Eq. (1)), and then generalizing the treatment to plastic contacts (cf. Eq. (3)).

3.1. Fully elastic response

Begin by considering relations for the contact radius a and load P in terms of the effective elastic modulus E' for the constituent bulk coating (c) and substrate (s) materials. From Eq. (1), in conjunction with $p_0 = P/\pi a^2$:

$$a_c = (3Pr/4E'_c)^{1/3} \tag{4a}$$

$$a_s = (3Pr/4E'_s)^{1/3} \tag{4b}$$

Suppose that we write an analogous relation for the composite coating/substrate bilayer (cs):

$$a = (3Pr/4E'_{cs})^{1/3} \tag{5}$$

with E'_{cs} an effective modulus for the bilayer. We can expect Eq. (5) to approach Eq. (4a) asymptotically at $a/d \ll 1$ (low P), and conversely Eq. (4b) asymptotically at $a/d \gg 1$ (high P), as indicated schematically in Fig. 2. In the intermediate region, E'_{cs} will depend on the mismatch parameter E'_c/E'_s and configuration variable a/d.

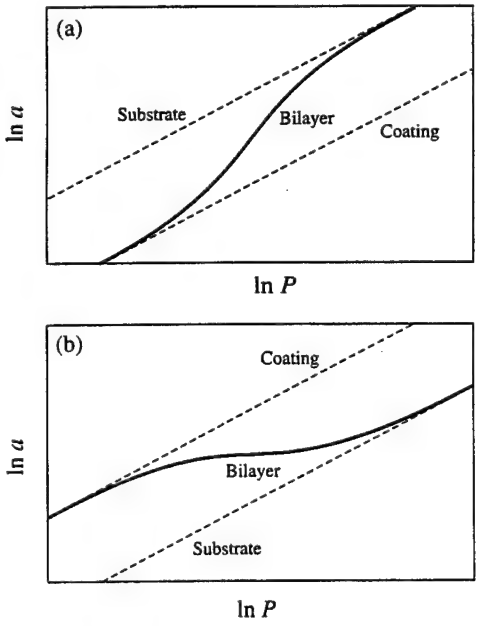

Fig. 2. Asymptotic behavior of $a(P)$ in Eq. (5) for bilayer, depicted schematically for (a) hard coating on soft substrate, (b) soft coating on hard substrate. Dashed lines are representations of Eqs. (4a) and (4b) for the monolithic coating and substrate materials respectively.

In order to evaluate E'_{cs} we adopt a procedure analogous in some ways to that used by Gao et al. [18] for elastic contacts on bilayers. We rewrite Eq. (5) in the reduced form

$$a = a_c(E'_c/E'_s)^{L/3} \tag{6}$$

such that, with Eqs. (4a) and (4b), the exponent L defines a nondimensional configurational function

$$L(a/d) = \ln(a/a_c)/\ln(a_s/a_c) \tag{7}$$

with $0 \le L \le 1$ in the region $0 \le a/d \le \infty$. The function $L(a/d)$ bears some resemblance to the modulus weighting function ('fraction coefficient') defined by Gao et al. [18] although the mathematical context in the present work is quite different. Along with $p_0 = P/\pi a^2$, Eq. (6) provides the indentation stress–strain relation for elastic bilayers:

$$p_0 = (4E'_c/3\pi)(E'_s/E'_c)^L(a/r) \tag{8}$$

In this relation the influence of the substrate is seen as a simple modification of the elastic response for the bulk coating, with mismatch factor E'_c/E'_s and configuration factor $L(a/d)$ now conveniently separated. This separation is helpful because it allows us to study the mismatch and geometry factors independently. From Eqs. (4a), (4b), (5) and (6), the effective modulus for the bilayer is

$$E'_{cs}(a/d) = E'_c(E'_s/E'_c)^{L(a/d)} \tag{9}$$

Note that in the trivial case of zero mismatch in Eq. (9) ($E'_{cs} = E'_c = E'_s$), Eq. (8) reduces to Eq. (1) for the bulk coating ($L = 0$, $a/d = 0$) or substrate ($L = 1$, $a/d = \infty$).

This leaves only determination of the configurational asymptotic function $L(a/d)$. We shall return to this issue in Section 4, after extending the analysis to elastic–plastic contacts.

3.2. Elastic–plastic response

The analysis for elastic bilayers may be extended to cover elastic–plastic bilayers by replacing Eq. (1) with Eq. (3). We write separate indentation stress–strain relations for coating (c) and substrate (s):

$$p_{0c} = (4E^*_c/3\pi)(a_c/r)^n \tag{10a}$$

$$p_{0s} = (4E^*_s/3\pi)(a_s/r)^m \tag{10b}$$

where n and m are plasticity exponents and E^*_c and E^*_s are effective nonlinear moduli. With $p_0 = P/\pi a^2$, we obtain analogous expressions for the contact radii a in Eqs. (4a) and (4b):

$$a_c = (3Pr^n/4E^*_c)^{1/(n+2)} \tag{11a}$$

$$a_s = (3Pr^m/4E^*_s)^{1/(m+2)} \tag{11b}$$

Following Eq. (5), we write an analogous relation for the coating/substrate (cs) bilayer:

$$a = \left(3Pr^N/4E_{cs}^*\right)^{1/(N+2)} \tag{12}$$

where E_{cs}^* is an effective modulus and N is an effective exponent in the elastic–plastic region.

Presuming the function $L(a/d)$ in Eq. (7) to remain material-insensitive, the analysis yields a nonlinear stress–strain relation for bilayers:

$$p_0 = (4E_c^*/3\pi)\left(E_s^*/E_c^*\right)^{l}(a/r)^{n-(n-m)l} \tag{13}$$

where l is another nondimensional configurational exponent,

$$l(a/d) = (n+2)L(a/d)/\left[(m+2) + (n-m)L(a/d)\right] \tag{14}$$

Like $L(a/d)$, $l(a/d)$ is an asymptotic function, with similar limits, i.e., $l = 0$ at $L = 0$ $(a/d = 0)$ and $l = 1$ at $L = 1$ $(a/d = \infty)$. Within these limits, $l > L$ $(0 \le a/d \le \infty)$. Again, the influence of the substrate represents a simple modification of the elastic–plastic response for the bulk coating, with mismatch factor E_s^*/E_c^* and configuration factor $l(a/d)$ separate entities. From Eqs. (12) and (13), the effective modulus and exponent are determined as

$$E_{cs}^*(a/d) = E_c^*\left(E_s^*/E_c^*\right)^{l(a/d)} \tag{15a}$$

$$N(a/d) = n - (n-m)l(a/d) \tag{15b}$$

Note that in the trivial case of zero mismatch ($E_{cs}^* = E_c^* = E_s^*$; $N = n = m$), we have $l = L$ in Eq. (14), in which case Eq. (13) reduces to Eq. (3) for the bulk coating ($L = 0$, $a/d = 0$) or substrate ($L = 1$, $a/d = \infty$).

Again, the stress–strain curve is asymptotically determined by the properties of the coating at small contacts ($a/d \to 0$), and by the properties of the substrate at large contacts ($a/d \to \infty$). For the special case of identical exponents $m = n$ ($l = L$ in Eq. (14)), Eq. (13) reduces to

$$p_0 = (4E_c^*/3\pi)\left(E_s^*/E_c^*\right)^{L}(a/r)^{n} \tag{16}$$

For the even more special case $m = n = 1$, the elastic solution of Eq. (8) is recovered.

4. Empirical calibration of asymptotic configuration functions

We are now left with determining the asymptotic configuration function $L(a/d)$, and thence $l(a/d)$, needed for predicting the response of the bilayer from the elastic–plastic constants of the individual coating and substrate materials. We resort here to empirical calibration, using $p_0(a/r)$ data for selected bilayer systems with a wide range of elastic–plastic mismatch: (i) a relatively hard glass–ceramic coating (Dicor, Dentsply/Caulk, Milford, DE) on a soft glass-filled polymer substrate (HCE, Kuraray, Osaka, Japan) [22]; (ii) a relatively soft porcelain coating (Vita ZahnFabrik, Bad Sackingen, Germany) on a hard glass-infiltrated alumina substrate (InCeram, Vita ZahnFabrik, Bad Sackingen, Germany) [22]; (iii) a hard silicon nitride coating on a softened silicon nitride containing 30 vol.% boron nitride platelets (Si_3N_4/Si_3N_4–30BN) [16,23]. Data for the first two systems are computer-generated in stepwise loading using an FEM algorithm for Hertzian contacts on layer structures, in conjunction with constitutive relations matching the elastic–plastic properties of the individual bulk materials [14] (Appendix A). Data for the silicon nitride system are taken from actual

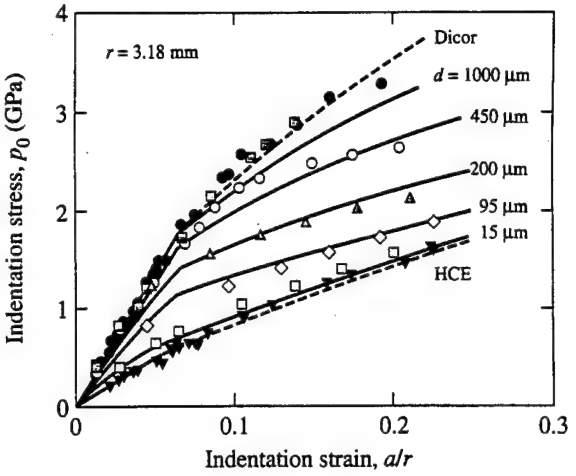

Fig. 3. Indentation stress–strain curve for Dicor glass–ceramic coatings on HCE polymer substrates, for coating thicknesses d indicated. Data points are FEM-generated results, using WC spheres $r = 3.18$ mm for bilayer data. Solid curves are generated from Eqs. (8), (10a) and (10b). Bounding curves for Dicor and HCE bulk materials are data fits; intermediate curves for bilayer data at prescribed coating thickness d are predictions. (Data courtesy of I.M. Peterson, Y.-G. Jung and S. Wuttiphan.)

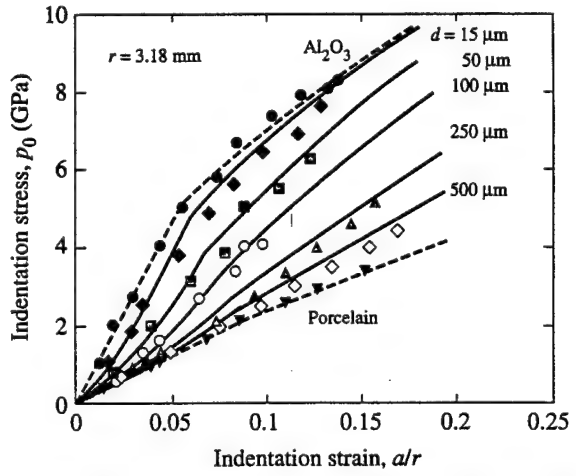

Fig. 4. Indentation stress–strain curve for porcelain coatings on glass-infiltrated alumina substrates, for coating thicknesses d indicated. Data points are FEM-generated results, using WC spheres $r = 3.18$ mm for bilayer data. Solid curves are generated from Eqs. (8), (10a) and (10b). Bounding curves for porcelain and alumina bulk materials are data fits; intermediate curves for bilayer data at prescribed coating thickness d are predictions. (Data courtesy of I.M. Peterson and S. Wuttiphan.)

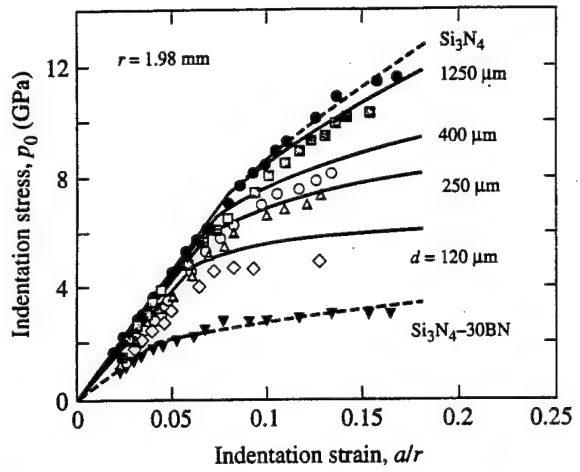

Fig. 5. Indentation stress–strain curves for Si_3N_4 coatings on Si_3N_4–30 wt.% BN substrates, for coating thicknesses d indicated. Data points are experimental results, using WC spheres $r = 1.98$ mm for bilayer data. Solid curves are generated from Eqs. (8) and (13), in conjunction with Eqs. (14) and (17). Bounding curves for Si_3N_4 and Si_3N_4–30 wt.% BN bulk materials are data fits; intermediate curves for bilayer data at prescribed coating thickness d are predictions. (Data from Ref. [16].)

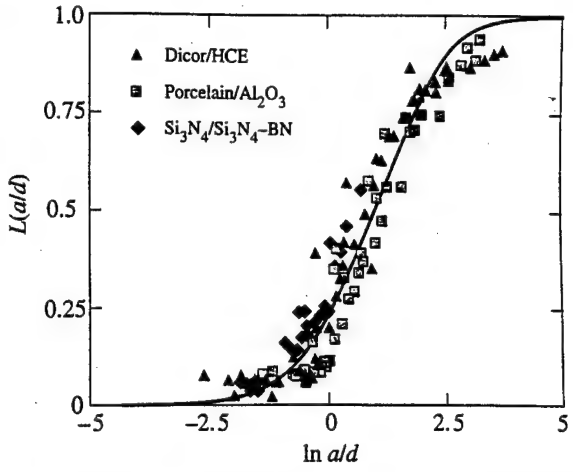

Fig. 6. Determination of configuration function $L(a/d)$. Points are from bilayer data in Figs. 3, 4 and 5. Solid curve is best-fit three-parameter Weibull function.

experimental measurements of contact radii over a range of contact loads [16]. In practice, the coatings in each of these material systems may be subject to some transverse (and perhaps also delamination) cracking at high loads [16,22,23], limiting the capacity to match experimental data in the upper regions of the stress–strain curve.

The indentation stress–strain data for the three bilayer systems are plotted in Figs. 3–5, for a range of coating thicknesses d, and for tungsten carbide spheres of radius $r = 3.18$ mm in Figs. 3 and 4 and $r = 1.98$ mm in Fig. 5. Data for the constituent bulk materials represent upper and lower bounds for the bilayer functions. Best fits of Eqs. (1) and (3) to these bounding data in the elastic and elastic–plastic regions are shown as dashed curves. We distinguish the elastic and plastic regions arbitrarily by $a/r = 0.05$, corresponding to a typical indentation strain at yield [1]. (Alternatively, and perhaps preferably, one might distinguish the two regions by actual measurements of the contact pressure p_Y at which yield is first observed experimentally [1,24–26].) The best fits to the bulk material data enable the evaluations of the coating and substrate moduli (E_c' and E_s', E_s^* and E_c^*) and exponents (n and m) in Table 1.

With this parametric calibration for the constituent materials, we then use the bilayer data in Figs. 3–5 to determine L as a function of $a/d = (a/r)(r/d)$, solving from Eq. (8) (elastic) or Eqs. (13) and (14) (elastic–plastic). The results for the three bilayer systems are plotted in Fig. 6. Note that the $L(a/d)$ data for the three systems overlap each other within the random scatter in data, suggesting a universal function, although some systematic shifts are apparent. The data are best-fitted by a three-parameter Weibull function,

$$L(a/d) = 1 - \exp\left\{-\left[A + B\ln(a/d)\right]^M\right\} \qquad (17)$$

yielding coefficients $A = 0.749$, $B = 0.173$ and $M = 4.72$. This best-fit function is plotted as the solid curve in Fig. 6. Note that the data tend asymptotically to the limits $L = 0$ at $a/d = 0$ and $L = 1$ at $a/d = \infty$, as required.

To illustrate the validity of this fitting procedure, we regenerate the indentation stress–strain functions $p_0(a/r)$ from Eqs. (8) and (13) for the bilayers as the solid curves in Figs. 3–5, using the best-fit function $L(a/d)$ in Eq. (17) together with the empirically calibrated material parameters in Table 1. Notwithstanding some systematic deviations from the data, the regenerated curves account for the broad trend from coating-controlled to substrate-controlled behavior as the indentation strain a/r increases, and as the coating thickness d diminishes.

Table 1
Elastic–plastic parameters in Eq. (1) for bulk coating (c) and substrate (s) materials represented in Figs. 3, 4 and 5

Material		Elastic modulus (GPa)	Inelastic modulus (GPa)	Inelastic exponent
Glass–ceramic (Dicor)	(c)	$E_c = 64.1$	$E_c^* = 22.4$	$n = 0.614$
Polymer (HCE)	(s)	$E_s = 23.5$	$E_s^* = 11.5$	$m = 0.764$
Porcelain	(c)	$E_c = 54.8$	$E_c^* = 39.7$	$n = 0.852$
Al_2O_3 (infiltrated)	(s)	$E_s = 218$	$E_s^* = 57.6$	$m = 0.540$
Si_3N_4	(c)	$E_c = 220$	$E_c^* = 89.0$	$n = 0.639$
Si_3N_4–30BN	(s)	$E_s = 113$	$E_s^* = 15.0$	$m = 0.368$

5. Discussion

In this study we have presented simple, analytical power-law relations for the stress–strain response $p_0(a/r)$ of elastic–plastic bilayer systems (Sections 2 and 3) for indentations with spheres. The configurational function $L(a/d)$ that lies at the core of the analysis has been evaluated from data on three material bilayer systems, and fitted with an empirical three-parameter Weibull function (Section 4). A feature of the formulation is the mathematical separation of material parameters (mismatch modulus factors E_c'/E_s' and E_c^*/E_s^*, exponents n and m) from geometrical parameters (a/d, or d/r), so that the roles of material and geometrical variables may be assessed independently. To make predictions for a given bilayer system it is still necessary to specify material parameters a prior for each layer component, or to calibrate these parameters directly from experimentally measured or FEM-generated data on monolith controls. The ensuing calculation of the composite $p_0(a/r)$ function using Eqs. (8) and (13) is more straightforward than conventional numerical analysis. In this context, the power-law formulation presents itself as a useful design adjunct for optimizing materials and geometries for layer structures.

The fact that we can fit a single function to the data in Fig. 6 for widely different coating/substrate bilayer systems suggests a certain universality in our function $L(a/d)$ for spherical indenters, providing confidence in using the analysis in a predictive capacity. Universality in $L(a/d)$ implies geometrical similarity in the contact field, essentially requiring that the geometry of the damage zones in Fig. 1b be the same for all material systems. This requirement is in fact unlikely to be satisfied for materials with widely different modulus and hardness properties, especially in the elastic–plastic regions where yield occurs preferentially and more extensively in the softer component [16,23]. Such departures from similarity could account for the small apparent system-to-system data shifts in Fig. 6, and thence for some of the discrepancies between data and predictions in Figs. 3–5. Nevertheless, the predicted curves do appear to predict the broader data trends in these figures.

In principal, one could derive analogous $L(a/d)$ functions for contacts with fixed-profile indenters, e.g., cones or pyramids, in terms of the (size-invariant) hardness values of the coating and substrate materials [17]. The advantage of spherical indenters is that they incorporate the complete range of elastic and plastic properties within the constituent $p_0(a/r)$ functions [21,25,27], whereas the same functions for fixed-profile indenters (at least in the loading half-cycle of the indentation) contain information only on the fully plastic state.

In the present work we have chosen bilayers with coating thicknesses in the range $\approx 0.1-1$ mm as illustrative case studies. However, universality in $L(a/d)$ means that the analysis should apply equally well to microscale and even nanoscale layers—it is necessary only to scale the indentation process to suit the scale of the coating. To establish a rule of thumb for this scaling we write $r/d = (r/a)(a/d)$, and insert the following representative values: (i) $a/d = 2.77$ at $L = 0.5$ in Eq. (17) (Fig. 6), corresponding to a contact configuration in which the substrate and coating contribute equally to the load-bearing capacity; (ii) $a/r = 0.1$, corresponding to the mid-range of elastic–plastic deformation (Figs. 3–5). This gives $r/d \approx 25$. Hence our use of sphere radius $r = 1.98$ and 3.18 mm is most appropriate to coatings of thickness $d \approx 0.1$ mm. Conversely, for $d = 1$ μm and $d = 1$ nm, we would choose spheres of radius $r \approx 25$ μm and $r \approx 25$ nm, respectively, which is in the range of instrumented nanoindenters.

We have used the properties of the constituent bulk materials to predict the indentation stress–strain response of composite bilayers. In many coating systems this course may not always be possible, because of difficulties in obtaining bulk specimens of the coating material for independent evaluation. Moreover, the properties of coatings may be very different from those of the corresponding bulk material. (A striking example is plasma-sprayed coatings, where the moduli may be diminished by more than an order of magnitude [12].) In this context, a potentially important application of our simple formulation is to deconvolute the coating properties from measurements on the composite bilayers. In principle, one should be able to evaluate all of the coating and substrate parameters (moduli E_c' and E_s', E_c^* and E_s^*, exponents n and m) by best-fitting the bilayer data sets to Eqs. (8) and (13) in the elastic and elastic–plastic regions, in conjunction with Eqs. (14) and (17). In practice, the reliability of any such evaluation will depend on the availability of a sufficient quantity of data; and, in the case of the coating, will be greatly improved if the properties of the substrate are

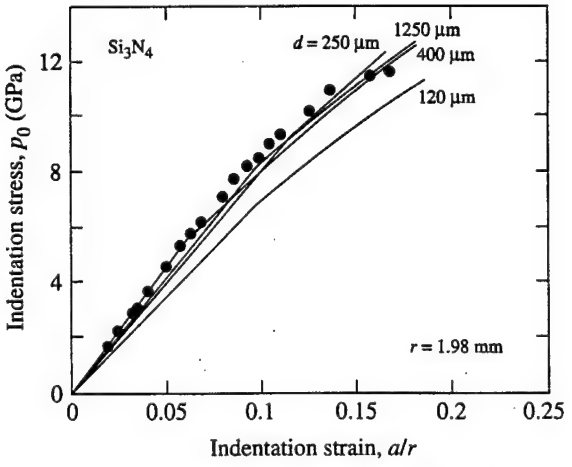

Fig. 7. Plot of indentation stress–strain curves for Si_3N_4 coating material. Data points are experimental measurements from Fig. 5. Solid curves are predictions from Eqs. (1) and (3) using coating parameters deconvoluted from bilayer data in Fig. 5.

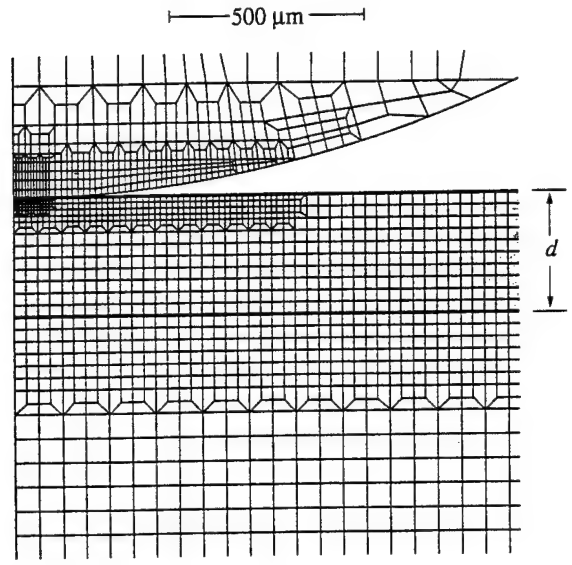

Fig. 8. Finite element grid for indentation of bilayer of coating thickness d with sphere of radius r (3.18 mm).

independently established. As an example, we use the bilayer data sets for each coating thickness d in Fig. 5 to determine the parameters for the silicon nitride coating material, using the substrate parameters listed in Table 1. With these determinations, we regenerate the coating stress–strain functions (solid curves) shown in Fig. 7, for comparison with the experimental data points. The correlation between predicted curves and experimental data is generally well within 10% in stress values, except for the smallest coating thickness d. The discrepancy in the latter case confirms that more reliable evaluations of the coating properties are likely to come from data at larger d.

Our power-law stress–strain formulation, notwithstanding its apparent capacity to predict trends, has acknowledged limitations. We have already alluded to departures from universal geometrical similarity as one such limitation. Invariably, adoption of empirical power-law functions provides mathematical expediency at the expense of physical insight. Such idealized power-law functions are unlikely to represent fundamental uniaxial stress–strain responses. (In fact, in quasi-plastic materials, the underlying elastic–plastic response is probably closer to bilinear [28], resulting in a nonlinear $p_0(a/r)$ function different from power-law [21].) We may expect the regenerated $p_0(a/r)$ curves to provide inaccurate representations in the transition region near the yield point, and at high stresses and strains as the deformation approaches full plasticity. In brittle coatings on soft substrates, experimental data points are expected to fall below the regenerated curves at high loads, as transverse cracks propagate and reduce the net compliance of the system [13,22]. (However, note that delamination cracks are less likely to influence the results, since these cracks tend to form predominantly at the end of unloading [13].) We may further expect the regenerated curves to be inaccurate in the presence of superposed residual in-plane coating stresses, e.g., from thermal expansion mismatch between interlayers, especially for residual stresses > 1 GPa (cf. values of p_0 in Figs. 3–5). FEM simulations are likely to provide more accurate and continuous representations over the data range, especially in the vicinity of the yield point [14,15], and if due allowance is also made in the code for the incidence of any transverse cracking [29].

Finally, it is envisioned that the procedure outlined in Sections 2 and 3 might equally well be used to derive load-displacement (P–z) relations of the kind measured in instrumented indentation testing [30,31].

Acknowledgements

Funding from the Australian Research Council and from the US Air Force Office of Scientific Research is acknowledged. The authors are grateful to S. Wuttiphan, I.M. Peterson and Y.G. Jung for providing the FEM data sets in Figs. 3 and 4 and Eq. (A1b), and to K.S. Lee and S.K. Lee for providing the experimental data in Fig. 5.

Appendix A. Finite element modelling of indentation stress–strain curves

A commercial FEM package (Strand, G&D Computing, Sydney, Australia) is used to construct an algorithm for generating the data in Figs. 3 and 4 [14,15]. The algorithm models an indenting sphere of given radius ($r = 3.18$ mm) in frictionless axisymmetric contact on a flat cylindrical specimen (4 mm radius and 4 mm thick), using the grid shown in Fig. 8. For the bilayer structures, each material layer is allowed to yield according to a

Table 2
Material parameters in constitutive relation Eq. (A1a) for bulk coating and substrate materials represented in Figs. 3 and 4

Material	Young's modulus [E] (GPa)	Yield stress [Y] (GPa)	Strain-hardening coefficient [α]
Glass–ceramic (Dicor)	69.0	1.95	0.40
Polymer (HCE)	25.0	0.59	0.75
Porcelain	66.6	1.95	1.00
Al_2O_3 (infiltrated)	252	4.35	0.40

critical shear stress condition, in conjunction with a bilinear uniaxial stress–strain function $\sigma(\varepsilon)$ [25]:

$$\sigma = E\varepsilon, \quad (\sigma < Y) \tag{A1a}$$

$$\sigma = Y + \alpha(\varepsilon E - Y), \quad (\sigma > Y) \tag{A1b}$$

with E Young's modulus, Y a uniaxial compression yield stress, and α a dimensionless strain-hardening coefficient ($0 \le \alpha \le 1$: $\alpha = 1$, fully elastic; $\alpha = 0$, fully plastic). Strong interfacial bonding is assumed between the adjacent layers in Fig. 8 (no delamination). Contact is incremented monotonically to peak load, with a maximum 50 iterations at each increment, with a tolerance 0.1% in force and 0.5% in displacement. At each load P the contact radius a is determined, from which $p_0 = P/\pi a^2$ and a/r are evaluated.

In order to generate a priori FEM stress–strain curves for the bilayers of specified coating thicknesses d in Fig. 8, the parameters, E, Y and α in Eq. (1) (as well as Poisson's ratio-taken here at a common value 0.25), must first be specified for each material. In practice, this is most readily done by 'calibration' against experimental $p_0(a/r)$ data for bulk specimens. The results of such parameter calibrations for the materials in Figs. 3 and 4 are summarized in Table 2, to be described in more detail elsewhere [22].

References

[1] D. Tabor, Hardness of Metals, Clarendon, Oxford, 1951.
[2] M.V. Swain, B.R. Lawn, Phys. Status Solidi 35 (1969) 909.
[3] M.V. Swain, J.T. Hagan, J. Phys. D 9 (1976) 2201.
[4] F. Guiberteau, N.P. Padture, H. Cai, B.R. Lawn, Philos. Mag. A 68 (1993) 1003.
[5] H. Cai, M.A. Stevens Kalceff, B.R. Lawn, J. Mater. Res. 9 (1994) 762.
[6] N.P. Padture, B.R. Lawn, J. Am. Ceram. Soc. 77 (1994) 2518.
[7] H.H.K. Xu, L. Wei, N.P. Padture, B.R. Lawn, R.L. Yeckley, J. Mater. Sci. 30 (1995) 869.
[8] A. Pajares, L. Wei, B.R. Lawn, D.B. Marshall, J. Mater. Res. 10 (1995) 2613.
[9] D.F. Diao, K. Kato, K. Hokkirigawa, Trans. ASME J. Tribology 116 (1994) 860.
[10] L. An, H.M. Chan, N.P. Padture, B.R. Lawn, J. Mater. Res. 11 (1996) 204.
[11] S. Wuttiphan, B.R. Lawn, N.P. Padture, J. Am. Ceram. Soc. 79 (1996) 634.
[12] A. Pajares, L. Wei, B.R. Lawn, N.P. Padture, C.C. Berndt, Mater. Sci. Eng. A 208 (1996) 158.
[13] A. Pajares, L. Wei, B.R. Lawn, C.C. Berndt, J. Am. Ceram. Soc. 79 (1996) 1907.
[14] A.C. Fischer-Cripps, B.R. Lawn, A. Pajares, L. Wei, J. Am. Ceram. Soc. 79 (1996) 2619.
[15] S. Wuttiphan, A. Pajares, B.R. Lawn, C.C. Berndt, Thin Solid Films 293 (1997) 251.
[16] K.S. Lee, S. Wuttiphan, X.Z. Hu, S.K. Lee, B.R. Lawn, J. Am. Ceram. Soc. (in press).
[17] A.K. Bhattacharya, W.D. Nix, Int. J. Solids Struct. 24 (1988) 1287.
[18] H. Gao, C.-H. Chiu, J. Lee, Int. J. Solids Struct. 29 (1992) 2471.
[19] H. Hertz, Hertz's Miscellaneous Papers, Macmillan, London, Chaps. 5–6, 1896.
[20] K.L. Johnson, Contact Mechanics, Cambridge Univ. Press, London, 1985.
[21] A.C. Fischer-Cripps, B.R. Lawn, Acta Metall. 44 (1996) 519.
[22] Y.G. Jung, S. Wuttiphan, I.M. Peterson, B.R. Lawn, J. Dent. Res. (in preparation).
[23] H. Liu, B.R. Lawn, S.M. Hsu, J. Am. Ceram. Soc. 79 (1996) 1009.
[24] R.M. Davies, Proc. R. Soc. London A 197 (1949) 416.
[25] A.C. Fischer-Cripps, B.R. Lawn, J. Am. Ceram. Soc. 79 (1996) 2609.
[26] S.K. Lee, S. Wuttiphan, B.R. Lawn, J. Am. Ceram. Soc. 80 (1997) 2367.
[27] A.C. Fischer-Cripps, J. Mater. Sci. 32 (1997) 727.
[28] B.R. Lawn, D.B. Marshall, J. Mech. Phys. Solids 46 (1998) 85.
[29] C. Kocer, R.E. Collins, J. Am. Ceram. Soc. (in press).
[30] M.V. Swain, J. Mencik, Thin Solid Films 253 (1994) 204.
[31] Y. Sun, A. Bloyce, T. Bell, Thin Solid Films 271 (1995) 122.

journal

J. Am. Ceram. Soc., 81 [8] 1977–94 (1998)

Indentation of Ceramics with Spheres: A Century after Hertz

Brian R. Lawn*

Materials Science and Engineering Laboratory, National Institute of Standards and Technology, Gaithersburg, Maryland 20899

In this article we review the nature and mechanics of damage induced in ceramics by spherical indenters, from the classical studies of Hertz over a century ago to the present day. Basic descriptions of continuum elastic and elastic–plastic contact stress fields are first given. Two distinct modes of damage are then identified: Hertzian cone cracks, in relatively hard, homogeneous materials, such as glasses, single crystals, fine-grain ceramics (tensile, "brittle" mode); and diffuse subsurface damage zones, in relatively tough ceramics with heterogeneous microstructures (shear, "quasi-plastic" mode). Ceramographic evidence is presented for the two damage types in a broad range of materials, illustrating how an effective brittle–ductile transition can be engineered by coarsening and weakening the grain structure. Continuum analyses for cone fracture and quasi plasticity, using Griffith–Irwin fracture mechanics and yield theory, respectively, are surveyed. Recent micromechanical models of the quasi-plastic mode are also considered, in terms of grain-localized "shear faults" with extensile "wing cracks." The effect of contact-induced damage on the ensuing strength properties of both brittle and quasi-plastic ceramics is examined. Whereas cone cracking causes abrupt losses in strength, the effect of quasi-plastic damage is more gradual—so that more heterogeneous ceramics are more damage tolerant. On the other hand, quasi-plastic ceramics are subject to accelerated strength losses in extreme cyclic conditions ("contact fatigue"), because of coalescence of attendant microcracks, with implications concerning wear resistance and machinability. Extension of Hertzian contact testing to novel layer structures with hard, brittle outer layers and soft, tough underlayers, designed to impart high toughness while preserving wear resistance, is described.

D. B. Marshall—contributing editor

Manuscript No. 190382. Received February 13, 1998; approved June 22, 1998.
*Member, American Ceramic Society.

I. Introduction

SINCE Hertz first investigated the beautiful cone-shaped fractures produced in contacts between glass lenses in the 1880s (see *Hertz's Collected Papers*[1]), indentation mechanics has become extensively used in the analysis and characterization of fracture and deformation properties of brittle ceramics,[2,3] as well as of metals and other materials.[4] Indentation damage bears profoundly on a wide range of other mechanical properties, such as strength, toughness, and wear. Such damage is now recognized as a key limiting factor in the lifetime of ceramics in many engineering applications,[2,3,5] especially bearings[6] and engine components,[7] in both monoliths and coatings. Indentation damage applications extend to areas as diverse as dental restorations[8] and the anthropological study of ancient tools.[9] Accordingly, it is timely in this centennial feature article to review the nature and mechanics of contact damage, with due attention to both its rich historical basis in brittle fracture and its topical applications in the latest generation of tough ceramics.

Traditionally, Hertzian cone cracks have been most widely studied in flat silicate glass plate, using spheres of hard steel or tungsten carbide. Extensions to other brittle solids, single crystals (especially those with the diamond structure) and some hard, fine-grain polycrystalline ceramics became more prevalent in the period 1950–1970.[3] The Hertzian fracture begins as a surface ring crack outside the elastic contact and then, at a critical load, propagates downward and flares outward within a modest tensile field into a stable, truncated cone configuration. Much of the early work centered on the mechanics of cone crack initiation, especially the empirically observed linear relation between critical load and sphere size, so-called Auerbach's law, dating from 1891.[10] Auerbach's law posed a paradox, in that it apparently violated the notion that cone cracks should initiate when the maximum tensile stress in the indented body exceeds the bulk strength of the material. Griffith–Irwin fracture mechanics analysis was first introduced in the late 1960s to account for this paradox,[11] with many refinements and reinventions during the ensuing three decades.

More recently, sphere-indentation methods have been extended to heterogeneous ceramics with weak internal interfaces, large and elongate grains, and high internal residual

centennialfeature

stresses—i.e., tougher ceramics characterized by *R*-curves. The *R*-curve can be due to several toughening mechanisms, but is most commonly associated with energy dissipation by internal friction at sliding grains, platelets or whiskers, or other microstructural elements that "bridge" the crack wake.[12–14] Such ceramics ordinarily appear completely brittle in traditional strength tests. However, the very same microstructural features that enhance long-crack toughness tend also to degrade short-crack toughness, compromising such important properties as wear resistance.[15] Hertzian fracture tends to be suppressed in these materials—instead, a "quasi-plastic" deformation zone develops in the strong shear–compression region below the contact. Macroscopically, this deformation region resembles the plastic zones that occur in metals.[4] Microscopically, however, the damage is altogether different, consisting of an array of "closed" mode II cracks with internal sliding friction ("shear faults") at the weak planes within the microstructure.[16] At high loads, secondary "extensile" microcracks initiate at the ends of the constrained faults. Much precedent for this type of distributed damage exists in the literature on grossly heterogeneous brittle rocks in confined compression fields.[17,18] It is implicit that one can control the degree of quasi plasticity relative to the brittle mode by suitably tailoring the ceramic microstructure.[16]

Experimental simplicity and amenability to materials evaluation are features of general indentation testing. Sometimes indentation is the only practical means of obtaining fundamental information on critical lifetime-limiting damage modes in some ceramics, particularly the quasi-plastic mode. However, we will not attempt to cover the entire field of indentation testing here, omitting in particular parallel developments in the 1970s using Vickers and Knoop indenters ("sharp" indenters). These parallel developments have been reviewed elsewhere.[2,3,5] We simply point out here one major advantage of "blunt," spherical indenters—they enable one to follow the entire evolution of damage modes, as a progressive transition from initial elasticity to full plasticity.[19]

The layout in this article is as follows. We begin with a consideration of the stress fields beneath a spherical indenter, in both elastic and elastic–plastic contact. Then we present micrographic evidence for the two modes of indentation damage, single cone cracking ("brittle mode") and distributed microdamage ("quasi-plastic mode"), in a broad range of glassy and polycrystalline ceramics. Specific attention is focused on the controlling role of microstructure in the competition between these two modes. Damage models for the two modes, at both the macroscopic and microscopic levels, are described. The practical issue of strength degradation from damage accumulation, in particular relation to damage tolerance, is then examined. Finally, the scope of Hertzian contact testing is illustrated by examining the most recent work on contact fatigue and damage in layer structures.

II. Contact Stress Fields

Consider the frictionless contact of a sphere, radius r, at normal load P, on a flat continuum specimen, Fig. 1. The field is initially elastic. Beyond a critical load, either a Hertzian cone crack ("brittle solid") or a subsurface deformation zone ("plastic solid") initiates. Here we outline the basic features of the stress fields associated with elastic and elastic–plastic contacts.

(1) Elastic Fields

The basic Hertzian elasticity solutions for a sphere of radius r at normal load P are well documented.[1,2,20,21] The contact radius a is given by

$$a^3 = 4kPr/3E \tag{1}$$

where E is Young's modulus and $k = (9/16)[(1 - \nu^2) + (1 - \nu'^2)E/E']$ is a dimensionless coefficient, with ν Poisson's ratio and the prime notation denoting the indenter material.[21] The

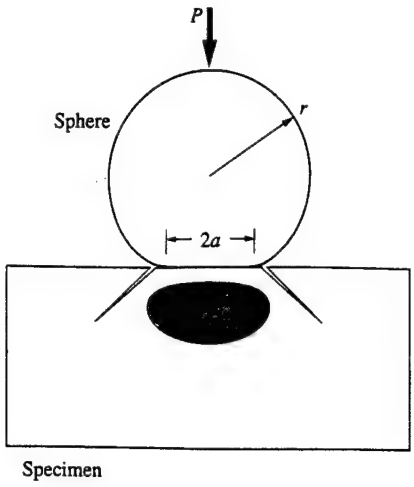

Fig. 1. Hertzian contact of sphere on flat ceramic specimen. Beyond elastic limit, contact initiates cone fracture ("brittle mode") or subsurface deformation zone ("quasi-plastic mode").

contact radius defines the spatial scale of the contact field. The mean contact pressure

$$p_0 = P/\pi a^2 \tag{2}$$

defines the intensity of the contact field. The maximum tensile stress in the specimen occurs at the contact circle:

$$\sigma_m = \frac{1}{2}(1 - 2\nu)p_0 \tag{3}$$

The maximum shear stress is located along the contact axis at a depth $\approx 0.5a$ below the surface:

$$\tau_m \approx 0.48p_0 \tag{4}$$

The mean contact pressure in Eq. (2) can be written in other useful forms by combining with Eq. (1). One such form expresses p_0 in terms of a and r:

$$p_0 = (3E/4\pi k)a/r \tag{5}$$

Equation (5) prescribes a linear relation between p_0, "indentation stress," and a/r, "indentation strain," leading to a procedure for obtaining basic stress–strain information.[4,22] Another useful form is given in terms of P and r:

$$p_0 = (3E/4k)^{2/3}(P/\pi r^2)^{1/3} \tag{6}$$

Principal normal and shear stresses are calculable from analytical solutions of the contact boundary conditions (Panel A). It is conventional to define $\sigma_1 \geq \sigma_2 \geq \sigma_3$ nearly everywhere within the Hertzian field, so that σ_1 is the most tensile principal stress and $\tau_{13} = \frac{1}{2}(\sigma_1 - \sigma_3)$ is the maximum principal shear stress. Figure 2 shows contours of σ_1, σ_3, and τ_{13} (σ_2 is a "hoop" stress). The σ_1 tensile stresses (shaded) in Fig. 2(a) concentrate in a shallow surface region, with maximum value σ_m at the contact circle (Eq. (3)). Included in Fig. 2(a) are σ_3 stress trajectories (dashed lines) from the specimen surface, defining paths always normal to σ_1 within the plane of the diagram. The rapid decrease of σ_1 along these trajectories is a characteristic feature of contact problems. Note that the σ_3 stresses in Fig. 2(b) are everywhere compressive. The principal shear stresses τ_{13} in Fig. 2(c) are constrained beneath the contact, with widely spaced contours and maximum value τ_m along the contact axis (Eq. (4)).

(2) Elastic–Plastic Fields

Above some yield point relatively soft materials, such as metals, undergo plastic flow beneath the contact. In relation to the uniaxial compression yield stress Y, the flow initiates at $\tau_m = \frac{1}{2}Y = 0.47p_Y$, corresponding to $p_Y \approx 1.1Y$.[4,21] At in-

Panel A. Hertzian Stress Fields

The stresses within the Hertzian elastic contact field are given by the following expressions, in cylindrical coordinates R,θ,z (with z along the axis of symmetry):[21,23]

$$\sigma_R/p_0 = \frac{1}{2}(1-2\nu)(a/R)^2[1-(z/u^{1/2})^3] + \frac{3}{2}(z/u^{1/2})\,[(1-\nu)u/(a^2+u) + (1+\nu)(u^{1/2}/a)\arctan(a/u^{1/2}) - 2]$$

$$\sigma_\theta/p_0 = \frac{1}{2}(1-2\nu)(a/R)^2[1-(z/u^{1/2})^3] + \frac{3}{2}(z/u^{1/2})^3[a^2u/(u^2+a^2z^2)] + \frac{3}{2}(z/u^{1/2})[(1-\nu)u/(a^2+u) + (1+\nu)(u^{1/2}/a)\arctan(a/u^{1/2}) + 2\nu]$$

$$\sigma_z/p_0 = \frac{3}{2}(z/u^{1/2})^3[a^2u/(u^2+a^2z^2)]$$

$$\tau_{Rz} = \frac{3}{2}[Rz^2/(u^2+a^2z^2)][a^2u^{1/2}/(a^2+u)]$$

where

$$u = \frac{1}{2}\{(R^2+z^2-a^2) + [(R^2+z^2-a^2)^2 + 4a^2z^2]^{1/2}\}$$

The principal normal stresses, defined such that $\sigma_1 \geq \sigma_2 \geq \sigma_3$ nearly everywhere,[11] are

$$\sigma_1 = \frac{1}{2}(\sigma_R+\sigma_z) + \left\{\left[\frac{1}{2}(\sigma_R+\sigma_z)\right]^2 + \tau_{Rz}^2\right\}$$

$$\sigma_2 = \sigma_\theta$$

$$\sigma_3 = \frac{1}{2}(\sigma_R+\sigma_z) - \left\{\left[\frac{1}{2}(\sigma_R+\sigma_z)\right]^2 + \tau_{Rz}^2\right\}$$

where σ_2 is a hoop stress. The maximum principal shear stress is

$$\tau_{13} = \frac{1}{2}(\sigma_1-\sigma_3)$$

The angle α between the σ_2–σ_3 stress trajectory surface (closely approximating the cone crack path) and the specimen free surface is given by

$$\tan 2\alpha = -2\tau_{Rz}/(\sigma_R-\sigma_z)$$

Analogous relations exist for a cylindrical flat punch end-loaded onto the specimen surface[21] and for a sliding spherical indenter.[24,25]

creasing load the plastic zone expands, but remains constrained within the elastic surrounds, enabling p_0 to increase steadily beyond p_Y, until a state of full plasticity is ultimately attained. In this region the Hertzian field is significantly modified. General analytical solutions for the transitional elastic–plastic field are not available. An "expanding-cavity" model embodying a spherically symmetrical half-spherical fully plastic zone encased in an elastic surround has been used with some success in soft metals with negligible strain-hardening in the region of fully plasticity.[21,26] However, the expanding-cavity model breaks down in harder materials with pronounced strain-hardening characteristics, which includes most ceramics.[27,28]

As foreshadowed in the previous subsection, the transition from elastic to plastic contacts can be conveniently demonstrated on indentation stress–strain curves, $p_0(a/r)$ (independent of sphere size r—geometrical similarity[4]). The development of plasticity becomes evident as an ever-increasing deviation from linearity in Eq. (5). Some heterogeneous ceramics, notwithstanding their incapacity to attain full plasticity, are nevertheless sufficiently deformable in sphere indentation to show significant nonlinearities on indentation stress–strain curves[16,22,29] (although generally much less pronounced than in metals). An extreme case is shown in Fig. 3, for a relatively soft micaceous glass-ceramic (Macor, Corning Inc., Corning, NY), noteworthy for its machinability.[30–32] The plot includes data for the material in its brittle base glass state. Above $p_0 = p_Y$ (indicated in Fig. 3) the quasi-plastic glass-ceramic shows distinctive yield characteristics (corresponding to the formation of well-defined residual impressions—see Section IV(1)). Clearly, the microstructural state of the material is crucial to the damage response.

In the absence of an analytical model for describing the indentation stress–strain response in ceramics, one usually resorts to numerical modeling of the contact process, e.g., finite-element modeling (FEM).[27,28] A constitutive yield condition is incorporated into the FEM algorithm, in conjunction with a bilinear stress–strain curve $\sigma(\varepsilon)$ in ideal uniaxial compression for each material (including the indenter):

$$\sigma = E\varepsilon \qquad (\sigma \leq Y) \tag{7a}$$

$$\sigma = Y + \alpha(\varepsilon E - Y) \qquad (\sigma \geq Y) \tag{7b}$$

where E is Young's modulus, Y is the uniaxial yield stress, and α is a dimensionless strain-hardening coefficient in the range $0 \leq \alpha \leq 1$ (with $\alpha = 0$ fully plastic and $\alpha = 1$ fully elastic). (Physical justification for Eq. (7) is given in Section IV(2).) The solid curves through the data in Fig. 3 are FEM-generated $p_0(a/r)$ functions, with independent determinations of E and Y and adjustments of α to give best fits.[28]

III. Hertzian Cone Fracture in Brittle Solids

(1) *Historical Survey*

As indicated, most early experiments on cone fracture were conducted on glass, notably soda–lime glass, in normal static loading. The transparency of this model brittle solid made it especially easy to follow the crack evolution. The 1950s saw the first serious attempts to understand the underlying mechanics of cone fracture in glass, highlighted by the systematic studies of Tillett[33] and Roesler.[34,35] Around the same time, papers on single crystals, notably on diamond,[36–39] germanium,[40] and silicon[41] began to appear, attesting to the generality of the phenomenon. The main distinguishing features in the single crystals were attendant cleavage tendencies in the surface crack patterns, reflecting crystallographic symmetries.

A photograph of a Hertzian cone crack in glass (in this instance, formed with an axisymmetric flat punch) is shown in Fig. 4(a).[34] The fully developed cone crack is the archetypical stable fracture system.[3,42] The crack base continues to grow steadily with subsequent increasing load. Roesler, using energy balance concepts in conjunction with Tillett's data, established the now well-known relation $P/R^{3/2} = constant$ between applied load P and cone base radius R. In the case of a spherical indenter, the expanding contact circle ultimately engulfs the surface ring, resulting in the generation of secondary ring cracks (a complication avoided with flat-punch indenters). Af-

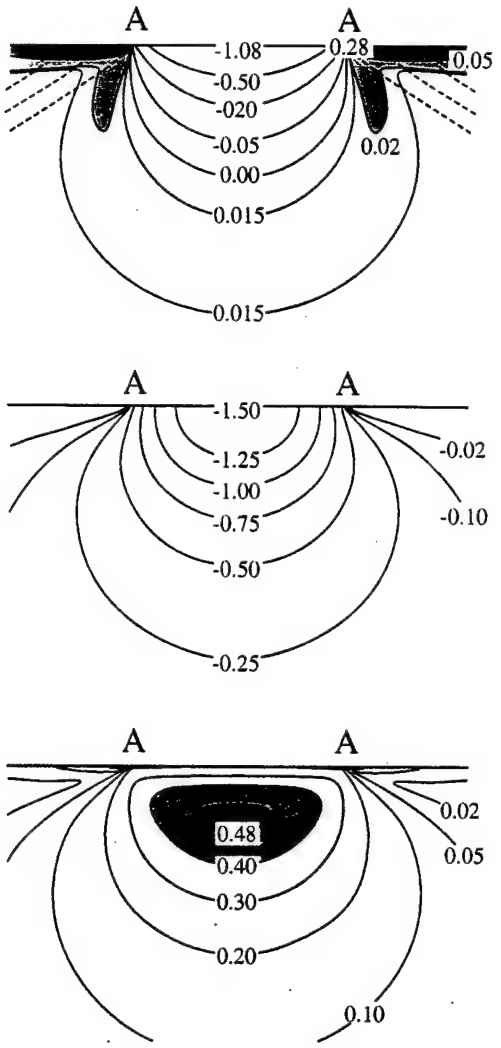

Fig. 2. Hertzian stress field: (a) principal normal stress σ_1, (b) principal normal stress σ_3, and (c) principal shear stress $\tau_{13} = \frac{1}{2}(\sigma_1 - \sigma_3)$. Dashed curves in (a) are σ_3 stress trajectories. Stresses in units of p_0. AA denotes contact diameter $2a$. Plotted for $\nu = 0.22$.

ter unloading, the fracture usually remains visible because of imperfect closure at the crack interface.[39,43]

The mechanics of cone crack *initiation* goes back to 1891, when Auerbach established his famous empirical law between critical load and sphere radius, $P_C \propto r$.[10] This relation and its limits were illustrated most compellingly by Tillett's data on glass,[33] reproduced in Fig. 5 as a plot of P_C/r vs r. Two regions of behavior are evident: the Auerbach region, $P_C/r = constant$, at small r; and a second region, asymptotic to $P_C/r^2 = constant$, at large r. Roesler subsequently reviewed the existing literature data on glass and demonstrated the commonality of Auerbach's law under a wide range of contact conditions, including impact.[35] From such studies arose one of the most celebrated paradoxes in brittle fracture theory: if it is assumed that cone cracking initiates when the maximum tensile stress exceeds the strength of the bulk solid, $\sigma_C = \sigma_m = \sigma_F$, Eqs. (3) and (6) predict $P_C \propto r^2$, independent of r. As Fig. 5 shows, this quadratic relation is approached only in the limit of infinite r. The stresses σ_C calculated from Eqs. (3) and (6) using measured P_C values are invariably higher than the measured bulk strengths σ_F on the same material, the more so at smaller r, implying breakdown of the critical stress concept; specifically, $P_C \propto r$ corresponds to $\sigma_m \propto r^{-1/3}$. At sufficiently small r, σ_C may become high enough that some form of plasticity generates before fracture, in even the most brittle materials, indicating a "brittle–ductile" transition with increasing indenter

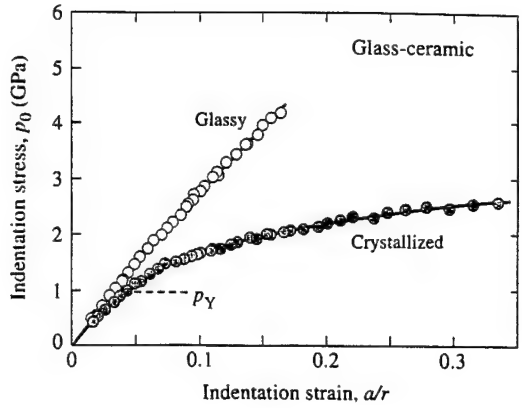

Fig. 3. Indentation stress–strain curve for glass-ceramic, in base glass and crystallized forms. Data taken with tungsten carbide spheres in the radius range $r = 0.79$ mm to 12.7 mm (not distinguished in plot). Curves through data are FEM fits using Eq. (7), with $\alpha = 1$ for the glassy state and $\alpha = 0.10$ for the crystallized state (E and Y independently determined). Initial yield pressure p_Y indicated for glass-ceramic. Data reproduced from Refs. 16 and 32.

"sharpness."[29,44–47] At the same time, σ_C generally remains well below the limiting cohesive strength of the solid over most practical ranges of r, indicating that the cone cracks must initiate from pre-present flaws.

This last point raises the issue of flaw statistics.[48,49] At one time it was proposed that Auerbach's law might be explained if the flaw distributions were sufficiently sparse. Assuming that the critical stress criterion remains valid, it was argued that smaller contacts have a lower probability of locating larger flaws within a given size population, accounting for an apparent increase in critical stress with decreasing r. This school pointed to the wide scatter in P_C data on smooth, carefully handled glass surfaces. However, later experiments on glass surfaces containing controlled flaws introduced by a wide range of abrasive grit sizes demonstrated an insensitivity of P_C to flaw size in the Auerbach region.[50]

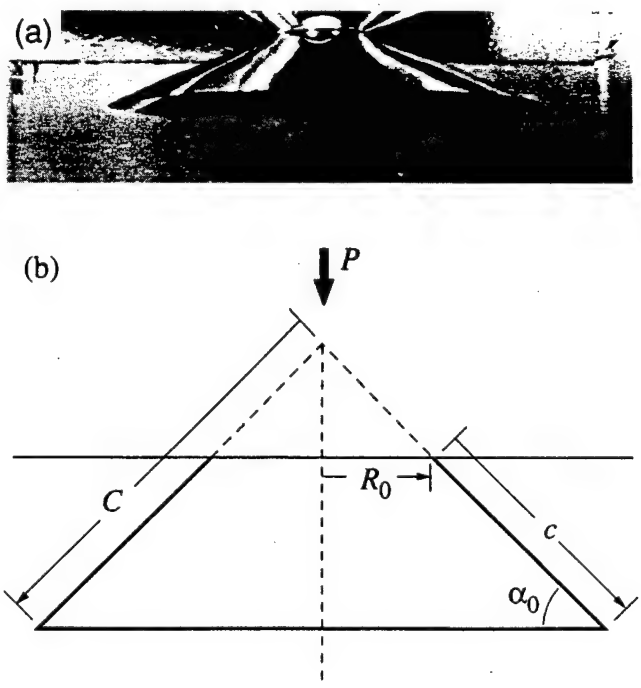

Fig. 4. Hertzian cone fracture: (a) photograph of crack in soda–lime glass, produced by indentation with cylindrical punch at $P = 40$ kN (block edge 50 mm), from Ref. 34; and (b) schematic showing critical geometrical parameters.

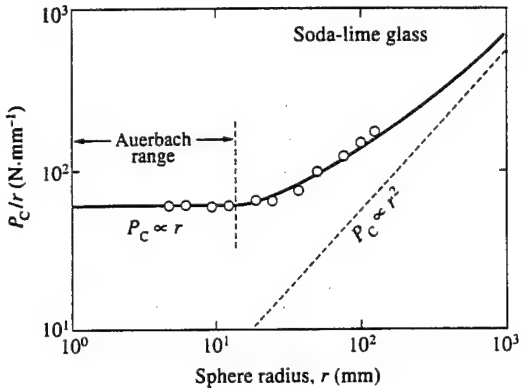

Fig. 5. Plot of P_C/r vs r for polished soda–lime glass, using steel spheres. Inclined dashed line is prediction for flaw in uniform field σ_m. Plot reproduced from Ref. 50, using Tillet's data.[33]

An important factor in the evolution of cone cracking is the test environment, particularly water. Early experimentalists noted that newly formed cone cracks in glass extend steadily at constant load, at first rapidly and then more slowly.[34,51] This growth was later demonstrated to be commensurate with conventional crack velocity laws.[52,53] The role of moisture is even stronger in the crack initiation. Figure 6 shows some data for soda–lime glass indented with steel spheres in different environments, plotted as critical load P_C vs contact time t_C (time to fracture at constant crosshead speed).[54] In any given environment, P_C decreases steadily with increasing t_C. At any given t_C, P_C decreases with increasing water content and with increasing temperature, highlighting the kinetic effect. Section-and-etch studies on cracks grown slowly in moist environments confirmed that the cone begins its life as a slowly penetrating embryonic surface ring prior to its abrupt full development.[55]

Later, experiments were extended to fine-grain polycrystalline and other ceramics.[56–63] Such materials are generally opaque, making it necessary to observe the specimen surface *a posteri* or to use acoustic emission to detect the crack initiation.

(2) *Introduction of Fracture Mechanics*

Introduction of Griffith–Irwin fracture mechanics into the Hertzian fracture problem was made in 1967 by Frank and Lawn,[11] with the express purpose of deriving Auerbach's law from first principles. The basic precepts of the fracture mechanics approach in the context of Hertzian fracture can be summarized as follows. Cone cracks tend to form in highly brittle solids with zero or insignificant R-curves, i.e., materials with single-valued toughness, $K_{IC} = T_0$. For such materials, extension of any crack of length c under equilibrium conditions is determined by the simple equality $K(c) = T_0$: if $dK(c)/dc > 0$, the equilibrium is unstable; if $dK(c)/dc < 0$, the equilibrium is stable.[3] When kinetic conditions prevail, extension is determined by a crack velocity relation $v = v(K)$.

Consider cone cracks in their well-developed state, Fig. 4(b). The actual crack length c is related to the dimension C of a "virtual" cone with the tip located above the contact surface:

$$C = c + R_0/\cos\alpha_0 \tag{8}$$

where R_0 is the surface ring radius and α_0 is the cone base angle. The stress-intensity factor for this virtual cone crack system is given by[3]

$$K(c) = \chi P/C^{3/2} \tag{9}$$

where χ is a crack geometry coefficient. At $K = T_0$, we have $P \propto C^{3/2}$, i.e., Roesler's relation. Sphere radius r enters Eqs. (8) and (9) only through R_0; therefore, $K(c)$ is insensitive to r in the region $c >> R_0$.

The mechanics of cone crack initiation is more complex. The Frank–Lawn treatment[11] addressed this issue in two key steps:

(i) The cone cracks start from flaws on the specimen top surface at (or just outside) the contact circle where the tensile stresses are concentrated. The embryonic cracks subsequently circumvent the contact circle as a shallow surface ring, then propagate downward and outward, closely (but not exactly) following the σ_3 trajectories (so as to be nearly normal at all points to the σ_1 tensile stresses) in the *prior* stress field (Fig. 2(a)).

(ii) A stress-intensity factor for the downward crack extension can be expressed uniquely in terms of the prior stress function $\sigma_1(s)$, where s is a coordinate along the σ_3 trajectory. The stress-intensity factor has the form

$$K(c/a) = p_0 a^{1/2} I(c/a,\beta,\nu) \tag{10}$$

where $\beta = R_0/a$ is the relative crack location and $I(c/a,\beta,\nu)$ is the dimensionless integral

$$I(c/a,\beta,\nu) = 2(c/\pi a)^{1/2}\int_0^{c/a}[\sigma_1(s/a,\beta,\nu)/p_0]\,d(s/a)/(c^2/a^2 - s^2/a^2)^{1/2} \tag{11}$$

Figure 7 sketches the normalized function $K(c/a)/T_0$ for a sequence of increasing loads ($P' \rightarrow P'' \rightarrow P'''$). The function has two unstable branches (1,3) and two stable (2,4) branches. Suppose the specimen contains surface flaws within the range $c_0 \le c_f \le c_*$ and that equilibrium conditions prevail. Then the crack evolves along the configurational path marked by the arrows, growing stably with load along $K/T_0 = 1$ until a critical penetration depth $c = c_*$ is reached, whence the full cone crack pops in and arrests on branch 4. Inserting $I_* = I(c_*/a) = constant$ and using Eqs. (1) and (2) to eliminate p_0 and a in Eq. (10), we obtain the critical condition for cone initiation:

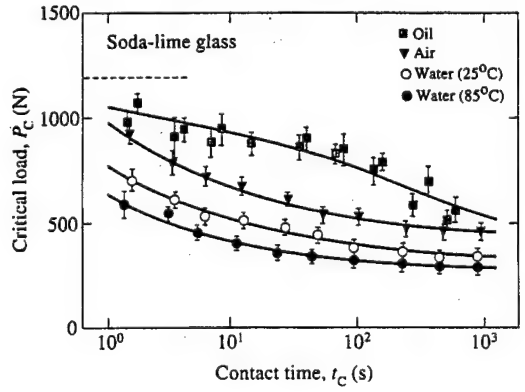

Fig. 6. Critical load for cone initiation as function of time to fracture in surface-abraded soda–lime glass, using steel spheres (r = 6.35 mm) at constant crosshead speeds in different environments. Reference horizontal dashed line is "inert" value (evaluated from sphere drop tests). Data from Ref. 54.

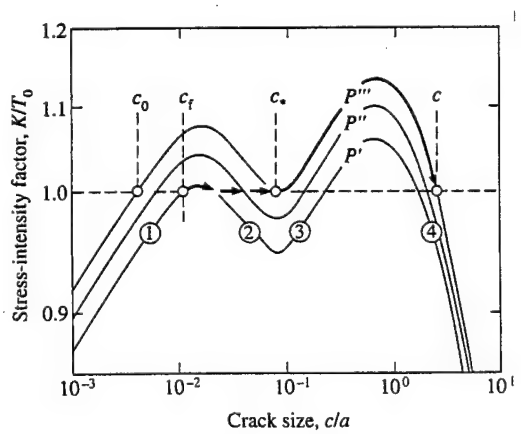

Fig. 7. Normalized $K(c)$ curves for Hertzian fracture (β = 1 and ν = 0.3). Arrows indicate evolution from surface flaw to full cone crack. Plots from Refs. 2 and 3.

$$P_C/r = AT_0^2/E = constant \quad (12)$$

where $A = 4\pi^2 k/3l_*^2 = constant$. Equation (12) is a formal statement of Auerbach's law.

The requirement that surface flaws must first grow to depth c_* before propagating into the full cone renders P_C independent of c_f in Eq. (12), consistent with the test results on variously abraded glass surfaces mentioned in the previous subsection.[50] For very small flaws in the range $c_f << c_0$, or for very large spheres (large r, large a), the initiation is spontaneous from branch 1 to branch 4—this is the domain of the asymptotic relation $P_C \propto r^2$ in Fig. (5). Interestingly, for very large flaws in the range $c_f >> c_*$ it can become increasingly difficult to initiate cone cracks at all, because of difficulties in accommodating the crack to the curved stress trajectory paths of maximum tension.[50,64,65]

A feature of Eq. (12) is the appearance of toughness T_0 (not apparent, of course, in the original empirical Auerbach's law).[11,34] This feature has been used to evaluate the toughness properties of several brittle glasses and single crystals[2,11,66,67] and fine-grain ceramics[58–63] (although Vickers indenters have proved to be more popular in this regard[68,69]).

Several variants of the above theory have appeared in the three decades since 1967.[53,61,70,71] Most have focused on modifications to the Greens function in Eq. (11), with allowance for several factors: a starting surface crack outside the contact ($\beta > 1$);[70,72] indenter–specimen interface friction (which redistributes the tensile stresses);[73] an ever-widening crack front;[53] and hybrid combination of flaw statistics with fracture mechanics.[71] One conclusion that can be drawn from these variant studies is that the exact form of the calculated $P_C(r)$ function is highly assumption-sensitive, making absolute predictions of toughness difficult. Some analyses question the existence of the "energy barrier" at $c = c_*$ in Fig. 7. In this context of analytical subjectivity, an approach by Kocer and Collins[74] using FEM simulations of cone crack evolution is worthy of special mention. In their algorithm, the cone crack is allowed to grow stepwise from a starting surface flaw, and the *actual* (as distinct from the *prior*) field at the crack tip is reevaluated at each step, using energy-release-rate principles to determine the next increment. The Kocer–Collins procedure is noteworthy for its accurate prediction of the observed cone crack angle, and offers the prospect of more-objective evaluations of toughness parameters.

Notwithstanding any persistent uncertainties in the fracture mechanics, the stabilizing role of the decreasing tensile stress function $\sigma_1(s)$ in Eq. (11) in the experimentally documented shift away from $P_C \propto r^2$ toward $P_C \propto r$ and the associated sphere-size dependence of the critical tensile stress σ_C are incontrovertible.

Finally, how restrictive is the presumption of a single-valued toughness in the equilibrium-crack analyses? For microstructurally heterogeneous ceramics with R-curves, $K(c)$ in Eqs. (9) and (10) should strictly be equated to a crack-size-dependent toughness function $K_R(c) = T(c)$ rather than to T_0 (equivalent to replacing the horizontal dashed line at $K/T_0 = 1$ in Fig. 7 by a K_R-curve), with consequent reduction in size of the cone crack. But a more dramatic consequence of microstructural heterogeneity, as shown in the next section, is a fundamental change in the damage mode.

IV. Quasi-Plastic Damage in Tough Ceramics

(1) Nature of Quasi-Plastic Deformation

Investigation of sphere-indentation quasi-plastic damage in tough, heterogeneous ceramics, although foreshadowed in some earlier studies,[22,29,75] began in earnest only in the 1990s.[16,19,32,76–79] We have already alluded to this damage mode in association with nonlinear stress–strain curves (Fig. 3) and to attendant suppression of cone cracking in such ceramics. The question remains: what is the nature of the quasi plasticity?

Contact-induced quasi plasticity is manifest as a residual surface impression above a threshold yield load P_Y. Combining $\tau_m = \frac{1}{2}Y$ with Eqs. (4) and (6) gives

$$P_Y/r^2 = (1.1\pi Y)^3(4k/3E)^2 = constant \quad (13)$$

Measurement of p_Y thereby affords a simple means for determining the yield stress Y.[80] The quadratic relation $P_Y \propto r^2$ implies geometrical similarity in the elastic–plastic field (valid as long as the contact dimension remains very much larger than the microstructure scale[4,81]). Again, comparison of $P_Y \propto r^2$ for yield with $P_C \propto r$ for cracking indicates an increasing tendency to dominant plasticity at "sharper" contacts.

But the most informative clues as to the nature of the quasi-plastic mode are obtained from subsurface sections. (Recall from Fig. 2(c) that the location of maximum shear stress is located beneath the contact surface.) One particularly useful technique, an adaptation from earlier workers,[29,82,83] involves *pre*sectioning a specimen into two half-blocks before indentation, using an adhesive to bond the two halves together again, and indenting across the surface trace of the bonded interface—Nomarski illumination of the separated half-blocks then reveals the subsurface damage.[32,76] Half-surface and section views obtained in this way are shown in Fig. 8(a) for the same crystal-

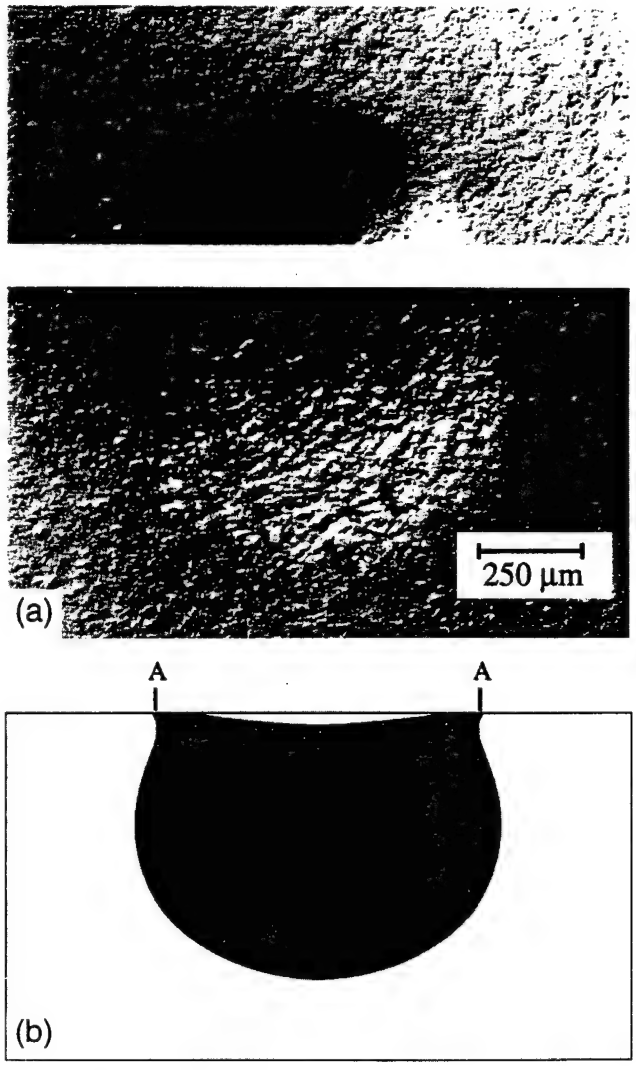

Fig. 8. Hertzian indentation damage in machinable glass-ceramic, from tungsten carbide sphere (r = 1.98 mm and P = 1000 N): (a) optical micrographs, half-surface and side view of indentation, bonded-interface specimen, surfaces gold coated after indentation, Nomarski interference, from Ref. 32; and (b) computed yield zone, contact diameter AA, using FEM algorithm, from Ref. 28.

lized glass-ceramic used to obtain the stress–strain data in Fig. 3. The subsurface quasi-plastic zone in this ceramic is macroscopically similar to the yield zones beneath hardness impressions in soft metals, except that it is much more highly constrained ("pinched") beneath the immediate contact. Observations of sequences of indentations at different loads allow one to follow the entire evolution of the quasi-plastic zone, from initial yield to "full plasticity."[28,32] Cone cracking is conspicuously absent in Fig. 8(a).

Bonded-interface observations on two other model ceramic systems serve to demonstrate the critical role of microstructure in the competition between fracture and deformation. Figure 9 shows damage patterns in pure, dense alumina over a broad range of grain sizes, 3–48 μm, under common indentation conditions.[19,76] A progressive "brittle–ductile" transition with increasing grain size, from well-defined cone cracking to diffuse subsurface damage, is apparent. Surface ring cracks form in all cases, but are increasingly inhibited in their downward growth in the coarser aluminas, ultimately to one grain depth or less. The quasi-plastic zones again remain severely constrained below the contact. The intensity of damage in such zones can be strongly enhanced in the alumina microstructure by including platelet phases with weak interphase boundaries[84,85] or pores.[86] Figure 10 is an analogous sequence of patterns in silicon nitride for microstructures with increasing grain size, aspect ratio, and β:α phase ratio, designated fine (F), medium (M), and coarse (C).[79,81] Once more, a progressive transition from well-defined cone crack to distributed subsurface damage is observed. In this material the response is highly sensitive to processing conditions, starting powder, etc.[87] It is interesting that the grades of silicon nitride used in practical bearing structures lie closest to the intermediate microstructure in Fig. 10,[81] suggesting a compromise between the extremes of dominant cracking and dominant quasi plasticity.

It is at the microstructural level that the underlying character of the quasi-plastic deformation is determined. Figure 11 is a magnified view of the damage in the glass-ceramic of Fig. 8(a), from a central section region.[32] Distributed shear-fault microfailures occur at weak interfaces between mica platelets and surrounding glass phase. (These weak interfaces enhance both machinability[30,31] and long-crack toughness.[88]) Other platelet structures, e.g., alumina with additive calcium hexaluminate phases[84,89] and silicon carbide with yttrium aluminum garnet (YAG) second phase,[77,90] exhibit similar shear-fault arrays. In monolithic structures, e.g., alumina (Fig. 9)[19,76] and silicon nitride,[79] the shear faults take the form of transgranular twinning or block slip. In zirconia, the shear-fault damage is augmented by phase transformations.[78,91] A general feature of the shear faults is their discreteness, localized by the grain structure. The constrained shear faults may in turn initiate secondary microcracks at their ends, especially where the faults intersect weak grain or interphase boundaries.[19,76]

Attempts at quantitative evaluation of the damage intensity have been made. Damage intensity is usually characterized

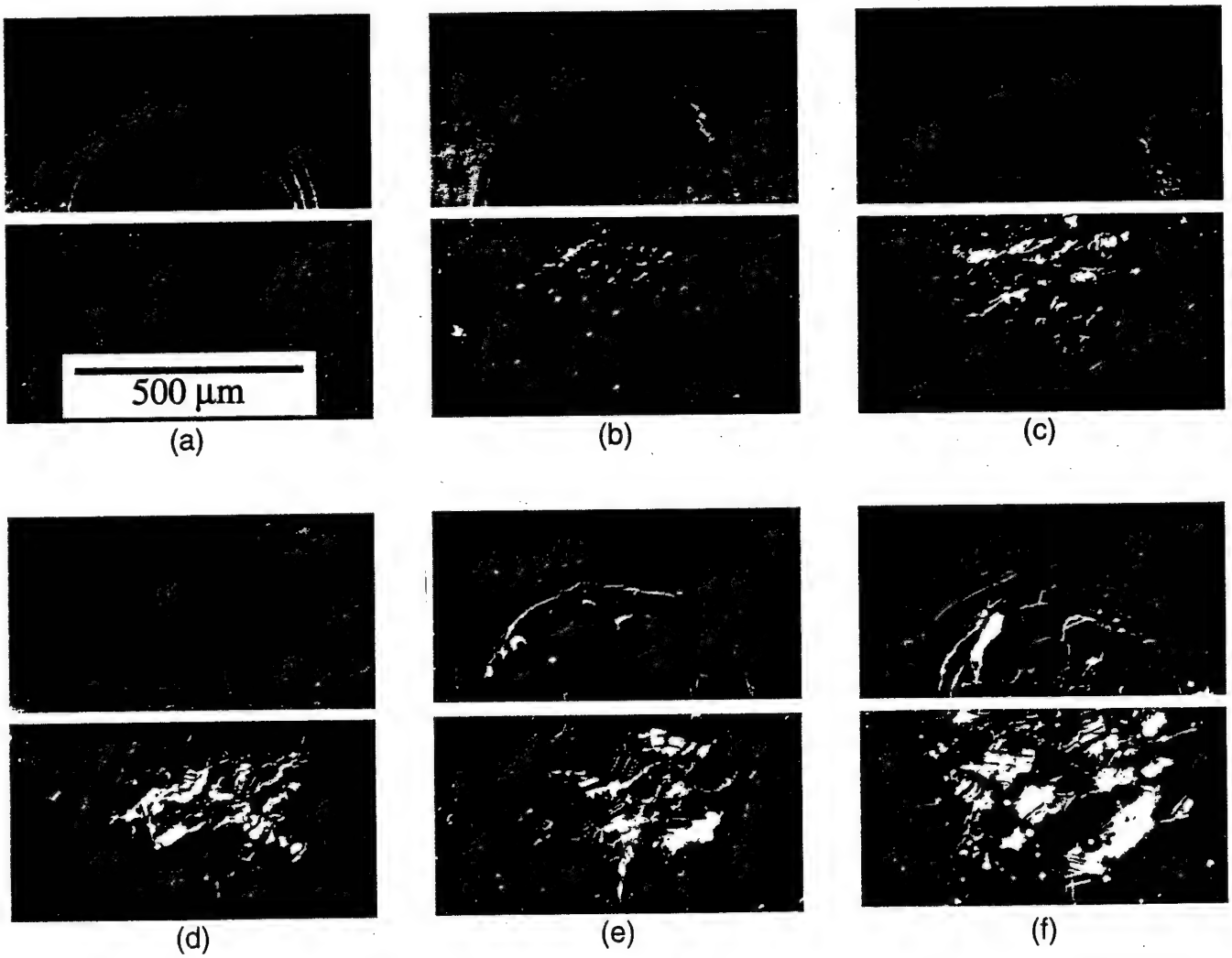

Fig. 9. Hertzian indentation damage in pure, dense alumina from tungsten carbide sphere (r = 3.18 mm and P = 2000 N), grain sizes (a) 3, (b) 9, (c) 15, (d) 21, (e) 35, and (f) 48 μm. Half-surface (upper) and section (lower) views, bonded-interface specimens. Optical micrographs, surfaces gold coated after indentation, Nomarski interference. Reproduced from Ref. 76.

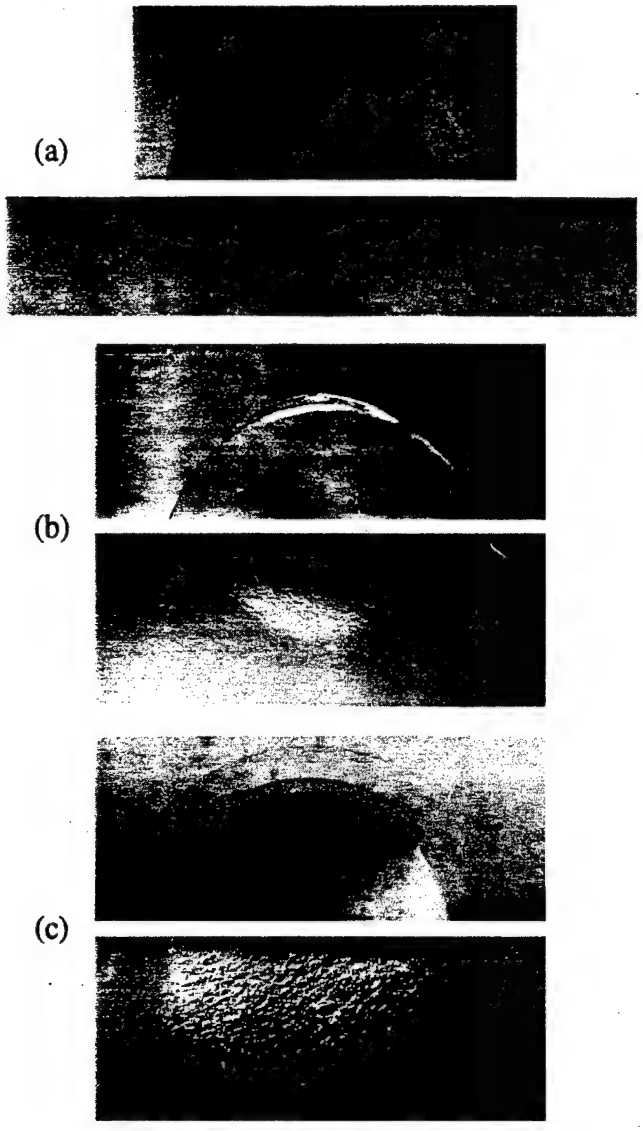

Fig. 10. Hertzian indentation damage in silicon nitride, from tungsten carbide sphere (r = 1.98 mm and P = 4000 N): (a) F fine, (b) M medium, and (c) C coarse. Half-surface (upper) and section (lower) views from bonded-interface specimens. Optical micrographs, surfaces gold coated after indentation, Nomarski interference. Reproduced from Ref. 81.

by a parameter Nl^3, where N is the number density and l the characteristic size of the composite faults (which, depending on the specific measurement technique, may or may not include both primary fault and secondary microcrack). *In situ* acoustic emission has revealed considerable activity from damage events in heterogeneous silicon carbide, during unloading as well as loading, enabling at least relative measurements of damage intensity.[77] Another nondestructive evaluation (NDE) technique, thermal wave imaging, has been used to provide absolute measurements in alumina and other ceramics (Panel B).

At high loads or large numbers of cycles (Section VI), the damage in the more heterogeneous ceramics can become so intense that neighboring microcracks coalesce (Fig. 11), leading ultimately to extensive material removal. As alluded to earlier, such materials tend to have inferior wear properties.

(2) Damage Mechanics

Macroscopic aspects of the quasi-plastic damage zone beneath a spherical indenter can be confirmed using numerical computational methods, such as the FEM algorithm described

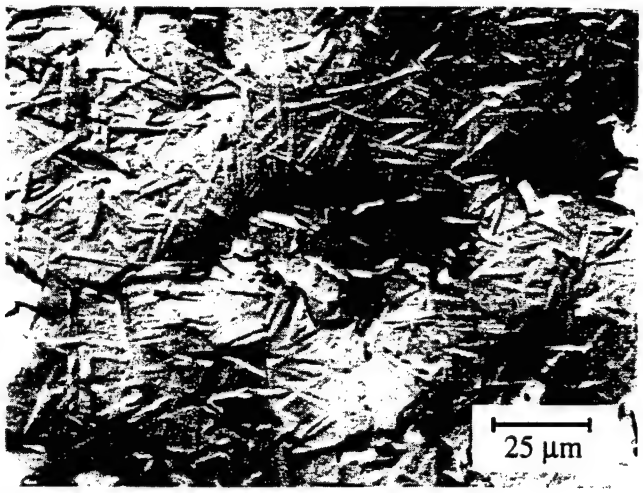

Fig. 11. Enlarged view of subsurface damage microcracks and coalescence in heavily damaged area of Fig. 8(a). Note microfailures at weak interfaces between mica platelets and glass phase. Reproduced from Ref. 32.

in Section II(2). In the FEM calculations, the material below the indenter is allowed to deform in accordance with the bilinear yield relation Eq. (7), using stress–strain data (e.g., Fig. 3) to "calibrate" the essential material parameters.[28] Boundaries of the damage zone at any given load are then determined as the shear-stress contour $\tau_{13} = Y/2$. For the glass-ceramic in Fig. 8, the computed contour shows geometrical correspondence with the experimental damage zone. This correspondence confirms that the damage is essentially shear-driven, i.e., is quasi plastic. The FEM computations also demonstrate that the yield can relax the tensile stresses outside the surface contact.[28]

To understand the role of microstructure it is necessary to model the discrete damage events within the confining shear–compression elastic–plastic contact field, Fig. 12(a). The generic picture is that of a closed sliding shear fault with attendant extensile "wing" cracks at the constrained fault ends, Fig. 12(b). This type of modeling, while highly phenomenological, has strong precedent in the rock mechanics literature.[17,18,96,97] Because of the compression across the shear fault surfaces the sliding must overcome an internal resistive "cohesion" stress τ_c, so that the net sliding shear stress is $\tau_* = \tau_P - \tau_c$, where τ_P is the applied shear stress associated with the applied field. (A more general expression includes an extra friction coefficient μ term, neglected here.[98]) For a body in uniform uniaxial compression containing an array of noninteracting, favorably aligned penny shear faults of number density N and size l (ignoring wing cracks for the moment), we recover the bilinear relation Eq. (7*b*), with[98]

$$Y = 2\tau_c \tag{14a}$$

$$\alpha = 1/(1 + 2Nl^3) \tag{14b}$$

Thus the yield stress Y is determined by the intrinsic shear stress to initiate sliding failure at internal interfaces, and the strain-hardening coefficient α is determined by the damage parameter Nl^3 (with limits $2Nl^3 << 1$ corresponding to a fully elastic response and $2Nl^3 >> 1$ to a fully plastic response). Equation (14) connects the micromechanics with the macroscopic stress–strain curves and opens the way, through N and l, to incorporation of microstructural variables (e.g., grain size and shape, volume fraction of particulate phases) into the analysis.[98]

Extensile wing cracks initiate at the faults above some critical stress, depending on the grain size.[99] (By effectively increasing the fault size, the wing cracks lower α even further than predicted in Eq. (14*b*), leading in extreme cases to "strain

Panel B. Quantifying Microcrack Damage Using Thermal Wave Imaging

With Lanhua Wei, Therma-Wave, Fremont, California

Several NDE methods exist for detecting contact damage accumulation. Acoustic emission has proved useful in some cases, revealing damage activity during both loading and unloading.[77] Instrumented nanoindenters have been used to probe damage zones on section surfaces (e.g., Fig. 10), and thus to evaluate damage intensities from relations between elastic modulus and microcrack density.[92] One of the more intriguing methods is instrumented thermal wave analysis, which is especially sensitive to the presence of open cracks. The technique can be used in scanning mode to provide a digitized image of the fracture damage distribution, and to quantify the density of microcracks.[93]

Figure B1 shows images of the same alumina specimens as in Fig. 9.[94] High-damage regions are indicated in red ("hot") and undamaged regions in green ("cold"). The patterns provide a pictorial illustration of the transition from single macrocrack in the fine structures to diffuse microcrack zone in the coarse structures, correlating with the optical observations in Fig. 9.

Quantitative data on crack densities are obtained from evaluations of thermal diffusivities α at each digitized pixel, using a modified version of a relation by Hasselman:[95]

$$Nl^3 = (9/8n) \sum_i^n (\alpha_0/\alpha_i - 1)$$

where α_i is evaluated over all n pixels within the damage zone and α_0 is evaluated without. Figure B2 plots Nl^3 as a function of grain size l. A systematic increase in microcrack damage intensity with microstructural heterogeneity is apparent above a threshold value of l.

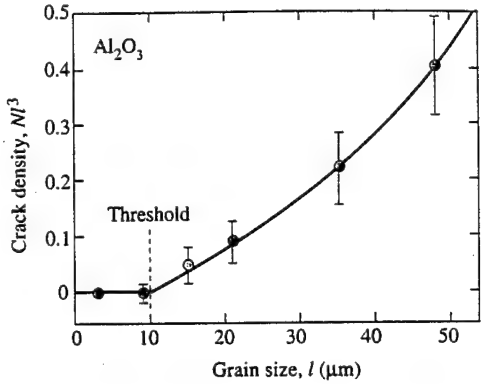

Fig. B2. Microcrack densities in indentation damage zones as function of grain size for alumina materials in Fig. B1. From Ref. 94.

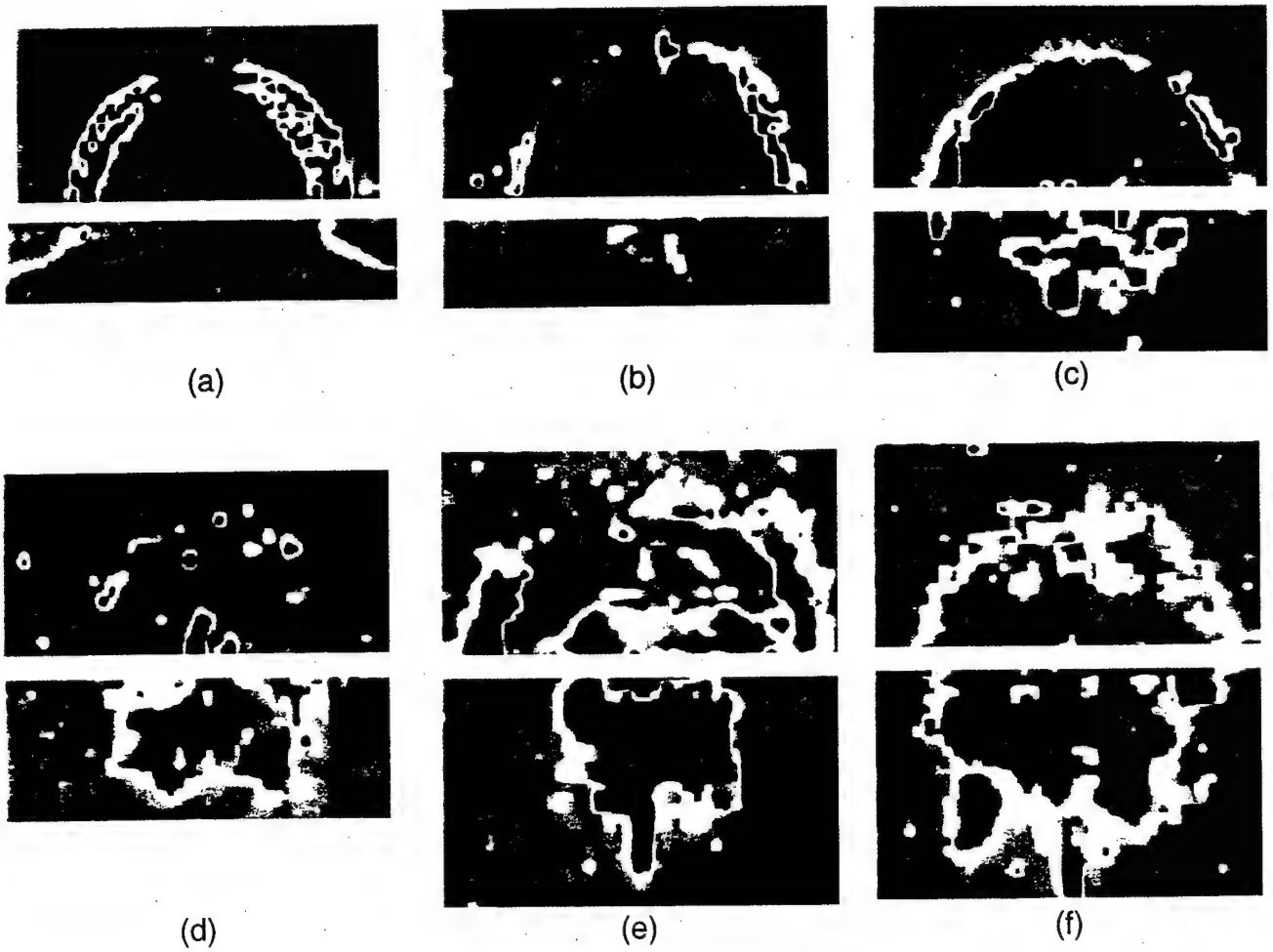

Fig. B1. Thermal wave images of same alumina materials as in Fig. 9. Red designates high crack densities. From Ref. 94.

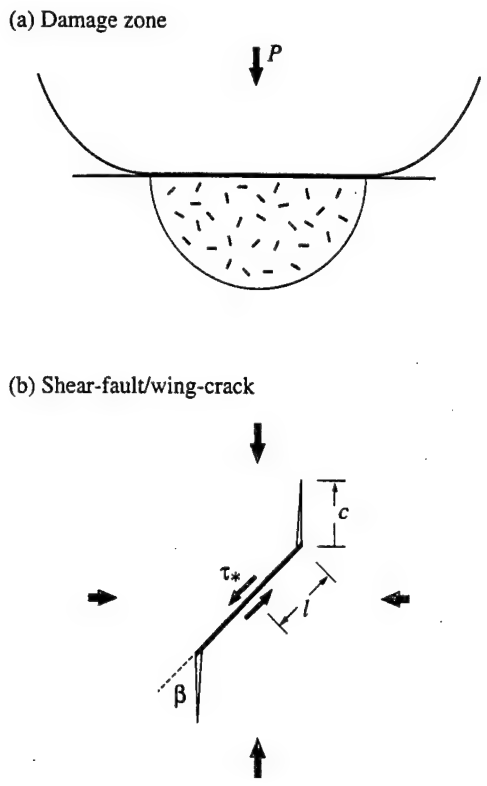

Fig. 12. Schematic of shear-fault/wing-crack system: (a) contact at load P forms array of shear faults within quasi-plastic zone; and (b) individual shear-fault/wing-crack in volume element, treated as pennylike crack with virtual radius $C = c + \gamma l$ and residual shear stress τ_*.

softening."[98]) Consider an individual penny shear fault of radius l and annular wing crack of width c, with persistent shear stress τ_* in Fig. 12(*b*) (neglecting any reverse sliding during unloading). Following Horii and Nemat-Nasser,[96] the kinked shear-fault/wing-crack can be approximated as a planar penny crack of effective radius

$$C = c + \gamma l \tag{15}$$

where $\gamma \approx 0.27$ is a dimensionless geometry "correction" coefficient,[96] acted upon by a residual center-opening force

$$Q = \lambda l^2 \tau_* \tag{16}$$

where λ is another dimensionless coefficient. A residual stress-intensity factor for the wing crack can then be written in familiar form:

$$K = \chi Q / C^{3/2} \tag{17}$$

Equations (15)–(17) provide a functional relation $K = K(c,\tau_*)$.

To connect the stress-intensity factor to the sphere-indentation problem, we need to relate τ_* to contact load P. For the general elastic–plastic contact field this is most practically done empirically, using FEM to compute the maximum shear stress τ_* beneath the indenter at each prescribed load P. From such a procedure we obtain the empirical relation[99]

$$\tau_*(P) = \alpha \tau_c [(P/P_Y)^{1/3} - 1] \tag{18}$$

which yields $K(c,P)$ in Eqs. (15)–(17). Then, imposing the equilibrium condition $K = K_{IC} = T_0$ (now, strictly, short-crack toughness), we can determine $c(P)$.[99] The cracks turn out to be exceedingly difficult to extend even at high loads, reflecting the strong stabilizing influence of the triaxially compressive contact field.[100] Nevertheless, when the loading is extreme (or number of cycles large—see Section VI), coalescence may occur between neighboring faults, signaling ultimate breakdown of the material.

Finally, we have noted the tendency for quasi plasticity in tougher ceramics to be accompanied by suppression of cone cracking. There are two reasons for this: coarser microstructures deflect surface flaws further along weak interfaces..away from tensile stress trajectories into compression regions of the contact field,[81] in a manner analogous to that referred to earlier in connection with large abrasion flaws (Section III(2)); and the onset of yield *below* the contact redistributes and relaxes the tensile stresses *outside* the contact.[28]

V. Strength Degradation from Contact Damage

(1) Experimental Data

A critical issue in designing with ceramics is damage tolerance: if damage does occur, will the component survive subsequent applied stresses? What effect does contact damage have on strength? Such consideration is crucial in many structural applications involving ceramics, e.g., bearings[6,101] and dental restorations.[8] Strength testing also provides a quantitative measure of the damage introduced by the contact event.

The indentation–strength test involves placement of sphere indentations into the centers of prospective tensile surfaces of flexure specimens at specified loads P and contact environments.[65,102–104] Strengths, σ_F, are then measured, usually in four-point or biaxial flexure, and in fast-loading and dry environment to avoid kinetic effects ("inert strengths"). When the damage provides the dominant flaw, the specimens fail from the indentation sites. Illustrative examples are shown in Fig. 13 for the F-, M-, and C-grade silicon nitride represented in Fig. 10.[101] Fractographic examination confirms failures from the bases of cone cracks in the F and M materials, and from within the subsurface damage zones in the C material.

Strengths for the same silicon nitride materials are plotted as functions of load in Fig. 14[101]—the data are experimental strength measurements, the solid curves theoretical fits (Section V(2)). Initially, each material holds its preindented strength with increasing load, corresponding to failures from natural flaws. In the more brittle F-grade silicon nitride ($P_C << P_Y$) and M-grade silicon nitride ($P_C < P_Y$), these strengths suffer abrupt losses at $P = P_C$. On the other hand, in the quasi-plastic C-grade silicon nitride ($P_Y << P_C$), the strengths decrease slowly, and only after some buildup of damage intensity, above $P_D \approx 2P_Y$. These results indicate a superior damage tolerance in the coarser microstructure. However, at very high loads or under fatigue conditions, when cracks coalesce, the quasi-plastic microstructures become subject to accelerated strength losses (Section VI).[99]

Hertzian damage analysis and strength testing are proving a powerful means of characterizing fracture and deformation properties in a broad range of ceramics, including dental ceramics (Panel C).

(2) Modeling

The strength degradation characteristics for indentation-damaged ceramics are calculated from the instability conditions for cone cracks (brittle materials) and shear-fault/wing-cracks (quasi-plastic materials) in uniform tensile fields.[65,99]

(A) Brittle Ceramics: Above the critical load $P = P_C$, failure initiates spontaneously from the base of a cone crack, propagating downward nearly normal to the applied tensile stress. Assuming again a single-valued toughness, $K_{IC} = T_0$ (and ignoring residual stresses from any accompanying quasi plasticity), the classical strength equation applies:

$$\sigma_F = T_0 / \Psi c^{1/2} \tag{19}$$

where Ψ is a crack geometry coefficient (determinable *a priori* from fracture mechanics considerations[65,99]). Combining Eq. (19) with Eqs. (8) and (9) yields $\sigma_F(P)$.

(B) Quasi-plastic Ceramics: Above $P = P_D$, failure initiates from the tip of a wing crack at a discrete shear fault within the diffuse quasi-plastic zone. Recalling the existence of

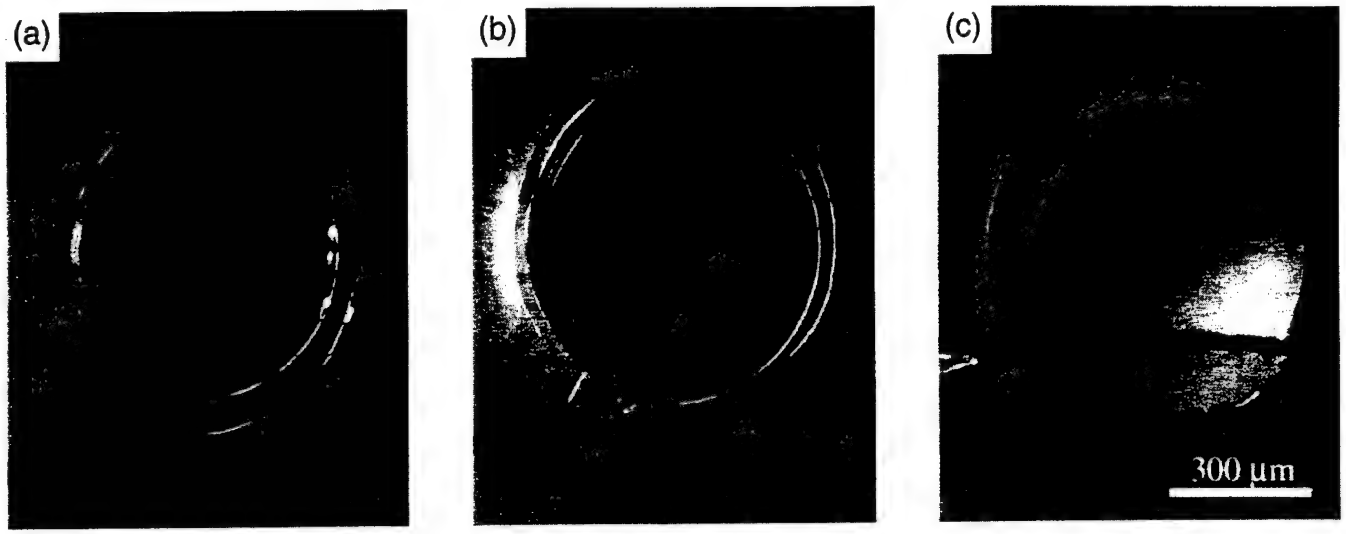

Fig. 13. Surface views of contact failure sites in silicon nitride specimens, from tungsten carbide sphere (r = 2.38 mm and P = 4000 N): (a) fine-, (b) medium-, and (c) coarse-grade silicon nitride. Surfaces gold coated after indentation, Nomarski interference. Four-point bend-strength specimens, tension axis vertical. From Ref. 101.

the residual driving force on the shear fault in Eq. (17) (but ignoring interactions between neighboring faults), we obtain the stress-intensity factor:

$$K = \chi Q/C^{3/2} + \Psi\sigma C^{1/2} = T_0 \tag{20}$$

(T_0 a short-crack toughness). Combining Eq. (20) with Eqs. (15) and (16), we can show that the wing crack extends stably prior to instability[99] at a failure stress

$$\sigma_F = (3/4\Psi)(T_0^4/4\chi\lambda l^2\tau_*)^{1/3} \tag{21}$$

This equation may then be combined with Eq. (18) to obtain $\sigma_F(P)$.

The solid curves in Fig. 14 represent fits of the theoretical $\sigma_F(P)$ functions to the experimental data.

Conditions for accelerated strength losses due to coalescence of adjacent shear faults at high loads, where neighboring wing cracks merge before attaining their critical dimensions, have also been considered.[99]

VI. Contact Fatigue

Repeated cycling can greatly exacerbate damage in ceramics, especially those with R-curves, thereby compromising useful life.[109–111] Mention has already been of the tendency for structural ceramic components such as bearings and dental restorations to fail prematurely in service. Contact fatigue testing with spheres provides a simple means of characterizing the fatigue properties of such ceramics in the critical short-crack domain.[19,78,112,113]

Examples of contact fatigue damage in ceramics are shown in Figs. 15 and 16. Figure 15 compares the surface damage on a moderately coarse alumina (grain size 23 μm)[19] after n = 1 and n = 10 cycles at the same frequency in water. There is conspicuous enhancement in the damage from cycling. Comparative cycling tests in dry nitrogen show reduced damage accumulation, affirming a chemical influence in the water environments. More tellingly, static tests in water with load held constant over the same time duration as Fig. 15(b) also show reduced damage, indicating that the underlying fatigue effect is nevertheless predominantly mechanical.

Figure 16 compares damage accumulation in two microstructural forms of silicon carbide: homogeneous–brittle (left) and heterogeneous–tough (right).[77,113] In the homogeneous form, cycling causes slight extension of cone cracks, and ultimately detaches a spurious surface collar from the cone mouth. In the heterogeneous form, damage accumulation is much more accelerated, beginning with a barely detectable quasi-plastic zone at n = 1 and ending with microcrack coalescence and wholesale surface expulsion of material at n = 10^6. Figure 17 is a scanning electron micrograph of the central severe damage zone in this latter case. Note the appearance of copious debris on the surface and attendant voids in the degraded microstructure. The implications concerning the susceptibility to wear are evident.[15,114]

Modeling of contact fatigue is in its infancy. In brittle ceramics, where the fatigue effect is essentially chemical, analysis simply requires the incorporation of an appropriate crack

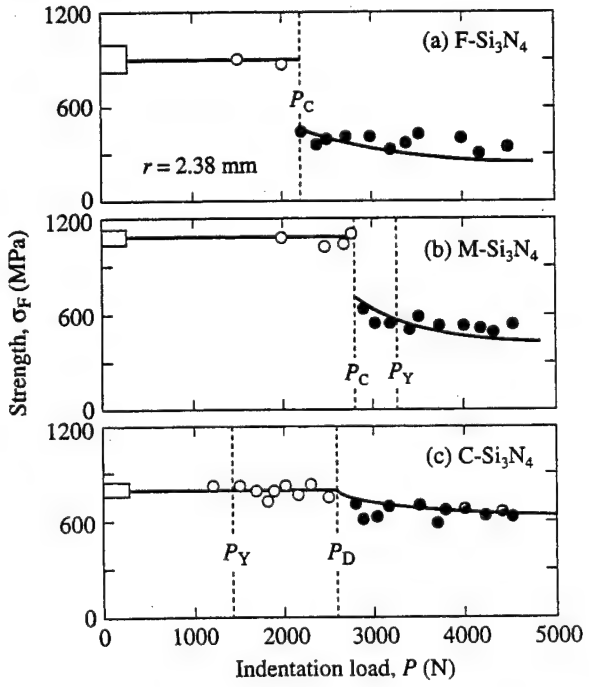

Fig. 14. Strength of silicon nitride specimens indented with tungsten carbide sphere (r = 2.38 mm), as function of indentation load. Data points are experimental measurements, indentation tests in air—black symbols represent failures from cone crack origins, gray symbols from quasi-plastic zones, and open symbols from other origins. Solid curves are theoretical fits. Boxes at left axis represent strengths of polished, unindented specimens. Vertical dashed lines indicate critical loads. From Refs. 99 and 101.

Panel C. Dental Ceramics

With Irene Peterson, Materials Science and Engineering Laboratory,
National Institute of Standards and Technology, Gaithersburg, Maryland

Ceramics are increasingly being used in dental restorations, especially in crowns.[105] Unfortunately, current ceramic restorations are susceptible to failure by some form of accumulated damage, from chewing, grinding ("bruxing") and inadvertent crunching—contact forces in the mouth can easily exceed 200 N, over cuspal radii of 2–4 mm. Durability, wear, and fatigue resistance are key mechanical issues, if subordinate to aesthetics (or even to cost and ease in preparation), in design considerations. Contact with spherical indenters offers a simple route to characterization of dental materials, under conditions that closely simulate oral function.[8]

The first quantities of interest are the critical loads to induce damage in the ceramic surface. Figure C1 plots the loads P_C (Fig. C1(a)) and P_Y (Fig. C1(b)) for cone cracking and yield as a function of sphere radius in three selected generic dental materials:[8] porcelain, micaceous glass-ceramic (analogous to the material in Fig. 8 but smaller mica platelet size), and glass-infiltrated alumina. Both $P_C(r)$ and $P_Y(r)$ increase monotonically, in approximate linear (Section III) and quadratic (Section IV) manner, respectively. The shaded boxes indicate the domain of oral forces and cuspal radii referred to above. The alumina–glass has the highest resistance to cracking, the porcelain the highest resistance to quasi plasticity. However, it is evident that all of the materials are vulnerable to some form of damage during severe contact, especially from spurious sharp objects and from sustained cyclic loading.

The next question is the survivability of a material once damage does occur. Figure C2 shows strength degradation plots (Section V) for the same three monolithic materials as above. Both porcelain and glass-ceramic fail from cone cracks above a critical load, whereas alumina–glass fails predominantly (but not exclusively) from quasi-plastic zones.[106] The porcelain is particularly weak and brittle. Unfortunately, the comparatively high strength properties of the alumina–glass are negated somewhat by inferior aesthetics, necessitating a porcelain veneer.

Indentation–strength tests establish a base for systematic investigation of the crucial role of microstructure in damage tolerance. Strength data on a range of glass-ceramics crystallized at increasing heat-treatment temperatures, with corresponding increasing microstructural scale, are plotted in Fig. C3.[107] Results are shown for surfaces broken after fine polishing ("pristine") and after damage by sphere indentation ("indented"). Whereas the pristine strengths decrease steadily with microstructural scale, those after indentation pass through a maximum as first cone cracking is suppressed then quasi plasticity proliferates. Note the ever-diminishing differential between the two curves in the coarser microstructures. Of these microstructures, that crystallized at or about 1040°C appears to offer an optimum combination of high strength and damage tolerance—this is the microstructure represented in Figs. C1 and C2 and that most closely resembles commercially available dental glass-ceramics.[107]

In actual crowns, dental ceramics are often configured in "veneer/core" layers. The lesson from natural teeth is that such combinations can produce extraordinarily resilient, damage tolerant structures,[105] with complex but stable crack patterns (cf. Fig. 19(c)). Contact studies of damage patterns in simulated dental layer structures are under way.[108]

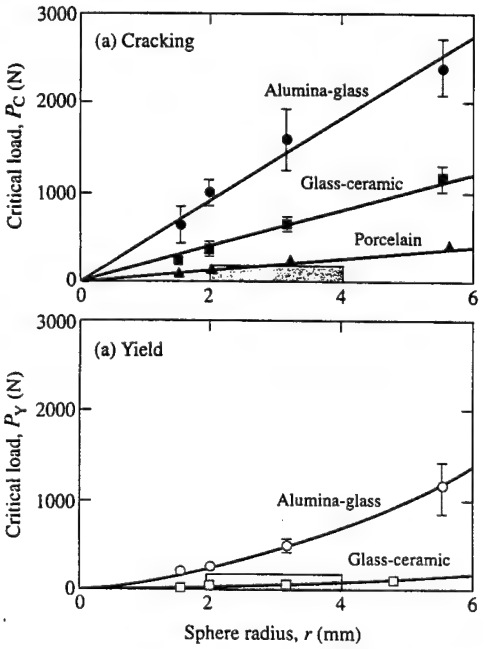

Fig. C1. Critical load functions $P_C(r)$ and $P_Y(r)$ for generic dental ceramics, for indentations with tungsten carbide spheres. Shaded box designates domain of typical dental function. Some data replotted from Ref. 8.

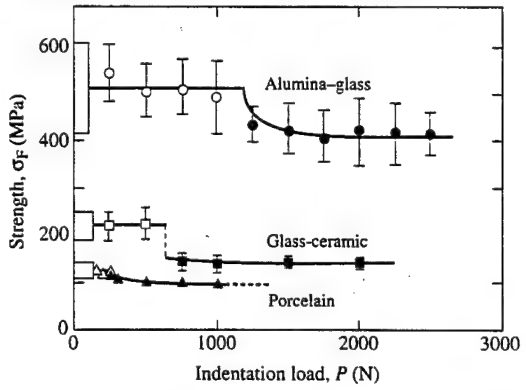

Fig. C2. Strength as function of contact load for same dental ceramics as in Fig. C1, for indentations with tungsten carbide sphere (r = 3.18 mm). Some data replotted from Ref. 8.

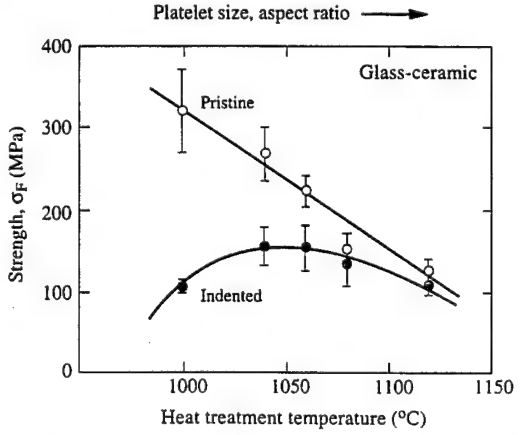

Fig. C3. Strengths of micaceous glass-ceramics as function of mica platelet size. Data for pristine (unindented) surfaces (open circles), and contact-damaged surfaces (tungsten carbide sphere, r = 3.18 mm, and P = 750 N)—black symbols represent failures from cone cracks, gray symbols failures from quasi-plastic zones, open symbols from other origins. Data courtesy A. Pajares and Y-G. Jung.

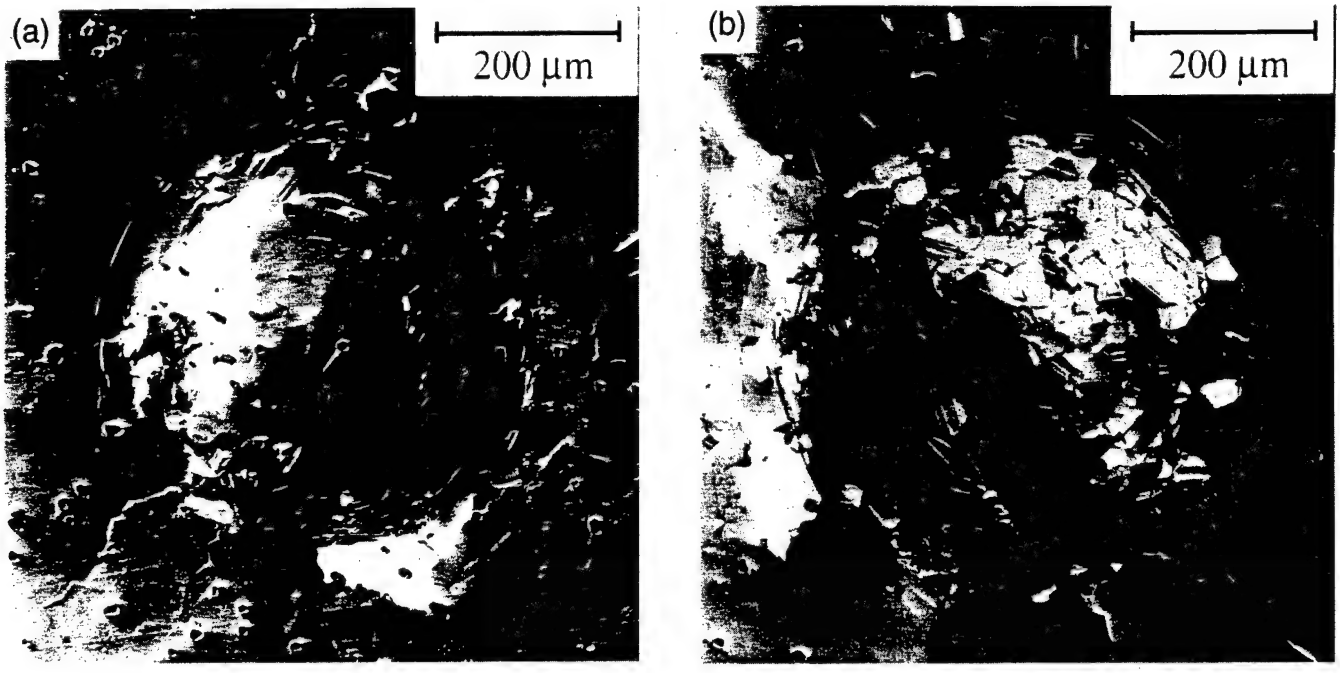

Fig. 15. Indentation damage in coarse alumina (l = 23 μm) from tungsten carbide sphere (r = 1.98 mm and P = 2000 N—cf. $P_Y \approx 1000$ N) at 0.002 Hz, in water: (a) n = 1 and (b) n = 10 cycles. Surfaces gold coated after indentation, Nomarski interference. From Ref. 19.

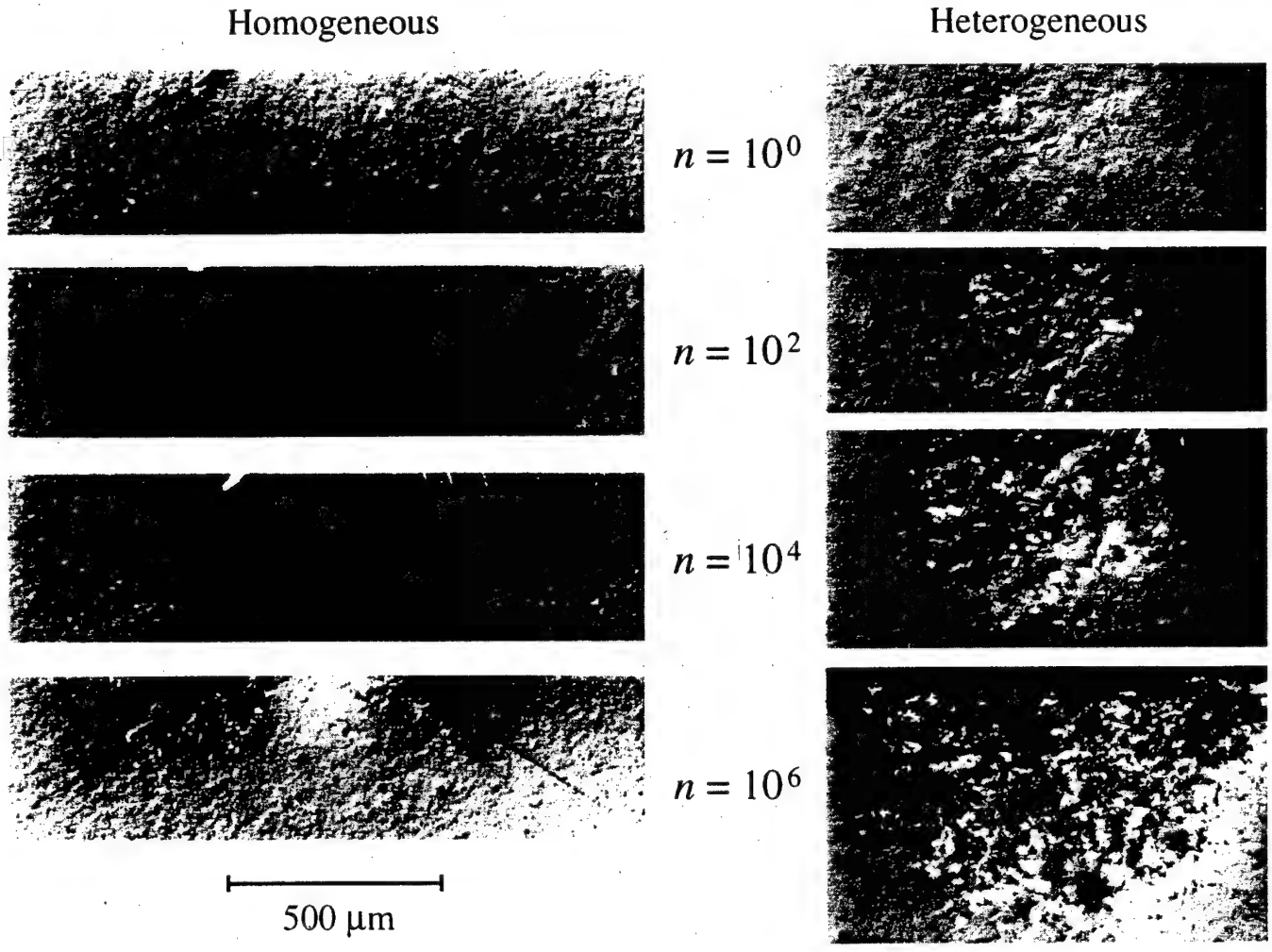

Fig. 16. Section views of Hertzian contact sites in brittle (homogeneous) and tough (heterogeneous) silicon carbide, from tungsten carbide sphere (r = 3.18 mm, P = 1000 N, and f = 10 Hz), in air. Bonded-interface specimens, surfaces gold coated after indentation, Nomarski interference. From Ref. 113.

velocity relation $v = v(K)$ into the cone fracture mechanics.[113] In quasi-plastic ceramics, mechanical processes dominate—damage accumulates primarily by decremental attrition at the sliding shear fault interfaces (Fig. 17). This attrition is manifested as a progressive reduction in the frictional sliding resistance at successive cycles, i.e., in the cohesion term τ_c (and/or μ terms),[115,116] effectively diminishing the yield stress in Eq. (14*a*). Complex interactions between chemical and mechanical effects can occur (e.g., by reducing the friction at shear faults and enhancing the extension of wing cracks), although these micro-interactions are not yet well understood. Macroscopic friction between the indenter and specimen can cause additional surface "fretting."[21,117]

Contact fatigue is quantifiable by its effect on strength, $\sigma_F(n)$, at given load P. Figure 18 shows strength data for the same silicon nitrides considered earlier (Fig. 10), for a load well below the single-cycle thresholds for cone cracks (P_C) in F-grade silicon nitride and M-grade silicon nitride and for quasi plasticity (P_D) in C-grade silicon nitride. As with the single-cycle $\sigma_F(P)$ curves (Fig. 14), the strengths for F- and M-grade silicon nitride are abruptly degraded at some critical value of n, whereas the degradation in C-grade silicon nitride is more continuous above the critical n. However, note the very rapid decrease in strengths of C-grade silicon nitride at very large n, signaling the end of the useful life of this material.

It is apparent from Figs. 16–18 that quasi-plastic ceramics are more susceptible to fatigue than their brittle counterparts. What makes the quasi-plastic damage mode especially insidious is the difficulty of detection and screening in its early stages. In ceramics where the competition between fracture and deformation is finely balanced, it is possible for the failure mode to change from brittle in single-cycle loading to quasi plastic in multi-cycling loading, making any predictions of fatigue responses from static test data especially suspect.

VII. Layer Structures

Finally, we indicate how current contact testing is contributing to a new design philosophy for ceramic-based layer structures. We have seen how microstructural weakening and coarsening, while improving long-crack toughness, tend to degrade strength and wear resistance. A potential way of averting compromise in design is to tailor laminates with hard/brittle outer ("protective") layers and soft/tough inner ("functional") layers. In principle, such layer systems should exhibit both high wear resistance and high toughness, with reduced susceptibility to strength degradation from damage accumulation. Critical

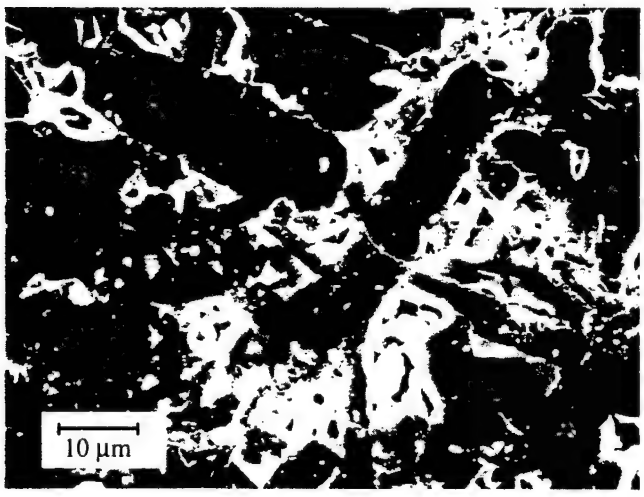

Fig. 17. Scanning electron micrograph of Hertzian cyclic-contact damage in heterogeneous silicon carbide, from center region of subsurface damage zone at $n = 10^6$ in Fig. 16. Note sliding-interface debris and surface cavities from material removal. From Ref. 113.

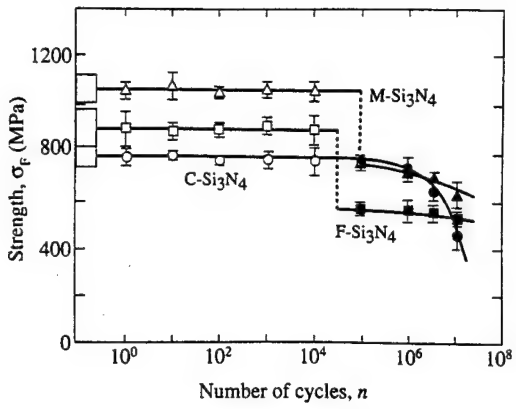

Fig. 18. Strength of silicon nitride specimens indented with tungsten carbide sphere ($r = 1.98$ mm and $P = 1000$ N) as function of number of contact cycles at $f = 10$ Hz, demonstrating fatigue. Data points are experimental measurements, indentation tests in air—black symbols represent failures from cone cracks, gray symbols failures from quasi-plastic zones, and open symbols from other origins. Boxes at left axis represent strengths of polished, unindented specimens. Data courtesy S. K. Lee.

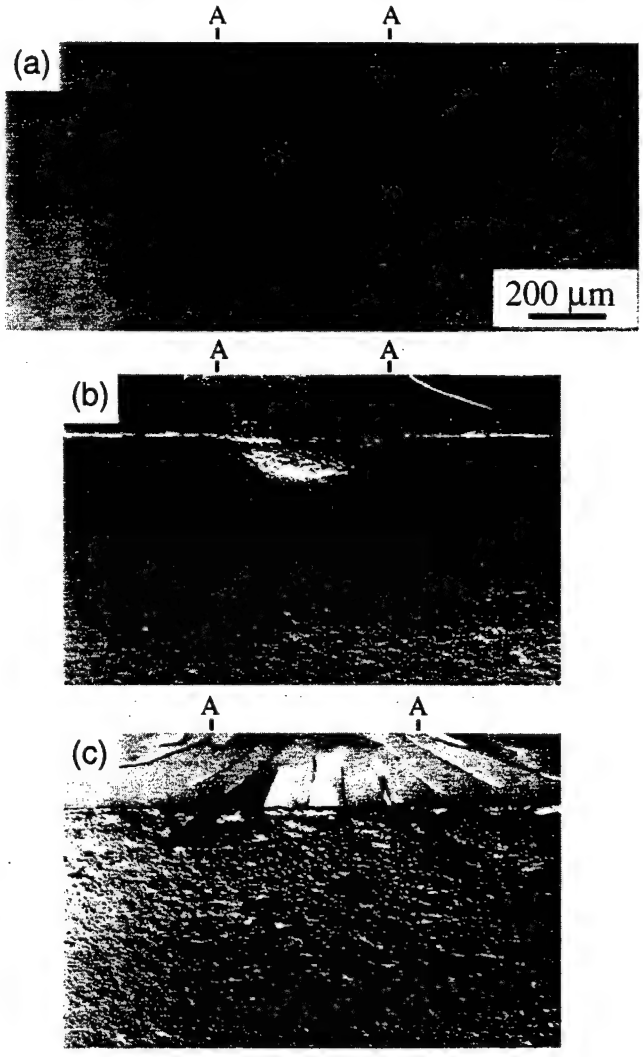

Fig. 19. Section views of Hertzian contact damage in silicon nitride bilayers, using tungsten carbide sphere ($r = 1.98$ mm and $P = 3000$ N): (a) monolith of fine-grain material, showing fully developed cone crack with barely detectable subsurface quasi plasticity; (b) bilayer of fine-grain coating on coarse-grain substrate; and (c) similar, but on substrate with 30% boron nitride additive. Bonded-interface specimens, Nomarski optical micrographs. Contact diameter AA indicated. From Ref. 123.

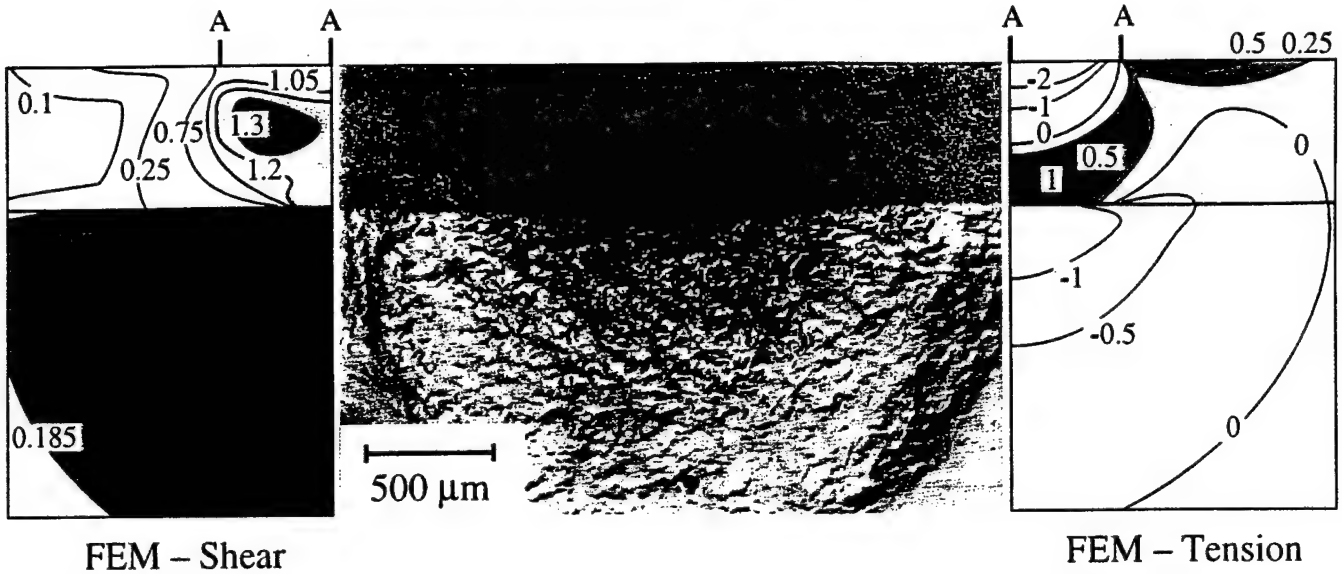

Fig. 20. Section view of Hertzian contact damage in plasma-sprayed alumina–40% titania coating on mild steel substrate, from tungsten carbide sphere (r = 3.18 mm and P = 1500 N). Note correspondence between locations of coating cracks and principal tensile stresses (right), and between yield zones and principal shear stresses in both coating and substrate (left). From Ref. 127.

elements of the new philosophy are: (i) incorporation of strong rather than weak interlayer interfaces, to avoid delamination; (ii) adjustment of elastic–plastic mismatch between layers so as to partition energy from the contact loading system into competing fracture and quasi-plastic modes, and thus to suppress (rather than deflect) any cone (or other) cracks that originate in the outer layers. This philosophy has been demonstrated on several material systems: ceramic bilayers, alumina/alumina,[84,118,119] glass/glass-ceramic,[120] and silicon nitride/silicon nitride;[121–123] thermal barrier coatings;[124–128] and simulated dental structures.[108] We briefly describe two examples here.

Our first example, Fig. 19, shows sphere indentations in two silicon nitride bilayers with a common homogeneous top layer ("coating") on two heterogeneous underlayers with quite different toughness properties ("substrates").[123] In its bulk state (Fig. 19(a)), the coating is a relatively fine silicon nitride (cf. Fig. 10(a)) with well-developed cone fracture. The substrate in the first bilayer (Fig. 19(b)) is a coarse but pure silicon nitride (cf. Fig. 10(c)), corresponding to modest coating/substrate elastic–plastic mismatch. A cone fracture is still evident, but is significantly shallower. Note the appearance of a deformation zone beneath the indenter. The substrate in the second bilayer (Fig. 19(c)) has a much more heterogeneous microstructure, with incorporated boron nitride platelets as a softening phase,[122] corresponding to a large coating/substrate elastic–plastic mismatch. The damage pattern is much more complex, with multiple transverse coating fractures extending both downward from the top surface and upward from the interlayer interface. Substrate yield is now pronounced. It is noteworthy that the transverse cracks remain fully contained with the coating in both bilayers—extreme loads are needed to drive these cracks through the coating thickness and cause failure—and that there is no substantial delamination at the interlayer interface. It is clear that the mismatch has a profound influence on the coating fracture, attesting to the damage tolerance of these structures.

Our second example concerns a plasma-sprayed alumina–titania coating on a mild steel substrate.[127] Such coatings are notorious for their extreme defect and pore content.[129] Figure 20 shows indentation damage in this system. Intense diffuse microcracking and yield in the substrate are observed. However, macroscopic cracking is limited: some delamination has occurred at the interlayer interface, but transverse cracks are conspicuously small. FEM analyses of tension and shear stress distributions provide correlations with these observed macroscopic cracking and yield patterns.[127] Thus, despite the wholesale damage intensity, the system remains essentially intact. The charm of these coatings is in the very defect complexion that facilitates the damage, dissipating and redistributing mechanical energy beneath the contact, resulting in exceptional damage tolerance as well as in other desirable (e.g., thermal resistance[129]) properties.

Contact mechanics of ceramic-based layer material systems from sphere indentations constitutes a relatively new area of research. Damage modes and geometries are still being identified, at both the macroscopic (above) and microscopic[130] levels, and the roles of elastic mismatch and interfacial bonding are being elucidated.[128] Analyses of elastic–plastic stress fields[108,126,131,132] and of indentation stress–strain curves[133] are being developed. Extensions of contact theory and experiment to multilayer[134] and graded structures are being reported.[135] The legacy of Hertz appears poised to survive well into the next century of ceramics research.

Acknowledgments: The author expresses deep gratitude to the many students, colleagues, and friends, too numerous to list here, whose critical contributions are represented in this article.

References

[1]H. Hertz, *Hertz's Miscellaneous Papers*; Chs. 5 and 6. Macmillan, London, U.K., 1896.

[2]B. R. Lawn and T. R. Wilshaw, "Indentation Fracture: Principles and Applications," *J. Mater. Sci.*, **10** [6] 1049–81 (1975).

[3]B. R. Lawn, *Fracture of Brittle Solids*; Ch. 8. Cambridge University Press, Cambridge, U.K., 1993.

[4]D. Tabor, *Hardness of Metals*. Clarendon, Oxford, U.K., 1951.

[5]R. F. Cook and G. M. Pharr, "Direct Observation and Analysis of Indentation Cracking in Glasses and Ceramics," *J. Am. Ceram. Soc.*, **73** [4] 787–817 (1990).

[6]R. N. Katz and J. G. Hannoosh, "Ceramics for High-Performance Rolling Element Bearings: A Review and Assessment," *Int. J. High Technol. Ceram.*, **1**, 69–79 (1985).

[7]D. W. Richerson, *Modern Ceramic Engineering*. Marcel Dekker, New York, 1992.

[8]I. M. Peterson, A. Pajares, B. R. Lawn, V. P. Thompson, and E. D. Rekow, "Mechanical Characterization of Dental Ceramics Using Hertzian Contacts," *J. Dent. Res.*, **77** [4] 589–602 (1998).

[9]B. R. Lawn and D. B. Marshall, "Mechanisms of Micro-Contact in Brittle Solids"; pp. 63–82 in *Lithic Use-Wear*. Edited by B. Hayden. Academic, New York, 1979.

[10]F. Auerbach, "Measurement of Hardness," *Ann. Phys. Chem.*, **43**, 61 (1891).

[11]F. C. Frank and B. R. Lawn, "On the Theory of Hertzian Fracture," *Proc. R. Soc. London*, **A299** [1458] 291–306 (1967).

[12]R. Knehans and R. Steinbrech, "Memory Effect of Crack Resistance During Slow Crack Growth in Notched Al_2O_3 Bend Specimens," *J. Mater. Sci. Lett.*, **1** [8] 327–29 (1982).

[13]P. L. Swanson, C. J. Fairbanks, B. R. Lawn, Y.-W. Mai, and B. J. Hockey, "Crack–Interface Grain Bridging as a Fracture Resistance Mechanism in Ceramics: I. Experimental Study on Alumina," *J. Am. Ceram. Soc.*, **70** [4] 279–89 (1987).

[14]R. W. Steinbrech, A. Reichl, and W. Schaarwächter, "*R*-Curve Behavior of Long Cracks in Alumina," *J. Am. Ceram. Soc.*, **73** [7] 2009–15 (1990).

[15]S.-J. Cho, B. J. Hockey, B. R. Lawn, and S. J. Bennison, "Grain-Size and *R*-Curve Effects in the Abrasive Wear of Alumina," *J. Am. Ceram. Soc.*, **72** [7] 1249–52 (1989).

[16]B. R. Lawn, N. P. Padture, H. Cai, and F. Guiberteau, "Making Ceramics 'Ductile'," *Science (Washington, D.C.)*, **263**, 1114–16 (1994).

[17]J. C. Jaeger and N. G. W. Cook, *Fundamentals of Rock Mechanics*; Chs. 3 and 12. Chapman and Hall, London, U.K., 1971.

[18]M. S. Paterson, *Experimental Rock Deformation—The Brittle Field*. Springer-Verlag, Berlin, Germany, 1978.

[19]F. Guiberteau, N. P. Padture, H. Cai, and B. R. Lawn, "Indentation Fatigue: A Simple Cyclic Hertzian Test for Measuring Damage Accumulation in Polycrystalline Ceramics," *Philos. Mag. A*, **68** [5] 1003–16 (1993).

[20]S. Timoshenko and J. N. Goodier, *Theory of Elasticity*; Ch. 13. McGraw-Hill, New York, 1951.

[21]K. L. Johnson, *Contact Mechanics*. Cambridge University Press, London, U.K., 1985.

[22]M. V. Swain and B. R. Lawn, "A Study of Dislocation Arrays at Spherical Indentations in LiF as a Function of Indentation Stress and Strain," *Phys. Status Solidi*, **35** [2] 909–23 (1969).

[23]M. T. Huber, "Zur Theorie der Berührung Fester Elasticher Körper," *Ann. Phys. (Leipzig)*, **43** [61] 153–63 (1904).

[24]G. M. Hamilton and L. E. Goodman, "The Stress Field Created by a Circular Sliding Contact," *J. Appl. Mech.*, **33**, 371–76 (1966).

[25]G. M. Hamilton, "Explicit Equations for the Stresses Beneath a Sliding Spherical Contact," *Proc. Inst. Mech. Eng.*, **197C**, 53–59 (1983).

[26]R. Hill, *The Mathematical Theory of Plasticity*. Oxford University Press, London, U.K., 1950.

[27]A. C. Fischer-Cripps, "Elastic–Plastic Behaviour in Materials Loaded With a Spherical Indenter," *J. Mater. Sci.*, **32**, 727–36 (1997).

[28]A. C. Fischer-Cripps and B. R. Lawn, "Stress Analysis of Contact Deformation in Quasi-Plastic Ceramics," *J. Am. Ceram. Soc.*, **79** [10] 2609–18 (1996).

[29]M. V. Swain and J. T. Hagan, "Indentation Plasticity and the Ensuing Fracture of Glass," *J. Phys. D: Appl. Phys.*, **9**, 2201–14 (1976).

[30]C. K. Chyung, G. H. Beall, and D. G. Grossman, "Microstructures and Mechanical Properties of Mica Glass-Ceramics"; pp. 1167–94 in *Electron Microscopy and Structure of Materials*. Edited by G. Thomas, R. M. Fulrath, and R. M. Fisher. University of California Press, Berkeley, CA, 1972.

[31]K. Chyung, G. H. Beall, and D. G. Grossman, "Fluorophlogopite Mica Glass-Ceramics"; pp. 33–40 in *Proceedings of 10th International Glass Congress*, No. 14. Edited by M. Kunugi, M. Tashiro, and N. Saga. The Ceramic Society of Japan, Kyoto, Tokyo, Japan, 1974.

[32]H. Cai, M. A. Stevens Kalceff, and B. R. Lawn, "Deformation and Fracture of Mica-Containing Glass-Ceramics in Hertzian Contacts," *J. Mater. Res.*, **9** [3] 762–70 (1994).

[33]J. P. Tillett, "Fracture of Glass by Spherical Indenters," *Proc. Phys. Soc. London*, **B69** [433] 47–54 (1956).

[34]F. C. Roesler, "Brittle Fractures Near Equilibrium," *Proc. Phys. Soc. London*, **B69**, 981–92 (1956).

[35]F. C. Roesler, "Indentation Hardness of Glass as an Energy Scaling Law," *Proc. Phys. Soc. London*, **B69** [433] 55–60 (1956).

[36]V. R. Howes and S. Tolansky, "Pressure Crack Figures on Diamond Faces: I. The Octahedral Face," *Proc. R. Soc. London*, **A230**, 287–93 (1955).

[37]V. R. Howes and S. Tolansky, "Pressure Crack Figures on Diamond Faces: II. The Dodecahedral and Cubic Faces," *Proc. R. Soc. London*, **A230**, 294–301 (1955).

[38]S. Tolansky and V. R. Howes, "Induction of Ring Cracks on Diamond Surfaces," *Proc. Phys. Soc. London*, **B70**, 521–26 (1957).

[39]B. R. Lawn and H. Komatsu, "The Nature of Deformation Around Pressure Cracks on Diamond," *Philos. Mag.*, **14** [130] 689–99 (1966).

[40]O. W. Johnson, "Damage Produced in Ge at Room Temperature by Indentation," *J. Appl. Phys.*, **37** [7] 2521–26 (1966).

[41]B. R. Lawn, "Hertzian Fracture in Single Crystals with the Diamond Structure," *J. Appl. Phys.*, **39** [10] 4828–36 (1968).

[42]G. I. Barenblatt, "The Mathematical Theory of Equilibrium Cracks in Brittle Fracture," *Adv. Appl. Mech.*, **7**, 55–129 (1962).

[43]J. S. Williams, B. R. Lawn, and M. V. Swain, "Cone Crack Closure in Brittle Solids," *Phys. Status Solidi A*, **2**, 7–29 (1970).

[44]K. Peter, "Sprödbruch und Mikroplastizität von Glas in Eindruckversuchen," *Glasstech. Ber.*, **37** [7] 333–45 (1964).

[45]B. R. Lawn, T. Jensen, and A. Arora, "Brittleness as an Indentation Size Effect," *J. Mater. Sci.*, **11** [3] 573–75 (1976).

[46]B. R. Lawn and D. B. Marshall, "Hardness, Toughness, and Brittleness: An Indentation Analysis," *J. Am. Ceram. Soc.*, **62** [7–8] 347–50 (1979).

[47]K. E. Puttick, "Energy Scaling, Size Effects, and Ductile–Brittle Transitions in Fracture," *J. Phys. D: Appl. Phys.*, **12**, L19–L23 (1979).

[48]A. S. Argon, "Distribution of Cracks on Glass Surfaces," *Proc. R. Soc. London*, **A250**, 482–92 (1959).

[49]H. L. Oh and I. Finnie, "The Ring Cracking of Glass by Spherical Indenters," *J. Mech. Phys. Solids*, **15**, 401–11 (1967).

[50]F. B. Langitan and B. R. Lawn, "Hertzian Fracture Experiments on Abraded Glass Surfaces as Definitive Evidence for an Energy Balance Explanation of Auerbach's Law," *J. Appl. Phys.*, **40** [10] 4009–17 (1969).

[51]C. J. Culf, "Fracture of Glass Under Various Liquids and Gases," *J. Soc. Glass Technol.*, **41**, 157T–167T (1957).

[52]M. V. Swain and B. R. Lawn, "A Microprobe Technique for Measuring Slow Crack Velocities in Brittle Solids," *Int. J. Fact. Mech.*, **9** [4] 481–83 (1973).

[53]R. Mouginot and D. Maugis, "Fracture Indentation Beneath Flat and Spherical Punches," *J. Mater. Sci.*, **20**, 4354–76 (1985).

[54]F. B. Langitan and B. R. Lawn, "Effect of a Reactive Environment on the Hertzian Strength of Brittle Solids," *J. Appl. Phys.*, **41** [8] 3357–65 (1970).

[55]A. G. Mikosza and B. R. Lawn, "Section-and-Etch Study of Hertzian Fracture Mechanics," *J. Appl. Phys.*, **42** [13] 5540–45 (1971).

[56]J. S. Nadeau and A. S. Rao, "Hertzian Fracture of a Lithium Silicate Glass and Glass-Ceramic," *J. Can. Ceram. Soc.*, **41**, 63–67 (1972).

[57]J. S. Nadeau, "Hertzian Fracture of Vitreous Carbon," *J. Am. Ceram. Soc.*, **56** [9] 467–72 (1973).

[58]M. T. Laugier, "Hertzian Fracture of Sintered Alumina," *J. Mater. Sci.*, **19**, 254–58 (1984).

[59]M. T. Laugier, "Toughness Determination of Some Ceramic Tool Materials Using the Method of Hertzian Indentation Fracture," *J. Mater. Sci. Lett.*, **4**, 1542–44 (1985).

[60]H. Matzke and R. Warren, "Hertzian Crack Growth in ThO_2 Observed by Serial Sectioning," *J. Mater. Sci. Lett.*, **1**, 441–44 (1982).

[61]K. Zeng, K. Breder, and D. J. Rowcliffe, "The Hertzian Stress Field and Formation of Cone Cracks: I. Theoretical Approach," *Acta Metall.*, **40** [10] 2595–600 (1992).

[62]K. Zeng, K. Breder, and D. J. Rowcliffe, "The Hertzian Stress Field and Formation of Cone Cracks: II. Determination of Fracture Toughness," *Acta Metall.*, **40** [10] 2601–605 (1992).

[63]P. D. Warren, "Determining the Fracture Toughness of Brittle Materials by Hertzian Indentation," *J. Eur. Ceram. Soc.*, **15**, 201–207 (1995).

[64]B. R. Lawn, T. R. Wilshaw, and N. E. W. Hartley, "A Computer Simulation Study of Hertzian Cone Crack Growth," *Int. J. Fract.*, **10** [1] 1–16 (1974).

[65]B. R. Lawn, S. M. Wiederhorn, and H. Johnson, "Strength Degradation of Brittle Surfaces: Blunt Indenters," *J. Am. Ceram. Soc.*, **58** [9–10] 428–32 (1975).

[66]N. E. W. Hartley and T. R. Wilshaw, "Deformation and Fracture of Synthetic α-Quartz," *J. Mater. Sci.*, **8**, 265–78 (1973).

[67]M. V. Swain, J. S. Williams, B. R. Lawn, and J. J. H. Beek, "A Comparative Study of the Fracture of Various Silica Modifications Using the Hertzian Test," *J. Mater. Sci.*, **8** [8] 1153–64 (1973).

[68]A. G. Evans and E. A. Charles, "Fracture Toughness Determinations by Indentation," *J. Am. Ceram. Soc.*, **59** [7–8] 371–72 (1976).

[69]G. R. Anstis, P. Chantikul, D. B. Marshall, and B. R. Lawn, "A Critical Evaluation of Indentation Techniques for Measuring Fracture Toughness: I. Direct Crack Measurements," *J. Am. Ceram. Soc.*, **64** [9] 533–38 (1981).

[70]T. R. Wilshaw, "The Hertzian Fracture Test," *J. Phys. D: Appl. Phys.*, **4** [10] 1567–81 (1971).

[71]A. C. Fischer-Cripps and R. E. Collins, "The Probability of Hertzian Fracture," *J. Mater. Sci.*, **29**, 2216–30 (1994).

[72]R. Warren, "Measurement of the Fracture Properties of Brittle Solids by Hertzian Indentation," *Acta Metall.*, **26**, 1759–69 (1978).

[73]K. L. Johnson, J. J. O'Connor, and A. C. Woodward, "The Effect of Indenter Elasticity on the Hertzian Fracture of Brittle Materials," *Proc. R. Soc. London*, **A334**, 95 (1973).

[74]C. Kocer and R. E. Collins, "The Angle of Hertzian Cone Cracks," *J. Am. Ceram. Soc.*, **81** [7] 1736–42 (1998).

[75]A. G. Evans and T. R. Wilshaw, "Quasi-Plastic Solid Particle Damage in Brittle Materials," *Acta Metall.*, **24**, 939–56 (1976).

[76]F. Guiberteau, N. P. Padture, and B. R. Lawn, "Effect of Grain Size on Hertzian Contact in Alumina," *J. Am. Ceram. Soc.*, **77** [7] 1825–31 (1994).

[77]N. P. Padture and B. R. Lawn, "Toughness Properties of a Silicon Carbide with an *in Situ*-Induced Heterogeneous Grain Structure," *J. Am. Ceram. Soc.*, **77** [10] 2518–22 (1994).

[78]A. Pajares, L. Wei, B. R. Lawn, and D. B. Marshall, "Damage Accumulation and Cyclic Fatigue in Mg-PSZ at Hertzian Contacts," *J. Mater. Res.*, **10** [10] 2613–25 (1995).

[79]H. H. K. Xu, L. Wei, N. P. Padture, B. R. Lawn, and R. L. Yeckley, "Effect of Microstructural Coarsening on Hertzian Contact Damage in Silicon Nitride," *J. Mater. Sci.*, **30**, 869–78 (1995).

[80]R. M. Davies, "Determination of Static and Dynamic Yield Stresses Using a Steel Ball," *Proc. R. Soc. London*, **A197** [1050] 416–32 (1949).

[81]S. K. Lee, S. Wuttiphan, and B. R. Lawn, "Role of Microstructure in Hertzian Contact Damage in Silicon Nitride: I. Mechanical Characterization," *J. Am. Ceram. Soc.*, **80** [9] 2367–81 (1997).

[82]T. O. Mulhearn, "The Deformation of Metals by Vickers-Type Pyramidal Indenters," *J. Mech. Phys. Solids*, **7**, 85–96 (1959).

[83]J. T. Hagan and M. V. Swain, "The Origin of Median and Lateral Cracks at Plastic Indents in Brittle Materials," *J. Phys. D: Appl. Phys.*, **11** [15] 2091–102 (1978).

[84]L. An, H. M. Chan, N. P. Padture, and B. R. Lawn, "Damage-Resistant Alumina-Based Layer Composites," *J. Mater. Res.*, **11** [1] 204–10 (1996).

[85]M. Belmonte and S. K. Lee, "Contact Damage in Alumina Reinforced with Silicon Carbide Platelets," *J. Mater. Sci.*, **16**, 379–81 (1997).

[86]B. A. Latella, B. H. O'Connor, N. P. Padture, and B. R. Lawn, "Hertzian Contact Damage in Porous Alumina Ceramics," *J. Am. Ceram. Soc.*, **80** [4] 1027–31 (1997).

[87]S. K. Lee, K. S. Lee, B. R. Lawn, and D. K. Kim, "Effect of Starting Powder on Damage Resistance of Silicon Nitrides," *J. Am. Ceram. Soc.*, **81** [8] 2061–70 (1998).

[88]C. J. Fairbanks, B. R. Lawn, R. F. Cook, and Y.-W. Mai, "Microstructure and the Strength of Ceramics"; pp. 23–37 in *Fracture Mechanics of Ceramics*, Vol. 8. Edited by R. C. Bradt, A. G. Evans, D. P. H. Hasselman, and F. F. Lange. Plenum, New York, 1986.

[89]L. An, K. Soni, and H. M. Chan, "Control of Calcium Hexaluminate Grain Morphology in *In-Situ*-Toughened Ceramic Composites," *J. Mater. Sci.*, **31**, 3223–29 (1996).

[90]N. P. Padture, "*In Situ* Toughened Silicon Carbide," *J. Am. Ceram. Soc.*, **77** [2] 519–23 (1994).

[91]A. Pajares, F. Guiberteau, B. R. Lawn, and S. Lathabai, "Hertzian Contact Damage in Magnesia-Partially-Stabilized Zirconia," *J. Am. Ceram. Soc.*, **78** [4] 1083–86 (1995).

[92]D. T. Smith and L. Wei, "Quantifying Local Microcrack Density in Ceramics: A Comparison of Instrumented Indentation and Thermal Wave Techniques," *J. Am. Ceram. Soc.*, **78** [5] 1301–304 (1995).

[93]L. Wei and G. S. White, "Thermal Diffusivity Maps: Case Studies in Ceramics," *J. Mater. Res.*, **12** [9] 2381–87 (1997).

[94]L. Wei and B. R. Lawn, "Thermal Wave Analysis of Contact Damage in Ceramics: Case Study on Alumina," *J. Mater. Res.*, **11** [4] 939–47 (1996).

[95]D. P. H. Hasselman, "Effect of Cracks on Thermal Conductivity," *J. Compos. Mater.*, **12**, 403–407 (1978).

[96]H. Horii and S. Nemat-Nasser, "Brittle Failure in Compression: Splitting, Faulting, and Brittle–Ductile Transition," *Philos. Trans. R. Soc. London*, **319** [1549] 337–74 (1986).

[97]J. M. Kemeny and N. G. W. Cook, "Micromechanics of Deformation in Rock"; pp. 287–311 in *Toughening Mechanisms in Quasi-Brittle Materials*. Edited by S. P. Shah. Kluwer Academic Publishers, Dordrecht, The Netherlands, 1991.

[98]B. R. Lawn and D. B. Marshall, "Nonlinear Stress–Strain Curves for Solids Containing Closed Cracks with Friction," *J. Mech. Phys. Solids*, **46** [1] 85–113 (1998).

[99]B. R. Lawn, S. K. Lee, I. M. Peterson, and S. Wuttiphan, "A Model of Strength Degradation from Hertzian Contact Damage in Tough Ceramics," *J. Am. Ceram. Soc.*, **81** [6] 1509–20 (1998).

[100]A. V. Dyskin, R. J. Jewell, H. Joer, E. Sahouryeh, and K. B. Ustinov, "Experiments on 3-D Crack Growth in Uniaxial Compression," *Int. J. Fract.*, **65** [4] R77–R83 (1994).

[101]S. K. Lee and B. R. Lawn, "Role of Microstructure in Hertzian Contact Damage in Silicon Nitride: II. Strength Degradation," *J. Am. Ceram. Soc.*, **81** [4] 997–1003 (1998).

[102]A. G. Evans, "Strength Degradation by Projectile Impacts," *J. Am. Ceram. Soc.*, **56** [8] 405–409 (1973).

[103]S. M. Wiederhorn and B. R. Lawn, "Strength Degradation of Glass Resulting from Impact with Spheres," *J. Am. Ceram. Soc.*, **60** [9–10] 451–58 (1977).

[104]B. R. Lawn, D. B. Marshall, P. Chantikul, and G. R. Anstis, "Indentation Fracture: Applications in the Assessment of Strength of Ceramics," *J. Aust. Ceram. Soc.*, **16** [1] 4–9 (1980).

[105]J. R. Kelly, "Ceramics in Restorative and Prosthetic Dentistry," *Ann. Rev. Mater. Sci.*, **27**, 443–68 (1997).

[106]Y.-G. Jung, I. M. Peterson, A. Pajares, and B. R. Lawn, "Contact Damage Resistance and Strength Degradation of Glass-Infiltrated Alumina and Spinel Ceramics," *J. Dent. Res.*, in press.

[107]I. M. Peterson, S. Wuttiphan, A. Pajares, and B. R. Lawn, "Role of Microstructure on Contact Damage and Strength Degradation in Micaceous Glass-Ceramics," *Dent. Mater.*, in press.

[108]Y. G. Jung, S. Wuttiphan, I. M. Peterson, and B. R. Lawn, "Damage Modes in Dental Layer Structures," *J. Dent. Res.*, in press.

[109]R. O. Ritchie, "Mechanisms of Fatigue Crack Propagation in Metals, Ceramics, Composites: Role of Crack-Tip Shielding," *Mater. Sci. Eng.*, **A103**, 15–28 (1988).

[110]S. Suresh, *Fatigue of Materials*. Cambridge University Press, Cambridge, U.K., 1991.

[111]S. Lathabai, J. Rödel, and B. R. Lawn, "Cyclic Fatigue from Frictional Degradation at Bridging Grains in Alumina," *J. Am. Ceram. Soc.*, **74** [6] 1340–48 (1991).

[112]H. Cai, M. A. S. Kalceff, B. M. Hooks, B. R. Lawn, and K. Chyung, "Cyclic Fatigue of a Mica-Containing Glass-Ceramic at Hertzian Contacts," *J. Mater. Res.*, **9** [10] 2654–61 (1994).

[113]N. P. Padture and B. R. Lawn, "Contact Fatigue of a Silicon Carbide with a Heterogeneous Grain Structure," *J. Am. Ceram. Soc.*, **78** [6] 1431–38 (1995).

[114]H. H. K. Xu and S. Jahanmir, "Microfracture and Material Removal in Scratching of Alumina," *J. Mater. Sci.*, **30**, 2235–47 (1995).

[115]B. R. Lawn, N. P. Padture, F. Guiberteau, and H. Cai, "A Model for Microcrack Initiation and Propagation Beneath Hertzian Contacts in Polycrystalline Ceramics," *Acta Metall.*, **42** [5] 1683–93 (1994).

[116]N. P. Padture and B. R. Lawn, "Fatigue in Ceramics with Interconnecting Weak Interfaces: A Study Using Cyclic Hertzian Contacts," *Acta Metall.*, **43** [4] 1609–17 (1995).

[117]P. J. Kennedy, A. A. Conte, E. P. Whitenton, L. K. Ives, and M. B. Peterson, "Surface Damage and Mechanics of Fretting Wear in Ceramics"; pp. 79–98 in *Friction and Wear of Ceramics*. Edited by S. Jahanmir. Marcel Dekker, New York, 1994.

[118]C. J. Russo, M. P. Harmer, H. M. Chan, and G. A. Miller, "Design of a Laminated Ceramic Composite for Improved Strength and Toughness," *J. Am. Ceram. Soc.*, **75** [12] 3396–3400 (1992).

[119]H. M. Chan, "Layered Ceramics: Processing and Mechanical Behavior," *Ann. Rev. Mater. Sci.*, **27**, 249–82 (1997).

[120]S. Wuttiphan, B. R. Lawn, and N. P. Padture, "Crack Suppression in Strongly Bonded Homogeneous/Heterogeneous Laminates: A Study on Glass/Glass-Ceramic Bilayers," *J. Am. Ceram. Soc.*, **79** [3] 634–40 (1996).

[121]H. Liu, B. R. Lawn, and S. M. Hsu, "Hertzian Contact Response of Tailored Silicon Nitride Multilayers," *J. Am. Ceram. Soc.*, **79** [4] 1009–14 (1996).

[122]K. S. Lee, S. Wuttiphan, X. Z. Hu, S. K. Lee, and B. R. Lawn, "Contact-Induced Transverse Fractures in Brittle Layers on Soft Substrates: A Study on Silicon Nitride Bilayers," *J. Am. Ceram. Soc.*, **81** [3] 571–80 (1998).

[123]K. S. Lee, S. K. Lee, B. R. Lawn, and D. K. Kim, "Contact Damage and Strength Degradation in Brittle/Quasi-Plastic Silicon Nitride Bilayers," *J. Am. Ceram. Soc.*, (in press).

[124]L. Wei, A. Pajares, and B. R. Lawn, "Effect of Mechanical Damage on Thermal Conduction of Plasma Sprayed Coatings," *J. Mater. Res.*, **11** [6] 1329–32 (1996).

[125]A. Pajares, L. Wei, B. R. Lawn, N. P. Padture, and C. C. Berndt, "Mechanical Characterization of Plasma-Sprayed Ceramic Coatings on Metal Substrates by Contact Testing," *Mater. Sci. Eng.*, **A208** [2] 158–65 (1996).

[126]A. C. Fischer-Cripps, B. R. Lawn, A. Pajares, and L. Wei, "Stress Analysis of Elastic–Plastic Contact Damage in Ceramic Coatings on Metal Substrates," *J. Am. Ceram. Soc.*, **79** [10] 2619–25 (1996).

[127]A. Pajares, L. Wei, B. R. Lawn, and C. C. Berndt, "Contact Damage in Plasma-Sprayed Alumina-Based Coatings," *J. Am. Ceram. Soc.*, **79** [7] 1907–14 (1996).

[128]S. Wuttiphan, A. Pajares, B. R. Lawn, and C. C. Berndt, "Effect of Substrate and Bond Coat on Contact Damage in Zirconia-Based Plasma Coatings," *Thin Solid Films*, **293** [1–2] 251–60 (1997).

[129]H. Herman, "Plasma-Sprayed Coatings," *Sci. Am.*, **256** [9] 113–88 (1988).

[130]M. V. Swain and J. Mencik, "Mechanical Property Characterization of Thin Films Using Spherical Tipped Indenters," *Thin Solid Films*, **253**, 204–11 (1994).

[131]K. Komvopolous, "Elastic–Plastic Finite Element Analysis of Indented Layered Media," *J. Tribology*, **111**, 430–39 (1989).

[132]P. Montmitonnet, M. L. Edinger, and E. Felder, "Finite Element Analysis of Elastoplastic Indentation: Part II—Application to Hard Coatings," *J. Tribology*, **115**, 15–19 (1993).

[133]X. Z. Hu and B. R. Lawn, "A Simple Indentation Stress–Strain Relation for Contacts with Spheres on Bilayer Structures," *Thin Solid Films*, in press.

[134]H. Liu and S. M. Hsu, "Fracture Behavior of Multilayer Silicon Nitride/Boron Nitride Ceramics," *J. Am. Ceram. Soc.*, **79** [9] 2452–57 (1996).

[135]J. Jitcharoen, N. P. Padture, A. E. Giannakopoulos, and S. Suresh, "Hertzian-Crack Suppression in Ceramics with Elastic-Modulus-Graded Surfaces," *J. Am. Ceram. Soc.*, in press. □

Brian R. Lawn gained his B.Sc. and Ph.D. degrees in physics at the University of Western Australia. After graduating, he was a Postdoctoral Fellow in the School of Physics at the University of Bristol and in the Department of Engineering and Materials Science at Brown University. Dr. Lawn then held a position as a lecturer in applied physics at the University of New South Wales for several years. During this tenure, he spent several periods of study leave in the Department of Materials Science at the University of Sussex and in the Ceramics Division at the National Institute of Standards and Technology (then the National Bureau of Standards). In 1981, Dr. Lawn joined the National Institute of Standards and Technology permanently, and, in 1987, was elected to the position of NIST Fellow. He currently holds appointments as Adjunct Professor in materials science at Lehigh University and the University of Maryland in the United States, and in applied physics at Curtin University in Western Australia. Dr. Lawn has published widely on the fracture properties of brittle materials, and is the author of *Fracture of Brittle Solids*, now in its second edition.

journal

J. Am. Ceram. Soc., 81 [4] 997–1003 (1998)

Role of Microstructure in Hertzian Contact Damage in Silicon Nitride: II, Strength Degradation

Seung Kun Lee*,† and Brian R. Lawn*

Materials Science and Engineering Laboratory, National Institute of Standards and Technology, Gaithersburg, Maryland 20899

In this Part II of a two-part study of the role of microstructure on Hertzian contact damage in silicon nitride we determine strength degradation properties. As previously, three microstructures are investigated: fine (*F*), medium (*M*) and coarse (*C*), representing a progressive transition from brittle to quasi-plastic damage. In both the *F* and *M* materials, failures originate from cone cracks (although limited quasi-plasticity is evident in the latter material). These two materials show abrupt losses in strength at the critical contact loads for cone crack initiation, and steady falloff thereafter at higher contact loads. In the *C* material, failures occur from critical shear faults within the damage "yield" zones. The strengths in this material fall off much more gradually, without abrupt drop, above about twice the critical load for the onset of yield. Fracture mechanics models for each type of failure mode provide explicit relations for the degraded strength as a function of contact load. These models account for all the essential features in the observed strength degradation data. Particular attention is given to indenter size effects in the strength responses. Sphere radius has a profound influence on the critical loads for the onset of degradation, but relatively little influence on the degraded strengths at higher loads. Implications of the results concerning contact fatigue and wear are briefly considered.

I. Introduction

In Part I,[1] we characterized the contact responses of silicon nitrides with different degrees of microstructural heterogeneity. There we demonstrated that the mode of damage from Hertzian contacts is fundamentally different in homogeneous and heterogeneous microstructures: in homogeneous, fine-equiaxed grain structures, macroscopic cone cracking (brittle mode); in relatively heterogeneous, coarse-elongate grain structures, distributed microscopic damage (quasi-plastic mode). The quasi-plastic response was shown to be governed by the shear component of the contact field, in the immediate subsurface region where the compressive stresses are triaxial and high. The question now arises: How well do silicon nitride ceramics of each microstructural type retain their strength properties after sustaining contact damage from spherical indenters, especially at high loads? This question, foreshadowed by Makino *et al.*,[2] forms the central theme of this part of the study.

Accordingly, we subject the same silicon nitride materials to strength testing after Hertzian contacts, over a broad range of sphere radii. The study focuses on three controlled silicon nitride microstructures: "fine" (*F*), "medium" (*M*), and "coarse" (*C*).[1] (Recall that, in addition to grain coarsening, the progression $F \rightarrow M \rightarrow C$ also represents increasing $\alpha \rightarrow \beta$ transformation and associated grain elongation.) The two types of contact damage, brittle and quasi-plastic, lead to highly distinct failure modes, from cone cracks in the *F* and *M* materials and from the quasi-plastic zone in the *C* material. Experimental data are represented on strength degradation curves, with inert strength plotted as a function of contact load. The *C* material, although characterized by a lower laboratory strength, shows a much more gradual strength loss with increasing load—it is more "damage tolerant." The results also indicate the important role of sphere size, not so much in the ultimate degraded strength at high loads but in the critical loads at which degradation first becomes manifest.

Basic fracture mechanics models are used to analyze the data for the two damage types, assuming failure directly from a macroscopic cone crack in the *F* and *M* materials and from an individual shear-activated microcrack ("shear fault") in the *C* material.[3] The models account for the essential data trends in the two material types: in the first type, an abrupt strength loss at the critical load for cone cracking, followed by a slow falloff at higher loading; in the second type, a continuous strength loss above a degradation load well in excess of the load for first yield, followed by an even slower falloff at higher loads. The model allows for an evaluation of the role of sphere size on the strength degradation, and identifies the important material variables for optimum resistance to degradation. It also contains provision for extension to contact fatigue.

II. Experimental Procedure

The silicon nitride materials used here were those described in Part I:[1] (i) "fine" (*F*-Si_3N_4), with ≈75 vol% equiaxed α grains of mean size ≈0.4 μm and ≈15 vol% elongated β grains of length 1.5 μm and diameter 0.4 μm; (ii) "medium" (*M*-Si_3N_4), with ≈20 vol% equiaxed α grains of mean size ≈0.5 μm and ≈70 vol% elongated β grains of length 4.0 μm and diameter 0.5 μm; (iii) "coarse" (*C*-Si_3N_4), elongated β grains of mean length ≈9 μm and diameter 1.5 μm. In each case the structure contained ≈10 vol% interboundary glassy phase.

Hertzian indentations were made in air, using WC spheres of radius $r = 1.59–3.18$ mm, on polished surfaces of prospective tensile specimens, at peak loads up to $P = 4500$ N. Indented surfaces were examined to determine critical loads for onset of fracture and yield, as described in Part I.

Some exploratory Vickers indentations were made at relatively low loads outside the periphery of the Hertzian contact impressions in *C*-Si_3N_4, using the lengths of the radial cracks to assess the magnitude of any long-range residual fields around the macroscopic quasi-plastic zones.

Four-point bend tests were made on bars 3 mm × 4 mm × 25 mm, inner span 10 mm and outer span 20 mm, with the

J. E. Ritter, Jr.—contributing editor

Manuscript No. 191111. Received April 1, 1997; approved July 14, 1997.
Supported by the U.S. Air Force Office of Scientific Research.
*Member, American Ceramic Society.
†Guest Scientist from the Department of Materials Science and Engineering, Lehigh University, Bethlehem, Pennsylvania 18015.

indented surfaces on the tensile side. The edges of the tensile surfaces were prechamfered and polished to minimize edge failures. All specimens were covered by a drop of silicone oil before testing, and were broken in fast fracture (<10 ms), to avoid the influence of moisture ("inert" strengths). All broken specimens were examined fractographically in Nomarski illumination to locate the source of failure, either indentations or extraneous flaws.

Control strength tests were also made on unindented specimens, to measure baseline "laboratory" strengths, as described in Part I.

III. Strength Degradation Curves

In this section we investigate the effects of microstructure and sphere radius on strength degradation, for each of the *F*-Si_3N_4, *M*-Si_3N_4, and *C*-Si_3N_4 materials.

Figure 1 shows broken surfaces of strength test specimens containing indentations made with a WC sphere of radius r = 2.38 mm at load P = 4000 N. This load is sufficient to produce strength-controlling contact damage in all cases (Part I[1]). Cone cracks are apparent—deep in *F*-Si_3N_4, intermediate in *M*-Si_3N_4, vestigial in *C*-Si_3N_4 (i.e., shallow surface ring cracks). Likewise, quasi-plastic impressions are apparent in *M*-Si_3N_4 and *C*-Si_3N_4, especially in the latter. In the *F* and *M* materials, the final fracture intersects the surface ring crack at a tangent, indicative of failure initiation at the cone base.[4] In the *C* material, on the other hand, the fracture traverses the inner contact zone, passing nearly orthogonal to the vestigial surface ring cracks, indicating a fracture origin from within the subsurface quasi-plasticity zone. The fracture origins are therefore fundamentally different in the two material types. Note that the fracture trace becomes more tortuous through the progression $F \rightarrow M \rightarrow C$, consistent with intergranular fracture in these ever-coarsening structures (Part I).

Results of the indentation–strength tests for the three Si_3N_4 materials are plotted as inert strength σ_F against indentation load P in Figs. 2–4. Data points are individual measured strengths: solid symbols represent specimens that broke at indentation sites; open symbols represent specimens that broke away from indentation sites, i.e., from extraneous flaws. Shaded areas on the left axes are laboratory strengths σ_0 of unindented specimens (Part I). Vertical dashed lines represent threshold loads P_C for cracking (*F*-Si_3N_4 and *M*-Si_3N_4) and P_Y for yield (*M*-Si_3N_4 and *C*-Si_3N_4), and P_D for the onset of degradation for failures from the quasi-plastic zone (*C*-Si_3N_4). Solid curves are fits from the subsequent fracture mechanics analyses (Section IV). The effects of microstructure and contact radius on the strength characteristics are investigated separately below.

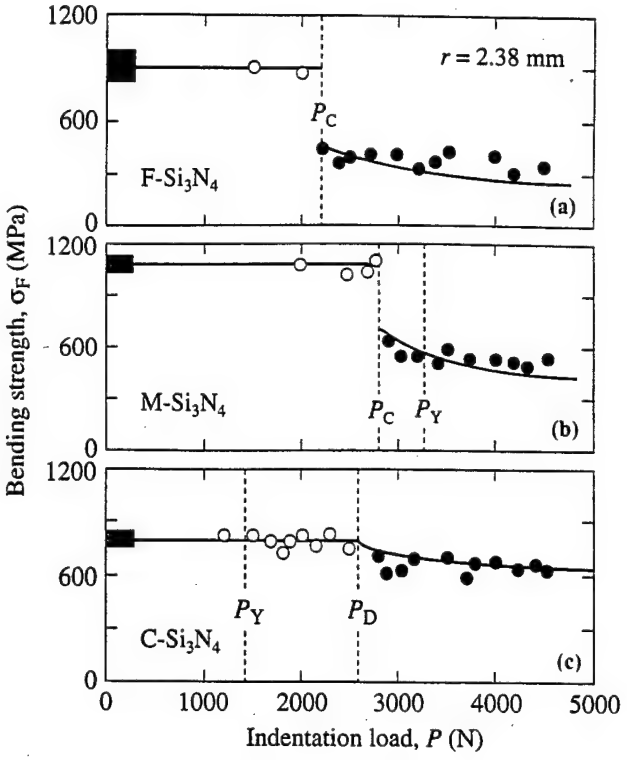

Fig. 2. Inert strength of Hertzian-indented Si_3N_4 specimens indented with WC sphere, r = 2.38 mm, as function of indentation load, illustrating effect of microstructure: (a) *F*-Si_3N_4, (b) *M*-Si_3N_4, (c) *C*-Si_3N_4. Data points are experimental measurements, indentation tests in air: closed symbols represent failures from indentation origins, open symbols from other origins. Shaded box at left axis represents strengths of polished, unindented specimens. Vertical dashed lines indicate critical loads P_C, P_Y, and P_D.

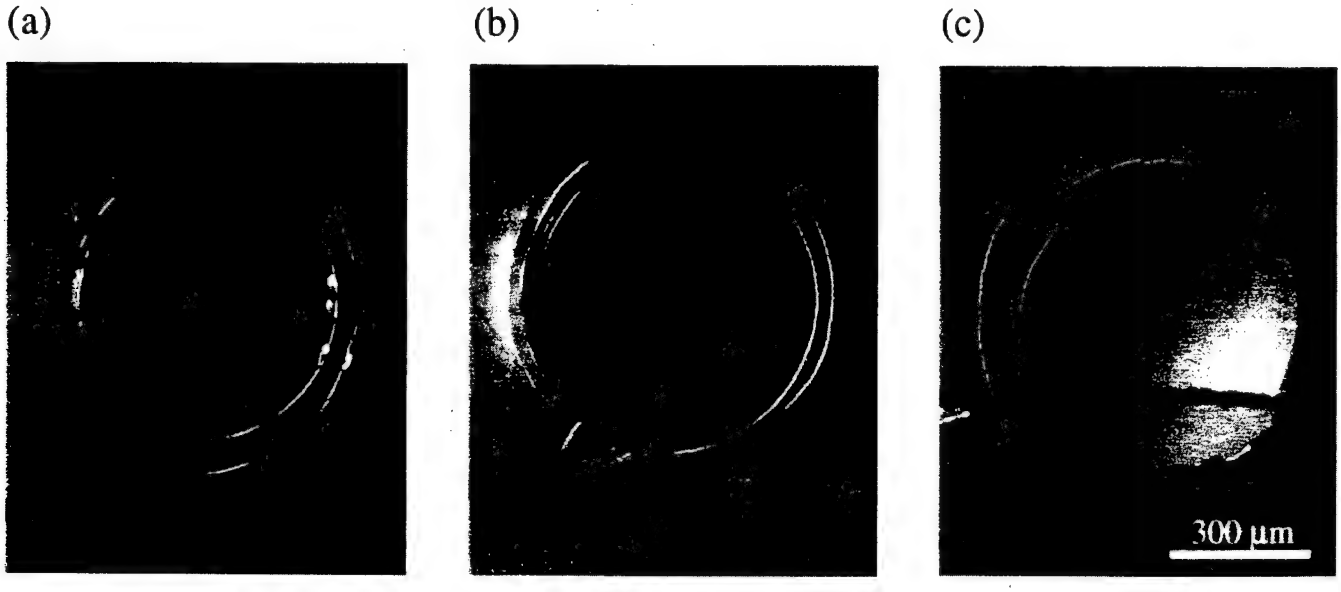

Fig. 1. Micrographs showing failure of silicon nitride specimens in strength tests under inert conditions, for WC sphere radius r = 2.38 mm at load P = 4000 N, indentation tests in air: (a) *F*-Si_3N_4, (b) *M*-Si_3N_4, (c) *C*-Si_3N_4. Nomarski illumination, surface gold coated. Tensile direction vertical in plane of diagram.

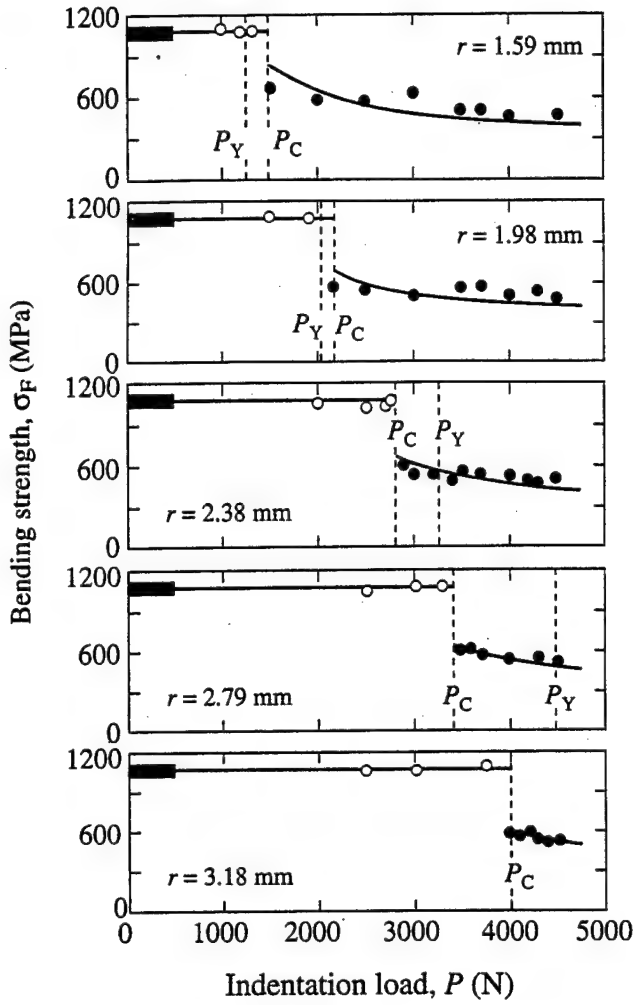

Fig. 3. Inert strength of Hertzian-indented M-Si_3N_4 specimens as function of indentation load, for WC sphere radii r indicated. Data points are experimental measurements, for indentation tests in air: closed symbols represent failures from indentation origins, open symbols from other origins.

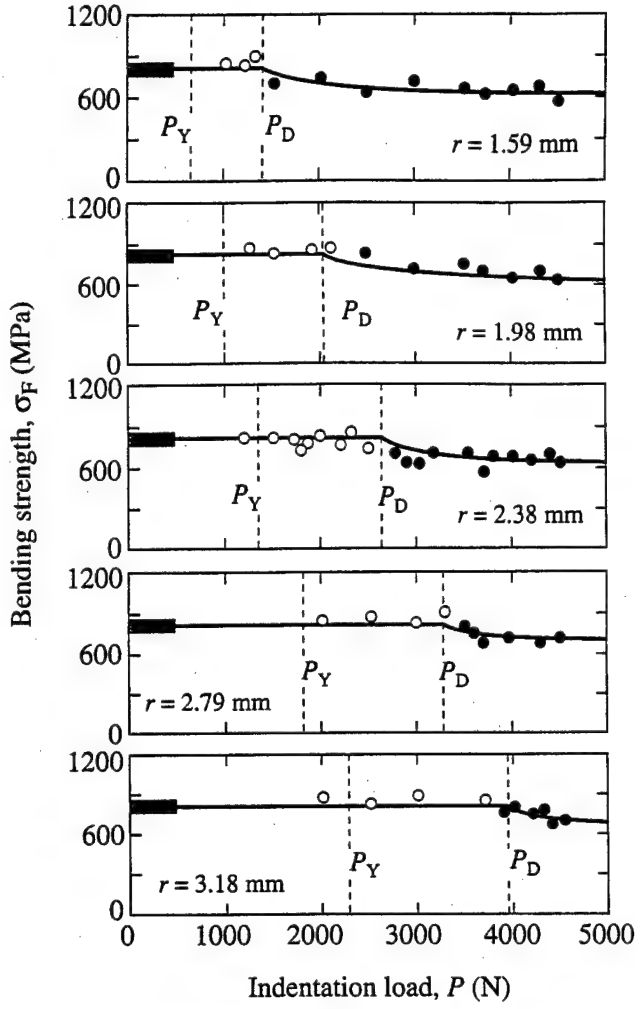

Fig. 4. Inert strength of Hertzian-indented C-Si_3N_4 specimens as function of indentation load, for WC sphere radii r indicated. Data points are experimental measurements, for indentation tests in air: closed symbols represent failures from indentation origins, open symbols from other origins.

The results of exploratory tests using small Vickers indentations in the field of the greater Hertzian contact impressions in C-Si_3N_4 revealed relatively insignificant macroscopic stress intensities from the quasi-plastic zone, ≈125 MPa at the contact periphery, over the sphere radius and contact load ranges studied here (Appendix).

(1) Effect of Microstructure

Figure 2 compares strength degradation data $\sigma_F(P)$ for Hertzian tests on F-Si_3N_4, M-Si_3N_4, and C-Si_3N_4, at a common sphere radius r = 2.38 mm. F-Si_3N_4 and M-Si_3N_4 (Figs. 2(a) and 2(b)) show typical brittle responses: no perceptible degradation at $P < P_C$, indicating failures from natural flaws; abrupt dropoff at $P = P_C$, highlighting the effectiveness of cone cracking as a source of strength degradation. The strength continues to fall at $P > P_C$ as the cone cracks are driven deeper with ever-increasing load, but this falloff is relatively slow. In M-Si_3N_4, the incidence of accompanying plasticity at $P > P_Y$ ($>P_C$) has no perceptible effect on the strength (Fig. 1(b)).

C-Si_3N_4 (Fig. 2(c)) shows an altogether different response. The ring cracks are only "skin deep" (Fig. 1(c)), and do not cause strength loss. Nor does the onset of plasticity at $P = P_Y$ immediately degrade the strength, even though failures ultimately do occur, at $P = P_D \approx 2P_Y$ in Fig. 1(c), from the quasi-plastic zone. At this point the strength starts to degrade, but without the abrupt falloff seen in F-Si_3N_4 and M-Si_3N_4, and decreases at an even slower rate at higher loads. Thus the quasi-plasticity mode is less deleterious to strength than the traditional cone crack mode. This indicates that the strength properties in C-Si_3N_4 are controlled by less severe flaws, individual shear faults, within the damage zone.[3]

Observe through the sequence $F \rightarrow M \rightarrow C$ in Fig. 2 that the degree of strength loss at the onset of degradation progressively diminishes, and the remaining strength at any given indentation load within the degradation region (closed symbols) progressively increases. Increased quasi-plasticity correlates with enhanced damage tolerance.

(2) Effect of Sphere Radius

Strength degradation data $\sigma_F(P)$ for Hertzian tests in air are plotted in Fig. 3 for M-Si_3N_4 (brittle response) and in Fig. 4 for C-Si_3N_4 (quasi-plastic response), for a range of sphere radii r. The designations on these plots are as in Fig. 2.

For M-Si_3N_4 (Fig. 3), abrupt strength drops are again evident at $P = P_C$. The critical load P_C itself increases monotonically with r. Although the degree of strength dropoff at P_C also increases with r, commensurate with larger popped-in cone cracks, the strengths at $P >> P_C$ tend to similar asymptotic levels. There is no detectable influence from quasi-plasticity, even at r = 1.59–2.79 mm where $P_Y < P_C$, confirming that cone cracking remains the dominant mode over the entire radius range studied in this material.

For C-Si_3N_4 (Fig. 4), strength degradation occurs smoothly at $P = P_D$. Note that $P_D \approx 2P_Y$ at all r (P_C for full-scale cone

cracking is off scale). Quasi-plasticity is now the dominant source of failure. Again, whereas P_D is sensitive to r, the degraded strength itself at $P > P_D$ is not. The extremely slow strength falloff in the degradation region again attests to the damage tolerance of this relatively heterogeneous material.

In Fig. 5 we replot the critical loads for first damage and degradation from Figs. 3 and 4 as functions of r. Note that whereas the $P_Y(r)$ curve for M-Si_3N_4 in Fig. 5(a) can be represented by the function $P_Y \propto r^2$, characteristic of a geometrically similar yield process,[5] the $P_C(r)$ curve is somewhat less dependent on r (somewhere between $P_C \propto r^2$ and $P_C \propto r$), indicative of a size dependence in the fracture stress (Part I). Accordingly, the $P_Y(r)$ and $P_C(r)$ curves cross each other (recall Fig. 7, Part I), so the response tends toward an increasing quasi-plasticity component at smaller sphere sizes. On the other hand, the $P_Y(r)$ and $P_D(r)$ curves for C-Si_3N_4 in Fig. 5(b) appear to have the same quadratic dependence, as may be expected for quantities governed by a common quasi-plasticity process, accounting for the near-constant ratio $P_D/P_Y \approx 2$ at all r in Fig. 4.

IV. Mechanics Analysis

As indicated above, the solid curves in Figs. 3 and 4 represent theoretical fits to the strength degradation data. We now briefly summarize the models used to obtain these fits—a detailed analysis is given elsewhere.[3] It is taken that no degradation occurs up to the critical loads P_C or P_D, in accordance with the observations in the previous section. Above these loads failure is assumed to occur from indentation damage, as indicated schematically in Fig. 6: in brittle materials, from fully developed cone cracks (Fig. 6(a)); in quasi-plastic materials, from dominant shear faults within the damage zone (Fig. 6(b)). In each case the aim is to derive analytical expressions for the strength degradation function $\sigma_F(P)$, in terms of underlying material variables.

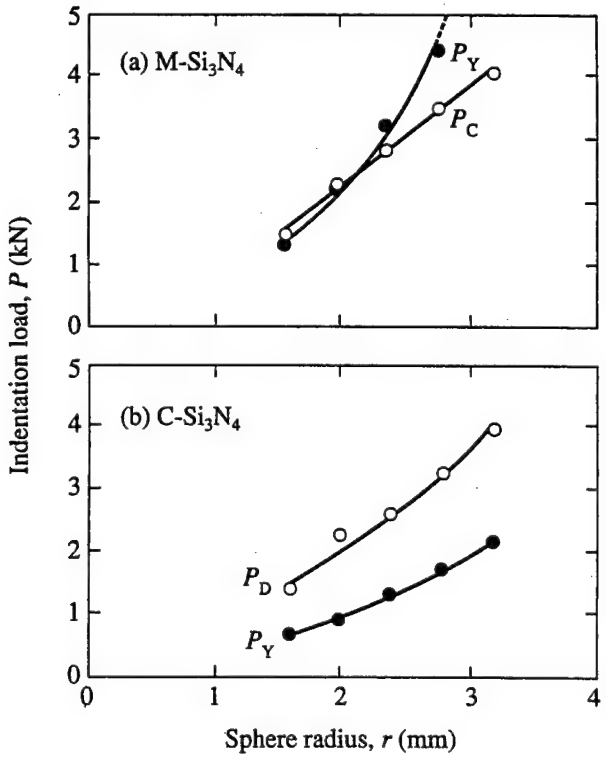

Fig. 5. Critical loads for silicon nitride as function of WC indenter size: (a) M-Si_3N_4, for cone cracking, P_C, and yield, P_Y (from Fig. 7(b), Part I); (b) C-Si_3N_4, for yield, P_Y (Fig. 7(c), Part I), and onset of degradation, P_D.

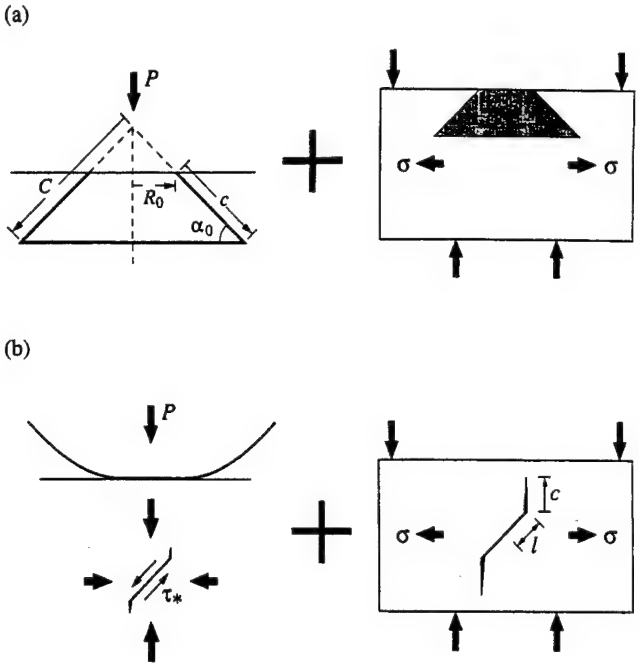

Fig. 6. Schematic showing critical flaws induced by contact with spherical indenter (left), and subsequent strength tests on indented specimens (right): (a) brittle response, failure from fully developed cone crack; (b) quasi-plastic response, failure from shear-fault/wing-crack within damage zone.

(1) Failure from Cone Cracks

For the F-Si_3N_4 and M-Si_3N_4 materials with their brittle responses, we use a simple modification of an analysis developed in an earlier study of Hertzian-induced strength degradation in glass.[6] For materials governed by a single-valued toughness $K_{IC} = T_0$, as is appropriate to both F-Si_3N_4 and M-Si_3N_4 (Part I[1]), and ignoring any macroscopic residual stresses associated with the indentation quasi-plasticity (Appendix), failure occurs spontaneously from a critical crack of size c at tensile stress $\sigma = \sigma_F$ according to the familiar strength relation

$$\sigma_F = T_0/\psi c^{1/2} \tag{1}$$

At $P < P_C$, the strength is governed by the size $c = c_f$ of the preexisting natural flaws (with $\psi = \pi^{1/2}$ for line flaws—cf. Eq. (1) in Part I). In this benign region, σ_F is equal to the laboratory (pre-indentation) strength σ_0, independent of P.

At $P > P_C$, the strength is governed by the size c of the well-developed cone crack, related to the size C of a virtual conical surface with tip located above the indented surface,[6]

$$c = C - R_0/\cos\alpha \tag{2}$$

with α the angle between the cone crack and the specimen surface (Fig. 6(a)). The size C in turn closely satisfies a relation for pennylike cracks (Eq. (3), Fig. 11, Part I),

$$P/C^{3/2} = T_0/\chi \tag{3}$$

with χ a crack geometry coefficient. The requisite strength degradation function $\sigma_F(P)$ may then be solved explicitly from Eqs. (1) to (3). In the asymptotically limiting region of extreme loads at $P >> P_C$ ($c >> R_0/\cos\alpha$), σ_F varies slowly, as $P^{-1/3}$.

While the critical load P_C for cone cracking is relatively dependent on r (somewhere between $P_C \propto r^2$ and $P_C \propto r$, Fig. 5(a)), the degraded strength beyond this point is only slowly dependent. An r dependence in σ_F enters only through Eq. (2), and is important only in the low load region (c comparable with $R_0/\cos\alpha$). Recalling from Part I that $R_0/a_C = 1.15$ = constant, where a is the contact radius, Hertzian elasticity theory[7,8] gives $R_0 = 1.15(4kP_Cr/3E)^{1/3}$, with E Young's modulus and k an

indenter/specimen elasticity coefficient: so that, if $P_C \propto r^2$, then $R_0 \propto r$; if $P_C \propto r$, then $R_0 \propto r^{2/3}$.

With the data from the cone crack size and geometry characterization in Part I, Eqs. (1) to (3) can be used to predict *a priori* the strength degradation curves for *F*-Si_3N_4 and *M*-Si_3N_4. At $P < P_C$ the values of σ_F are given directly by the laboratory strengths σ_0 (Section II(3), Part I). At $P > P_C$, the cone crack parameters are $\alpha = 19°$ (Section III(3), Part I) and $\chi = 0.0154$ (Section IV(3), Part I). The crack geometry coefficient ψ is determinable from an analysis of crack reinitiation from the cone crack base,[6] yielding $\psi(\alpha) = 0.71$ for $\alpha = 19°$.[3]

The functions $\sigma_F(P)$ from Eqs. (1) to (3) are included as the solid curves for *F*-Si_3N_4 and *M*-Si_3N_4 at $P > P_C$ in Figs. 2 and 3. The predicted strengths pass through the experimental data, within the scatter.

(2) Failure from Quasi-plastic Damage Zones

For the *C*-Si_3N_4 material with its quasi-plastic response, we use a recent model for the strength of solids containing shear-activated microcracks.[3] Specifically, the model assumes that failure occurs from a single pennylike shear fault of radius l with an "extensile" wing crack of annular width c at its edges (Fig. 6(b)). The critical shear fault is assumed to be located and oriented so as to experience the maximum principal shear stress within the contact field. Similarly, the wing crack is assumed oriented so as to experience maximum tensile stress within the subsequent flexure field. The system goes to failure when the applied tensile stress is sufficient to drive the equilibrium wing crack to instability.

During contact loading, the fault surfaces slide against frictional tractions, leaving a local residual net shear stress at the fault plane,

$$\tau_* = \tau_P - \tau_c \tag{4}$$

where τ_P is the resolved shear stress on the fault plane at peak load and τ_c is a resistance "cohesion" stress. (We omit a possible additional Coulombic contribution to the friction from the resolved compressive stresses across the fault plane.[3,9]) The magnitude of the shear stress $\tau_* = \tau_*(P)$ in Eq. (4) determines the size of the wing cracks.

The driving force from τ_* on the wing cracks persists after contact, and superposes onto the driving force from the subsequent applied tensile stress σ. This driving force is localized at the mouth of the wing crack, and stabilizes the cracks within the superposed tensile field. Accordingly, the wing cracks are predicted to undergo a stage of precursor growth prior to instability, typically by a fault dimension l or so.[3] For materials with single-valued toughness $K_{IC} = T_0$, the equilibrium solution of the composite stress-intensity factor for this stabilized microcrack system yields the strength[3]

$$\sigma_F = (3/4\psi)(T_0^4/4\chi\lambda l^2\tau_*)^{1/3} \tag{5}$$

where ψ (cf. Eq. (1) and λ are crack geometry terms and χ is from Eq. (3). (Strictly, the assumption of single-valued toughness for *C*-Si_3N_4 is not correct, since this material has a rising toughness curve (Fig. 3, Part I); but since the wing crack extensions are relatively small prior to failure, we ignore this complication.)

To obtain the requisite function $\sigma_F(P)$, we need only determine $\tau_*(P)$. This we obtain empirically from FEM analyses of the elastic–plastic contact stress field.[3] Specifically, values of τ_* are evaluated for a fault located at the point of maximum shear stress beneath the contact, at progressively increasing loads P. For indenters which deform elastically, these values can be well represented by the relation[3]

$$\tau_*/\tau_c = \alpha[(P/P_Y)^{1/3} - 1] \qquad (P > P_Y) \tag{6}$$

In Eq. (3), $\sigma_F\tau_*^{1/3} = \sigma_0\tau_D^{1/3} =$ constant defines the net shear stress $\tau_* = \tau_D$ at which the strength σ_F just equals the laboratory strength σ_0, corresponding to $P = P_D$ in Figs. 2 and 4. Insertion of this "boundary condition" along with Eq. (6) into Eq. (5) yields

$$\sigma_F = \sigma_0[(P_D^{1/3} - P_Y^{1/3})/(P^{1/3} - P_Y^{1/3})]^{1/3} \qquad (P > P_D) \tag{7}$$

Actually, the WC spheres in our experiments are not ideally elastic, as assumed in Eq. (6), but deform plastically (Part I). However, the sensitivity of Eq. (7) to P is so slow that this is unlikely to lead to serious discrepancy. In any case, plasticity in the indenter will only reduce the value of τ_* in Eq. (6), so that Eq. (7) will, if anything, underestimate the strength ("conservative" prediction).

The resultant strength–load function $\sigma_F(P)$ for *C*-Si_3N_4, using the curve-fitted functions $P_Y(r)$ and $P_D(r)$ from Fig. 5(b), is included as the solid curves at $P > P_D$ in Figs. 2(c) and 4. (The horizontal lines at $P < P_D$ correspond to the mean laboratory strengths σ_0 for each material.) The fits account for the continuous, ultraslow strength falloff. Note that sphere radius r enters Eq. (7) only through P_D and P_Y (Fig. 5(b)), corresponding to a simple shift along the load axis in Fig. 4.

V. Discussion

In this paper we have presented strength degradation data for three silicon nitride microstructures, nominally fine (*F*), medium (*M*), and coarse (*C*). The response in *F*-Si_3N_4 and *M*-Si_3N_4 is essentially brittle, with failures originating from cone cracks. Conversely, the response in *C*-Si_3N_4 is essentially quasi-plastic, with failures originating from shear faults within the subsurface "yield" zone. Analytical models for fitting the data, and for providing a predictive capability for other potential microstructures, have been described. These models are equipped for an account of indentation size effects and for developing design concepts for bearing and other contact configurations.

The foremost interest here is the role of the Si_3N_4 microstructure. *M*-Si_3N_4 represents the compromise structure, with dominant cone cracks but also with partial quasi-plasticity. It is this material that most closely resembles current bearing-grade silicon nitride (Part I[1]). It is stronger than its more brittle counterpart, *F*-Si_3N_4, apparently because it contains a higher fraction of the more resilient β phase, even though it has a coarser grain structure and larger flaw size (Part I). Its drawback is that it still shows a substantial strength drop above the critical load P_C for cone crack initiation (Figs. 2(b) and 3), down to a level of almost one half the laboratory strength. In *C*-Si_3N_4 cone cracking is effectively suppressed, with quasi-plasticity damage dominant. The strength shows no abrupt falloff above the degradation load P_D at which the stable wing cracks associated with the shear faults become the dominant flaws (Figs. 2(c) and 4). The degraded strength is not as low as in *M*-Si_3N_4, even though the starting laboratory strength is considerably lower. Hence the development of pervasive quasi-plasticity below the contact imparts damage tolerance to the silicon nitride microstructure. Potential effects of other variables, such as oxynitride glass composition,[10] are equally amenable to exploration by the contact testing methodology.

The models are explicit in specifying the important material variables in the strength degradation responses for both cone cracking and quasi-plasticity modes. For the brittle materials, high toughness T_0 in Eqs. (1) to (3) is the usual prime requirement for optimum resistance to strength loss from cone cracking. (Low Young's modulus and high Poisson's ratio are secondary requirements, the first to diminish the tensile stresses in the contact field at any given load, and the second to further diminish these stresses and to keep the cone angle α small.[6]) For the quasi-plastic materials, high T_0 is also a factor in Eq. (5) (although the value of T_0 that is pertinent here is the short-crack toughness, which can have an inverse relation with the conventional long-crack toughness[11]). Another factor in the quasi-plastic case is the microstructural fault size l, with inverse dependence in Eq. (5), so that continued coarsening is

expected to enhance the strength degradation. Yet another factor that enters indirectly in Eq. (5), but is of critical importance in the context of fatigue (see below), is the internal friction term τ_c, or yield stress $Y = 2\tau_c$, via τ_* in Eq. (4). Diminishing τ_c increases τ_*, thereby degrading the strength at any given load in Eq. (5). Figure 7 quantifies this degradation in terms of a diminishing "attrition parameter" β ($0 \leq \beta \leq 1$), representing the function $\sigma_F(P)$ derived from Eqs. (5) to (7) as before but with τ_c replaced by $\beta\tau_c$ in Eq. (6) (recalling from Eq. (2) in Part I that $P_Y \propto Y^3 \propto \tau_c^3$). From these considerations we may expect that greater microstructural heterogeneity (reducing T_0 and Y, increasing l) is likely to enhance plasticity-induced strength degradation, even while increasing long-crack toughness.[10,12–16]

Another potentially adverse effect of excessively increasing microstructural heterogeneity is enhancement of material removal from the damage zone,[17,18] by coalescence of adjacent wing cracks under extreme loading conditions.[3] Such coalescence is enhanced by the very high local driving stresses from the slipped shear faults (>1 GPa—recall stress–strain curves, Part I) acting on the wing cracks. Considerations of this kind are likely to be important in applications where wear resistance is a major concern. Again, the goals of high toughness and high wear resistance appear to be mutually exclusive. It is on such grounds that the choice of M-Si_3N_4 as a compromise material for bearing applications is physically justifiable.

Figures 3 and 4 demonstrate the strong effect of sphere size in the critical loads for the onset of strength loss, and converse weak effects thereafter in the strength values at higher loads. This distinctive behavior reflects the differences between near fields, which are highly sensitive to local contact conditions, and far fields, which are not.[11,19] For M-Si_3N_4 in Fig. 5(a), there is a trend toward increased quasi-plasticity at smaller sphere sizes, indicative of the size-dependent brittle–ductile transitions that characterize contact fields.[20–22] At very small radii (e.g., $r \ll 1$ mm),[2] the quasi-plasticity mode will inevitably become the dominant source of degradation in M-Si_3N_4 ($P_Y \ll P_C$), and, ultimately, even in the ostensibly brittle F-Si_3N_4 (Part I). At this microcontact level where the stress concentrations are high the quasi-plastic zones can be accompanied by the radial cracks that typify "sharp" indenters.[2,23]

We have alluded to the relevance of the strength degradation data to the issues of damage tolerance. It is well established that the laboratory strengths of homogeneous materials are much more sensitive to extraneous flaws than those of heterogeneous materials.[24] The critical loads for cone cracking are also more sensitive to extraneous flaws, especially surface finish flaws,[6] than the critical loads for yield, since the latter process occurs subsurface. We have also seen in Figs. 2–4 how F-Si_3N_4 and M-Si_3N_4 are much more susceptible to abrupt strength losses than is C-Si_3N_4. (Similar flaw sensitivities are observed in strength data on fine and coarse silicon nitrides subjected to thermal shock.[15]) Moreover, in C-Si_3N_4 the losses do not occur until well above the first signs of damage, i.e., $P_D \approx 2P_Y$. Unlike their homogeneous counterparts, the heterogeneous materials are capable of sustaining substantial distributed, and detectable, damage before strength is impaired. This raises the prospect of an "early warning" prior to component failure, opening the possibility of nondestructive evaluation.

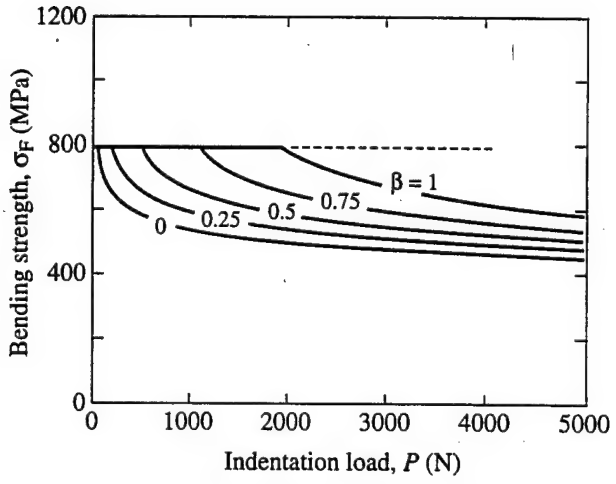

Fig. 7. Hypothetical strength–load functions for C-Si_3N_4, for various values of attrition parameter β, illustrating effect on strength of diminished frictional resistance $\beta\tau_c$ (see text).

Of the two damage models described in Section IV, that for cone cracking in brittle materials is more amenable to *a priori* predictions of strength degradation behavior. That is because the cone-crack dimensions and geometry in Eqs. (1) to (3) are readily "calibrated" by direct measurement (Part I). The shear-fault/wing-crack model for quasi-plastic materials requires an empirical determination of P_D in Eq. (7) from the actual strength degradation data, so the data analysis represents more a fit than a prediction. Experimentally, it is not so simple to "calibrate" the microscopic wing-crack configurations from direct measurements, thus necessitating the empirical fitting routine. And since the models are subject to several assumptions and approximations, including the assumption that the toughness remains single-valued (even in the C-Si_3N_4—see Part I), evaluations of material variables from these parameters fits should not be taken too literally.[3] This caution extends to the predicted forms of the strength degradation functions—on the other hand, since the $\sigma_F(P)$ data are slowly varying in Figs. 2–4, such uncertainties are unlikely to be an important limitation in the modeling.

Finally, we acknowledge the restriction of the present study to single-cycle contacts, and to comparatively innocuous laboratory atmospheres. The Hertzian testing procedure is readily extendible to multiple-contact loading, under any specifiable adverse chemical environment, and thus to the study of accelerated strength degradation from contact fatigue.[17,18,25–27] Any such fatigue in highly brittle solids would appear to be exclusively *chemical*, from water-assisted slow growth crack of the cone cracks, by reducing P_C and enhancing c in Eqs. (1) to (3).[17] Slow crack growth could also enhance the growth of wing cracks in quasi-plastic materials, if water were to gain access to the subsurface shear faults, as would certainly ensue if any microcrack coalescence were to occur. Deleterious effects of water in contact fatigue tests have been well demonstrated in coarse-grain alumina.[25] But potentially more damaging in the heterogeneous materials is *mechanical* fatigue, from reductions in friction stress τ_c (and μ) at the repeatedly sliding shear fault surfaces.[18] This mode of fatigue has been demonstrated strikingly at multiple-contact sites in heterogeneous silicon carbide, as attritional surface debris within the contact damage zone, and ultimately as excessive material spalling,[17] and has been foreshadowed in earlier contact tests on silicon nitride.[28] A more detailed study of the role of microstructure in contact fatigue of silicon nitride is under way.

APPENDIX

Evaluation of Macroscopic Residual Stresses around Hertzian Impressions Using Exploratory Vickers Indents

In this Appendix we describe evaluations of macroscopic residual stresses around the quasi-plastic Hertzian impressions in C-Si_3N_4, using simple exploratory Vickers tests. This test has been employed by Makino *et al.*[2] to explore around Hertzian impressions made with a harder (diamond) and much smaller ($r \approx 200$ μm) sphere than used here (WC, $r > 1$ mm), in a coarse silicon nitride material analogous to our C-Si_3N_4. The contact impressions in that study represent much higher contact pressures, as indicated by strong anisotropy in the Vickers radial crack patterns, than in our present work (note

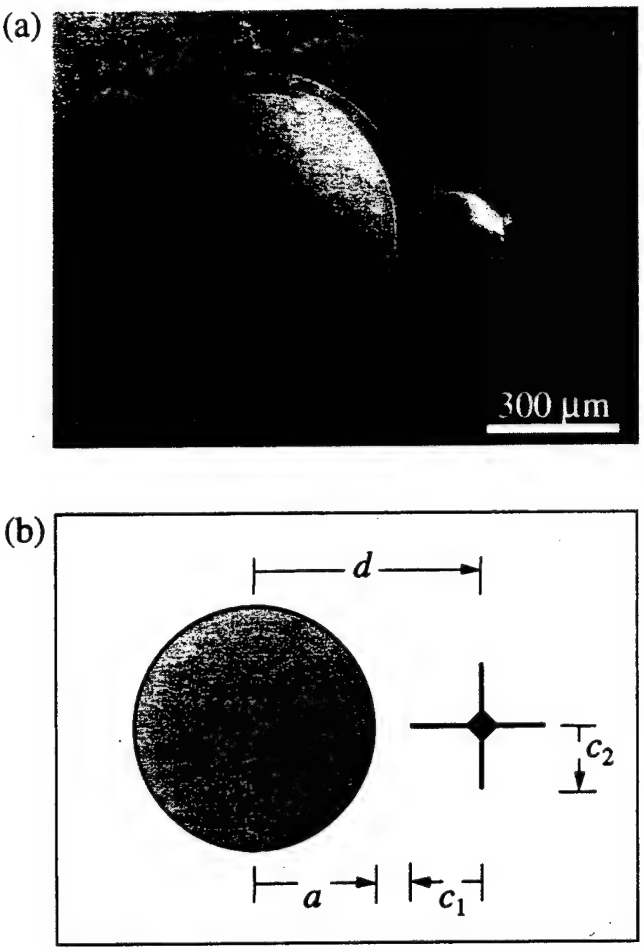

Fig. A1. Exploratory Vickers indentation, formed at load 100 N, in field of preceding Hertzian impression, formed at load 4000 N with WC sphere of radius $r = 1.98$ mm: (a) micrograph, showing slightly larger Vickers radial crack length for arm closest to Hertzian impression; (b) schematic, showing coordinate system used to evaluate macroscopic residual Hertzian stress field.

from Fig. 4, Part I, that the indentation stress–strain curve in our *C*-Si_3N_4 does not approach hardness saturation over the range of contact conditions covered).

Figure A1(a) shows a 100 N Vickers indentation made on the surface of a *C*-Si_3N_4 specimen previously indented with a WC sphere of radius $r = 1.98$ mm at a relatively high load $P = 4000$ N (cf. Fig. 4). Figure A1(b) indicates the coordinate system used to quantify the test. The Vickers indentation in Fig. A1 is located at a radial distance $d = 520$ μm from the center of Hertzian contact, relative to the impression radius $a = 333$ μm. The radial cracks at the corners of the Vickers indent show comparatively small asymmetry, $c_1 = 133$ μm vs $c_2 = 124$ μm.

To a first approximation, the radial and tangential components of the stress field around the residual contact field at radial distance $d > a$ are given by[29]

$$\sigma_r = -\sigma_a(a/d)^3, \qquad \sigma_t = \tfrac{1}{2}\sigma_a(a/d)^3 \tag{A-1}$$

where σ_a is the radial stress at the impression periphery, $d = a$. These macroscopic stresses contribute to the net stress-intensity factors on the Vickers radial cracks, superposing onto the residual stress term from the Vickers elastic–plastic field. Ignoring stress gradients along the radial crack lengths, we have

$$K = \chi_V P/c_1^{3/2} + \tfrac{1}{2}\psi_V\sigma_a(a/d)^3c_1^{1/2} = T_0 \tag{A-2a}$$

$$K = \chi_V P/c_2^{3/2} - \psi_V\sigma_a(a/d)^3c_2^{1/2} = T_0 \tag{A-2b}$$

at equilibrium, where χ is a material-dependent coefficient, the subscript V denoting the Vickers configuration. From measurements on 10 Vickers indentations under the same load conditions as specified in Fig. A1, but at various values of ratio d/a, Eqs. (A-2) yield $\sigma_a \approx -125 \pm 20$ MPa, which we consider negligible relative to the much larger values of *local* residual stresses about the shear faults (>1 GPa) referred to in the text.

Acknowledgment: We wish to thank Sataporn Wuttiphan, Irene M. Peterson, Kee Sung Lee, and Nitin P. Padture for helpful discussions.

References

[1]S. K. Lee, S. Wuttiphan, and B. R. Lawn, "Role of Microstructure in Hertzian Contact Damage in Silicon Nitride: I. Mechanical Characterization," *J. Am. Ceram. Soc.*, **80** [9] 2367–81 (1997).

[2]H. Makino, N. Kamiya, and S. Wada, "Effects of Grain Size of Hot-Pressed Silicon Nitride on Contact Damage Morphology and Residual Strength," *J. Am. Ceram. Soc.*, **74** [8] 2001–2004 (1991).

[3]B. R. Lawn, S. K. Lee, I. M. Peterson, and S. Wuttiphan, "A Model of Strength Degradation from Hertzian Contact Damage in Tough Ceramics," *J. Am. Ceram. Soc.*, in press.

[4]B. R. Lawn, S. M. Wiederhorn, and D. E. Roberts, "Effect of Sliding Friction Forces on the Strength of Brittle Materials," *J. Mater. Sci.* **19**, 2561–69 (1984).

[5]D. Tabor, *Hardness of Metals*. Clarendon, Oxford, U.K., 1951.

[6]B. R. Lawn, S. M. Wiederhorn, and H. Johnson, "Strength Degradation of Brittle Surfaces: Blunt Indenters," *J. Am. Ceram. Soc.*, **58** [9–10] 428–32 (1975).

[7]K. L. Johnson, *Contact Mechanics*. Cambridge University Press, London, U.K., 1985.

[8]S. Timoshenko and J. N. Goodier, *Theory of Elasticity*. McGraw-Hill, New York, 1951.

[9]B. R. Lawn and D. B. Marshall, "Nonlinear Stress–Strain Curves for Solids Containing Closed Cracks With Friction," *J. Mech. Phys. Solids*, **46** [1] 85–113 (1998).

[10]P. F. Becher, S. L. Hwang, H. T. Lin, and T. N. Tiegs, "Microstructural Contributions to the Fracture Resistance of Silicon Nitride Ceramics"; pp. 87–100 in *Tailoring of Mechanical Properties of Si_3N_4*. Edited by M. J. Hoffmann and G. Petzow. Kluwer Academic Publishers, Dordrecht, Netherlands, 1994.

[11]B. R. Lawn, *Fracture of Brittle Solids*. Cambridge University Press, Cambridge, U.K., 1993.

[12]C.-W. Li and J. Yamanis, "Super-Tough Silicon Nitride with *R*-Curve Behavior," *Ceram. Eng. Sci. Proc.*, **10** [7–8] 632–45 (1989).

[13]N. Ramachandran and D. K. Shetty, "Rising Crack-Growth-Resistance (*R*-Curve) Behavior of Toughened Alumina and Silicon Nitride," *J. Am. Ceram. Soc.*, **74** [10] 2634–41 (1991).

[14]C.-W. Li, D.-J. Lee, and S.-C. Lui, "*R*-Curve Behavior and Strength of *In Situ* Reinforced Silicon Nitride with Different Microstructures," *J. Am. Ceram. Soc.*, **75** [7] 1777–85 (1992).

[15]M. J. Hoffmann, "Analysis of Microstructural Development and Mechanical Properties of Si_3N_4"; pp. 59–72 in *Tailoring of Mechanical Properties of Si_3N_4*. Edited by M. J. Hoffmann and G. Petzow. Kluwer Academic Publishers, Dordrecht, Netherlands, 1994.

[16]C.-W. Li, S.-C. Lui, and J. Goldacker, "Relation Between Strength, Microstructure, and Grain-Bridging Characteristics in *In Situ* Reinforced Silicon Nitride," *J. Am. Ceram. Soc.*, **78** [2] 449–59 (1995).

[17]N. P. Padture and B. R. Lawn, "Contact Fatigue of a Silicon Carbide with a Heterogeneous Grain Structure," *J. Am. Ceram. Soc.*, **78** [6] 1431–38 (1995).

[18]N. P. Padture and B. R. Lawn, "Fatigue in Ceramics with Interconnecting Weak Interfaces: A Study Using Cyclic Hertzian Contacts," *Acta Metall.*, **43** [4] 1609–17 (1995).

[19]B. R. Lawn and T. R. Wilshaw, "Indentation Fracture: Principles and Applications," *J. Mater. Sci.*, **10** [6] 1049–81 (1975).

[20]B. R. Lawn and D. B. Marshall, "Hardness, Toughness, and Brittleness: An Indentation Analysis," *J. Am. Ceram. Soc.*, **62** [7–8] 347–50 (1979).

[21]K. E. Puttick, "Energy Scaling, Size Effects and Ductile–Brittle Transitions in Fracture," *J. Phys. D: Appl. Phys.*, **12**, L19–23 (1979).

[22]K. Puttick, "The Correlation of Fracture Transitions," *J. Phys. D: Appl. Phys.*, **13**, 2249–62 (1980).

[23]B. R. Lawn, E. R. Fuller, and S. M. Wiederhorn, "Strength Degradation of Brittle Surfaces: Sharp Indenters," *J. Am. Ceram. Soc.*, **59** [5–6] 193–97 (1976).

[24]S. J. Bennison, N. P. Padture, J. L. Runyan, and B. R. Lawn, "Flaw-Insensitive Ceramics," *Philos. Mag. Lett.*, **64** [4] 191–95 (1991).

[25]F. Guiberteau, N. P. Padture, H. Cai, and B. R. Lawn, "Indentation Fatigue: A Simple Cyclic Hertzian Test for Measuring Damage Accumulation in Polycrystalline Ceramics," *Philos. Mag.*, **A68** [5] 1003–16 (1993).

[26]H. Cai, M. A. S. Kalceff, B. M. Hooks, B. R. Lawn, and K. Chyung, "Cyclic Fatigue of a Mica-Containing Glass-Ceramic at Hertzian Contacts," *J. Mater. Res.*, **9** [10] 2654–61 (1994).

[27]A. Pajares, L. Wei, B. R. Lawn, and D. B. Marshall, "Damage Accumulation and Cyclic Fatigue in Mg-PSZ at Hertzian Contacts," *J. Mater. Res.*, **10** [10] 2613–25 (1995).

[28]H. H. K. Xu, L. Wei, N. P. Padture, B. R. Lawn, and R. L. Yeckley, "Effect of Microstructural Coarsening on Hertzian Contact Damage in Silicon Nitride," *J. Mater. Sci.*, **30**, 869–78 (1995).

[29]J. Selsing, "Internal Stresses in Ceramics," *J. Am. Ceram. Soc.*, **44** [8] 419 (1961). □

journal

J. Am. Ceram. Soc., 81 [8] 2061–70 (1998)

Effect of Starting Powder on Damage Resistance of Silicon Nitrides

Seung Kun Lee,*,† Kee Sung Lee,‡ and Brian R. Lawn*

Materials Science and Engineering Laboratory, National Institute of Standards and Technology, Gaithersburg, Maryland 20899

Do Kyung Kim*

Department of Materials Science and Engineering, Korea Advanced Institute of Science and Technology, Yusong, Taejon 305-701, Korea

The role of starting powder in the resistance of silicon nitride (Si_3N_4) ceramics to strength-impairing contact damage is studied. Si_2N_4 materials are prepared from three starting powders, at selectively increasing hot-pressing temperatures to coarsen the microstructures: (i) from relatively coarse α-phase powder, essentially equiaxed α-Si_3N_4 grains, with limited, slow transformation to β-Si_3N_4 grains toward the latter half of the temperature range; (ii) from relatively fine α-phase powder, a more rapid transformation to β-Si_3N_4, with attendant grain elongation; (iii) from fine β-phase powder, an essentially equiaxed β-Si_3N_4 structure over the entire temperature range. The resulting microstructures thereby provide a spectrum of β/α phase ratios and grain sizes and shapes for investigation. Indentations with hard spheres (Hertzian test) are used to induce damage into the Si_3N_4 specimens. Examination of the indentation sites indicates a competition between brittle and quasi-plastic damage modes: in structures with relatively equiaxed grains, the damage takes the form of classical cone cracking; in structures with large elongate grains, the damage is distributed beneath the contact as grain-localized microfailures within a subsurface "yield" zone. Bend tests on specimens containing single-cycle contact damage reveal those structures with well-developed cone cracks to be highly susceptible to strength degradation. The microstructures with the greatest resistance to strength loss are those formed from fine α-phase starting powder at intermediate firing temperatures (1700°C), with characteristic large, elongate β grains. Implications of the results in the context of other mechanical properties, e.g., toughness, wear, and fatigue resistance, are discussed.

I. Introduction

SILICON NITRIDE (Si_3N_4) has been studied extensively for two decades because of its attractive combination of mechanical properties, such as strength, toughness, and wear and fatigue resistance. It is recognized that microstructure is central to these mechanical properties.[1–13] Nevertheless, the role of microstructure remains poorly understood in Si_3N_4 ceramics, because of the complex interplay between such variables as grain size and aspect ratio, ratio of α to β phase, and composition of glassy second phase—generally, these microstructural variables tend to vary in an interdependent manner during the sintering process. When α-Si_3N_4 is used as a starting powder, transformations to β-Si_3N_4 during sintering result in pronounced grain elongation.[2,14,15] In turn, elongated grain structures give rise to enhanced long-crack toughness (strong *R*-curve).[5,7,10,11,13,16] However, this improvement in toughness does not usually extrapolate back to the domain of short cracks, where important properties like strength[17–20] and wear[21] are determined. In this light, there is a need for exploring routes to the microstructural design of Si_3N_4 for improved damage resistance properties at the microscale.

This paper investigates the specific roles of β/α phase ratio and grain size and shape on damage accumulation in Si_3N_4. We achieve control of these microstructural variables via the Si_3N_4 starting powders[11] (but keeping the composition of oxide sintering additives fixed) and by varying the sintering temperature. By choosing powders of different initial phase content and particle size, the following microstructures are produced with increasing temperature: from relatively coarse α-Si_3N_4 starting powder, a progressively coarsening, equiaxed α-Si_3N_4 structure, but with limited, slow transformation to β-Si_3N_4 toward the latter half of the temperature range; from relatively fine α-Si_3N_4 starting powder, a much more rapid transformation to β-Si_3N_4, with attendant grain elongation and coarsening; from fine β-Si_3N_4 starting powder, an essentially equiaxed β-Si_3N_4 structure over the entire temperature range, with progressive coarsening. Selected hot-pressing temperatures between 1570° and 1800°C provide a matrix of microstructures covering a spectrum of β/α ratios and grain geometries for systematic analysis.

To characterize damage accumulation of the Si_3N_4 microstructures we use indentations with spheres (Hertzian test). The Hertzian test has shown itself to be a powerful means of identifying and quantifying damage in ceramics,[22–26] including Si_3N_4.[20,27,28] It reveals in a most compelling manner the critical role of microstructure on the competition between classical cracking (ring, or cone fracture) and quasi-plastic damage (distributed shear-activated microfaulting).[29] Distinction between these two damage modes is directly relevant to applications where highly concentrated loads occur, e.g., in bearings. Indications are that the damage mode in Si_3N_4 progresses from cracking to quasi-plasticity as the microstructure coarsens and elongates,[20,27] and as the β/α ratio increases.[27] By examining these trends in the present structures we illustrate how crucial control of starting powders can be in the design of Si_3N_4 ceramics for damage resistance.

R. K. Bordia—contributing editor

Manuscript No. 190858. Received July 8, 1997; approved November 19, 1997.
Supported by the U.S. Air Force Office of Scientific Research and by the Korea Science and Engineering Foundation.
*Member, American Ceramic Society.
†Guest Scientist from the Department of Materials Science and Engineering, Lehigh University, Bethlehem, Pennsylvania 18015. Now at Advanced Materials Technology, Technical Center, Caterpillar Inc., Mossville, Illinois 61552.
‡Graduate student in the Department of Materials Science and Engineering, Korea Advanced Institute of Science and Technology, Yusong, Taejon 305-701, Korea.

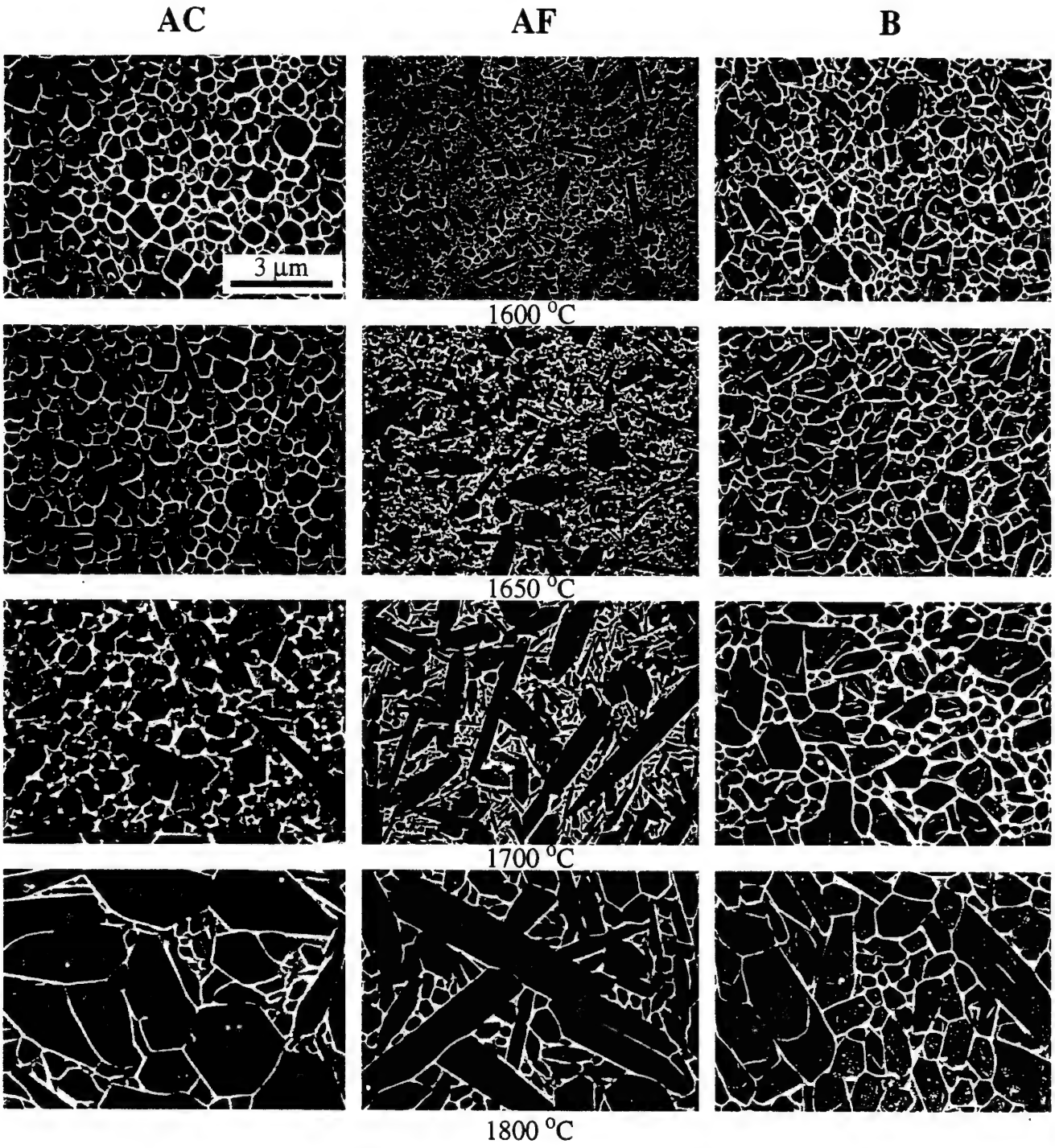

Fig. 1. SEM micrographs of Si_3N_4 polished surfaces, fired at 1600°, 1650°, 1700°, and 1800°C for 1 h. Specimen designation as follows: **AC** (E3 powder, α phase, coarse); **AF** (E10 powder, α phase, fine); **B** (KSN-80SP powder, β phase). Specimens plasma etched in CF_4 and O_2 gas for 10 min to reveal grain structures.

II. Experimental Procedure

(1) Materials Processing and Preparation

Three starting silicon nitride powders were used: relatively coarse α-Si_3N_4 (UBE-SN-E3, mean particle size 1.0 μm, Ube Industries, Tokyo, Japan), with ≈5 vol% β-Si_3N_4; relatively fine α-Si_3N_4 (UBE-SN-E10, mean particle size 0.3 μm, Ube Industries, Tokyo, Japan), again with ≈5 vol% β-Si_3N_4; and β-Si_3N_4 (KSN-80SP, mean particle size 0.5 μm, ShinEtsu, Tokyo, Japan), with ≈20 vol% α-Si_3N_4. Sintering additives, 5 wt% Y_2O_3 (Fine Grade, H. C. Starck GmbH, Goslar, Germany), 2 wt% Al_2O_3 (AKP50, Sumitomo Chemical Co. Ltd., Tokyo, Japan), and 1 wt% MgO (High Purity, Baikowski Co., NC), were mixed with each starting powder. The mixed batches were ground as slurries in 2-propanol for 24 h in a planetary mill using zirconia balls in a polypropylene container. After drying, the softly agglomerated powders were crushed and sieved through a 60-mesh screen. These resulting mixes were designated according to the Si_3N_4 starting powders: **AC** (E3 powder, α phase, coarse); **AF** (E10 powder, α phase, fine); **B** (KSN-80SP powder, β phase).

Hot pressing of sample blocks with 50 mm diameter and 5 mm thickness from each powder batch was performed in nitrogen gas at 1 atm under uniaxial compression 30 MPa in

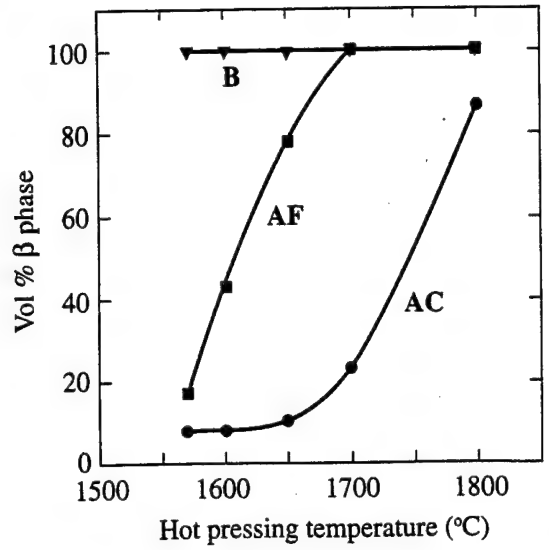

Fig. 2. XRD determination of volume fractions of β and α phases in **AC**, **AF**, and **B** Si_3N_4 (see Fig. 1), as function of hot-pressing temperature.

a graphite die, at 1570°, 1600°, 1650°, 1700°, and 1800°C for 1 h. Top and bottom surfaces of the fired blocks were ground on a diamond wheel, and the blocks diamond sawn into bars 25 mm × 4 mm × 3 mm for evaluation and testing.

Specimen surfaces were polished normal to the hot-press direction to 1 μm finish for characterization. These surfaces were plasma etched to highlight the grain structures. After gold coating, the etched surfaces were examined by scanning electron microscopy (SEM), and grain sizes and shapes determined from micrographs using an image analyzer (Bioscan OPTIMAS 4.1, Bioscan Inc., Edmonds, WA), as follows: mean grain sizes, from linear intercepts over all grain boundaries; aspect ratios, as length/width of the 10% largest elongate β grains;[14] volume fractions, from grain area determinations of all β grains with aspect ratio ≥3.[12] X-ray diffraction (XRD) was used to determine the β/α phase ratio for each material.

Densities were measured using the Archimedes method.

(2) Mechanical Testing

Hertzian contact tests were made on polished Si_3N_4 surfaces to determine damage characteristics.[27] In these tests, tungsten carbide (WC) spheres of radius r = 1.98 mm were used at peak loads up to P = 4000 N and at fixed crosshead speed 1.67 μm·s^{-1}. The WC spheres themselves tended to deform during indentation,[30] so were constantly rotated and ultimately replaced. Section views of the damage patterns were obtained using bonded-interface specimens.[23,24] These specimens were prepared by bonding together two polished half-bars at a common interface with a thin layer of adhesive, and then polishing the top surfaces. Rows of indentations were then made on these top surfaces, symmetrically along the surface trace of the bonded interface. The adhesive was dissolved in acetone, and the top and side surfaces of the separated half-blocks gold coated for optical examination in Nomarski illumination. Supplementary observations of the damage were made using SEM to determine the basic nature of the cracking and quasi-plasticity in relation to the microstructure.[20]

Additional indentation tests were made with the same WC spheres on polished surfaces of each of the Si_3N_4 materials, to obtain critical loads for "yield," P_Y, and for cracking, P_C. The critical configurations were determined by examining the postindented surfaces over a range of loads, and searching for the signs of first damage.[27] Nomarski examination of surfaces

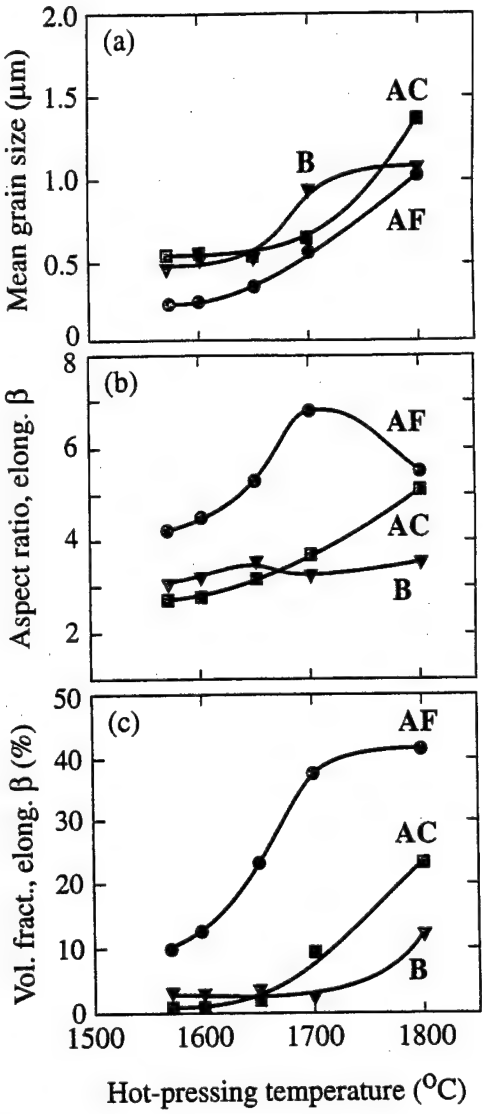

Fig. 3. Microstructural characterization of **AC**, **AF**, and **B** Si_3N_4 materials as function of hot-pressing temperature: (a) mean grain size, (b) aspect ratio of largest 10% elongate β grains, (c) volume fraction of elongate β grains with aspect ratio >3.

gold-coated after indentation was again used for this purpose. Acoustic detectors were also useful for detecting the critical pop-in load for full cone cracks.[27]

Strength tests were made on sets of Si_3N_4 specimens fired at 1700°C, to quantify the degrading effects of the contact damage.[28] Four-point bend tests were made on polished and prechamfered bars (25 mm × 4 mm × 3 mm, inner span 10 mm and outer span 20 mm), with the indented surfaces on the tensile side. The contact damage itself was made over a load range P = 0–4000 N. Specimens were covered by a drop of silicon oil before testing, and were broken in fast fracture (<10 ms), to avoid the influence of moisture ("inert" strengths). Broken specimens were examined fractographically in Nomarski illumination to locate the source of failure, i.e., indentations or other sites.

Routine measurements of Young's modulus (sonic method) and hardness (load/projected area, Vickers indenter[31]) were carried out on these specimens.

III. Results

(1) Materials Characterization

Results of the microstructural characterization are shown in Figs. 1–3. Figure 1 shows scanning electron microscopy (SEM)

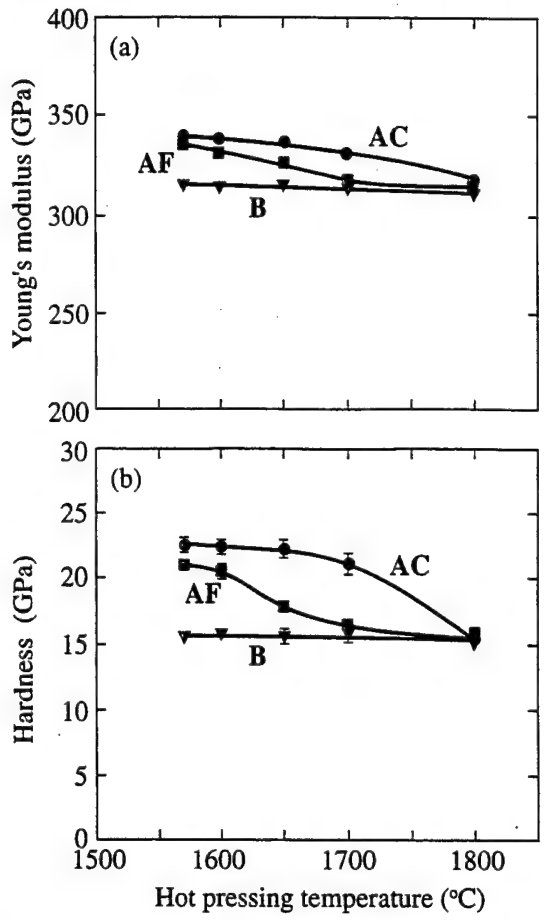

Fig. 4. Plot of (a) Young's modulus and (b) hardness of **AC**, **AF**, and **B** Si_3N_4 materials as function of hot-pressing temperature.

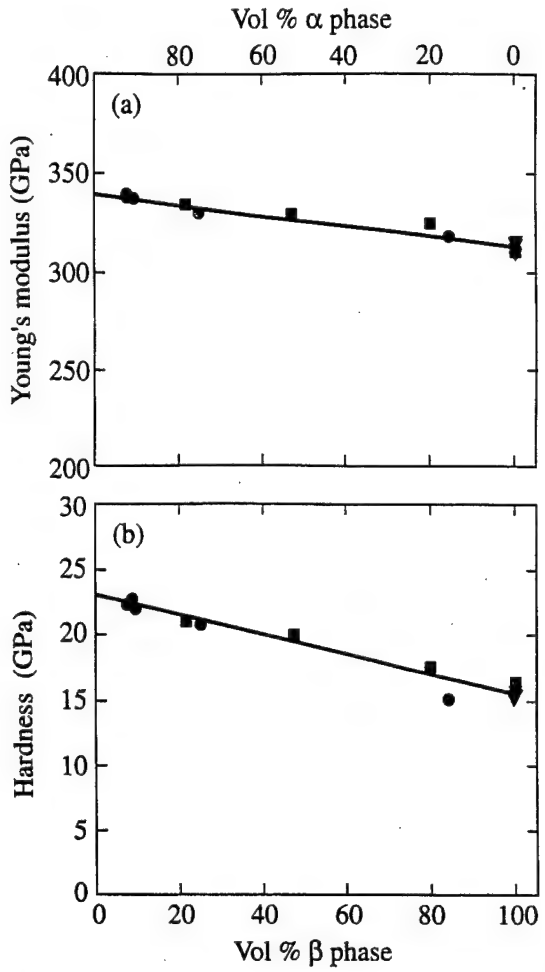

Fig. 5. Replot of (a) Young's modulus and (b) hardness data from Fig. 4 as function of volume fractions of β and α phases.

micrographs of the different Si_3N_4 microstructures for each starting powder:

(i) **AC** Si_3N_4. After hot pressing at 1600°C, this material reveals a microstructure with mainly equiaxed α grains of mean grain size ≈0.6 μm, but with minor β phase. At 1650°C, the equiaxed α grains are larger, but occasional elongate β grains are now apparent. At 1700°C, the β grains continue their elongated growth, but the α phase still dominates. Finally, at 1800°C, the β phase dominates, but the structure is again predominantly equiaxed.

(ii) **AF** Si_3N_4. At 1600°C, the material contains mainly equiaxed α grains of mean grain size ≈0.2 μm, but some elongated β grains are already apparent. At 1650°C these β grains have continued their elongate growth, but at a much faster rate than in **AC** Si_3N_4; the smaller α grains have also begun to transform to β phase. At 1700°C, the β phase is dominant. At 1800°C, the β grains enlarge further, as in **AC**, but remain elongate.

(iii) **B** Si_3N_4. At 1600°C, the structure consists totally of equiaxed β grains, mean grain size ≈0.5 μm. On heating through 1800°C, the β phase persists, and the microstructures enlarge but remain predominantly equiaxed with just occasional elongate grains.

Density determinations indicate a porosity level <0.1% in all microstructures in Fig. 1.

Figure 2 plots volume percent β and α phase for the three Si_3N_4 starting powder types as a function of hot-pressing temperature, from XRD. In **AC** Si_3N_4 an α → β transformation takes place, but is relatively sluggish, accelerating only above 1700°C (note that some α phase remains even at 1800°C). The same transformation occurs in **AF** Si_3N_4, but much more rapidly, reaching completion at 1700°C. There is no detectable phase transformation at all in **B** Si_3N_4; the β phase dominates over the entire temperature range.

Mean grain sizes and aspect ratios are plotted for the Si_3N_4 materials as a function of hot-pressing temperature in Fig. 3. Overall mean grain sizes (Fig. 3(a)) increase steadily with temperature in all three materials. Aspect ratios (Fig. 3(b)) and volume fractions (Fig. 3(c)) of the elongate β grains increase strongly with temperature in the **AF** material to 1700°C, and increase only slightly, above 1700°C, in the **B** material, with **AC** intermediate. Note especially the dominant population of elongate β grains in **AF** at 1700°C.

Figure 4 plots Young's modulus and hardness against hot-pressing temperature for each material. Both modulus (Fig. 4(a)) and hardness (Fig. 4(b)) decline with temperature: in **AC** Si_3N_4, starting with relatively high values at 1570°C, declining only slightly between 1570° and 1700°C, and finally falling off between 1700° and 1800°C; in **AF** Si_3N_4, starting a little lower at 1570°C, but declining much more quickly, and approaching a similar reduced level at 1700°C; in **B** Si_3N_4, starting low and staying low over the temperature range. Noting the (inverse) correlation of the curves in Fig. 4 with those in Fig. 2, we replot the modulus and hardness data as a function of phase content in Fig. 5. The results are consistent with a "rule of mixtures": for modulus (Fig. 5(a)), between extrapolation limits of high-modulus α phase (340 GPa) and low-modulus β phase (312 GPa);[32] for hardness (Fig. 5(b)), between extrapolation limits of high-hardness α phase (23.1 GPa) and low-hardness β phase (15.5 GPa).[33] Note that whereas the trends are similar in Figs. 4 and 5, the rate of decline relative to temperature is considerably faster in the hardness than in the modulus.

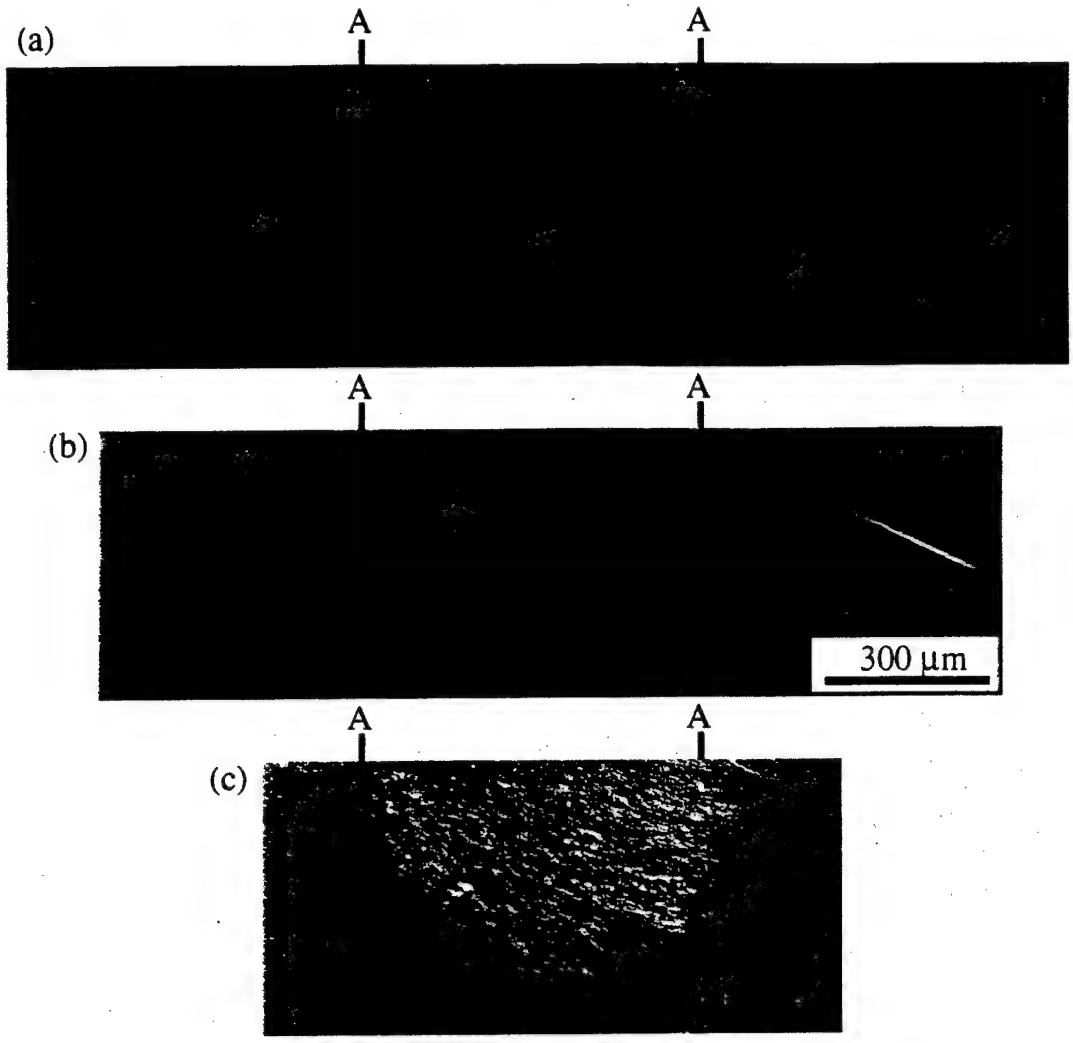

Fig. 6. Side views of Hertzian contact damage in **AC** Si_3N_4, fired at (a) 1650°, (b) 1700°, and (c) 1800°C. Indentations made using WC sphere radius r = 1.98 mm at load P = 4000 N. AA denotes contact diameter. Nomarski optical micrographs of bonded-interface specimens.

(2) Contact Damage

Figures 6–8 illustrate bonded-interface section views of contact damage formed at a relatively high load P = 4000 N, for the Si_3N_4 materials fired at 1650°, 1700°, and 1800°C:

(i) **AC** Si_3N_4, Fig. 6. (a) 1650°C—a classical cone crack forms outside the contact, indicative of a highly brittle material, and signs of minor quasi-plasticity damage are just visible beneath the contact; (b) 1700°C—the cone crack persists, but is smaller, and the quasi-plastic zone, although still comparatively minor, is more apparent; (c) 1800°C—only a barely visible shallow surface ring crack persists (more evident in surface views, not shown), but the quasi-plasticity zone is now well developed.[27]

(ii) **AF** Si_3N_4, Fig. 7. (a) 1650°C—a much shortened cone crack, and already a substantial quasi-plasticity zone, are apparent; (b) 1700°C—the damage zone is well developed, and only the vestigial trace of a surface ring crack remains; (c) 1800°C—the shallow ring crack is no longer visible in the section view (although, again, is evident in surface views), and the quasi-plasticity is now totally dominant. The "brittle–ductile" transition evident in this **AF** sequence is therefore similar to that in **AC**, but occurs much more rapidly.

(iii) **B** Si_3N_4, Fig. 8. (a) 1650°C—*both* cone cracking and quasi-plasticity zones are already well developed; (b) 1700°C—the cone cracking is reduced, and the quasi-plasticity further enhanced; (c) 1800°C—only shallow ring crack traces remain, and the plastic zone is dominant. The quasi-plasticity is more developed than in either **AC** or **AF**, and the cone cracking as strongly developed as in **AC**, foreshadowing a highly damage-susceptible material.

SEM observations confirmed previous observations of the microstructural nature of the damage processes: the cone and ring cracks in Figs. 6–8 were predominantly (>75%) intergranular;[27] and the quasi-plasticity zone consisted of individual shear faults at the grain boundaries, with some indication of some shear faulting within some of the elongate β grains.[20]

Figure 9 plots critical loads for yield, P_Y, and cracking, P_C, as a function of hot-pressing temperature. (Note that these P_Y and P_C data all lie below the value P = 4000 N used to produce the damage patterns in Figs. 6–8.) In Fig. 9(a), P_Y decreases steadily with firing temperature for **AC** and **AF** Si_3N_4, ultimately to the temperature-insensitive low value for **B** Si_3N_4. These temperature dependencies are broadly similar to those for the hardness (Fig. 4(b)), consistent with the well-documented interrelationship between yield stress and hardness.[30,31] This in turn implies a fundamental correlation between yield properties and β/α phase ratio (Fig. 5(b)). In Fig. 9(b), P_C increases only slightly with firing temperature (recall that the cracks contract from well-developed cones to very shallow surface rings at the higher temperatures). Values of P_C are highest for **AF**, lowest for **B**. These trends in the P_C data correlate with density of elongate β grains (Fig. 3(b) and (c)), consistent with the dominance of a microstructural geometry factor in the cone crack initiation.[27]

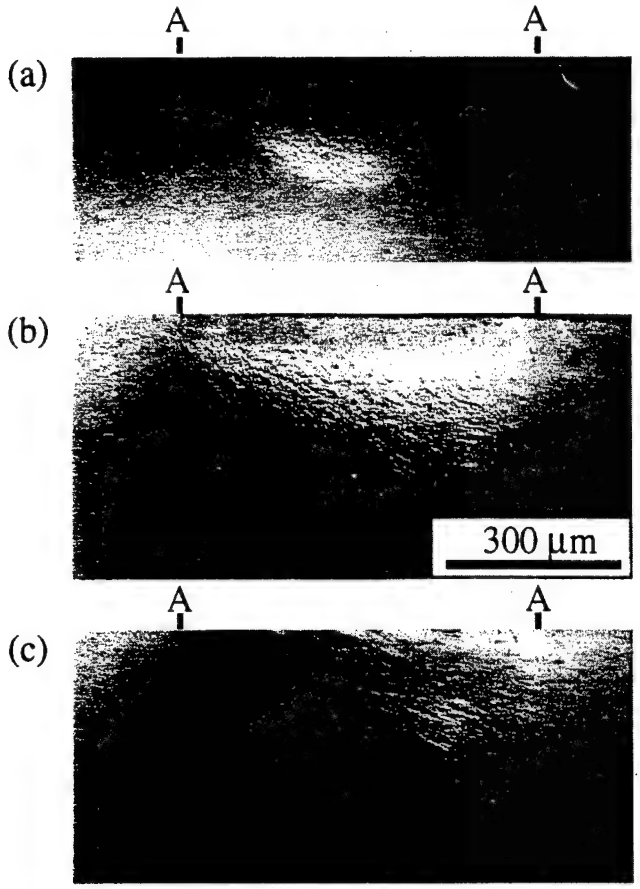

Fig. 7. Side views of Hertzian contact damage in **AF** Si_3N_4, fired at (a) 1650°, (b) 1700°, and (c) 1800°C. Indentations made using WC sphere radius r = 1.98 mm at load P = 4000 N. AA denotes contact diameter. Nomarski optical micrographs of bonded-interface specimens.

Figure 10 shows characteristic tensile-surface fracture patterns for **AF**, **AC**, and **B** Si_3N_4 bend-test specimens fired at 1700°C and damaged at contact load P = 4000 N:[28,34] in **AC** and **B**, fracture traces outside the ring-crack peripheries, corresponding to failures from subsurface cone-crack fronts (Figs. 10(a) and (c)); in **AF**, fracture traces orthogonal to the surface ring cracks, corresponding to failures from subsurface quasi-plastic zones (Fig. 10(b)) (in this case, the accompanying shallow ring cracks play no role). Figure 11 plots strength degradation data as a function of contact load P for the same materials. In each material the strengths remain undiminished at subcritical loads, indicating failures from natural flaws. Beyond critical loads, P_C for **AC** and **B**, $P_D \approx 2P_Y$ for **AF**[34] (see Fig. 9 at 1700°C) the strengths fall off slowly—solid curves in this region are data fits from fracture mechanics models (Appendix).

IV. Discussion

In the present study we have investigated the role of starting powder on Si_3N_4 microstructures (Figs. 1–5), and the relationship of these microstructures to damage accumulation in contacts with spheres (Figs. 6–10). We have shown that by controlling the starting powders and firing temperatures we can produce microstructures with different ratios of β to α phase (Fig. 2), and different grain sizes, shapes, and volume fractions of each phase (Fig. 3). These crystallographic and geometrical microstructural elements determine the competition between fracture (ring cracking) and deformation (diffuse quasi-plasticity) in concentrated stress fields. Specifically, for coarser, predominantly α-phase starting powder (**AC**), we produce steadily coarsening structures that retain their α-phase identity up to about 1700°C, with significant transformation to β phase only above this temperature. This material tends to be highly susceptible to cone cracking, with major quasi-plasticity only in specimens fired above 1700°C (Fig. 6). For finer α-phase powder (**AF**), the structures again coarsen, but much more rapidly with respect to temperature, and with larger volume fractions of elongate β grains. This material shows suppressed cracking and enhanced quasi-plasticity over the entire temperature range (Fig. 7). For the β-phase starting powder (**B**), the structures once more coarsen with temperature, although relatively slowly, and with retention of the β-phase identity throughout. Thus this material is highly susceptible to both fracture and deformation (Fig. 8).

It is of interest to identify more closely those elements of the Si_3N_4 microstructure that govern the deformation and fracture modes. Note that subsurface quasi-plasticity zones are equally well developed in all three materials at 1800°C in Figs. 6–8. (Recall that the hardnesses in Fig. 4(b) and critical loads P_Y in Fig. 9(a) each attain near-identical low values at this temperature.) The microstructural feature most closely common to the three materials at 1800°C is the near-saturation β content in Fig. 2. By contrast, there is no such commonality of grain size, shape, or density at 1800°C in Fig. 3. At 1650°C, the incidence of quasi-plasticity is barely lessened in the **B** material, but is substantially reduced in **AF** and even more in **AC**, consistent with reduced content of the relatively soft β phase in Fig. 2. For the fracture mode, we note that cone cracks are equally well developed in two of the materials at 1650°C, **B** and **AC**, and relatively suppressed in **AF**, in Figs. 6–8. (Also, the critical loads P_C in Fig. 9(b) are highest for **AF** at this temperature.) In this case there is no correlation between material order and β content in Fig. 2. On the other hand, **AF** has by far the most elongate β-grain shape in Fig. 3(b) and density in Fig. 3(c), if not the largest mean grain size in Fig. 3(a). At higher temperatures, cone cracking diminishes in all three materials, most abruptly between 1700° and 1800°C, where the density of β grains in Fig. 3(c) increases. We conclude that it is β content which constitutes the primary controlling factor in the quasi-plasticity mode, and β grain geometry in the fracture mode.

An important consideration in bearing and other stress-concentrating applications is retention of strength after the introduction of contact-related damage. The plots in Fig. 11 for the Si_3N_4 materials fired at 1700°C indicate that it is the **AF** structure that is most immune to strength degradation. That is because only shallow ring cracks form in this structure at and above 1700°C (Figs. 7(b) and 9(b)). In this context, the relative proliferation of large elongate β grains in the **AF**(1700) material (Fig. 1) is a key feature. It has been argued in an earlier study[27] that suppression of full cone fracture initiation in coarse, heterogeneous polycrystalline ceramics with intergranular fracture is attributable, at least in part, to intergranular deflection of the downward propagating ring cracks away from the trajectories of maximum tensile stresses in the contact field by such long grains. As we have intimated, the damage in **AF**(1700) (Fig. 7(b)) is instead distributed as highly stabilized, grain-localized shear faults within a dominant quasi-plasticity zone. Failure then occurs from one such fault within this zone, at a contact load P sufficiently in excess of P_Y to grow this fault to a dominant size (Appendix).[28,34] Ultimately, at excessive loads, or at a sufficiently large number of repeated contacts, microcrack coalescence may occur within the quasi-plastic zone, with reduction in strength to a level approximately equal to that for failure from cone cracks.[34] Nevertheless, for the single-cycle load range considered here, **AF** produced from the finer α-phase powder appears to be the Si_3N_4 material of choice for superior strength properties.

Our conclusions concerning the central role of microstructure on contact damage and associated strength degradation also have strong implications concerning mechanical properties like toughness and wear and fatigue resistance. Correlations between quasi-plastic contact damage and toughness have been

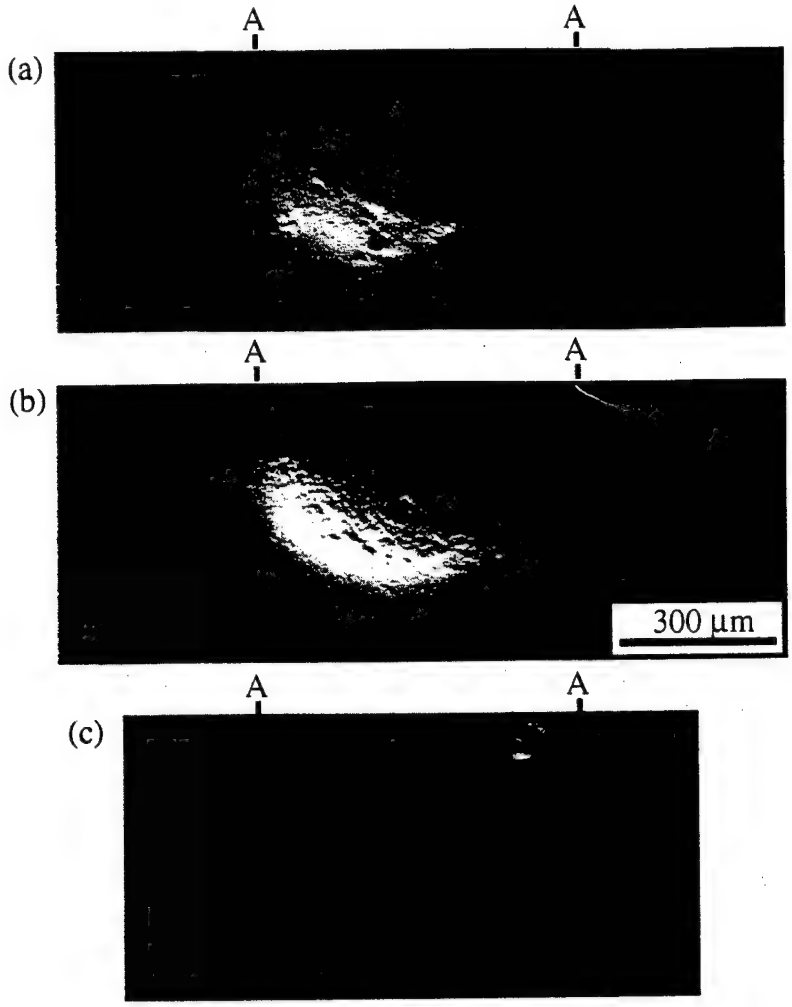

Fig. 8. Side views of Hertzian contact damage in **B** Si_3N_4, fired at (a) 1650°, (b) 1700°, and (c) 1800°C. Indentations made using WC sphere radius r = 1.98 mm at load P = 4000 N. AA denotes contact diameter. Nomarski optical micrographs of bonded-interface specimens.

noted in an earlier study.[27] There it was shown that reductions in the size of any well-developed cone cracks from microstructural coarsening and elongation can be attributed to enhancement of the underlying *R*-curve (hence long-crack toughness), via increased grain bridging.[16] Other groups[7,10–13] have demonstrated this link between microstructural heterogeneity and *R*-curve behavior even more compellingly. The connection between contact damage and toughness is not superficial: it is the same microstructural features responsible for steep *R*-curves (large and elongate grains, weak grain or interphase boundaries) that promote quasi-plasticity in the contact damage response, via weakness on the microscale.[29] The combination of suppressed cone cracking and limited quasi-plasticity evident for **AF** Si_3N_4 in Fig. 7 indicates that the microstructures sintered from the finer α-phase powder, because of their relatively pronounced microstructural heterogeneity, are the best suited of our materials for high toughness applications. At the same time, as noted for **B** Si_3N_4 in Fig. 8, it is possible to fabricate microstructures with both extensive quasi-plasticity *and* large cone cracks, so the existence of an extensive yield zone does not itself necessarily lead to high toughness—recall from Figs. 1 and 3(b) that the **B** material does not contain the elongate grains generally so effective in enhancing toughness.

From the standpoint of wear and fatigue, it is avoidance of quasi-plasticity (and only to a lesser extent ring cracking) that is important, because distributed microfailure damage can lead to easy removal of material on the microscale.[21,35–37] This suggests that the high modulus and hardness **AC** Si_3N_4 developed from coarser α-phase powder (Fig. 4) may be best suited for maximum wear and fatigue resistance.

Finally, we would emphasize that we have considered only two processing variables, starting powder and firing temperature. There are other important variables, most notably type and amount of additive oxides, that can have profound influences on the microstructural complexion of Si_3N_4 ceramics, especially on the composition of the oxynitride glassy phase.[10,11] More detailed and systematic investigations of chemical and geometrical aspects of the processing and microstructural characterization, in the special context of tailoring damage properties for specific applications, constitute a ripe area for further study.

APPENDIX

Fracture Mechanics Models for Failure from Indentation Cone Crack and Quasi-Plastic Damage Sites in Strength Tests

In this appendix we apply previously described fracture mechanics models for failure from cone cracks and quasi-plasticity zones[28,34] to fit the strength data in the region where breaks occur from indentation sites in Fig. 10.

(1) Failure from Cone Crack Sites

For the **AC** and **B** Si_3N_4 materials, failure occurs from cone cracks (Fig. 12). This kind of failure is governed by the following three simultaneous relations:[34]

(i) A geometrical relation connecting the dimension c of the actual ring crack to the dimension C of a "virtual" cone with its tip located above the contact surface,

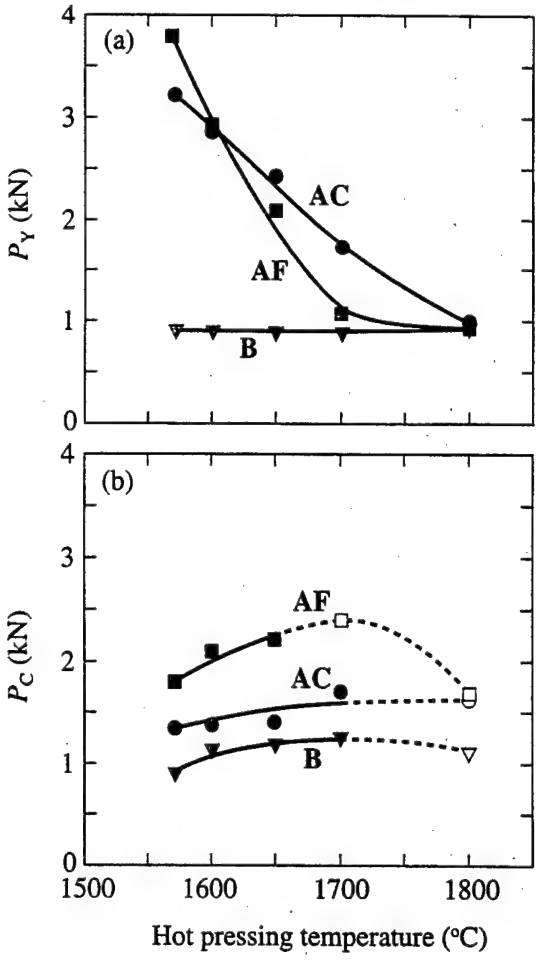

Fig. 9. Critical loads for indentation-induced damage as function of hot-pressing temperature, in **AC**, **AF**, and **B** Si_3N_4 materials: (a) P_Y for quasi-plastic damage; (b) P_C for ring cracking. Indentations made using WC sphere radius r = 1.98 mm. In (b), open symbols and solid curves denote full cone cracks, closed symbols and dashed curves denote very shallow surface ring cracks only.

$$C = c + R_0/\cos\alpha_0 \tag{A-1}$$

with R_0 the surface ring radius and α_0 the angle between cone crack and specimen surface (Fig. 12).

(ii) For materials governed by a single-valued toughness $K_{IC} = T_0$, an equilibrium stress-intensity factor relation for pennylike cracks,[38]

$$K = \chi P/C^{3/2} = T_0 \tag{A-2}$$

with χ a crack geometry coefficient. The parameter χ is calibrated from measurements of equilibrium cone crack lengths at given loads (e.g., Figs. 6 and 8), using $C = (\chi P/T_0)^{2/3}$.

(iii) The Griffith strength relation

$$\sigma_F = T_0/\Psi c^{1/2} \tag{A-3}$$

with Ψ a geometry coefficient determined from consideration of the cone crack geometry.[39]

The following parameters in Eqs. (A-1) to (A-3) are predetermined for **AC** and **B** Si_3N_4 (1700°C) as follows:

(i) In Eq. (A-1), cone angle α_0 = 19°, and surface inner ring crack radius R_0 = 238 μm (**AC**) and 226 μm (**B**), from section micrographs (e.g., Figs. 6 and 8).

(ii) Coefficients in Eqs. (A-2) and (A-3), χ = 0.0154 and Ψ = 0.71, from previous calibration on Si_3N_4 materials with similar cone crack geometry.[27,28]

(iii) In Eq. (A-3), toughness $K_{IC} = T_0$ = 4.2 MPa·m$^{1/2}$ (**AC**) and 3.0 MPa·m$^{1/2}$ (**B**), from independent measurements of radial cracks at Vickers indentations.[40]

The resulting calculated functions $\sigma_F(P)$ are included as the solid curves for **AC** Si_3N_4 and **B** Si_3N_4 in Fig. 11.

(2) Failure from Quasi-Plasticity Sites

For the **AF** Si_3N_4 material, failure occurs from "wing" cracks[41–43] associated with individual shear faults within the quasi-plasticity zones (Fig. 12).[34] This type of failure is governed by the strength relation[34]

$$\sigma_F = \sigma_0[(P_D^{1/3} - P_Y^{1/3})/(P^{1/3} - P_Y^{1/3})]^{1/3} \quad (P > P_D > P_Y) \tag{A-4}$$

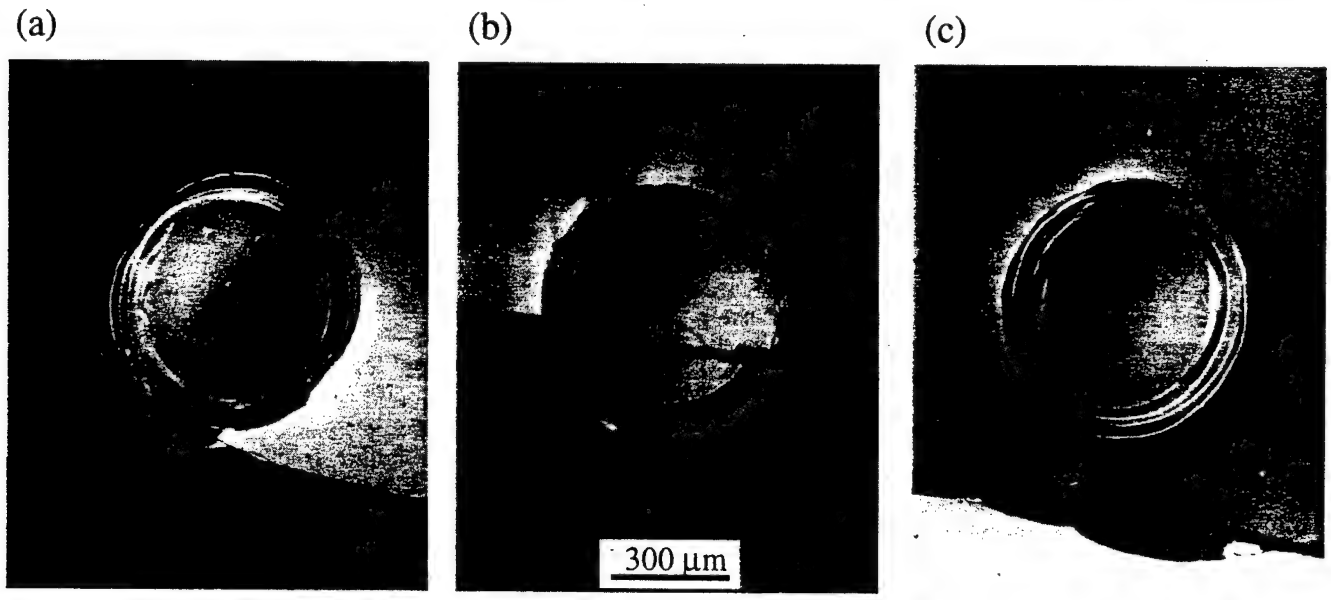

Fig. 10. Micrographs showing failure of (a) **AC**, (b) **AF**, and (c) **B** Si_3N_4 materials fired at 1700°C, from strength specimens containing indentations made with WC sphere, r = 1.98 mm, P = 4000 N. Nomarski illumination, surface gold coated. Tensile direction vertical in plane of diagram.

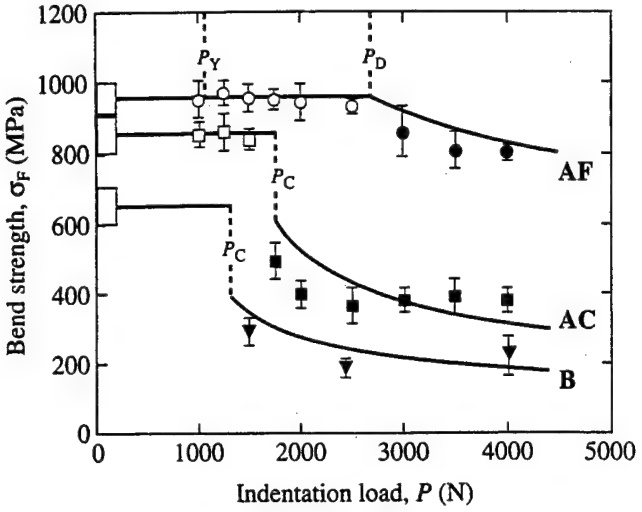

Fig. 11. Strength degradation for **AC**, **AF**, and **B** Si_3N_4 materials fired at 1700°C, for contacts with WC sphere, r = 1.98 mm. Open symbols indicate failures away from indentation sites, gray symbols failures from quasi-plastic zones, black symbols failures from ring cracks. Points with error bars represent means and standard deviations of a minimum of five specimens; points without error bars are individual breaks. Boxes at left axis denote natural strengths (unindented specimens). Vertical dashed lines indicate critical loads for strength-degrading damage (see Fig. 9).

where P_Y is the critical load for yield (Fig. 9(a), 1700°C), σ_0 is the natural strength (no indentation damage), and $P = P_D$ at $\sigma_F = \sigma_0$ is the load at which breaks first occur from the quasi-plasticity zone.

The solid curve for **AF** Si_3N_4 in Fig. 11 is obtained by inserting σ_0 = 960 MPa, P_Y = 1100 N, and P_D = 2700 N from a direct fit to the data.

Acknowledgments: We wish to thank H. H. K. Xu and I. M. Peterson for discussions.

References

[1]F. F. Lange, "Relation Between Strength, Fracture Energy, and Microstructure of Hot-Pressed Si_3N_4," *J. Am. Ceram. Soc.*, **59** [10] 518–22 (1973).

[2]F. F. Lange, "Fracture Toughness of Si_3N_4 as a Function of the Initial α-Phase Content," *J. Am. Ceram. Soc.*, **62** [7–8] 428–30 (1979).

[3]G. Himsolt, H. Knoch, H. Huebner, and F. W. Kleinlein, "Mechanical Properties of Hot-Pressed Silicon Nitride with Different Grain Structures," *J. Am. Ceram. Soc.*, **62** [1–2] 29–32 (1979).

[4]G. Wötting and G. Ziegler, "Influence of Powder Properties and Processing Conditions on Microstructure and Mechanical Properties of Sintered Si_3N_4," *Ceram. Int.*, **10** [1] 18–22 (1984).

[5]C.-W. Li and J. Yamanis, "Super-Tough Silicon Nitride with *R*-Curve Behavior," *Ceram. Eng. Sci. Proc.*, **10** [7–8] 632–45 (1989).

[6]T. Kawashima, H. Okamoto, H. Yamamoto, and A. Kitamura, "Grain Size Dependence of the Fracture Toughness of Silicon Nitrides Ceramics," *J. Ceram. Soc. Jpn.*, **99**, 1–4 (1991).

[7]C.-W. Li, D.-J. Lee, and S.-C. Lui, "*R*-Curve Behavior and Strength of *In Situ* Reinforced Silicon Nitride with Different Microstructures," *J. Am. Ceram. Soc.*, **75** [7] 1777–85 (1992).

[8]N. Hirosaki and Y. Akimune, "Effect of Grain Growth of β-Silicon Nitride on Strength, Weibull Modulus, and Fracture Toughness," *J. Am. Ceram. Soc.*, **76** [7] 1892–94 (1993).

[9]A. J. Pyzik and D. R. Beaman, "Microstructure and Properties of Self-Reinforced Silicon Nitride," *J. Am. Ceram. Soc.*, **76** [11] 2737–44 (1993).

[10]P. F. Becher, S. L. Hwang, H. T. Lin, and T. N. Tiegs, "Microstructural Contributions to the Fracture Resistance of Silicon Nitride Ceramics"; pp. 87–100 in *Tailoring of Mechanical Properties of Si_3N_4*. Edited by M. J. Hoffmann and G. Petzow. Kluwer Academic Publishers, Dordrecht, Netherlands, 1994.

[11]M. J. Hoffmann, "Analysis of Microstructural Development and Mechanical Properties of Si_3N_4"; pp. 59–72 in *Tailoring of Mechanical Properties of Si_3N_4*. Edited by M. J. Hoffmann and G. Petzow. Kluwer Academic Publishers, Dordrecht, Netherlands, 1994.

[12]P. Sajgalik, J. Dusza, and M. J. Hoffmann, "Relationship between Microstructure, Toughness Mechanisms, and Fracture Toughness of Reinforced Silicon Nitride Ceramics," *J. Am. Ceram. Soc.*, **78** [10] 2619–24 (1995).

[13]C.-W. Li, S.-C. Lui, and J. Goldacker, "Relation Between Strength, Microstructure, and Grain-Bridging Characteristics in *In Situ* Reinforced Silicon Nitride," *J. Am. Ceram. Soc.*, **78** [2] 449–59 (1995).

[14]M. Mitomo, M. Tsutsumi, H. Tanaka, S. Uenosono, and F. Saito, "Grain Growth During Gas-Pressure Sintering of β-Silicon Nitride," *J. Am. Ceram. Soc.*, **73** [8] 2441–45 (1990).

[15]M. Mitomo and S. Uenosono, "Microstructural Development During Gas-Pressure Sintering of α-Silicon Nitride," *J. Am. Ceram. Soc.*, **75** [1] 103–108 (1992).

[16]P. L. Swanson, C. J. Fairbanks, B. R. Lawn, Y.-W. Mai, and B. J. Hockey, "Crack-Interface Grain Bridging as a Fracture Resistance Mechanism in Ceramics: I, Experimental Study on Alumina," *J. Am. Ceram. Soc.*, **70** [4] 279–89 (1987).

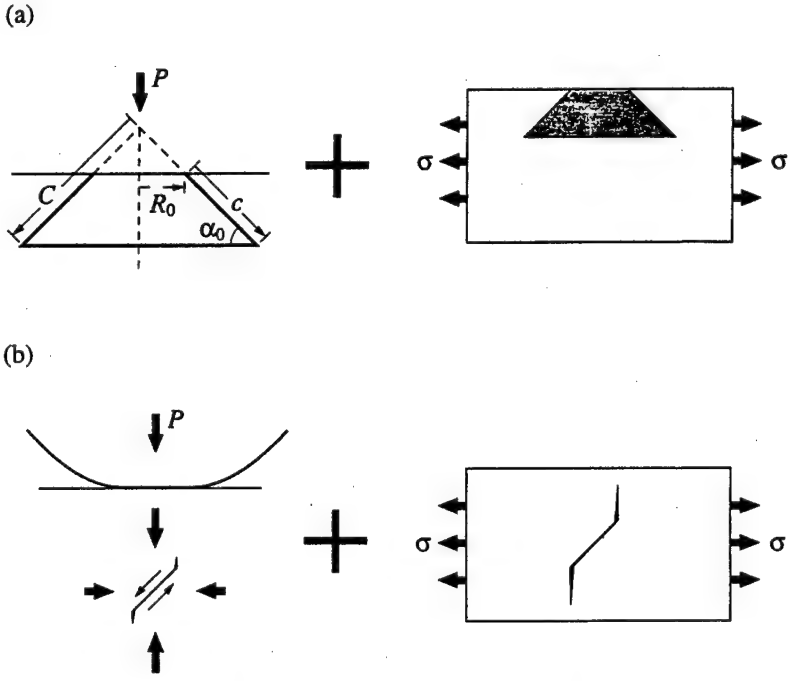

Fig. 12. Schematic showing critical flaws induced by contact with spherical indenter (left), and subsequent strength tests on indented specimens (right): (a) brittle response, failure from fully developed cone crack; (b) quasi-plastic response, failure from shear fault with wing crack within damage zone. After Refs. 28 and 34.

[17]S. J. Bennison and B. R. Lawn, "Role of Interfacial Grain-Bridging Sliding Friction in the Crack-Resistance and Strength Properties of Nontransforming Ceramics," *Acta Metall.*, **37** [10] 2659–71 (1989).

[18]B. R. Lawn, *Fracture of Brittle Solids*; Ch. 7. Cambridge University Press, Cambridge, U.K., 1993.

[19]N. P. Padture, J. L. Runyan, S. J. Bennison, L. M. Braun, and B. R. Lawn, "Model for Toughness-Curves in Two-Phase Ceramics: II, Microstructural Variables," *J. Am. Ceram. Soc.*, **76** [9] 2241–47 (1993).

[20]H. K. Xu, L. Wei, N. P. Padture, B. R. Lawn, and R. L. Yeckley, "Effect of Microstructural Coarsening on Hertzian Contact Damage in Silicon Nitride," *J. Mater. Sci.*, **30**, 869–78 (1995).

[21]H. K. Xu, S. Jahanmir, and L. K. Ives, "Material Removal and Damage Formation Mechanisms in Grinding Silicon Nitride," *J. Mater. Res.*, **11** [7] 1717–24 (1996).

[22]F. Guiberteau, N. P. Padture, H. Cai, and B. R. Lawn, "Indentation Fatigue: A Simple Cyclic Hertzian Test for Measuring Damage Accumulation in Polycrystalline Ceramics," *Philos. Mag. A*, **68** [5] 1003–16 (1993).

[23]H. Cai, M. A. Stevens Kalceff, and B. R. Lawn, "Deformation and Fracture of Mica-Containing Glass-Ceramics in Hertzian Contacts," *J. Mater. Res.*, **9** [3] 762–70 (1994).

[24]F. Guiberteau, N. P. Padture, and B. R. Lawn, "Effect of Grain Size on Hertzian Contact in Alumina," *J. Am. Ceram. Soc.*, **77** [7] 1825–31 (1994).

[25]A. Pajares, F. Guiberteau, B. R. Lawn, and S. Lathabai, "Hertzian Contact Damage in Magnesia-Partially-Stabilized Zirconia," *J. Am. Ceram. Soc.*, **78** [4] 1083–86 (1995).

[26]N. P. Padture and B. R. Lawn, "Toughness Properties of a Silicon Carbide with an *In-Situ*-Induced Heterogeneous Grain Structure," *J. Am. Ceram. Soc.*, **77** [10] 2518–22 (1994).

[27]S. K. Lee, S. Wuttiphan, and B. R. Lawn, "Role of Microstructure in Hertzian Contact Damage in Silicon Nitride: I, Mechanical Characterization," *J. Am. Ceram. Soc.*, **80** [9] 2367–81 (1997).

[28]S. K. Lee and B. R. Lawn, "Role of Microstructure in Hertzian Contact Damage in Silicon Nitride: II, Strength Degradation," *J. Am. Ceram. Soc.*, **81** [4] 997–1003 (1998).

[29]B. R. Lawn, N. P. Padture, H. Cai, and F. Guiberteau, "Making Ceramics 'Ductile'," *Science*, **263**, 1114–16 (1994).

[30]A. C. Fischer-Cripps and B. R. Lawn, "Stress Analysis of Contact Deformation in Quasi-Plastic Ceramics," *J. Am. Ceram. Soc.*, **79** [10] 2609–18 (1996).

[31]D. Tabor, *Hardness of Metals*. Clarendon, Oxford, U.K., 1951.

[32]H. Makino, N. Kamiya, and S. Wada, "Grain Size Effects of Si_3N_4 on Damage Morphology Induced by Localized Contact Stress"; pp. 229–34 in *Proceedings of the 1st International Symposium on the Science of Engineering Ceramics*. Edited by S. Kimura and K. Niihara. Koda, Aichi-Prefecture, Japan, 1991.

[33]C. Greskovich and G. E. Gazza, "Hardness of Dense α- and β-Si_3N_4 Ceramics," *J. Mater. Sci. Lett.*, **4**, 195–96 (1985).

[34]B. R. Lawn, S. K. Lee, I. M. Peterson, and S. Wuttiphan, "A Model of Strength Degradation from Hertzian Contact Damage in Tough Ceramics," *J. Am. Ceram. Soc.*, **81** [6] 1509–20 (1998).

[35]N. P. Padture and B. R. Lawn, "Contact Fatigue of a Silicon Carbide with a Heterogeneous Grain Structure," *J. Am. Ceram. Soc.*, **78** [6] 1431–38 (1995).

[36]N. P. Padture and B. R. Lawn, "Fatigue in Ceramics with Interconnecting Weak Interfaces: A Study Using Cyclic Hertzian Contacts," *Acta Metall.*, **43** [4] 1609–17 (1995).

[37]H. K. Xu, S. Jahanmir, L. K. Ives, L. S. Job, and K. T. Ritchie, "Short-Crack Toughness and Abrasive Machining of Silicon Nitride," *J. Am. Ceram. Soc.*, **79** [12] 3055–64 (1996).

[38]B. R. Lawn and T. R. Wilshaw, "Indentation Fracture: Principles and Applications," *J. Mater. Sci.*, **10** [6] 1049–81 (1975).

[39]B. R. Lawn, S. M. Wiederhorn, and H. Johnson, "Strength Degradation of Brittle Surfaces: Blunt Indenters," *J. Am. Ceram. Soc.*, **58** [9–10] 428–32 (1975).

[40]G. R. Anstis, P. Chantikul, D. B. Marshall, and B. R. Lawn, "A Critical Evaluation of Indentation Techniques for Measuring Fracture Toughness: I, Direct Crack Measurements," *J. Am. Ceram. Soc.*, **64** [9] 533–38 (1981).

[41]H. Horii and S. Nemat-Nasser, "Compression-Induced Microcrack Growth in Brittle Solids: Axial Splitting and Shear Failure," *J. Geophys. Res.*, **90** [B4] 3105–25 (1985).

[42]H. Horii and S. Nemat-Nasser, "Brittle Failure in Compression: Splitting, Faulting and Brittle–Ductile Transition," *Philos. Trans. R. Soc. London*, **319** [1549] 337–74 (1986).

[43]M. F. Ashby and S. D. Hallam, "The Failure of Brittle Solids Containing Small Cracks Under Compressive Stress States," *Acta Metall. Mater.*, **34** [3] 497–510 (1986). □

journal

J. Am. Ceram. Soc., 81 [9] 2394–404 (1998)

Contact Damage and Strength Degradation in Brittle/Quasi-Plastic Silicon Nitride Bilayers

Kee Sung Lee,† Seung Kun Lee,*,‡ and Brian R. Lawn*

Materials Science and Engineering Laboratory, National Institute of Standards and Technology, Gaithersburg, Maryland 20899

Do Kyung Kim*

Department of Materials Science and Engineering, Korea Advanced Institute of Science and Technology, Yusong, Taejon 305-701, Korea

A study is made of the damage resistance of silicon nitride bilayers consisting of a hard overlayer (coating) on a soft underlayer (substrate). The two layers are fabricated with different starting powders, to provide distinctive elongate-grain microstructures, and are cosintered, to provide strong interfacial bonding and thus to minimize subsequent delamination. Contact testing with spherical indenters is used to characterize the damage response. The elastic-plastic mismatch between the layers is sufficiently high as to produce distinctive damage modes in the two layers: predominantly cone cracking in the coating, and quasi-plasticity in the substrate. However, the mismatch is also sufficiently low as to preclude secondary transverse cracks of the kind observed in other bilayer systems to initiate immediately beneath the contact at the coating/substrate interface and propagate upward within the coating. The dominant damage mode shifts from coating fracture to substrate quasi-plasticity with increasing contact load and decreasing coating thickness. Significantly, the presence of the soft underlayer inhibits growth of the coating cone cracks as the latter approach and intersect the interface. The underlayer also substantially diminishes strength losses from the contact-induced damage, especially in bilayers with thinner coatings. The implication is that bilayer structures with thin, hard coatings can preserve benefits from the inherent toughness of soft substrate materials, and at the same time afford surface protection (high wear resistance) to the underlayer.

I. Introduction

Over the last decade there has been a drive to improve the toughness of silicon nitride (Si_3N_4) and other silicon-based ceramics via *in situ* growth of long, elongate grains.[1–12] In Hertzian contacts with spherical indenters these enlarged and elongated microstructures produce diffuse energy-absorbing subsurface quasi-plastic zones, consisting of individual, grain-localized microfailures ("shear faults"[13]), instead of conventional surface-initiated cone cracks.[14–18] At moderate contact loads this quasi-plastic damage has a comparatively minor degrading effect on strength in ensuing flexure or tension.[19,20] However, at higher contact loads or numbers of repeat cycles the microfailures tend to coalesce within the damage zone, with consequent accelerated strength loss and material removal.[21] Accordingly, quasi-plastic damage can have a highly adverse effect on resistance to fatigue[21] and wear[22] (although it can also promote machinability[23]). Improvement in mechanical properties from *in situ* tailoring of microstructures is not universal.

The search for ceramic structures with superior property combinations has led to a novel concept of layered homogeneous/heterogeneous microstructures with relatively hard surfaces (coatings) on soft underlayers (substrates).[24,25] A critical element of this concept is the incorporation of interlayer elastic–plastic mismatch, so as to partition energy from the contact loading system into competing fracture and quasi-plasticity modes, with the principal intent of containing the former mode without unduly promoting the latter. Another critical element is incorporation of strong rather than weak interlayer interfaces, so as to avoid delamination—the aim is to suppress rather than to deflect cone (or other) cracks that originate in the coating. The existence of any compression stresses in the coating from thermal expansion mismatch with the substrate will further inhibit the extension of any such cracks.[26,27] In principle, such a composite layer system should exhibit both high wear resistance and high toughness, with reduced susceptibility to strength degradation from damage accumulation.

In a recent study we investigated these critical elements in Si_3N_4 bilayers with uncommonly large elastic–plastic mismatch,[28] achieved by incorporating boron nitride (BN) platelets into the sublayer structure.[29,30] In Hertzian contact tests these bilayers showed confined transverse cracking in the coatings, along with extensive yield in the substrates. In thinner coatings with higher mismatch the soft substrate allowed the hard coating to "flex" beneath the contact, further enhancing the transverse cracking. In these cases some of the transverse cracks initiated from the coating/substrate interface rather than from the coating top surface, at relatively low loads. The cracks were highly stabilized, requiring exceptionally high loads to drive them upward through the coating, thereby enabling the crack population to multiply. It was clear that any such proliferation of cracks, while contributing to damage tolerance, could ultimately compromise the structural integrity of the coating, especially if the bilayer were to be subjected to high or repeat loading. It would seem that there are upper limits to the useful range of mismatch in these structures.

In the present work we investigate an analogous Si_3N_4 bilayer system, but with much smaller elastic–plastic mismatch, in an attempt to retain the advantages of the layer concept without inducing excessive transverse cracking. Bilayers with

G. M. Pharr—contributing editor

Manuscript No. 190682. Received September 22, 1997; approved December 19, 1997.

Supported by the U.S. Air Force Office of Scientific Research.

*Member, American Ceramic Society.

†Graduate student at the Department of Materials Science and Engineering, Korea Advanced Institute of Science and Technology, Yusong, Taejon 305-701, Korea.

‡Now at Advanced Material Technology Division, Technical Center, Caterpillar Inc., Mossville, Illinois 61552.

relatively brittle and quasi-plastic Si_3N_4 components are fabricated, but without addition of a softening agent in the substrate. The two Si_3N_4 layers are fabricated from different starting powders, at specified layer thicknesses, but are cosintered to produce a strong adjoining interface. Contacts with spheres are used to induce controlled damage patterns into the layered specimens and ceramographic sectioning techniques used to examine these patterns. Bend tests on damaged bar specimens are carried out to investigate the role of the different damage modes on strength degradation.

We shall show that whereas the Si_3N_4 coating layers are still subject to cone cracking, they show no deleterious interface-initiated transverse cracking. Quasi-plastic damage is more limited than in the previous BN-doped substrate structures,[28] but nevertheless appears to play an important role in restricting extension of the surface ring cracks within the coating. Strengths of contact-damaged bilayers are enhanced relative to those of the (comparatively weak) coating material, tending at small coating thicknesses to those of the (comparatively strong) substrate material. The results suggest the prospect of designing layer structures for both high toughness and high wear resistance.

II. Experimental Procedure

(1) Powders and Processing

Two different Si_3N_4 powders were selected for preparation of the bilayers. The starting powder for the coating layers was α-Si_3N_4 of mean particle size 1.0 μm (UBE-SN-E3, Ube Industries, Tokyo, Japan), with additives 5 wt% Y_2O_3 (Fine Grade, H. C. Starck GmbH, Goslar, Germany), 2 wt% Al_2O_3 (AKP 50, Sumitomo Chemical Co. Ltd., Tokyo, Japan), and 1 wt% MgO (High Purity, Baikowski Co., NC). The powder for the substrate layers was α-Si_3N_4 of average particle size 0.3 μm (UBE-SN-E10, Ube Industries, Tokyo, Japan), with the same sintering additives. Previously,[18] these two final batches were designated **AC** (α-coarse) and **AF** (α-fine), according to Si_3N_4 starting powder—here, we use the simpler designation **C** (coating) and **S** (substrate).

A Si_3N_4 powder batch with 30 vol% BN softening additive from another preceding study[28] was used as a comparison substrate—this material is here designated **S30.**

The powder batches were each mixed in isopropyl alcohol for 24 h in a planetary ball-mill using zirconia balls in a polypropylene container, to form a slurry. After drying, the softly agglomerated powder was crushed and sieved through a 60-mesh screen. The powders were cold-pressed in a graphite mold of 50 mm diameter to form green state bilayers of coating thickness 1 mm and substrate thickness 3–4 mm. The composite structure was hot-pressed at 1700°C at a pressure of 30 MPa in nitrogen for 1 h.[18] Some monolithic samples of each powder mix were prepared for control studies.

Surfaces of some specimens were polished to 1 μm finish, plasma etched, gold coated, and examined by scanning electron microscopy (SEM) to reveal the microstructures.

(2) Mechanical Testing

Fired bilayers and monolithic controls were cut into bars for mechanical testing. Routine measurements of Young's modulus, using a sonic method, and hardness, using Vickers indentations (load/projected area), were carried out on representative monolithic specimens. For the bilayers, the **C** (coating) structure was placed on the top, and the **S** (substrate) structure on the bottom. The top surfaces of the bars were then ground and polished to 1 μm diamond paste finish to produce coating thicknesses d_c = 20–600 μm. Additional Vickers indentations were made on polished sides of representative bilayer specimens to evaluate any differential thermal expansion stresses in the coatings, from radial crack measurements.[31] Some specimens were cut in half and the opposing surfaces polished and glued together to produce "bonded-interface" specimens[18,32,33] for investigation of subsurface damage in indentation tests. Other specimens were edge chamfered and polished for strength testing.

Hertzian indentations were made on the top surfaces of bilayer specimens, as well as on control monolith specimens, using WC spheres of radius r = 1.98 mm at loads up to P = 4000 N, in air. On as-polished specimens, rows of indentations were made at small load intervals to determine the critical loads P_Y and P_C for first incidence of yield and cracking. Application of a gold coat greatly enhanced detection of the initial damage in Nomarski illumination.[17] For the cracking an acoustic detector placed on the top surface adjacent to the indenter was a useful adjunct.[14,17] On bonded-interface specimens the indentations were made in rows symmetrically across the interface traces at the top surfaces. After separating the indented specimen halves in solvent and coating with gold, Nomarski illumination was used to view the subsurface damage.

Four-point flexure tests were run on bilayer and monolith bar specimens (25 mm × 4 mm × 3 mm, inner span 10 mm, outer span 20 mm) after indentation. The indentation sites were covered with a drop of silicone oil before testing and centered on the tensile side of the bend fixture. The bars were then broken in fast fracture (<10 ms) to avoid the influence of moisture ("inert" strengths). "Effective strengths" were calculated from beam theory, using the conventional relation

$$\sigma_F = 3Ql/4wd^2 \qquad (1)$$

with l the moment span, w the bar width, d the composite bilayer half-thickness, and Q the breaking load. Later, in Section III(3), we shall take into account the influence of thermal expansion mismatch (Appendix A) and interlayer modulus mismatch (Appendix B) on strengths evaluated from fracture mechanics considerations (Appendix C).

The broken specimens were examined in Nomarski illumination and scanning electron microscopy to locate the sources and modes of failure, i.e., from cone cracks or quasi-plastic zones.[19] Control strength tests on unindented specimens were made to measure baseline "natural" strengths.

III. Results

(1) Characterization of Silicon Nitride Layer Materials

Figure 1 shows bimodal microstructures for the two materials.[18] Common to both microstructures at the high end of the bimodal distribution are enlarged, elongated β-phase grains of length ≈5 μm and width ≈1.0 μm. In the **C** material (Fig. 1(a)) the volume fraction of this high-end grain component is relatively small (≈23 vol%)—the bulk of the microstructure consists of finer, equiaxed α-phase grains of diameter ≈1.2 μm (≈77 vol%). In the **S** material (Fig. 1(b)) the volume fraction of the high-end grain component is increased (≈40 vol%)—in this case the bulk of the microstructure consists of finer elongate β-phase grains of length ≈2 μm and width ≈0.5 μm (≈60 vol%).

Young's modulus and hardness are shown for **C** Si_3N_4 and **S** Si_3N_4 in the bar chart of Fig. 2, along with comparison values for **S30** Si_3N_4. The **C** material is slightly stiffer and harder than **S,** which in turn is very much stiffer and harder than **S30.** Note that the relative differences are considerably greater in the hardness than in the modulus, corresponding to greater plastic than elastic mismatch. For reference, bearing grade Si_3N_4 typically falls somewhere between the **C** and **S** materials—e.g., measurements on commercially available NBD200 (Norton/TRW Ceramics, Northboro, MA) give modulus 320 GPa and hardness 17.5 GPa.

The bar chart in Fig. 3 shows critical loads P_Y and P_C for first incidence of yield and cracking beneath Hertzian contacts in the same monolith material set. The critical load P_Y falls off strongly through the sequence **C–S–S30,**[18,28] commensurate

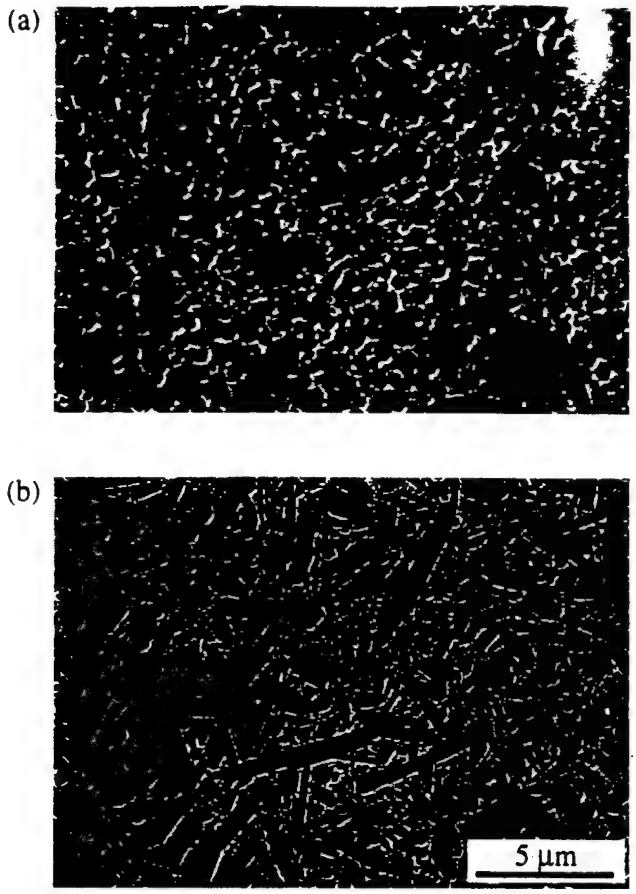

Fig. 1. SEM of Si_3N_4 materials used in bilayer: (a) **C** (coating), (b) **S** (substrate). Surfaces plasma etched (10 min in CF_4 and O_2).

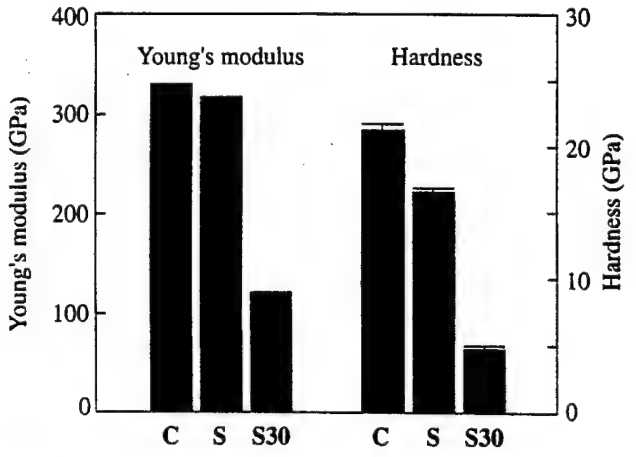

Fig. 2. Bar chart showing Young's modulus and indentation hardness of **C**, **S**, and **S30** (Si_3N_4–30 vol% BN). Data from Ref. 18.

with the hardness trend in Fig. 2. Conversely, P_C increases strongly, such that whereas full cone cracks are generated in **C**, only shallow surface ring cracks appear in **S**,[18] and no ring cracking is observed at all in **S30** over the load range.[28] Note that for **C** the values of P_Y and P_C are comparable, suggesting a relatively balanced competition between yield and fracture in this material.

Figure 4 plots biaxial compression stresses σ_R associated with differential thermal expansion between **C** and **S** layers, as a function of coating thickness d_c. The data are evaluations from radial crack measurements on the coating sections; the

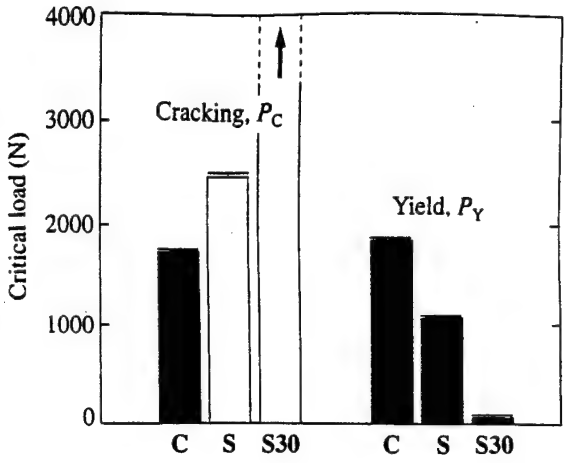

Fig. 3. Bar chart showing critical loads for onset of yield, P_Y, and cracking, P_C, of **C**, **S**, and **S30** Si_3N_4, tests in air. For P_C data, unfilled bar indicates only surface ring crack (as distinct from fully developed cone); absence of bar for **S30** indicates absence of any ring cracking at all. Data from Refs. 18 and 28.

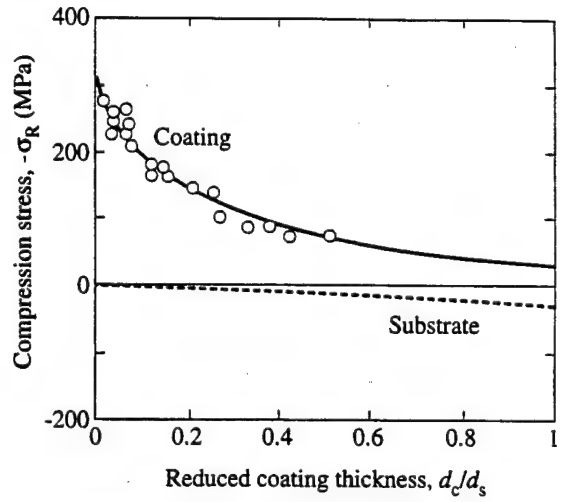

Fig. 4. Compression stresses in **C** layers from thermal expansion mismatch with **S** substrates, as a function of reduced coating thickness d_c/d_s, for constant bilayer thickness $d_c + d_s = 3000$ μm. Data from Vickers indentations (plotted here with compression stress on positive axis). Solid curve is fitted theoretical function through coating data; dashed curve is corresponding function for substrate (Appendix A).

solid curve is a theoretical fit to these data. Details of the data evaluations and fit are described in Appendix A.

(2) Contact Damage in Bilayers

Figure 5 compares bonded-interface section views of damage sites in bulk and bilayer Si_3N_4 structures, from indentations with a WC sphere of radius $r = 1.98$ mm at load $P = 3000$ N made on the top surface. In the bulk **C** specimen (Fig. 5(a)) we observe the developed cone crack (a faint trace of the subsurface quasi-plasticity zone below the contact becomes apparent in this material at high magnification). In the bilayer **C/S** specimen (Fig. 5(b)) the cone crack is substantially shallower and is contained wholly within the **C** layer (thickness $d_c = 180$ μm). The quasi-plasticity zone is now more intense and extends into the softer **S** underlayer. In a **C/S30** bilayer specimen (Fig. 5(c)), included here from the earlier study[28] for comparison as a case of extreme mismatch, the coating ($d_c = 250$ μm) contains an array of transverse cracks, including both cone cracks initiated from the top surface and upward-extending "inverted

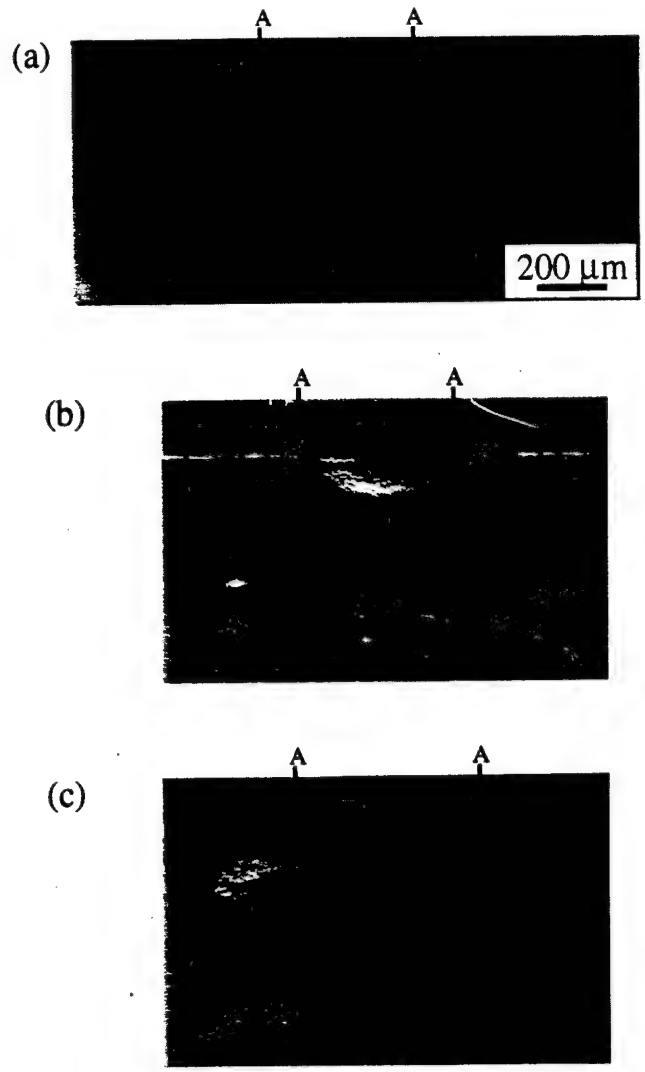

Fig. 5. Side views of Hertzian contact damage in Si_3N_4 configurations, using WC sphere of radius r = 1.98 mm at load P = 3000 N: (a) **C** monolith, showing fully developed cone crack with modest subsurface quasi-plasticity; (b) **C/S** bilayer, d = 180 μm, showing shortened cone crack in **C** layer and enhanced quasi-plasticity extending into **S** layer; (c) **C/S30** bilayer, d_c = 250 μm, showing proliferation of transverse cracks in **C** and extensive yield in **S30** (from Ref. 28). Nomarski optical micrographs of bonded-interface specimens. Contact diameter AA indicated. Interlayer interface revealed by relief polishing.

cone'' cracks initiated at the interlayer interface.[28] Yield and associated microcrack damage in the **S30** sublayer is now extensive. and some interfacial delamination is evident. It is apparent that incorporation of a soft underlayer can inhibit fracture if the mismatch with the coating material is small, but can enhance fracture if the mismatch is large. Note that the load P = 3000 N used in Fig. 5 exceeds both P_Y and P_C for the monolithic **C** material (Fig. 3), consistent with the appearance of both yield and cracking in the coating layer.

Now consider results for **C/S** bilayers in greater detail, taking the effects of contact load and coating thickness in turn:

(A) Effect of Contact Load: Micrographs of Hertzian contact damage in **C/S** Si_3N_4 bilayers with **C** coating thickness d_c = 180 μm (±10 μm) are shown in Fig. 6 over a sequence of contact loads. At P = 2000 N (Fig. 6(a)) a cone crack has initiated and there is a limited quasi-plasticity zone, both confined to the coating. At higher loads P = 2500 N (Fig. 6(b)), P = 3000 N (Fig. 6(c)), and P = 3500 N (Fig. 6(d)) both cracking and quasi-plasticity zone expand. However, whereas the cone crack remains confined to the coating, the quasi-

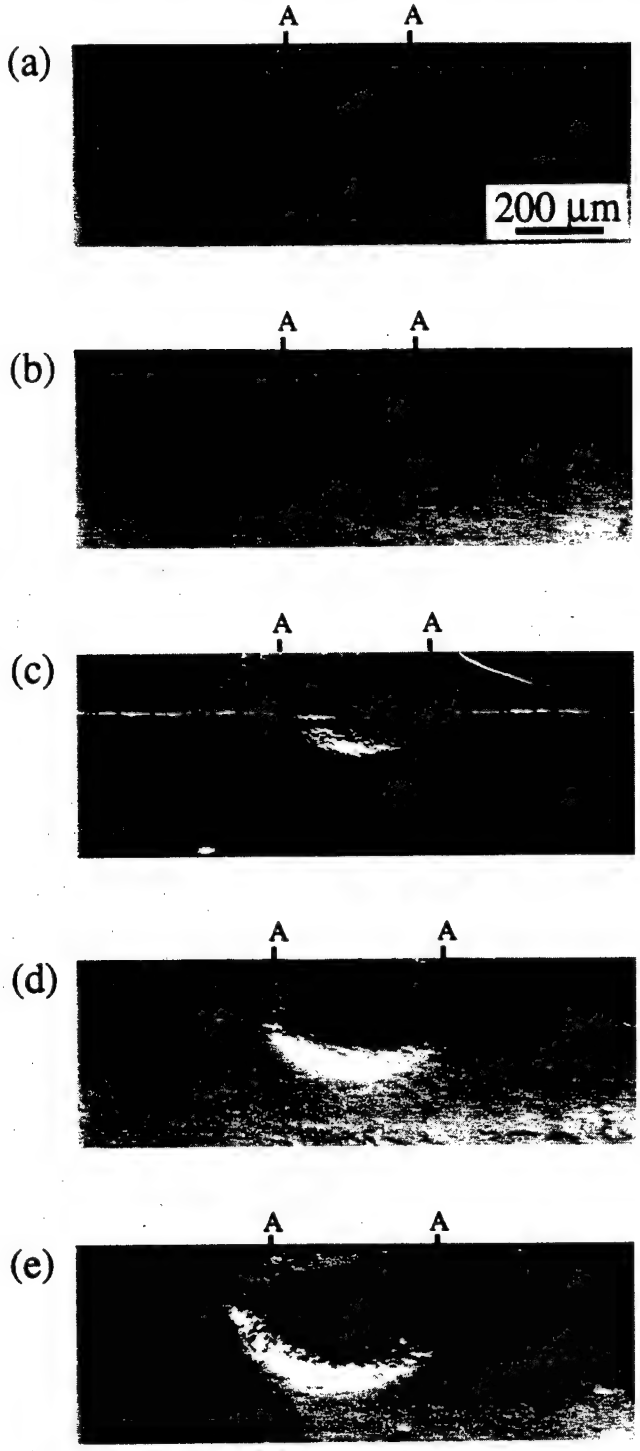

Fig. 6. Side views of Hertzian contact damage in **C/S** Si_3N_4 bilayers, fixed coating thickness d_c = 180 ± 10 μm, using WC sphere radius r = 1.98 mm: at loads (a) P = 2000 N, (b) 2500 N, (c) 3000 N, (d) 3500 N, (e) 4000 N. Nomarski optical micrographs of bonded-interface specimens. Contact diameter AA indicated.

plasticity now extends into the substrate. With further loading to P = 4000 N (Fig. 6(e)) the cone crack penetrates the interlayer interface, but remains inhibited (note that a second cone crack has now appeared), while the quasi-plasticity expands and intensifies within the substrate. The sequence in Fig. 6 suggests that the response is dominated by coating fracture at low load and by substrate plasticity at high load.[24]

Measured cone crack depths h below the top surface are plotted as a function of load P in Fig. 7 for both the **C/S** bilayer and the **C** monolith, for the coating thickness d_c = 180 μm

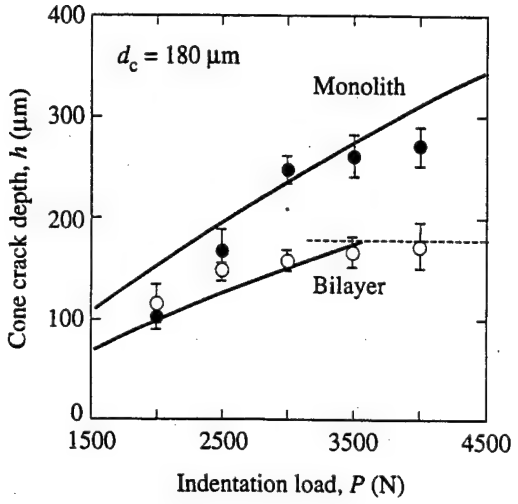

Fig. 7. Plot of cone crack depth as function of indentation load for **C/S** Si_3N_4 bilayers (open symbols), at fixed coating thickness d_c = 180 μm (horizontal dashed line), WC sphere r = 1.98 mm. Data for **C** monolith (closed symbols) provide baseline reference. Solid curves represent fracture mechanics best-fit to monolith data and ensuing prediction for bilayer.

indicated by the horizontal shaded line. The solid curves are representations of fracture mechanics relations for pennylike cone cracks in layers subjected to superposed uniform stresses σ_R, described in detail in Appendix C. The curve through the monolith data is a best-fit to these relations in the limit σ_R = 0—this fit is used to "calibrate" essential crack-geometry parameters. The curve through the bilayer data is an ensuing prediction for coatings with σ_R = −190 MPa (d_c = 180 μm in Fig. 4), using the calibrated crack-geometry parameters. (Note that this latter curve remains valid only while the cone crack remains embedded in the coating, i.e., $h < d_c$ in Fig. 7.) The presence of the expansion mismatch stress would appear to account for the bulk of the data shift between bilayer and monolith, notwithstanding the scatter in data.

(B) Effect of Coating Thickness: The sequence of micrographs of Hertzian contact damage in **C/S** Si_3N_4 bilayers at fixed contact load P = 3000 N in Fig. 8 illustrates the effect of coating thickness on the damage pattern. For a relatively thick coating layer, d_c = 600 μm (Fig. 8(a)), both cone crack and quasi-plasticity zone are wholly contained within the coating. As the coating is made thinner, d_c = 400 μm (Fig. 8(b)), both crack and plasticity zone remain contained within the coating, with attendant slight diminution in the cone crack depth. At d_c = 180 μm (Fig. 8(c)), the cracks are still contained, but the yield zone penetrates into the substrate. In the thinnest coatings, d_c = 80 μm (Fig. 8(d)) and d_c = 40 μm (Fig. 8(e)) the cracks, although still highly constrained, occasionally penetrate into the substrate (e.g., right side of Fig. 8(d)); the quasi-plasticity zone is now contained largely within the substrate. The sequence in Fig. 8 suggests that the response is dominated by coating fracture at high thicknesses, and by substrate plasticity at low thicknesses.

Figure 9 plots cone crack depth h as a function of coating thickness d_c, at fixed load P = 3000 N. The horizontal dashed line denotes the cone crack depth in the **C** monolith and the inclined dashed line denotes the locus $h = d_c$ for which the cone crack just intersects the **C/S** interface. The plot demonstrates quantitatively the extent to which the interface increasingly constrains the cone crack as the coating layer becomes thinner. At small coating thicknesses, d_c < 180 μm, some limited penetration into the substrate does occur, but the constraining influence nevertheless persists down to the smallest coating thicknesses. The solid curve is the fracture mechanics prediction for cone cracks in coatings with nonzero $\sigma_R(d_c)$, using the calibrated crack-geometry parameters from the monolith data

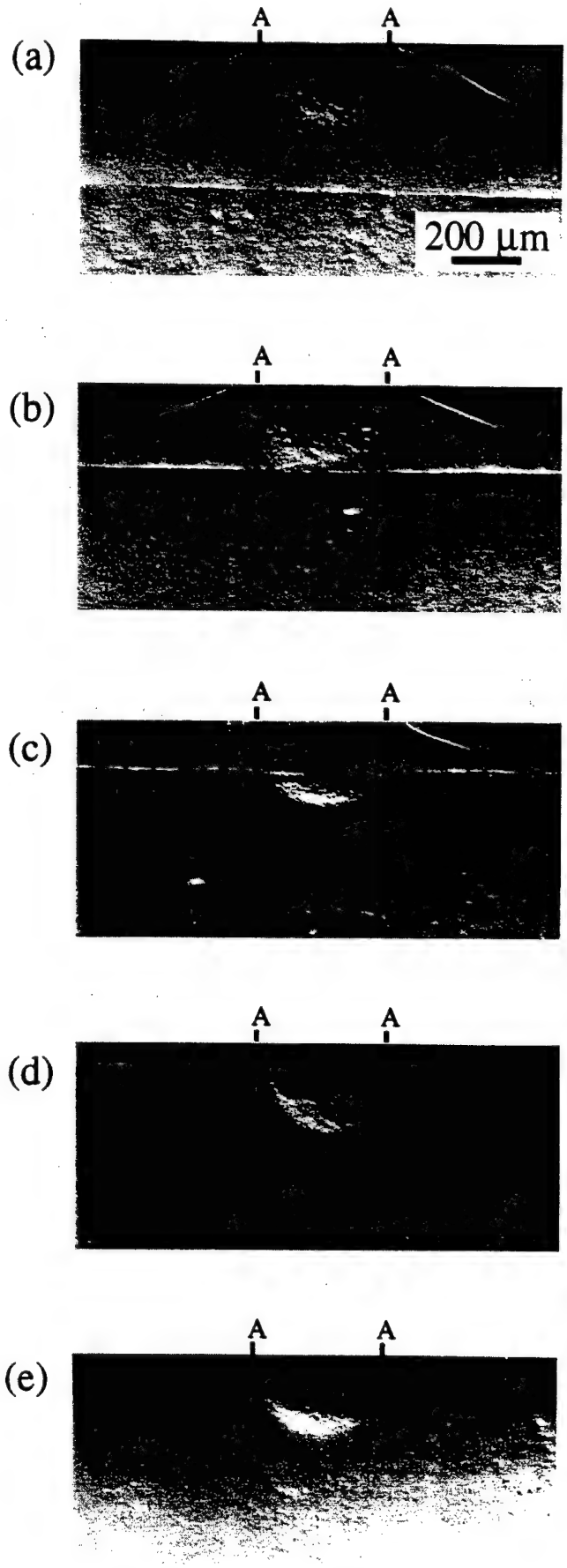

Fig. 8. Side views of Hertzian contact damage in **C/S** Si_3N_4 bilayers, at fixed load P = 3000 N using WC sphere radius r = 1.98 mm: at coating thicknesses (a) d_c = 400 μm, (b) 250 μm, (c) 180 μm, (d) 80 μm, (e) 40 μm. Nomarski optical micrographs of bonded-interface specimens. Contact diameter AA indicated.

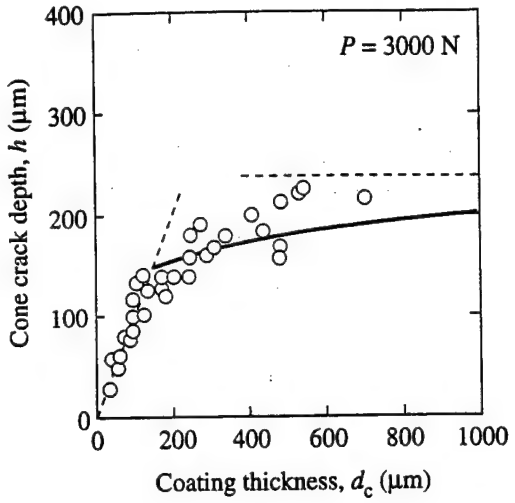

Fig. 9. Plot of cone crack depth as function of coating thickness for **C/S** Si_3N_4 bilayers (open symbols), WC sphere r = 1.98 mm, at fixed load P = 3000 N. Solid curve is fracture mechanics prediction. Inclined dashed line indicates configurations $h = d_c$ for which cracks just intersect the interface; horizontal dashed line indicates crack depth in **C** monolith.

in Fig. 7 (Appendix C). (Once more, this curve remains valid only while the cone crack remains embedded in the coating, i.e., $h < d_c$). Again, the presence of expansion mismatch stresses would appear to account for the data trends, within the scatter.

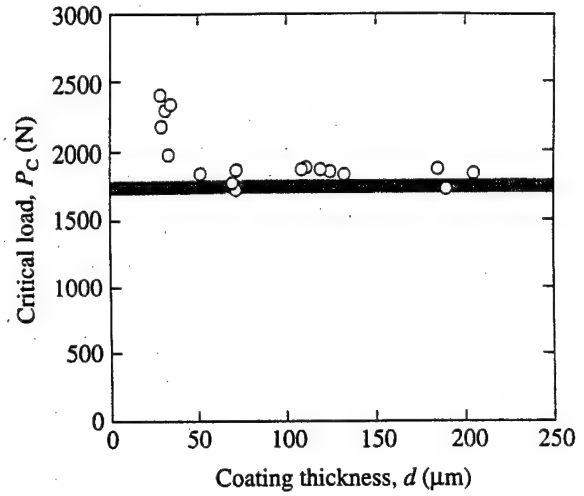

Fig. 11. Critical loads P_C for cone crack initiation as a function of coating thickness d_c for **C/S** Si_3N_4 bilayers, WC sphere radius r = 1.98 mm. Horizontal dashed line indicates P_C for the coating monolith.

On those occasions when the coating cone cracks do penetrate into the substrate the crack paths undergo only minor deflections at the **C/S** interface, without delamination. Figure 10 is an example, for an indentation in a thin coating, d_c = 40 μm, at high load, P = 4000 N. Note the continuity of the grain structure across the interface in this figure, confirming a strong interface.

While the presence of the substrate clearly has an important

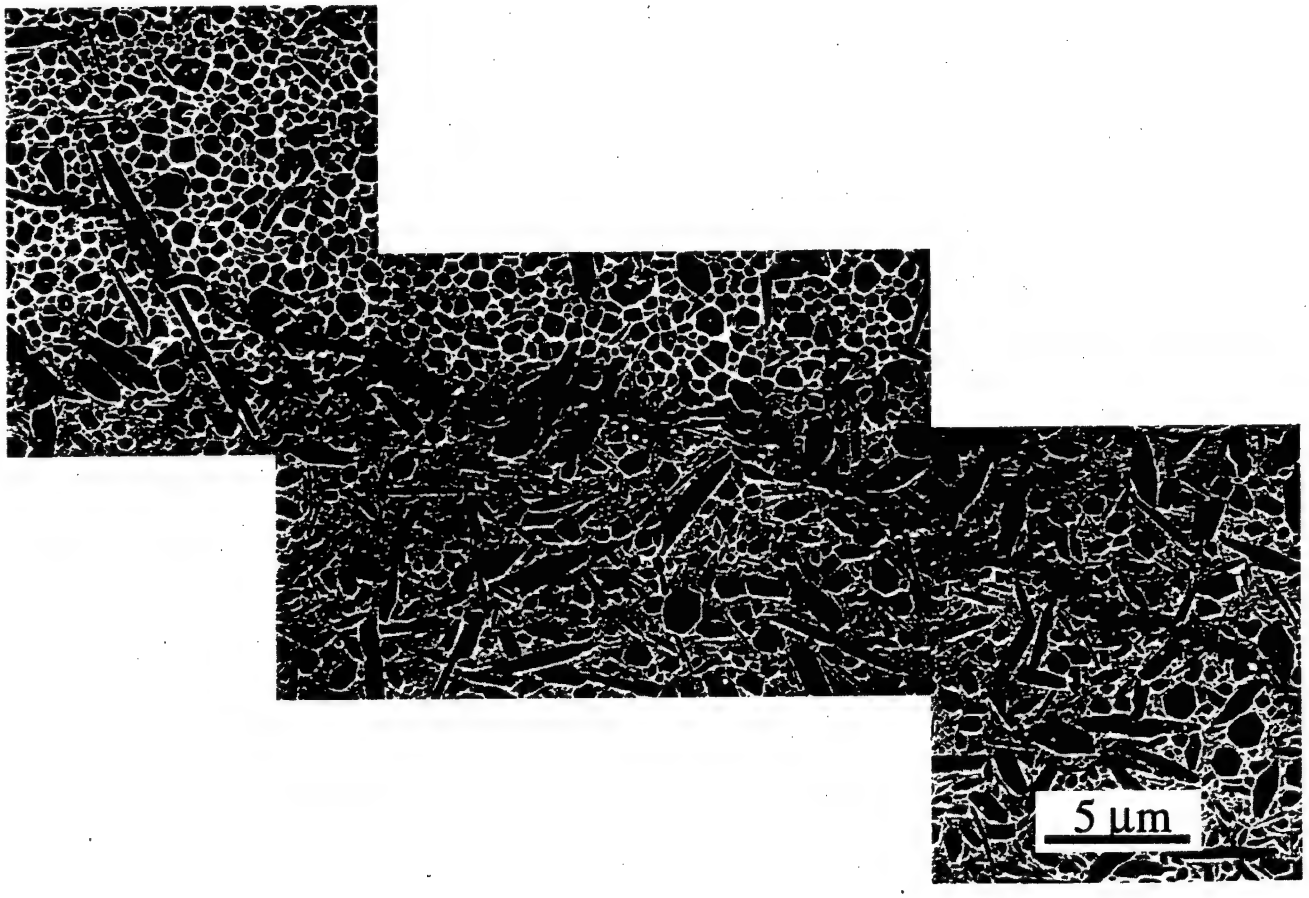

Fig. 10. Side view of Hertzian cone crack near **C/S** interface in Si_3N_4 bilayer of coating thickness d_c = 40 μm, at load P = 4000 N using WC sphere radius r = 1.98 mm. Note crack penetration from coating (top) to substrate (bottom) without delamination. Scanning electron micrograph.

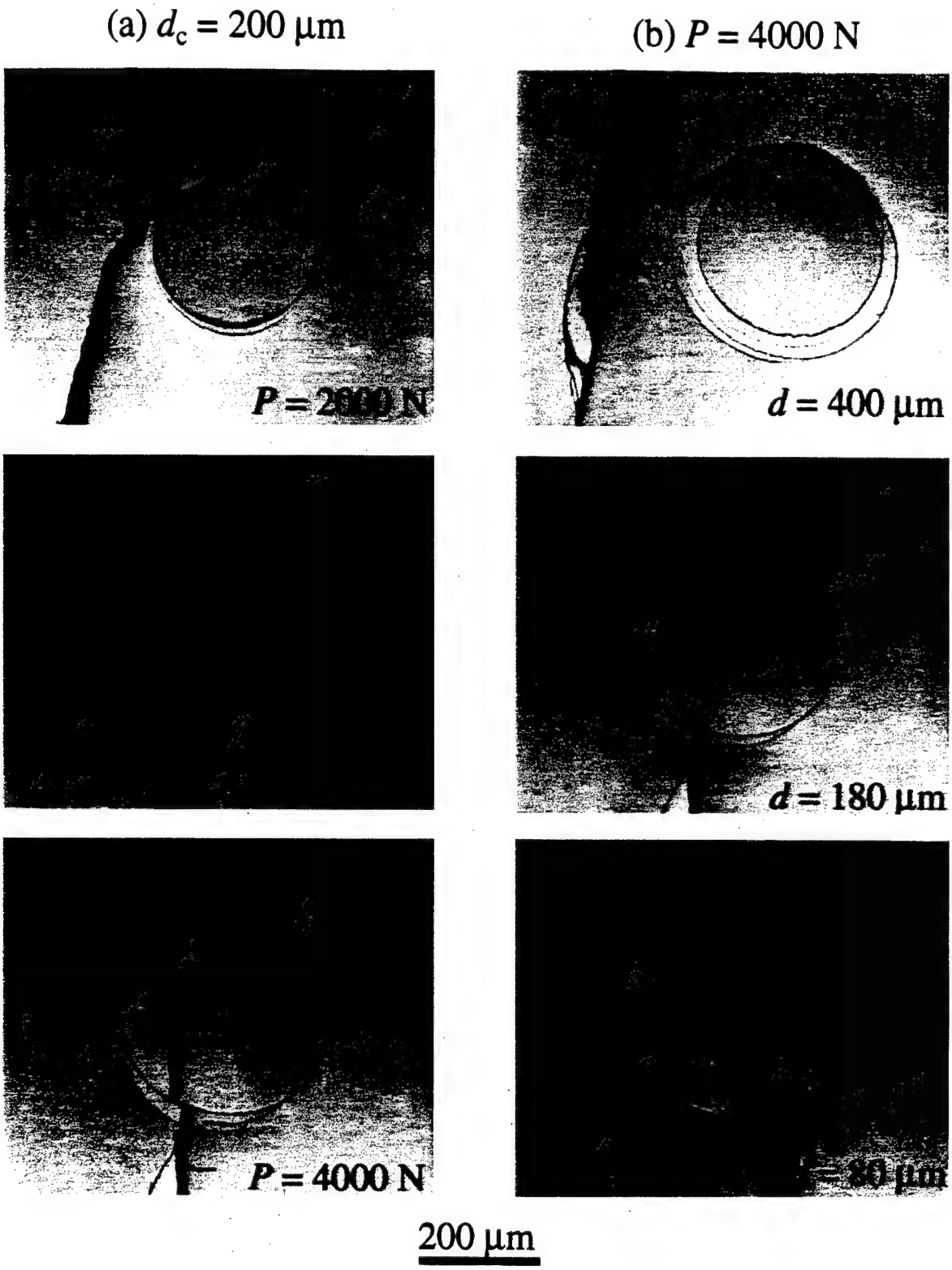

Fig. 12. Failure origins in bend specimens of **C/S** Si_3N_4 bilayers, for contacts with WC sphere radius r = 1.98 mm: (a) d_c = 200 μm, at P = 2000, 3000, and 4000 N; (b) P = 4000 N, at d_c = 400, 200, and 80 μm. Failure paths tangential to ring crack indicate brittle failure in **C** layer, through ring crack indicate quasi-plastic failure in **S** substrate. Tensile axis horizontal.

influence on the cone crack *size,* it does not appear to be a strong factor in the critical load for cone crack *initiation.* A plot of P_C as a function of coating thickness d_c is presented in Fig. 11. The values are relatively unchanged from those for the **C** monolith (shaded band—see Fig. 3) at thicknesses down to $d_c \approx 40$ μm, below which P_C increases.

(3) Strength Degradation

Figure 12 shows failure origins on broken bilayer strength-test specimens containing indentations from WC spheres of radius r = 1.98 mm, for two sets of conditions: (a) for fixed coating thickness d_c = 200 μm, at increasing (postcritical) loads; (b) for fixed load P = 4000 N, at decreasing thick-

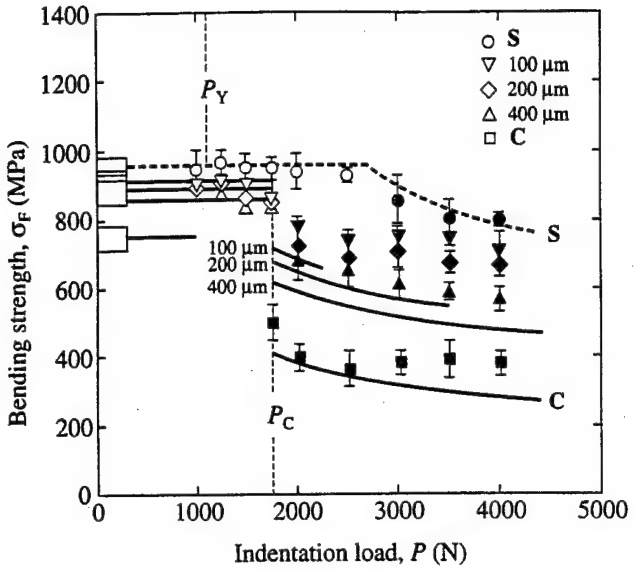

Fig. 13. Strength degradation of **C/S** Si_3N_4 bilayers, plus **C** and **S** monoliths, for contacts with WC sphere radius r = 1.98 mm. Data plotted as a function of indentation load P, for coating thicknesses indicated. Open symbols indicate breaks away from indentation sites, gray symbols failures from quasi-plastic zones, black symbols failures from cone cracks. Boxes at left axis denote strengths of unindented specimens. Vertical dashed lines indicate values of P_Y for **S**, P_C for **C**. Solid curves are theoretical predictions assuming failure from cone cracks at $P > P_C$ and from microstructural flaws at $P < P_C$, for **C** monoliths (lowest curve) and **C/S** bilayers at 400, 200, and 100 μm (upper three curves, truncated at loads and coating thicknesses where cones penetrate into substrate). Dashed curve is empirical fit to **S** data.[18]

nesses. Characteristic failure modes are indicated by peripheral fracture paths tangent to the ring cracks at low P and high d_c, and by more centralized fracture paths through the ring cracks at high P and low d_c. In conjunction with Figs. 6 and 8, we may associate the first kind of failure with cone cracks in the coating (brittle mode) and the second kind with yield zones in the substrate (quasi-plastic mode).[28]

Experimental data for the strength σ_F of **C/S** Si_3N_4 bilayers as a function of contact load P are plotted in Fig. 13, for **C** layer thicknesses d_c = 100, 200, and 400 μm, as well as for the **C** and **S** monoliths. Data points are from indented specimens: open symbols indicate breaks away from indentation sites, gray symbols failures from substrate quasi-plastic zones, and black symbols failures from coating cone cracks. Different regions of load dependence are apparent in the strength data: at $P < P_C$ (vertical dashed line), no significant load dependence; at $P = P_C$, abrupt falloff; at $P > P_C$, slowly continuing falloff, with failures first from cone cracks and later, at higher loads and thinner coatings, from quasi-plastic zones. The effects of coating thickness are manifest: whereas at $P < P_C$ the strength values for the bilayers differ little either from each other or from the **C** or **S** bounds, at $P > P_C$ the data shift strongly upward from the **C** lower bound toward the **S** upper bound.

Fracture mechanics analyses of strength degradation for failures from cone cracks have been developed for monolithic materials,[34] including Si_3N_4.[19] Analogous computation of strengths in bilayer systems is complicated by the additional stress terms associated with mismatch between coating and substrate: from mismatch in thermal expansion coefficients during initial cooling[26,27] (Appendix A); and from mismatch in elastic moduli during subsequent flexure (Appendix B). For a flaw of characteristic dimension c with negligible residual contact field, the strength under such conditions may be written (Appendix C)

$$\sigma_F = (T_0/\psi_\alpha c^{1/2} - \sigma_R)/k \qquad (2)$$

with ψ_α a crack geometry coefficient for Hertzian cones inclined at angle α to the top surface, T_0 the toughness (assumed single-valued), σ_R an expansion mismatch stress (Appendix A), and k an elastic mismatch coefficient (Appendix B). The solid curves in Fig. 13 are *a priori* predictions of $\sigma_F(P)$ for failure from cone cracks, using Eq. (2) in conjunction with appropriate expressions for the cone crack depth h ($= c \sin \alpha$) as a function of load P, for each of the coating thicknesses d_c represented. These curves truncate at the loads corresponding to cone crack penetration into the substrate, i.e., at depth $h = d_c$. The predictions appear to account for the broad data shifts for those specimens that fail from cone cracks in Fig. 13, although the absolute predictions lie outside the range of data scatter.

Once the cone cracks approach and penetrate into the tough substrate, failure occurs from the subsurface quasi-plasticity zones. Corresponding analyses of strength degradation from grain-localized "shear faults" within quasi-plasticity zones are being developed.[34] These are even more complex than the analyses for cone cracks, because of additional driving forces associated with residual local stress fields at the slipped shear faults.[34,35]

IV. Discussion

In this study we have confirmed that microstructural tailoring can have a vital influence on the damage tolerance of bilayer structures. An essential element in the tailoring is avoidance of a weak interface at the interlayer junction, in the present instance by cosintering the starting powders. We have focused specifically on Si_3N_4 bilayers with harder coatings on softer substrates, with modest mismatch. In contacts with spheres the coatings show mainly cone cracking and the substrates mainly quasi-plasticity (Figs. 5, 6, and 8). Which mode dominates the composite damage depends on the contact load and coating thickness: cone cracking tends to dominate at low loads and thick overlayers; conversely, quasi-plasticity tends to dominate at high loads and thin overlayers. The failure mode of the bilayer structure in flexure strength tests (Fig. 12) is also sensitive to these factors: coating cracks provide the sources of failure at low loads and thick coatings, and quasi-plasticity zones the sources at high loads and thin coatings—delamination is not observed in these modest-mismatch bilayers.

These results suggest some prescriptions for layer design using adjoining materials with modest elastic–plastic mismatch. In the case of the Si_3N_4 bilayers studied here the important microstructural elements are fine α-phase grains in the coating microstructure, to improve hardness, and coarse, elongate β grains in the substrate microstructure, to enhance quasi-plasticity. For these kinds of structures it may be concluded that thin, harder (and more brittle) wear-resistant coatings on softer (and tougher) underlayers may usefully provide surface protection without seriously compromising strength properties. Where possible, the layers should be cofired to minimize the risk of delamination failure.

The typical damage pattern in the present Si_3N_4 bilayer system provides a marked contrast to that in analogous bilayer substrates containing BN platelets (cf. Figs. 5(b) and (c)).[28] In the latter system the elastic–plastic mismatch is much greater (Fig. 2), and the yield in the substrate consequently much more extensive, allowing the coating to undergo a substantial component of "flexure" on the soft support beneath the contact. Such flexure leads to intense concentration of tensile stresses within the coating at the coating/substrate interface,[36] with consequent generation of upward-extending transverse cracks[37,38] at relatively low loads. While such cracks tend to be highly stable, they also tend to proliferate within the coating, compromising the subsequent integrity of the bilayer. In the present Si_3N_4 system the mismatch is too small to allow significant buildup of coating tensile stresses at the substrate interface, restricting the fracture to conventional cone cracking. At the

same time, as we have seen, the mismatch is sufficient to promote failures from subsurface quasi-plasticity zones at high loads and thin coatings.

The data in Figs. 11 and 13 warrant further comment, because collectively they characterize the contact loading conditions under which bilayer structures with modest (but nonzero) mismatch may operate without incurring intolerable strength losses from contact damage. Figure 11 indicates that the critical contact load P_C for cone crack initiation is largely insensitive to coating thickness d_c in the present bilayer system, at least down to $d_c \approx 50$ μm (relative to the sphere radius 1.98 mm used in our experiments). On the other hand, Fig. 13 indicates that the ensuing abrupt strength decrement at $P = P_C$ is very much sensitive to d_c. This behavior is consistent with St. Venant's principle in elasticity theory:[39] in the near field outside the contact circle at the top coating surface, where the cone cracks initiate during indentation, the maximum tensile stresses are very high and are relatively unaffected by the presence of moderate thermal expansion stresses or yield in the remote substrate; in the far field below the contact, where the cone cracks propagate (Fig. 8), the tensile stresses are much more strongly influenced by these extraneous factors, especially at higher P and smaller d_c.[28] In the thinner coatings the higher thermal expansion stresses and increased subsurface yield ultimately suppress cone fracture, leading to the change in mode of failure observed in Fig. 12.

A complete understanding of this latter kind of quasi-plasticity-initiated failure in layered structures is currently under study.

APPENDIX A

Differential Thermal Expansion Stresses in Bilayer Coatings

In-plane biaxial stresses σ_R from C/S coating/substrate thermal expansion mismatch are measured from the lengths of radial cracks at the vertical corners of Vickers indentations on coating sections (Fig. A1). The stress-intensity factor K for Vickers radial cracks of half-length c is given by[31]

$$K = \chi_V P/c^{3/2} + \psi_V \sigma_R c^{1/2} = K_{IC} = T_0 \qquad \text{(A-1)}$$

with $\chi_V = 0.066$ an indentation coefficient for fine-grain Si_3N_4,[17] $\psi_V = 0.77$ a geometrical radial crack coefficient,[40] and T_0 the toughness (assumed single-valued[17]). Measurements from comparative Vickers indentations in the C monolith ($\sigma_R = 0$) enable the determination $T_0 = 4.2$ MPa·m$^{1/2}$.

The stresses σ_R can also be calculated from a force balance relation for bilayers with thermal expansion mismatch between coating (c) and substrate (s):[27]

$$\sigma_R = (\alpha_c - \alpha_s)E_c\Delta T/\{(1 - \nu_c) + (1 - \nu_s)(E_c/E_s)(2d_c/d_s)\} \qquad \text{(A-2)}$$

where α is the thermal expansion coefficient, E is Young's modulus, ν is Poisson's ratio, and d_c is layer thickness. The solid curve through the coating data in Fig. 4 is a best fit of Eq. (A-2) to the data, with the adjustments $(\alpha_c - \alpha_s)E_c\Delta T/(1 - \nu_c) = -311$ MPa and $E_c(1 - \nu_s)/E_s(1 - \nu_c) = 4.92$. Inserting $\alpha_c = 4.16 \times 10^{-6}$ °C^{-1} and $\alpha_s = 4.62 \times 10^{-6}$ °C^{-1} (dilatometer measurements, N_2 atmosphere, 25–1000°C), $E_c = 335$ GPa and $\nu_c = 0.29$ (sonic wave measurements), the fit yields the following estimates: $\Delta T = 1430$°C, which would appear to be a little higher than the temperature range over which stresses no longer relax; and $E_s/(1 - \nu_s) = 95.9$ GPa, which is substantially lower than the measured value 315 GPa/$(1 - \nu_s) = 431$ GPa (sonic wave measurements).

In view of the numerical discrepancies between Eqs. (1) and (2), the values of σ_R in Fig. 4 should be regarded as no more than first approximation estimates.

Equivalent stresses in the substrate can be similarly evaluated by inverting the subscripts c and s in Eq. (A-2).

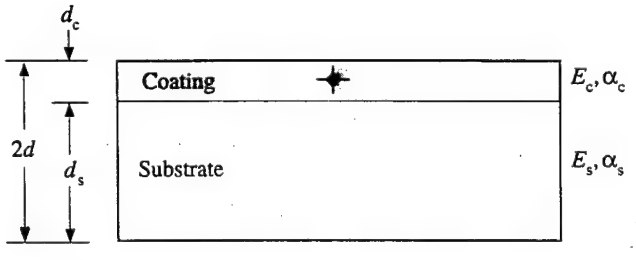

Fig. A1. Coating/substrate bilayer, with elastic and thermal expansion mismatch. Vickers indentations are used to evaluate thermal expansion mismatch stresses in coating.

APPENDIX B

Bending Stresses in Layer Structures with Different Elastic Moduli

Consider a bilayer consisting of two rectangular bars of same width w, but of different thickness d_c and d_s and modulus E_c and E_s (c = coating, s = substrate), perfectly bonded at the common interface (Fig. B1). The composite bar is subjected to bending, with layer c on the tensile side and layer s on the compression side. Although the strain distribution across the bilayer is linear and continuous, the stress distribution suffers a discontinuity at the interface.

We are specifically concerned with the maximum tensile stresses in the coating at the top surface, σ_c, and in the substrate at the interlayer interface, σ_s. The stresses of interest in four-point bending are related to the effective strength σ_F in Eq. (1) by

$$\sigma = (3Pl/4wd^2)k = k\sigma_F \qquad \text{(B-1)}$$

where k is a dimensionless factor (unity for $d_c = d_s$, $E_c = E_s$). The stress distributions can be determined in a straightforward manner from thin beam theory.[41] Let us write

$$\delta = d_c/d_s \qquad \text{(B-2}a\text{)}$$

$$\varepsilon = E_c/E_s \qquad \text{(B-2}b\text{)}$$

For the tensile stress in the top surface of the coating (layer 1), we obtain

$$k_c = \varepsilon(2 + 1/\delta + \varepsilon\delta)/\{3\varepsilon + (1 + 1/\delta^3)(1 + \varepsilon\delta)/(1 + 1/\delta)^2\} \qquad \text{(B-3)}$$

For the tensile stress in the substrate at the interlayer interface we have

$$k_s = (1/\delta - \varepsilon\delta)/\{3\varepsilon + (1 + 1/\delta^3)(1 + \varepsilon\delta)/(1 + 1/\delta)^2\} \qquad \text{(B-4)}$$

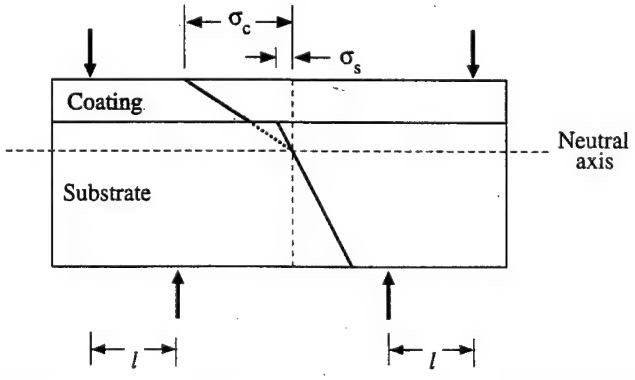

Fig. B1. Four-point bending of bilayer, generating maximum stress σ_c in the coating and σ_s in the substrate.

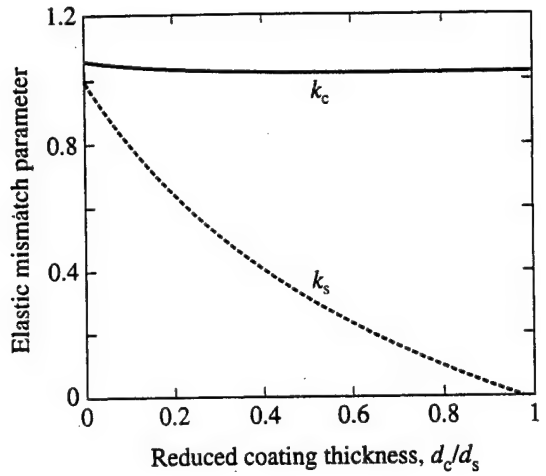

Fig. B2. Plot of elastic mismatch parameters k_c and k_s for coating and substrate in flexure, as function of reduced coating thickness d_c/d_s.

The coefficients k_c and k_s are plotted as a function of δ in Fig. B2, for $\varepsilon = E_c/E_s = 335/315 = 1.06$ appropriate to our Si_3N_4 bilayer system.

APPENDIX C

Calculation of Cone Crack Depths and Strengths for Bilayers

For the Si_3N_4 bilayers that fail from cone cracks in the coating we use a fracture mechanics analysis developed elsewhere.[19,34]

The cone crack depth is determined from the following geometrical relations, from Fig. C1:

$$h = c \sin \alpha \tag{C-1}$$

$$c = C - R_0/\cos\alpha \tag{C-2}$$

with α the cone angle, C the face length of a virtual conical surface with tip located above the indented surface, and R_0 the radius of the surface ring crack. To a first approximation, the cone cracks at contact load P satisfy an equilibrium stress-intensity relation for penny-like cracks[17]

$$K = \chi_H P/C^{3/2} + \Psi_0(\sigma_R \sin^2 \alpha)c^{1/2} = T_0 \tag{C-3}$$

with χ_H and ψ_0 Hertzian coefficients for straight-ahead cone extension, and T_0 the toughness (again assumed single-valued). This latter relation incorporates allowance for the action of the (resolved) stress σ_R on the cone crack response (Appendix A).

Equations (C-1) to (C-3) form the basis for the computations of cone crack depths in Figs. 7 and 9, plotted in those two figures as the solid curves. We take $\alpha = 25°$ and $R_0 = 238$ μm from direct measurements (e.g., Figs. 6 and 8), along with $T_0 = 4.2$ MPa·m$^{1/2}$ (Appendix A). (Actually, α and R_0 may be expected to vary with σ_R, and hence with coating thickness, but any such variations are slight enough to be masked by the data scatter in our Si_3N_4 system.) The value of the parameter ψ_α is simply that for mode I straight-ahead extension, $\psi_0 = \pi^{1/2} = 1.77$.[42] The parameter $\chi_H = 0.0311$ is "calibrated" from a best fit of Eqs. (C-1) to (C-3) to the $h(P)$ data for *monolithic* C Si_3N_4 in Fig. 7 ($\sigma_R = 0$). The corresponding curves for the *bilayer* data in Figs. 7 and 9 are predictions, using appropriate values of $\sigma_R(d_c)$ from Appendix A in Eqs. (C-1) to (C-3). (Note that this analysis is valid only while the cone crack remains embedded in the coating, i.e., $h < d_c$ in Fig. 9.)

Strength degradation functions may be determined from conventional fracture mechanics for failure from cone cracks in flexure.[34,42] Above the critical load P_C for cone initiation, the stress-intensity factor for equilibrium cone cracks in an applied field σ_A and superposed field σ_R is

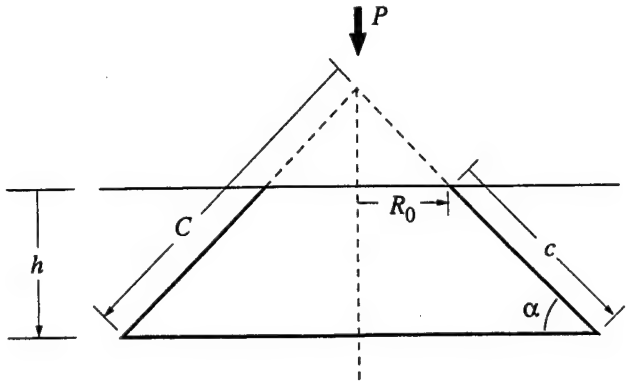

Fig. C1. Cone crack geometry.

$$K = \psi_\alpha \sigma c^{1/2} = T_0 \tag{C-4}$$

where $\sigma = \sigma_A + \sigma_R = k_c\sigma_F$. Failure then occurs spontaneously from the cone base according to the strength relation

$$\sigma_F = (T_0/\psi_\alpha c^{1/2} - \sigma_R)/k_c \tag{C-5}$$

with ψ_α a crack geometry coefficient for Hertzian cones at angle α. This relation again makes allowance for the presence of thermal expansion mismatch stresses σ_R (Appendix A) and for stress modifications associated with the elastic mismatch parameter k_c in flexure (Appendix B). At failure, the cone crack reinitiates unstably in predominantly tensile mode from its base, at some angle to α, thereby determining ψ_α. Below the critical load P_C, the ψ term in Eq. (C-5) is governed by the geometry of preexisting natural flaws, independent of P.

The functions $\sigma_F(P)$ calculated from Eq. (C-5), in conjunction with Eqs. (C-2) and (C-3), are included as the solid curves at $P > P_C$ in Fig. 13. For these calculations, ψ_α is determined from a previous analysis of crack reinitiation from the cone crack base, from which $\psi_\alpha = 0.037\alpha = 0.93$ approximately for $\alpha = 25°$.[34] Appropriate values of $k(d_c)$ are computed from Appendix B. (Note again that this analysis is valid only while the cone crack remains embedded in the coating.)

Acknowledgment: We thank T.-J. Chuang for providing the solution in Appendix B.

References

[1]C.-W. Li and J. Yamanis, "Super-Tough Silicon Nitride with *R*-Curve Behavior," *Ceram. Eng. Sci. Proc.*, **10** [7–8] 632–45 (1989).

[2]T. Kawashima, H. Okamoto, H. Yamamoto, and A. Kitamura, "Grain Size Dependence of the Fracture Toughness of Silicon Nitrides Ceramics," *J. Ceram. Soc. Jpn.*, **99**, 1–4 (1991).

[3]C.-W. Li, D.-J. Lee, and S.-C. Lui, "*R*-Curve Behavior and Strength of *In-Situ* Reinforced Silicon Nitride with Different Microstructures," *J. Am. Ceram. Soc.*, **75** [7] 1777–85 (1992).

[4]N. Hirosaki and Y. Akimune, "Effect of Grain Growth of β-Silicon Nitride on Strength, Weibull Modulus, and Fracture Toughness," *J. Am. Ceram. Soc.*, **76** [7] 1892–94 (1993).

[5]A. J. Pyzik and D. R. Beaman, "Microstructure and Properties of Self-Reinforced Silicon Nitride," *J. Am. Ceram. Soc.*, **76** [11] 2737–44 (1993).

[6]P. F. Becher, S. L. Hwang, H. T. Lin, and T. N. Tiegs, "Microstructural Contributions to the Fracture Resistance of Silicon Nitride Ceramics": pp. 87–100 in *Tailoring of Mechanical Properties of Si_3N_4*. Edited by M. J. Hoffmann and G. Petzow. Kluwer Academic Publishers, Dordrecht, Netherlands, 1994.

[7]M. J. Hoffmann, "Analysis of Microstructural Development and Mechanical Properties of Si_3N_4"; pp. 59–72 in *Tailoring of Mechanical Properties of Si_3N_4*. Edited by M. J. Hoffmann and G. Petzow. Kluwer Academic Publishers, Dordrecht, Netherlands, 1994.

[8]N. P. Padture, "*In Situ* Toughened Silicon Carbide," *J. Am. Ceram. Soc.*, **77** [2] 519–23 (1994).

[9]S. K. Lee and C. H. Kim, "Effects of α-SiC versus β-SiC Starting Powders on Microstructure and Fracture-Toughness of SiC Sintered with Al_2O_3-Y_2O_3 Additives," *J. Am. Ceram. Soc.*, **77** [6] 1655–58 (1994).

[10]C.-W. Li, S.-C. Lui, and J. Goldacker, "Relation Between Strength, Microstructure, and Grain-Bridging Characteristics in *In-Situ* Reinforced Silicon Nitride," *J. Am. Ceram. Soc.*, **78** [2] 449–59 (1995).

[11]P. Sajgalik, J. Dusza, and M. J. Hoffmann, "Relationship between Microstructure, Toughness Mechanisms, and Fracture Toughness of Reinforced Silicon Nitride Ceramics," *J. Am. Ceram. Soc.*, **78** [10] 2619–24 (1995).

[12]J. J. Cao, W. J. Moberly Chan, L. C. DeJonghe, C. J. Gilbert, and R. O. Ritchie, "*In Situ* Toughened Silicon Carbide with Al–B–C Additives," *J. Am. Ceram. Soc.*, **79** [2] 461–69 (1996).

[13]B. R. Lawn, N. P. Padture, H. Cai, and F. Guiberteau, "Making Ceramics 'Ductile'," *Science*, **263**, 1114–16 (1994).

[14]N. P. Padture and B. R. Lawn, "Toughness Properties of a Silicon Carbide with an *In-Situ*-Induced Heterogeneous Grain Structure," *J. Am. Ceram. Soc.*, **77** [10] 2518–22 (1994).

[15]H. H. K. Xu, L. Wei, N. P. Padture, B. R. Lawn, and R. L. Yeckley, "Effect of Microstructural Coarsening on Hertzian Contact Damage in Silicon Nitride," *J. Mater. Sci.*, **30**, 869–78 (1995).

[16]A. C. Fischer-Cripps and B. R. Lawn, "Indentation Stress–Strain Curves for "Quasi-Ductile" Ceramics," *Acta Metall.*, **44** [2] 519–27 (1996).

[17]S. K. Lee, S. Wuttiphan, and B. R. Lawn, "Role of Microstructure in Hertzian Contact Damage in Silicon Nitride: I, Mechanical Characterization," *J. Am. Ceram. Soc.*, **80** [9] 2367–81 (1997).

[18]S. K. Lee, K. S. Lee, B. R. Lawn, and D. K. Kim, "Effect of Starting Powder on Damage Resistance of Silicon Nitrides," *J. Am. Ceram. Soc.*, in press.

[19]S. K. Lee and B. R. Lawn, "Role of Microstructure in Hertzian Contact Damage in Silicon Nitride: II, Strength Degradation," *J. Am. Ceram. Soc.*, **81** [4] 997–1003 (1998).

[20]B. R. Lawn, N. P. Padture, F. Guiberteau, and H. Cai, "A Model for Microcrack Initiation and Propagation Beneath Hertzian Contacts in Polycrystalline Ceramics," *Acta Metall.*, **42** [5] 1683–93 (1994).

[21]N. P. Padture and B. R. Lawn, "Contact Fatigue of a Silicon Carbide with a Heterogeneous Grain Structure," *J. Am. Ceram. Soc.*, **78** [6] 1431–38 (1995).

[22]H. H. K. Xu, S. Jahanmir, L. K. Ives, L. S. Job, and K. T. Ritchie, "Short-Crack Toughness and Abrasive Machining of Silicon Nitride," *J. Am. Ceram. Soc.*, **79** [12] 3055–64 (1996).

[23]N. P. Padture, C. J. Evans, H. H. K. Xu, and B. R. Lawn, "Enhanced Machinability of Silicon Carbide via Microstructural Design," *J. Am. Ceram. Soc.*, **78** [1] 215–17 (1995).

[24]L. An, H. M. Chan, N. P. Padture, and B. R. Lawn, "Damage-Resistant Alumina-Based Layer Composites," *J. Mater. Res.*, **11** [1] 204–10 (1996).

[25]S. Wuttiphan, B. R. Lawn, and N. P. Padture, "Crack Suppression in Strongly-Bonded Homogeneous/Heterogeneous Laminates: A Study on Glass/Glass-Ceramic Bilayers," *J. Am. Ceram. Soc.*, **79** [3] 634–40 (1996).

[26]O. Prakash, P. Sarkar, and P. S. Nicholson, "Crack Deflection in Ceramic/Ceramic Laminates with Strong Interfaces," *J. Am. Ceram. Soc.*, **78** [4] 1125–27 (1995).

[27]H. Wang and X.-Z. Hu, "Surface Properties of Ceramic Laminates Fabricated by Die Pressing," *J. Am. Ceram. Soc.*, **79** [2] 553–56 (1996).

[28]K. S. Lee, S. Wuttiphan, X. Z. Hu, S. K. Lee, and B. R. Lawn, "Contact-Induced Transverse Fractures in Brittle Layers on Soft Substrates: A Study on Silicon Nitride Bilayers," *J. Am. Ceram. Soc.*, **81** [3] 571–80 (1998).

[29]H. Liu and S. M. Hsu, "Fracture Behavior of Multilayer Silicon Nitride/Boron Nitride Ceramics," *J. Am. Ceram. Soc.*, **79** [9] 2452–57 (1996).

[30]H. Liu, B. R. Lawn, and S. M. Hsu, "Hertzian Contact Response of Tailored Silicon Nitride Multilayers," *J. Am. Ceram. Soc.*, **79** [4] 1009–14 (1996).

[31]D. B. Marshall and B. R. Lawn, "An Indentation Technique for Measuring Stresses in Tempered Glass Surfaces," *J. Am. Ceram. Soc.*, **60** [1–2] 86–87 (1977).

[32]H. Cai, M. A. Stevens Kalceff and B. R. Lawn, "Deformation and Fracture of Mica-Containing Glass-Ceramics in Hertzian Contacts," *J. Mater. Res.*, **9** [3] 762–70 (1994).

[33]F. Guiberteau, N. P. Padture, and B. R. Lawn, "Effect of Grain Size on Hertzian Contact in Alumina," *J. Am. Ceram. Soc.*, **77** [7] 1825–31 (1994).

[34]B. R. Lawn, S. K. Lee, I. M. Peterson, and S. Wuttiphan, "A Model of Strength Degradation from Hertzian Contact Damage in Tough Ceramics," *J. Am. Ceram. Soc.*, **81** [6] 1509–20 (1998).

[35]B. R. Lawn and D. B. Marshall, "Nonlinear Stress–Strain Curves for Solids Containing Closed Cracks with Friction," *J. Mech. Phys. Solids*, **46** [1] 85–113 (1998).

[36]K. Komvopolous, "Elastic–Plastic Finite Element Analysis of Indented Layered Media," *ASME J. Tribol.*, **111**, 430–39 (1989).

[37]A. Pajares, L. Wei, B. R. Lawn, N. P. Padture, and C. C. Berndt, "Mechanical Characterization of Plasma-Sprayed Ceramic Coatings on Metal Substrates by Contact Testing," *Mater. Sci. Eng.*, **A208** [2] 158–65 (1996).

[38]A. Pajares, L. Wei, B. R. Lawn, and C. C. Berndt, "Contact Damage in Plasma-Sprayed Alumina-Based Coatings," *J. Am. Ceram. Soc.*, **79** [7] 1907–14 (1996).

[39]S. Timoshenko and J. N. Goodier, *Theory of Elasticity*, McGraw-Hill, New York, 1951.

[40]L. M. Braun, S. J. Bennison, and B. R. Lawn, "Objective Evaluation of Short-Crack Toughness-Curves Using Indentation Flaws: Case Study on Alumina-Based Ceramics," *J. Am. Ceram. Soc.*, **75** [11] 3049–57 (1992).

[41]W. C. Young, *Roark's Formulas for Stress and Strain*; pp. 118–19. McGraw-Hill, New York, 1989.

[42]B. R. Lawn, S. M. Wiederhorn, and H. Johnson, "Strength Degradation of Brittle Surfaces: Blunt Indenters," *J. Am. Ceram. Soc.*, **58** [9–10] 428–32 (1975). □

journal

J. Am. Ceram. Soc., 81 [3] 571-80 (1998)

Contact-Induced Transverse Fractures in Brittle Layers on Soft Substrates: A Study on Silicon Nitride Bilayers

Kee Sung Lee,† Sataporn Wuttiphan,‡ Xiao-Zhi Hu,§ Seung Kun Lee,*,¶ and Brian R. Lawn*

Materials Science and Engineering Laboratory, National Institute of Standards and Technology, Gaithersburg, Maryland 20899

An analysis of transverse cracks induced in brittle coatings on soft substrates by spherical indenters is developed. The transverse cracks are essentially axisymmetric and geometrically conelike, with variant forms dependent on the location of initiation: outer cracks that initiate at the top surface outside the contact and propagate downward; inner cracks that initiate at the coating/substrate interface beneath the contact and propagate upward; intermediate cracks that initiate within the coating and propagate in both directions. Bilayers consisting of hard silicon nitride (coating) on a composite underlayer of silicon nitride with boron nitride platelets (substrate), with strong interfacial bonding to minimize delamination, are used as a model test system for Hertzian testing. Test variables investigated are contact load, coating/substrate elastic–plastic mismatch (controlled by substrate boron nitride content), and coating thickness. Initiation of the transverse coating cracks occurs at lower critical loads, and shifts from the surface to the interface, with increasing elastic–plastic mismatch and decreasing coating thickness. This shift is accompanied by increasing quasi-plasticity in the substrate. Once initiated, the cracks pop in and arrest within the coating, becoming highly stabilized and insensitive to further increases in contact load, or even to coating toughness. A finite element analysis of the stress fields in the loaded layer systems enables a direct correlation between the damage patterns and the stress distributions: between the transverse cracks and the tensile (and compressive) stresses; and between the subsurface yield zones and the shear stresses. Implications of these conclusions concerning the design of coating systems for damage tolerance are discussed.

I. Introduction

THE mechanics of contact-induced cracks in hard, brittle layers on deformable but tough substrates are of interest in relation to the potential failure of practical coating systems in concentrated loadings. Examples include wear-resistant ceramic coatings on metal substrates,[1,2] thermal barrier coatings,[3,4] ceramic layer structures with alternating homogeneous and heterogeneous microstructures,[5–7] and biocoatings like teeth (enamel on dentin) and bone. The chief aim in designing such systems is to provide an optimum combination of underlying substrate toughness with surface protection by the coating layer. In terms of failure mode, the literature has focused almost exclusively on delamination at the coating/substrate interfaces;[8–10] indeed, existing engineering design virtually mandates that these interfaces be made weak, in order to deflect cracks and so enhance the toughness.[11] More recently, however, layer structures have been fabricated with relatively strong interfaces, with the explicit aim of suppressing the delamination failure mode and relying on the substrate to absorb penetrant fractures.[5,6,12,13] The limiting factor then becomes the brittle failure of the coating itself.

The layer fractures under explicit consideration here are those of near-axisymmetric form that initiate from the top surface at external contacts and that propagate transversely through the coating. These transverse cracks are most readily studied using spherical indenters ("Hertzian contact").[5,6] They are of practical importance because they provide for potential removal of part or all of the coating and for access of the environment to the substrate. Two forms of these fractures have been previously identified:[5,6] cracks that initiate at the coating-free surface outside the contact circle and extend downward; cracks that initiate at the coating/substrate interface within the contact circle and extend upward. We shall encounter both forms here, plus another that initiates between the first two from within the coating interior. We propose that all such transverse cracks can be usefully considered in terms of a generic quasi-conical geometry.

The principal aim of this paper is to demonstrate the fundamental nature of this class of contact-induced transverse cracks, and to describe the stress states that drive them. As a model material system for study we choose a composite silicon nitride bilayer system with large elastic–plastic mismatch.[7,14] The top coating layer is a hard, wear-resistant silicon nitride of moderate grain size; the underlying substrate layer is a relatively soft, damage-tolerant silicon nitride material with boron nitride platelet inclusions. Hertzian contacts are used to induce the damage in the layered specimens, and ceramographic sectioning techniques are used to examine these damage patterns. Key variables investigated are coating layer thickness, ranging from 120 to 1200 μm, and substrate composition, ranging from 5 to 30 wt% boron nitride additive phase. We show that crack densities in the coating increase with decreasing coating thickness and with increasing substrate boron nitride content. Quasi-plastic deformation†† in the soft underlayer (and to a lesser extent also in the coating) enhances the cracking. Once initiated, the cracks are highly stable, somewhat insensitive in dimension to the contact load and to material (and environment) properties such as toughness, arresting as they approach the bounding surfaces or interfaces of the coating. This arrest con-

J. E. Ritter—contributing editor

Manuscript No. 191250. Received January 24, 1997; approved June 19, 1997.

Supported by the U.S. Air Force Office of Scientific Research. Additional support for K. S. Lee was provided by the Korea Advanced Institute of Science and Technology (KAIST) Ph.D. program. S. Wuttiphan received financial support from the Royal Thai Scholarship program.

*Member, American Ceramic Society.

†Graduate Student at the Department of Materials Science and Engineering, Korea Advanced Institute of Science and Technology, Yusong, Taejon 305-701, Korea.

‡Graduate Student at the Department of Materials and Nuclear Engineering, University of Maryland, College Park, Maryland 20742.

§Guest Scientist from the Department of Mechanical and Materials Engineering, University of Western Australia, Nedlands, WA 6907, Australia.

¶Guest Scientist from the Department of Materials Science and Engineering, Lehigh University, Pennsylvania 18015.

††We use the term "quasi-plasticity" in the context of ceramics that deform by a microstructural shear fault mode,[15] to distinguish from traditional dislocation-driven plasticity deformation in metals.

dition leads to multiple but still-confined cracking at higher loads, plus some subsidiary cracking in the substrate, contributing to the damage tolerance of these structures. Ultimately, at even higher loads, the coating fails.

Stress analysis of the Hertzian-type contact fields in the coating/substrate structures is conducted using finite element modeling (FEM). Attention is focused on the distributions of principal tensile stresses, to quantify the fracture patterns, and shear stresses, to quantify the quasi-plastic zones. These considerations confirm that the cracks propagate in predominantly mode I, and highlight the role of elastic–plastic mismatch in enhancing these fractures. Calculations performed for the different experimental coating thicknesses and substrate compositions show how the tensile stress distributions are modified by layer geometry and degree of mismatch. In particular, these calculations reveal how the nature of the stress field changes from essentially classical Hertzian, in thick coatings with low substrate mismatch, to essentially flexural, in thin coatings with high substrate mismatch.

II. Experiment and Calculation

(1) Processing and Preparation of Silicon Nitride Bilayer Specimens

Silicon nitride bilayers were prepared using a derivative of the procedures previously described for producing monolithic[16] and multilayer structures.[7,14] A common powder processing and firing procedure was used for the coating and substrate layers, to ensure strong interlayer bonding in the finished product.

The silicon nitride starting powder for the coating layers was α-Si_3N_4 (UBE-SN-E10, Ube Industries, Tokyo, Japan) with sintering additives 2 wt% Al_2O_3 (AKP50, Sumitomo Chemical Co. Ltd., Tokyo, Japan), 5 wt% Y_2O_3 (H. C. Starck GmbH, Goslar, Germany), and 1 wt% MgO (High Purity, Baikowski Co., NC). Substrate layer compositions were prepared from the same starting powder, but with BN (Aldrich Chemical, Milwaukee, WI) additions of 5, 10, 20, 30 wt%. All powder batches were ball-milled using alumina balls in isopropyl alcohol for 24 h. After oven drying and sieving, the powder mixes were cold-pressed in a graphite mold of 50 mm diameter to form green state bilayers of coating thickness 1–2 mm and substrate thickness 3–4 mm. These were then hot-pressed at 1730°C at a pressure of 30 MPa in nitrogen for 1 h.

The top surfaces of the fired bilayer specimens were then ground and polished to 1 μm diamond paste finish to produce final coating thicknesses d = 120, 250, 400 and 1250 μm for indentation testing. Some side surfaces normal to the coating surface were also polished, for exploratory cross-section indentation tests. Other specimens were cut in half and the opposing surfaces polished and glued together to produce "bonded-interface" specimens,[17,18] for investigation of subsurface damage in Hertzian contact tests. Microstructural examination was carried out by scanning electron microscopy (SEM).

(2) Indentation Tests

Exploratory Vickers and Hertz indentation tests were made on polished surfaces, both normal and parallel to the hot-pressing direction. One set of Vickers indentations was made at load P = 100 N in specimens of each of the component materials, to determine elemental deformation and fracture responses. Another set was made in polished side sections of bilayer specimens (i.e., in a plane containing the hot press direction), with the pyramid center located a fixed distance 75 μm from the interfaces and with the diagonals aligned parallel and orthogonal to the coating/substrate interfaces, to confirm that the lower radial crack may penetrate into the substrate without substantial delamination.[6] Hertzian indentations were made with a WC sphere of radius 1.98 mm at loads P = 1000–2000 N, symmetrically across the interfaces, as a further test for delamination.

Indentation stress–strain curves were measured on the top surfaces of individual coating and substrate and composite bilayer specimens, using WC spherical indenters of radii r = 1.21–12.7 mm at loads up to P = 4000 N. For these tests, it was useful to coat the top surfaces with a gold film *before* indentation, to render the ensuing residual contact impressions visible in Nomarski illumination. From measurements of contact radius a at each value of P and r, indentation stress, $p_0 = P/\pi a^2$, and indentation strain, a/r, could be evaluated, enabling construction of the stress–strain curves. Indentations were also made on individual component materials to determine critical loads P_Y for first residual impressions, and thence yield stresses Y, from $p_Y = P_Y/\pi a^2 = 1.1Y$.[19]

To evaluate the contact damage, Hertzian indentations were made on polished surfaces, which were then gold coated and viewed in Nomarski contrast. Subsurface damage was examined using bonded-interface specimens. The indentations were made symmetrically along the traces of these interfaces on the top surfaces, using WC spheres of radius r = 1.98 mm at loads up to P = 4000 N. After separating the indented specimen halves in solvent, a gold coat was once more applied to the side surfaces for viewing in Nomarski contrast.

Some serial sectioning by polishing away the top indented surface was also conducted on indented bilayer specimens to confirm the crack geometry inferred from the bonded-interface specimens.

(3) FEM Analysis

An FEM algorithm, described in detail elsewhere[20–22] and foreshadowed in earlier studies by others,[23,24] was used to determine the contact stress fields in the bilayer systems. In this algorithm, a sphere of radius 1.98 mm is loaded incrementally onto the top surface of the prescribed layer structure. The interface between coating and substrate is maintained intact throughout the loading process. The sphere and specimen are represented by a grid with maximum mesh dimension << sphere radius r or coating thickness d.[21,22]

For a given set of input parameters representing the individual bilayer materials, a stress–strain curve can be reconstructed and calibrated against corresponding experimental data (with data for the sphere material from a previous study[20]). Input material parameters for each of the constituent layer components were determined in this way, in accordance with a shear stress criterion for deformation. This criterion is expressible in terms of a constitutive uniaxial compression stress–strain function $\sigma(\varepsilon)$:[20,21]

$$\sigma = E\varepsilon \qquad (\sigma \le Y) \tag{1a}$$

$$\sigma = Y + \alpha(\varepsilon E - Y) \qquad (\sigma \ge Y) \tag{1b}$$

with E Young's modulus, Y a uniaxial yield stress, and α a strain-hardening coefficient in the range $0 \le \alpha \le 1$ (α = 1, elastic; α = 0, plastic).

Calculations using this algorithm were performed for layer structures with coating thicknesses d = 120, 250, 400, and 1250 μm, for each substrate composition specified in the preceding subsection. Corresponding point-by-point computations of the principal stresses σ_1, σ_2, and σ_3 below the contact were derived from these calculations:[21,22] for evaluation of fracture, contours of the most tensile stress σ_1, and corresponding σ_2–σ_3 stress trajectories; for evaluation of quasi-plasticity, contours of maximum principal shear stress $\tau = \frac{1}{2}(\sigma_3 - \sigma_1)$, specifically the yield zone boundary, $\tau = \frac{1}{2}Y$.

III. Results: Characterization of Layer Materials

In this section we present results of initial characterization tests carried out on the composite silicon nitride bilayer systems, beginning with the individual material components in order to establish a proper basis for the ensuing fracture analysis in Section IV. Table I summarizes the quantitative results.

(1) Basic Properties of Component Materials

SEM examinations of the polished specimens revealed microstructures similar to those reported in earlier studies, rela-

Table I. Characteristics of Coating and Substrate Materials

Composition	Hardness H (GPa)†	Young's modulus E (GPa)	Yield stress Y (GPa)	Strain-hardening coeff α
Si_3N_4	14.6	320	8.4	0.7
Si_3N_4 + 5BN	12.0	278	6.7	0.5
Si_3N_4 + 10BN	11.1	222	4.5	0.4
Si_3N_4 + 20BN	7.4	160	2.8	0.1
Si_3N_4 + 30BN	4.7	119	1.6	0

†Hardness defined as $H = P/2a^2$.

tively isotropic in the monolithic Si_3N_4 and highly anisotropic in the Si_3N_4–BN composites. For the Si_3N_4 coating, the microstructure had elongated β grains of length ≈5 μm and diameter ≈0.8 μm, with ≈10 wt% glassy phase.[16] For the Si_3N_4–BN substrate layer, the BN had the form of platelets 1.5–10 μm in diameter and 0.2–0.6 μm thick, with these platelets strongly aligned normal to the hot-pressing direction, i.e., parallel to the coating/substrate interfaces.[7]

Exploratory Vickers indentations on polished surfaces normal and parallel to the hot-pressing direction provided a useful semiquantitative guide to material properties. Hardness values H on bulk material surfaces were found to be insensitive to the surface orientation relative to the hot-press direction. These values are seen in Table I to decrease with increasing BN content, by more than a factor of 3 in the 30 wt% composite material, confirming the softening effect of the additive phase. No such isotropy was apparent in the radial crack patterns. In the substrate materials the radial crack lengths were markedly greater in the direction normal to the hot-pressing direction, by ≈40% in Si_3N_4–10% BN, ≈80% in Si_3N_4–20% BN, and ≈120% in Si_3N_4–30% BN. This trend is consistent with the observed textural anisotropy in the composite structures. (A smaller discrepancy of <10%, and of the same sign, was also observed in the base Si_3N_4 coating material, suggesting some minor texturing in the microstructure.) In all materials the radial cracks deflected locally along interphase boundaries, especially at the large BN platelets in the composite structures, indicating the existence of weak internal interfaces.

Values of Young's modulus E in Table I were determined for the different material components from the initially linear slopes of indentation stress–strain curves[3] (see Section III(3)). The values of E decrease with increasing BN content, commensurate with a more compliant platelet phase.[14] Yield stresses Y measured from first detection of residual impressions also decrease significantly with increasing BN content, in accordance with the trend in hardness values listed in Table I. These results confirm that the addition of the BN phase has a substantial softening effect on the silicon nitride structure.

(2) Crack Behavior at Coating/Substrate Interface

Vickers indentations made at polished sections of coating/substrate bilayers are useful in confirming the intrinsic strength of the interfaces. First, indentations made in the coatings and substrates away from the interfaces show the same radial crack dimensions as the tests on the bulk specimens, within experimental scatter (≈5%). This indicates that the level of residual stress in the coating is negligibly small. Indentations made in the coating close to the interface, at fixed distance 75 μm and load $P = 100$ N, show significant departures from symmetry. Examples are shown in Fig. 1, for substrates with 10, 20, and 30 wt% BN additive. The key observation is the absence of any delamination along the interfaces, indicating that the toughness of the interface is at least one half that of the substrate material.[25] Instead, the lower radial cracks penetrate into the tougher substrate (Table I), where they are arrested. Note that the initially orthogonal radial cracks appear to be attracted toward the interface as they extend, most noticeably in the bilayer with the highest BN content, as commonly observed with indentation cracks adjacent to a low modulus layer.[26] Hence elastic–plastic mismatch between the coating and substrate materials is a factor in the fracture behavior.

Hertzian indentations across the coating/substrate bilayer interface serve to reinforce the above Vickers results. Figure 2 shows a damage pattern using a WC sphere of $r = 1.98$ mm at increasing $P = 2000$ N on a bilayer with 10 wt% BN substrate. Multiple ring cracks initiate on the Si_3N_4 coating side, and penetrate the interface onto the Si_3N_4–BN substrate side, where they quickly arrest. Again, delamination is absent. There is indication of a residual depression at the contact area within the ring cracks, especially in the softer substrate material.

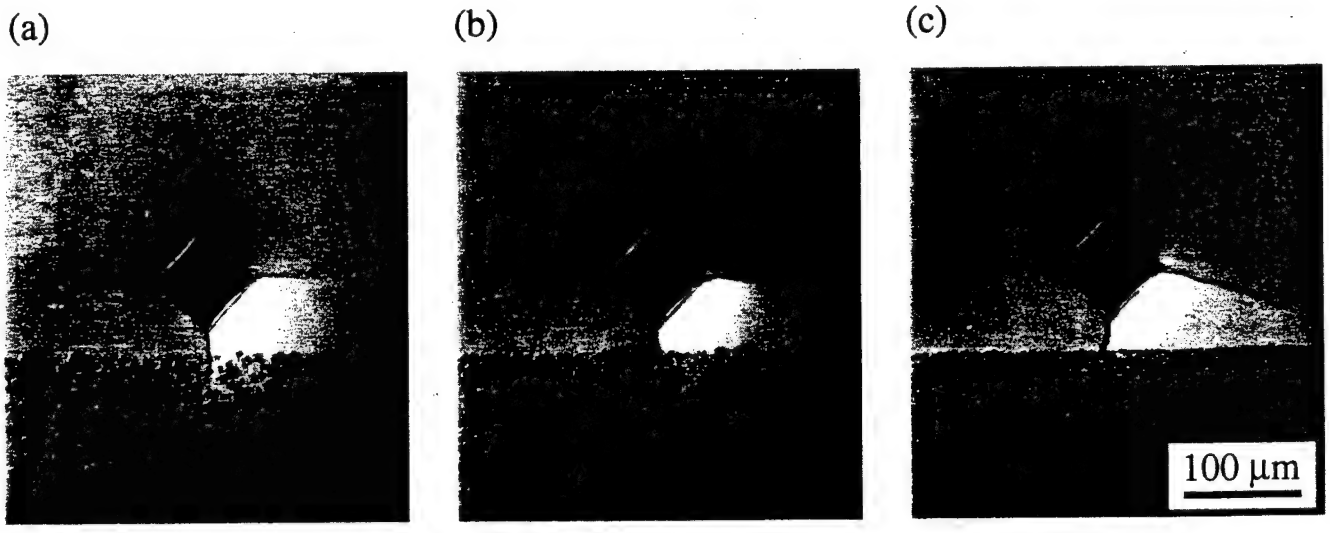

Fig. 1. Micrographs of Vickers radial cracks in Si_3N_4 coatings (upper layer), distance 75 μm from interface with Si_3N_4–BN substrates (lower layer): compositions (a) 10 wt% BN, (b) 20 wt% BN, (c) 30 wt% BN. Indentations at $P = 100$ N. Note how lower radial crack approaches and penetrates interface without delamination. Note also distortion of radial crack pattern at higher BN contents, indicating elastic–plastic mismatch.

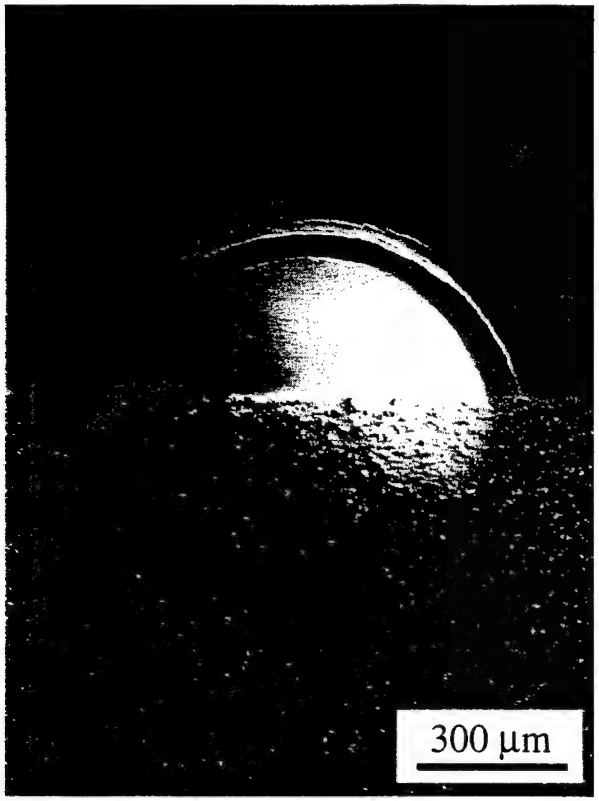

Fig. 2. Hertzian indentations in Si_3N_4/Si_3N_4–10 wt% BN bilayer, made symmetrically across interface trace, with WC sphere r = 1.98 mm at P = 2000 N. Note crack penetration from Si_3N_4 side to Si_3N_4–BN side, without delamination.

(3) Calibration of Indentation Stress–Strain Curves

Indentation stress–strain data for the individual component materials are plotted in Fig. 3. The solid curves in this figure are FEM-generated functions using measured values of Y, with E in the initial elastic region and α in the subsequent quasi-plastic region adjusted to give best fits (Table I). The monolithic silicon nitride shows slight nonlinearity in the stress–strain curve above the yield point at $p_Y = 1.1Y = 9.2$ GPa (Section II(2)).[16] As the BN content increases, and Y and α simultaneously decrease (Table I), the curves deviate more from linearity, indicating the enhanced quasi-plasticity.[7]

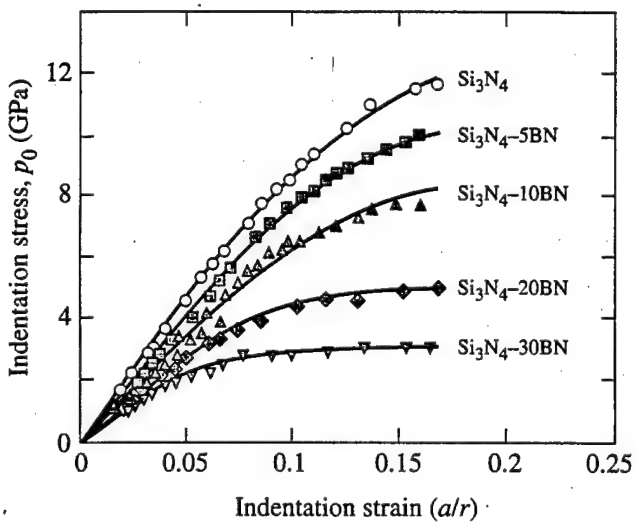

Fig. 3. Indentation stress–strain curves for component materials used in fabrication of Si_3N_4/Si_3N_4–BN bilayers. Solid curves are FEM fits.

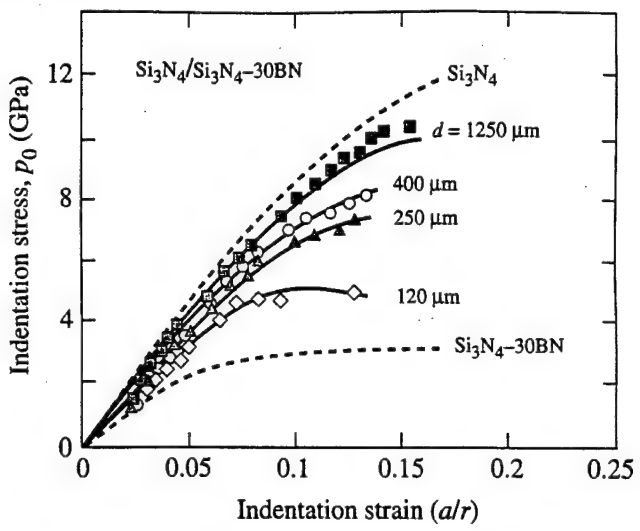

Fig. 4. Indentation stress–strain curves for Si_3N_4/Si_3N_4–30 wt% BN bilayer composites, for Si_3N_4 coating thicknesses d indicated. Solid curves are FEM predictions, using material parameters calibrated from Fig. 3. Upper and lower dashed curves are bounds for Si_3N_4 and Si_3N_4–30 wt% BN component materials, respectively, from Fig. 3.

Indentation stress–strain data for the Si_3N_4/Si_3N_4–BN coating/substrate systems are shown in Figs. 4 and 5. In these figures the solid curves are now *a priori* FEM predictions, using the parameters calibrated from Fig. 3. Figure 4 shows curves for the different coating thicknesses, d = 120, 250, 400, and 1250 μm, at fixed substrate composition 30 wt% BN. In this figure, the upper and lower dashed curves are bounds for monolithic Si_3N_4 and Si_3N_4–30% BN respectively (from Fig. 3). The solid curves show a progressive shift away from the hard Si_3N_4 upper bound toward the soft Si_3N_4–30% BN lower bound as the coating thickness decreases, indicating a correspondingly greater influence of the substrate material.[4] (Note how this transition manifests itself as a maximum in the stress–strain curve in the d = 120 μm data, indicative of load transfer from coating to substrate.[4]) Figure 5 shows curves for the different substrate compositions, 10, 20, and 30 wt% BN, at fixed coating thickness d = 250 μm. Again, the upper dashed curve is the upper bound for monolithic Si_3N_4. Once more, the

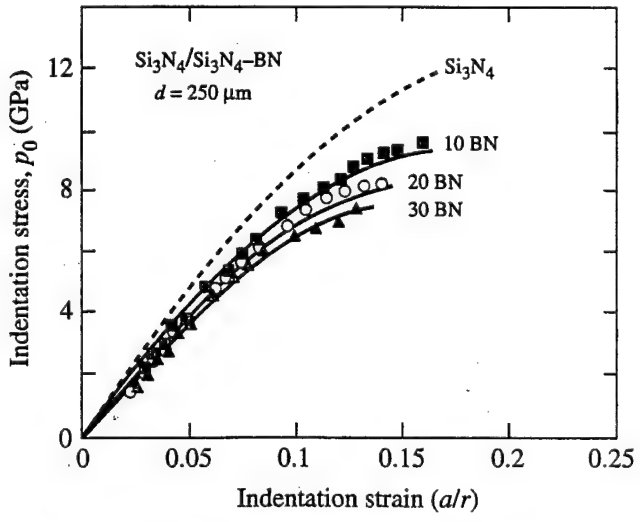

Fig. 5. Indentation stress–strain curves for Si_3N_4/Si_3N_4–BN bilayer composites, Si_3N_4 coating thickness d = 250 μm, showing effect of BN content in substrate. Solid curves are FEM predictions, using material parameters calibrated from Fig. 3. Upper dashed curve is bound for Si_3N_4 from Fig. 3.

role of the soft substrate in determining the stress-bearing capacity of the composite bilayer is apparent.

IV. Results: Analysis of Transverse Fracture Patterns

We are now in a position to describe the fracture patterns observed in the silicon nitride bilayers, and to analyze the stress distributions responsible for this damage. In Figs. 6–9 we show section-view micrographs from bonded-interface specimens indented with a WC sphere of radius $r = 1.98$ mm, representing the effects of indentation load, substrate composition, and coating thickness. Corresponding FEM-generated contours of principal stresses are included in Figs. 6, 8, and 9: principal shear stresses at left, shaded areas indicating yield zones ($\sigma_3 - \sigma_1 = Y$); principal normal stresses at right, shaded areas indicating tensile zones ($\sigma_1 \geq 0$), dashed curves indicating σ_3 stress trajectories (Fig. 6 only).

In this section we limit analysis of the stress fields to essentially qualitative aspects, deferring quantitative considerations to the Discussion.

(1) Effect of Indentation Load

Figure 6 shows a sequence of micrographs of Hertzian contact damage at increasing indentation load, $P = 800$, 1000,

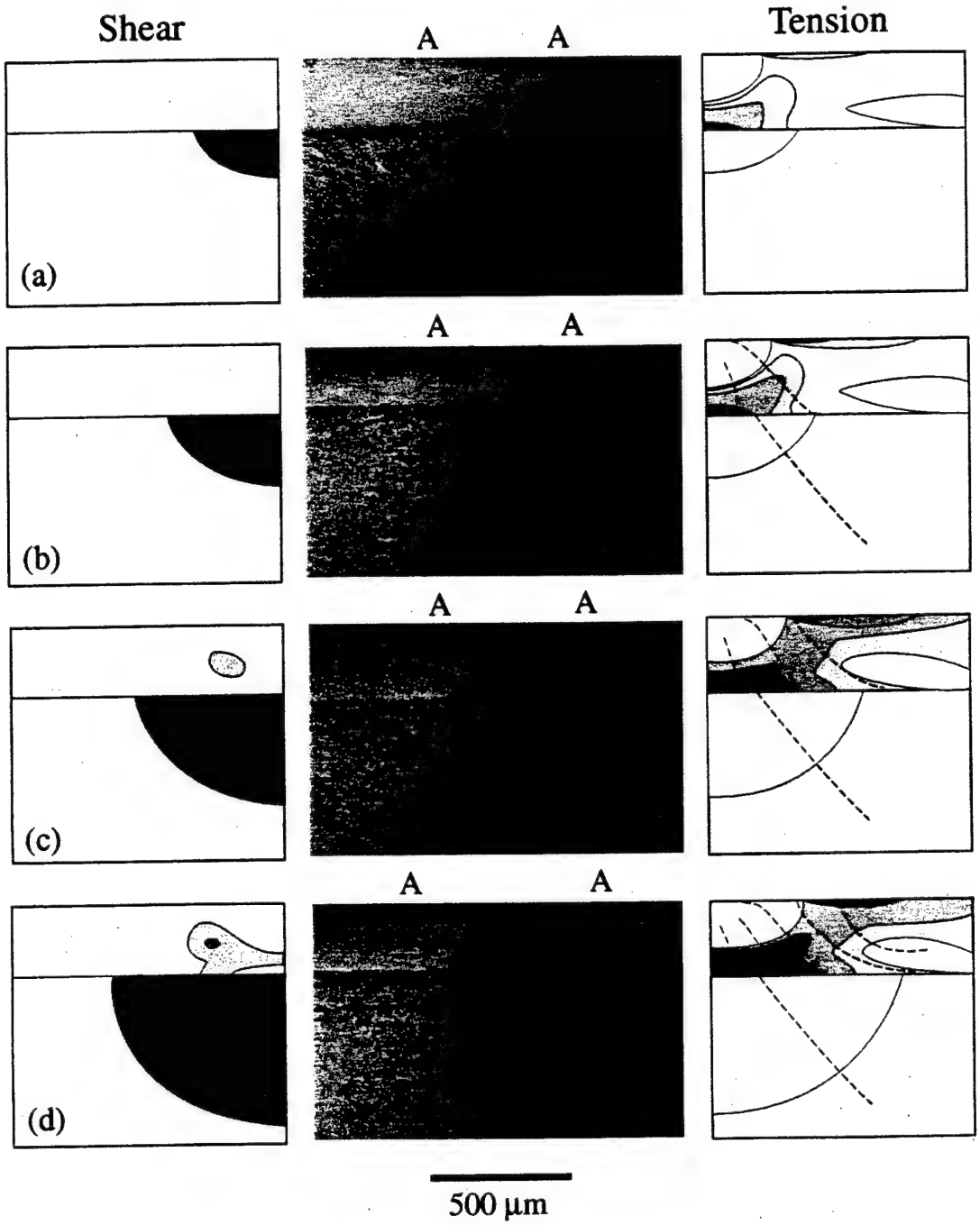

Fig. 6. Contact fracture in Si_3N_4/Si_3N_4–30 wt% BN bilayer composite, Si_3N_4 coating thickness $d = 250$ μm, using WC sphere $r = 1.98$ mm, illustrating the effect of indentation load: (a) $P = 800$ N, (b) $P = 1000$ N, (c) $P = 1500$ N, (d) $P = 2000$ N. Micrographs at center from bonded-interface specimens, Nomarski contrast. Arrows indicate contact diameter. Inner cracks initiate from coating/substrate interface, outer cracks from top surface, and intermediate cracks from within coating. Note the formation of a macroscopic quasi-plastic zone within the soft substrate at the higher loads. Corresponding FEM-generated contours of principal stresses included for comparison: left, principal shear stress, with shading indicating yield zones ($\sigma_3 - \sigma_1 = Y$); right, highest principal normal stress, shading indicating tensile zones ($\sigma_1 \geq 0$), dashed curves indicating σ_3 stress trajectories.

1500, and 2000 N, in Si_3N_4/Si_3N_4–30 wt% BN fixed composition bilayers with coating thickness $d = 250$ μm. The most conspicuous damage in the hard Si_3N_4 coatings is a variety of transverse cracks, increasing in number with load: outer cracks initiating at the top surface outside the contact circle, extending downward and outward, in near-classical cone crack manner;[16] inner cracks initiating from the coating/substrate interface closer to the inner contact axis, extending upward and inward;[5] cracks initiating within the coating beneath the contact circle, intermediate in radial location between the prior two types in Fig. 6(d), extending upward and inward toward the top surface and downward and outward toward the lower interface. Serial sectioning by polishing away the top indented surface confirms that all of these cracks are essentially axisymmetrical, with consequent common (if distorted) quasi-conical geometry. For the coating/substrate configuration shown in Fig. 6, the first cracks to appear are those initiated at the interface ($P < 800$ N), followed by those initiated within the coating ($P \approx 1000$ N), and finally those initiated at the top surface ($P \approx 1200$ N). A feature of the transverse cracks in Fig. 6 is that they appear to arrest as they approach the bounding surfaces of the coating, even through large load increases—the crack *density* is sensitive to load, crack *size* is not.

Substantial damage also occurs in the soft Si_3N_4–30 wt% BN substrates in Fig. 6. There are indications of extensive quasi-plasticity in this sublayer.[7,16] (Actually, limited quasi-plasticity is observed in the coatings as well, at higher magnification than in the micrographs in Fig. 6, especially at the higher loads.) Some accompanying cracking is also observed in the substrate, extending from the quasi-plastic damage zones and in some cases back to the interface. This combination of quasi-plasticity and cracking appears to contribute to minor interfacial delamination at the highest loads in Fig. 6. Control indentation tests on bulk Si_3N_4–30 wt% BN specimens reveal only quasi-plastic damage, without any such accompanying cracking, indicating again that it is the layer configuration that enhances the fracture tendency.

The damage patterns in Fig. 6 may be compared with the FEM-generated shear and tensile stress fields at left and right. The intensity and spatial scale of these stress fields expand with the indentation load. In the coating, the locations of transverse crack initiation correlate strongly with the regions of high tensile stress concentration, indicated by degree of shading. A primary maximum in the tensile field occurs at the intersection of the coating/substrate interface with the contact axis; a secondary maximum occurs at the top surface outside the contact circle; and a saddle point occurs between these two maxima. Only the second of these concentrations is manifest in the classical Hertzian field in homogeneous solids,[16,27] demonstrating again a significant influence of elastic–plastic mismatch on the stress distribution in the bilayer structure. The location of the surface maximum displaces increasingly beyond the contact circle with increasing load in Fig. 6, implying a progressive dilution of this maximum. Qualitatively, there also appears to be a correlation between the crack profiles and the FEM-generated stress trajectories[27] (although quantitatively, the trajectories are more steeply inclined to the top surface than the corresponding cracks by ≈5–10°, a discrepancy not atypical of Hertzian fractures[28]). This correlation confirms that the fractures are predominantly mode I.

In the substrate, the locations of the quasi-plasticity zones correlate with the FEM-predicted yield boundaries in the shear contour plots in Fig. 6. (Note also that the shear stress contours indicate limited yield in the coating at the higher loads, consistent with the high-magnification observations referred to above.) The substrate yield zones become extensive at the higher loads; the implication is that the harder coating on its softer substrate support base sustains an ever-increasing component of "plate flexure" in its loading.[4] The relatively minor cracking observed in the highly deformed anisotropic substrate layer does not appear to correlate quite as well with the tensile stress contour and trajectory patterns.

At higher loads, the damage intensifies and the system ultimately fails. An example is shown in Fig. 7 at $P \approx 4000$ N, in a bilayer with 20 wt% BN substrate. In this case we show the half-surface as well as the side view. Excessive cracking is apparent. Comprehensive damage has occurred in the substrate, resulting in material removal and coating failure. The coating itself exhibits strong residual flexure from yield and multiple cracking.

(2) Effect of Substrate Composition

Figure 8 shows micrographs of Hertzian contact damage in Si_3N_4/Si_3N_4–BN bilayers with 10, 20, and 30 wt% BN content in the substrate, for fixed coating thickness $d = 250$ μm and load $P = 2000$ N. In this sequence, the extent of transverse fracture in the coating and yield in the substrate increase markedly with BN content. Indeed, whereas the damage is well developed in the bilayer with 30 wt% BN substrate (Fig. 8(c), cf. Fig. 6(d)), the damage is only in its initiation stage in the bilayer with 10 wt% BN substrate (Fig. 8(a)). These results confirm most strongly the critical role of elastic–plastic mismatch in the damage mechanics. Again, the transverse fractures dominate delamination.

Comparison with the computed tensile and shear stress fields in Fig. 8 adds weight to the micrographic results. The intensity of both the coating tensile stress and substrate shear stress increases strongly with the elastic–plastic mismatch. Another manifestation of the mismatch is evident in the location of the primary maximum in the tensile field, at the top surface in the bilayer with 10 wt% BN substrate (as in the classical Hertzian field) but at the coating/substrate interface in the bilayer with 30 wt% BN substrate (cf. Fig. 11, later). Again, this implies an increasing component of plate flexure in the coating stress distribution with increasing mismatch. The yield boundaries in the shear field correlate with the sizes of the observed quasi-plasticity zones in the substrates.

(3) Effect of Coating Thickness

Figure 9 shows micrographs of Hertzian contact damage for diminishing Si_3N_4 coating thickness, $d = 1200$, 400 and 250

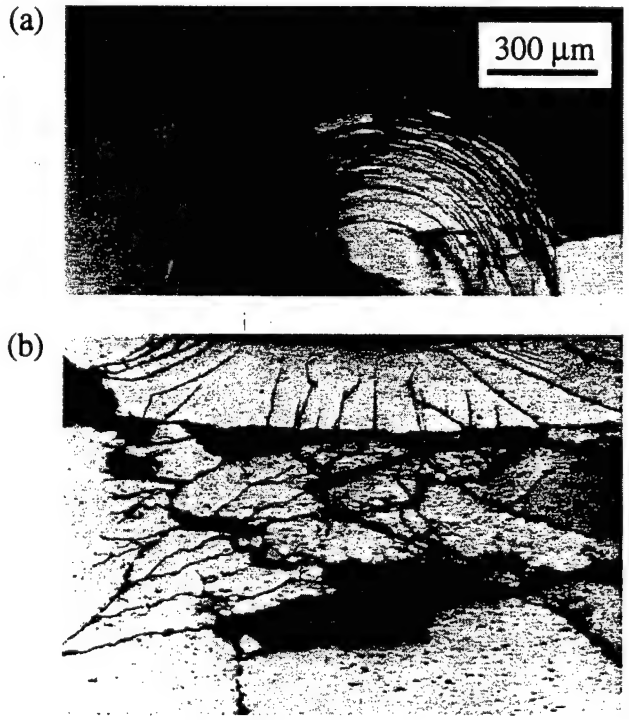

Fig. 7. Contact fracture in Si_3N_4/Si_3N_4–20 wt% BN bilayer composite, Si_3N_4 coating thickness $d = 250$ μm, using WC sphere $r = 1.98$ mm at $P = 4000$ N, showing half-surface (upper) and profile (lower) views. Note severe residual flexure of coating and coalescence of cracks leading to failure of coating and substrate.

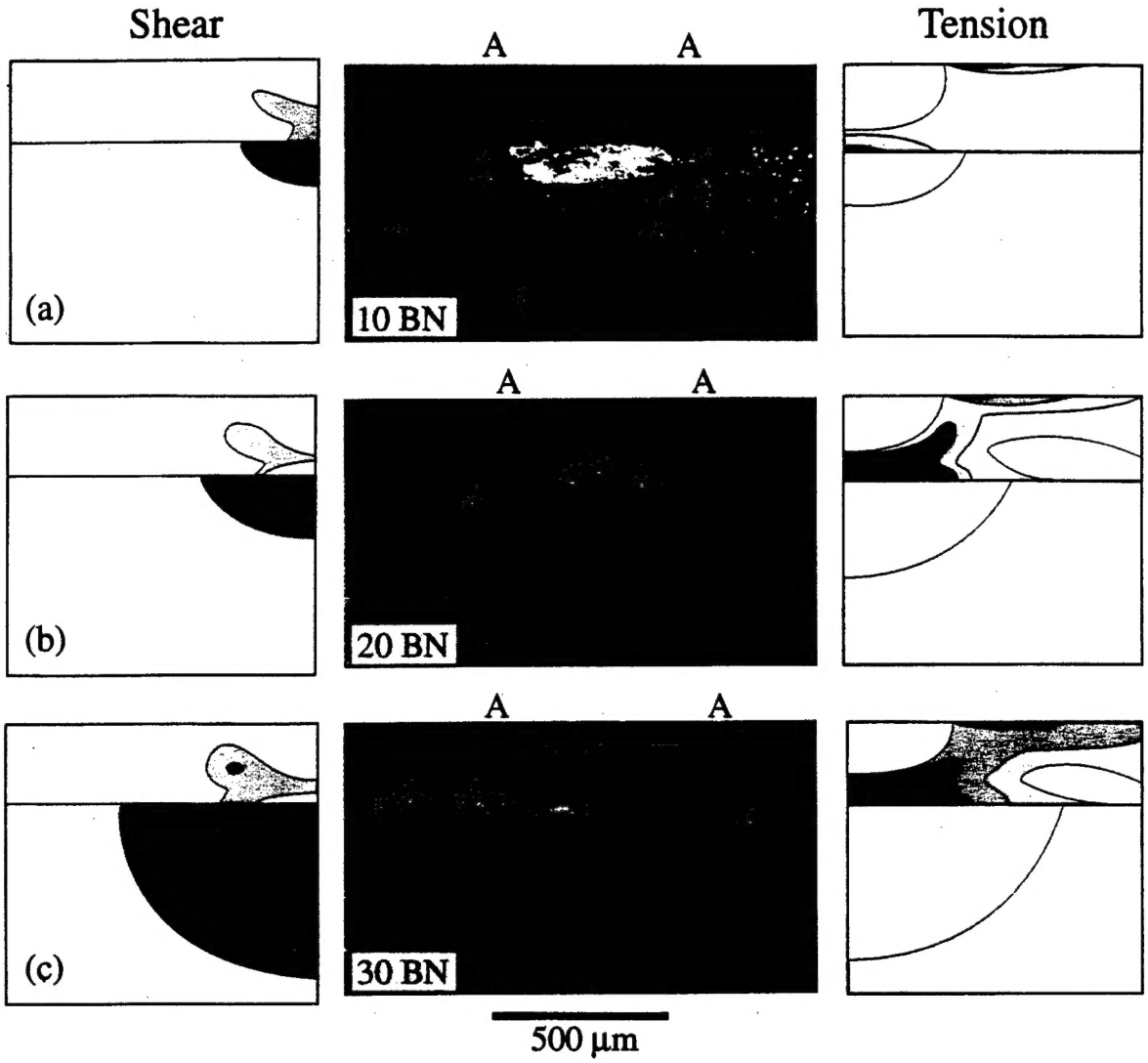

Fig. 8. Contact fracture in Si_3N_4/Si_3N_4–BN bilayer composites, Si_3N_4 coating thickness d = 250 μm, using WC sphere r = 1.98 mm at P = 2000 N, illustrating effect of substrate composition: (a) 10 wt% BN, (b) 20 wt% BN, (c) 30 wt% BN. Note increased damage at higher BN contents.

μm, in Si_3N_4/Si_3N_4–30 wt% BN fixed composition bilayers at fixed load P = 2000 N. No cracks are evident in the thickest coating (Fig. 9(a)): instead, the only damage is a limited subsurface quasi-plastic zone, akin to the damage seen in tougher monolithic Si_3N_4 materials.[16] In the coating of intermediate thickness (Fig. 9(b)) the quasi-plastic damage is suppressed in favor of transverse fractures, in this case in their early stage of formation. On the other hand, some quasi-plasticity is now evident in the soft substrate. In the thinnest coating (Fig. 9(c)) the transverse crack pattern is well developed (cf. Fig. 6(d)), and yield in the substrate is substantial. The influence of layer geometry in promoting fracture in the coating is apparent.

Comparison with the computed stress fields accounts for the observed transition in mechanical response with coating thickness. The coating thickness in Fig. 9(a) is large compared with the contact zone, so the damage is little influenced by the presence of the substrate. In this case the stress fields are virtually indistinguishable from those of an ideal Hertzian contact: the maximum tensile stresses are concentrated at the outer top surface, and the maximum shear stresses directly below the contact area. In Fig. 9(b) the coating thickness and contact zone size are comparable, and the substrate begins to influence the damage pattern. The tensile stresses at the coating/substrate interface are now slightly greater than those at the top surface, as reflected in the appearance of interface as well as surface transverse cracks in the micrograph. Some yield is now evident in the substrate. In Fig. 9(c) the coating thickness is smaller than the contact size, and the transverse crack pattern is well developed. The tensile stresses have intensified strongly at the coating/substrate interface. At the same time, the compression zones have also intensified, so the cracks, once initiated, are highly stabilized. This stabilization allows for the initiation of multiple transverse cracks. The yield zone in the substrate below the thin coating is now highly developed, implying once more an increased component of flexure in the overlying coating.

V. Discussion

In this study we have investigated the fracture behavior of silicon nitride bilayers with hard coatings of different thicknesses on softer substrates of different compositions. A feature of the bilayers is the presence of a relatively strong coating/substrate interface, where fracture energy is absorbed in the substrate rather than at the interface, with crack arrest rather than crack deflection.[5,6,12,13] We have used Hertzian contacts on bonded-interface specimens to demonstrate the damage modes in these structures—transverse cracks in the coating, and quasi-plasticity in the substrate. The transverse cracks initiate at various locations in the coating: at the top surface, outside the contact circle (as in classical Hertzian fractures); within the interior of the coating, closer in below the contact

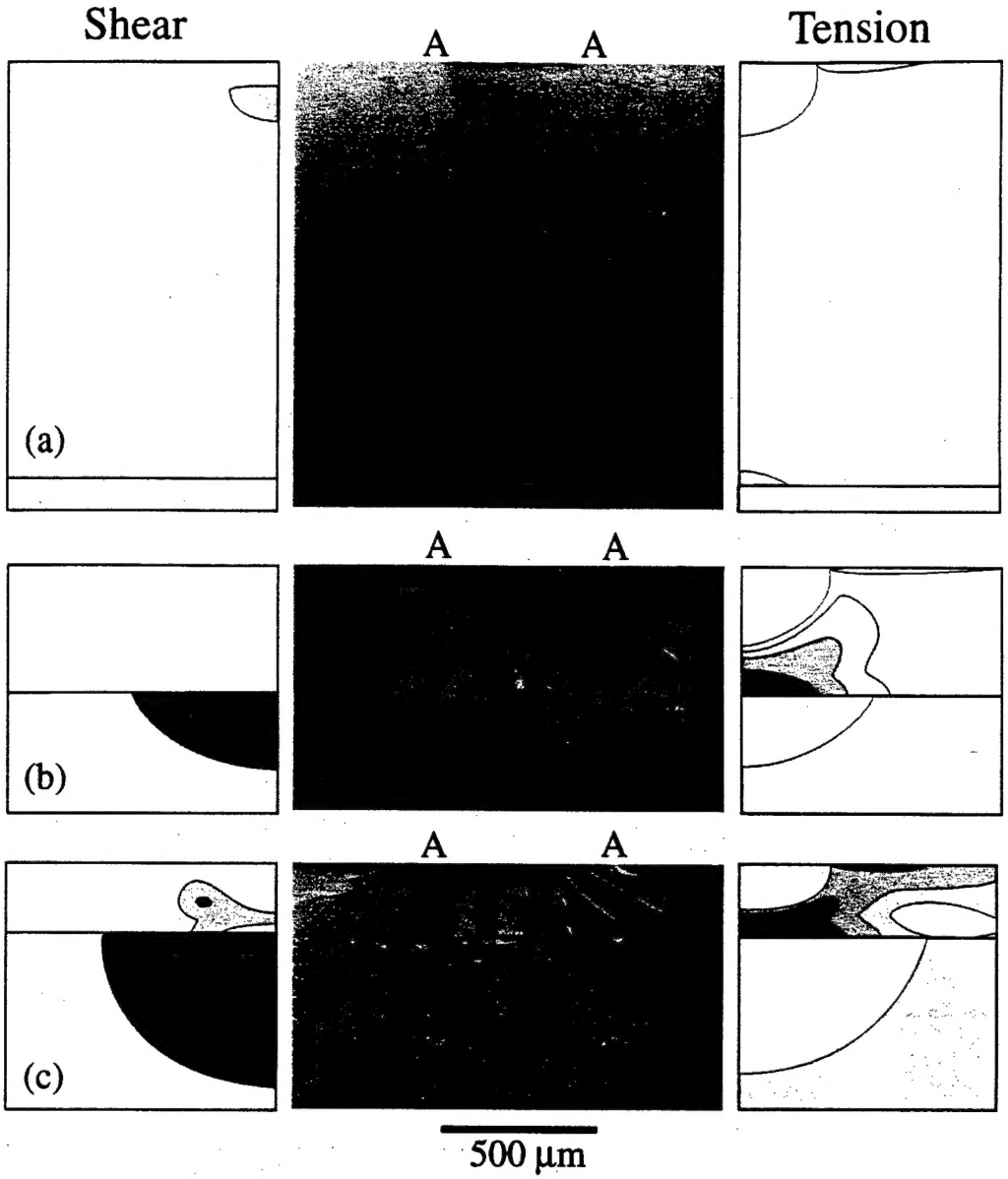

Fig. 9. Contact fracture in Si_3N_4/Si_3N_4–30 wt% BN bilayer composites, Si_3N_4, using WC sphere $r = 1.98$ mm at $P = 2000$ N, illustrating effect of coating thickness: (a) $d = 1200$ μm, (b) $d = 400$ μm, (c) $d = 250$ μm. Note increased damage at decreasing coating thickness.

circle; at the coating/substrate interface, immediately below the contact center. All three types are essentially axisymmetrical, with essentially quasi-conical geometry. There is a distinctive tendency away from surface-initiated toward interface-initiated fracture with increasing indenter load, decreasing coating thickness, and increasing elastic–plastic mismatch between layers.

The experimental observations in the bilayer structures are supported by FEM stress analysis, using calibrated elastic–plastic parameters from control tests on bulk constituent materials. For the coatings, we have demonstrated strong qualitative correlations between the calculated tensile stress extrema and the observed crack starting points, and between calculated stress trajectories and observed crack paths, implying predominantly mode I fracture. Some quantitative evaluations of the tensile stress maxima at the top surface and lower interface, for the same WC sphere radius $r = 1.98$ mm represented in Figs. 6–9, reinforce these correlations:

(i) Effect of indentation load. The solid curves in Fig. 10 are plots of the computed stress maxima as a function of load, for Si_3N_4 coating thickness $d = 250$ μm and Si_3N_4–30 wt% BN substrate. The points on these curves correspond to the experimental loads $P = 800$, 1000, 1500, and 2000 N in Fig. 6. Also indicated in Fig. 10 are the loads at which each kind of cracking initiates (C). Both maxima increase monotonically with load, the interface stress at a much faster rate than the surface stress. This is symptomatic of a highly nonlinear system (Fig. 4). Note that the interface maximum dominates the surface maximum above $P \approx 250$ N, explaining why the upward-extending interface cracks tend to form before the downward-extending surface cracks. The surface and interface stresses at the critical fracture loads in Fig. 10 are both significantly higher than the strengths of equivalent bulk Si_3N_4 monolith specimens (≈1000 MPa[16]), and are unequal, which is not atypical of crack systems in highly inhomogeneous stress fields.[29]

(ii) Effect of substrate composition. In Fig. 11 we show the tensile stress maxima as a function of substrate BN composition, for Si_3N_4/Si_3N_4–BN bilayers with Si_3N_4 coating thickness $d = 250$ μm at load $P = 2000$ N: again, the solid curves are the computed functions, and the data points correspond to the experimental BN contents 10, 20, and 30 wt% from Fig. 8. The interface stress maximum is sensitive to the BN content, but the surface stress maximum is not. This accounts for the increased density of upward-extending interface cracks for the 20% and 30% BN contents in Fig. 8. However,

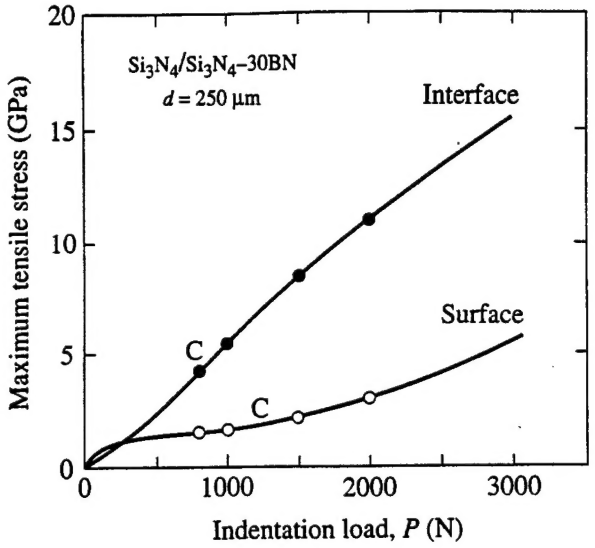

Fig. 10. Maximum principal tensile stresses in contact field in Si_3N_4/Si_3N_4–30 wt% BN bilayer composites as function of load, using WC sphere $r = 1.98$ mm. The two maxima shown occur at the top surface outside the contact and at the coating/substrate interface along the contact axis. Points C indicate onset of fracture. (Cf. Fig. 6.)

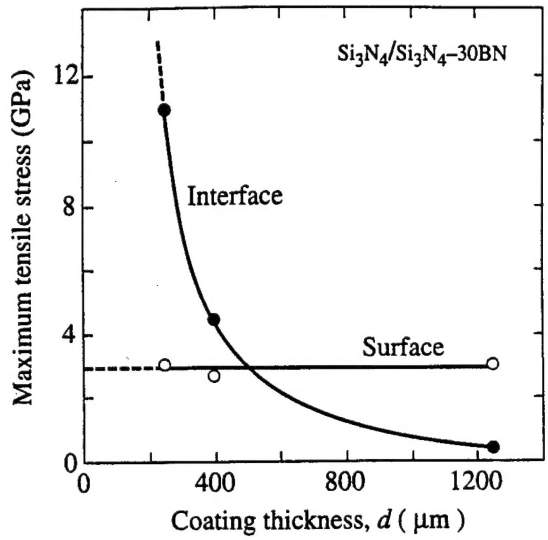

Fig. 12. Maximum principal tensile stresses in contact field in Si_3N_4/Si_3N_4–30 wt% BN bilayer composites as function of coating thickness, using WC sphere $r = 1.98$ mm at $P = 2000$ N. Dashed curves are extrapolations back to values at same locations in Si_3N_4 monolithic material. (Cf. Fig. 9.)

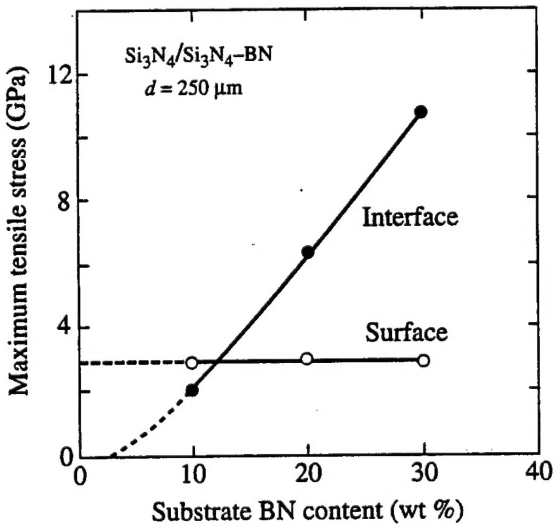

Fig. 11. Maximum principal tensile stresses in contact field in Si_3N_4/Si_3N_4–BN bilayer composites with coating thickness $d = 250$ μm as function of BN composition in substrate, using WC sphere $r = 1.98$ mm at $P = 2000$ N. Dashed curves are extrapolations back to values at same locations in Si_3N_4 monolithic material. (Cf. Fig. 8.)

it does not account for the comparable increase in downward-extending surface cracks. It would appear that initiation of the first kind of cracks (interface) makes it easier to initiate the second (surface)—i.e., there are interaction effects. These observations highlight the influence of elastic–plastic mismatch.

(iii) Effect of coating thickness. In Fig. 12 we plot the tensile stress maxima as a function of Si_3N_4 coating thickness for Si_3N_4/Si_3N_4–30 wt% BN bilayers, at load $P = 2000$ N: the solid curves are the computed functions and the data points correspond to the experimental d values in Fig. 9. In similar fashion to Fig. 11, the interface stress maximum is sensitive to coating thickness, but the surface stress maximum is not. The interface maximum becomes increasingly dominant at smaller thicknesses. Accordingly, the density of upward-extending interface-initiated cracks, and subsequent accompanying interior-initiated and surface-initiated cracks, is considerably higher in the thinner coatings in Fig. 9.

These results indicate the changing nature of the coating tensile stress field from ideal "Hertzian" to effectively "flexural" with increasing load, decreasing substrate hardness relative to the coating (mismatch), and decreasing coating thickness. At high loads hard, thin coatings on thick, soft substrates deform more as flexing plates with supported outer edges (where the encasing substrate remains elastic), shifting the tensile stress concentration progressively away from the upper outer free surface through the coating interior toward the lower coating/substrate interface.[3,4,7,21,22] At the same time, the flexure induces highly compressive stresses on the opposing sides of the neutral planes within the coating. The result is the arrays of highly stabilized transverse coating fractures seen in Figs. 6–10.

The quantitative analysis of the crack systems described here is by no means complete. The FEM algorithm enables one to investigate prescribed indentation and coating variables (load, mismatch, coating thickness) numerically. The complexity of the highly nonlinear and inhomogeneous tensile stress fields would appear to preclude analytical fracture mechanics solutions. Moreover, even the elastic–plastic FEM solutions described in Sections III and IV are restrictive. They pertain strictly to uncracked bodies, whereas the coatings considered here contain multiple cracks. The capacity of fracture mechanics to determining ensuing crack energies and paths from pre-existing (precrack) contact fields in finite bodies with an acceptable degree of accuracy has been shown to be limited, even for single cone fractures in monolithic, homogeneous elastic bodies.[28] Such limitations are likely to be even more apparent in the multiple crack systems in the layered, inhomogeneous inelastic bodies of interest here. More objective numerical procedures that enable piecewise determinations of crack growth in the ever-evolving rather than the prior stress field would appear to be necessary for the determination of appropriate mechanical-energy-release rates or stress-intensity factors.[28] This is especially the case in determining crack evolution histories, and in seeking accounts of the enhanced crack stability and multiplicity in thinner coatings on softer substrates.

There are other potential complications that we have minimized in this study. First, macroscopic in-plane layer residual stresses from thermal expansion mismatch or sintering stresses can also have a strong influence on the crack behavior, leading to suppression of coating fracture in favorable circumstances.[12,13] In our bilayer systems such in-plane stresses ap-

pear to be negligibly small (Section III(2)). Second, local residual tensile stresses around indentation quasi-plasticity zones are known to have profound effects on crack evolution during unloading,[30,31] especially in layer structures with yielding substrates; whereas residual stresses do not appear to have much influence on the transverse cracks, they can be especially effective in opening up any interfacial delamination cracks during the unloading half-cycle.[4] The observation that delamination is minimal in our silicon nitride bilayer systems provides some justification for ignoring unloading effects in our FEM calculations. Finally, anisotropy is another factor that can exert a strong influence on fracture behavior. The highly textured microstructures in the Si_3N_4–BN bilayers may explain the tendency for substrate cracks to align themselves parallel to the interface in Figs. 6–9.

The crack patterns identified in this study are of interest in relation to engineering layer design. Transverse cracks may be expected to play a major role in the failure of ceramic coating structures where contact stress concentrations are a common form of loading, e.g., in bearings, cutting tools, surface-coated engine components, and so on. This class of cracks is particularly relevant to layer structures with strongly bonded coating/substrate interfaces. In this context, the transverse cracks are highly stable, leading to multiple initiation with consequent energy absorption, so that even highly brittle coating systems can be damage tolerant. (Again, superposed compression stresses could help reduce or even suppress transverse coating fracture.) This high stability means that the crack sizes are governed more by the layer thickness than by material properties; the cracks tend to contain themselves within the boundaries of the coating over a wide range of contact loads. On the other hand, initiation of the cracks will surely be sensitive to material properties, such as elastic–plastic mismatch (e.g., Fig. 8) and coating toughness. For optimum substrate protection the present results indicate hard, tough coatings with low elastic–plastic mismatch, with thicknesses at least as large as the characteristic contact dimensions. As always, these requirements must ultimately be balanced against the costs of fabrication and finishing.

Acknowledgments: K. S. Lee and S. Wuttiphan wish to thank Do Kyung Kim at the Korea Advanced Institute of Science and Technology and Isabel K. Lloyd at the University of Maryland for their encouragement and support. Ralph F. Krause assisted with the hot pressing of the silicon nitride structures. Anthony C. Fischer-Cripps set up the original finite element algorithm used in this study. Shi-Woo Lee and Jae-Hun Kim assisted with the plasma etching and SEM analysis.

References

[1]J. C. Knight, T. F. Page, and I. M. Hutchings, "The Influence of Substrate Hardness on the Response of TiN-Coated Steels to Surface Deformation," *Thin Solid Films*, **177**, 117–32 (1989).

[2]M. V. Swain and J. Mencik, "Mechanical Property Characterization of Thin Films Using Spherical Tipped Indenters," *Thin Solid Films*, **253**, 204–11 (1994).

[3]A. Pajares, L. Wei, B. R. Lawn, N. P. Padture, and C. C. Berndt, "Mechanical Characterization of Plasma-Sprayed Ceramic Coatings on Metal Substrates by Contact Testing," *Mater. Sci. Eng.*, **A208** [2] 158–65 (1996).

[4]A. Pajares, L. Wei, B. R. Lawn, and C. C. Berndt, "Contact Damage in Plasma-Sprayed Alumina-Based Coatings," *J. Am. Ceram. Soc.*, **79** [7] 1907–14 (1996).

[5]L. An, H. M. Chan, N. P . Padture, and B. R. Lawn, "Damage-Resistant Alumina-Based Layer Composites," *J. Mater. Res.*, **11** [1] 204–10 (1996).

[6]S. Wuttiphan, B. R. Lawn, and N. P. Padture, "Crack Suppression in Strongly-Bonded Homogeneous/Heterogeneous Laminates: A Study on Glass/Glass-Ceramic Bilayers," *J. Am. Ceram. Soc.*, **79** [3] 634–40 (1996).

[7]H. Liu, B. R. Lawn, and S. M. Hsu, "Hertzian Contact Response of Tailored Silicon Nitride Multilayers," *J. Am. Ceram. Soc.*, **79** [4] 1009–14 (1996).

[8]A. G. Evans and J. W. Hutchinson, "On the Mechanics of Delamination and Spalling in Compressed Films," *Int. J. Solids Struct.*, **20** [5] 455–66 (1984).

[9]J. B. Davis, H. C. Cao, G. Bao, and A. G. Evans, "The Fracture Energy of Interfaces: An Elastic Indentation Technique," *Acta Metall.*, **39** [5] 1019–24 (1991).

[10]J. W. Hutchinson and Z. Suo, "Mixed-Mode Cracking in Layered Structures," *Adv. Appl. Mech.*, **29**, 64 (1991).

[11]W. J. Clegg, K. Kendall, N. M. Alford, T. W. Button, and J. D. Birchall, "A Simple Way to Make Tough Ceramics," *Nature (London)*, **347**, 455–57 (1991).

[12]O. Prakash, P. Sarkar, and P. S. Nicholson, "Crack Deflection in Ceramic/Ceramic Laminates with Strong Interfaces," *J. Am. Ceram. Soc.*, **78** [4] 1125–27 (1995).

[13]H. M. Chan, "Layered Ceramics: Processing and Mechanical Behavior," *Annu. Rev. Mater. Sci.*, **27**, 249–82 (1997).

[14]H. Liu and S. M. Hsu, "Fracture Behavior of Multilayer Silicon Nitride/Boron Nitride Ceramics," *J. Am. Ceram. Soc.*, **79** [9] 2452–57 (1996).

[15]B. R. Lawn, N. P. Padture, H. Cai, and F. Guiberteau, "Making Ceramics 'Ductile'," *Science*, **263**, 1114–16 (1994).

[16]S. K. Lee, S. Wuttiphan, and B. R. Lawn, "Role of Microstructure in Hertzian Contact Damage in Silicon Nitride: I, Mechanical Characterization," *J. Am. Ceram. Soc.*, **80** [9] 2367–81 (1997).

[17]H. Cai, M. A. Stevens Kalceff, and B. R. Lawn, "Deformation and Fracture of Mica-Containing Glass-Ceramics in Hertzian Contacts," *J. Mater. Res.*, **9** [3] 762–70 (1994).

[18]F. Guiberteau, N. P. Padture, H. Cai, and B. R. Lawn, "Indentation Fatigue: A Simple Cyclic Hertzian Test for Measuring Damage Accumulation in Polycrystalline Ceramics," *Philos. Mag. A*, **68** [5] 1003–16 (1993).

[19]D. Tabor, *Hardness of Metals*. Clarendon, Oxford, U.K., 1951.

[20]A. C. Fischer-Cripps and B. R. Lawn, "Indentation Stress–Strain Curves for "Quasi-Ductile" Ceramics," *Acta Metall.*, **44** [2] 519–27 (1996).

[21]A. C. Fischer-Cripps, B. R. Lawn, A. Pajares, and L. Wei, "Stress Analysis of Elastic–Plastic Contact Damage in Ceramic Coatings on Metal Substrates," *J. Am. Ceram. Soc.*, **79** [10] 2619–25 (1996).

[22]S. Wuttiphan, A. Pajares, B. R. Lawn, and C. C. Berndt, "Effect of Substrate and Bond Coat on Contact Damage in Zirconia-Based Plasma Coatings," *Thin Solid Films*, **293** [1–2] 251–60 (1997).

[23]K. Komvopolous, "Elastic-Plastic Finite Element Analysis of Indented Layered Media," *J. Tribol.*, **111**, 430–39 (1989).

[24]P. Montmitonnet, M. L. Edinger, and E. Felder, "Finite Element Analysis of Elastoplastic Indentation: Part II—Application to Hard Coatings," *J. Tribol.*, **115**, 15–19 (1993).

[25]M.-W. He and J. W. Hutchinson, "Crack Deflection at an Interface Between Dissimilar Elastic Materials," *Int. J. Solids Struct.*, **25** [9] 1053–67 (1989).

[26]T. J. Lardner, J. E. Ritter, M. L. Shiao, and M. R. Lin, "Behavior of Indentation Cracks Near Free Surfaces and Interfaces," *Int. J. Fract.*, **44**, 133–43 (1990).

[27]F. C. Frank and B. R. Lawn, "On the Theory of Hertzian Fracture," *Proc. R. Soc. London*, **A299** [1458] 291–306 (1967).

[28]C. Kocer and R. E. Collins, "The Angle of Hertzian Cone Cracks," *J. Am. Ceram. Soc.*, in press.

[29]B. R. Lawn and T. R. Wilshaw, "Indentation Fracture: Principles and Applications," *J. Mater. Sci.*, **10** [6] 1049–81 (1975).

[30]D. B. Marshall and B. R. Lawn, "Residual Stress Effects in Sharp-Contact Cracking: I. Indentation Fracture Mechanics," *J. Mater. Sci.*, **14** [8] 2001–12 (1979).

[31]B. R. Lawn, A. G. Evans, and D. B. Marshall, "Elastic/Plastic Indentation Damage in Ceramics: The Median/Radial Crack System," *J. Am. Ceram. Soc.*, **63** [9–10] 574–81 (1980). □